Structure Borne Sound In Motor-vehicles using Statistical Energy Analysis

By

Grant Fraser

This Thesis is submitted in accordance with
the requirements of Heriot-Watt University for
the degree of Doctor of Philosophy.

Department of Mechanical and Chemical Engineering
Heriot-Watt University

May 1998

Contents

List of Figures

Chapter 2

Chapter 3

Chapter 4

Chapter 5

Chapter 6

List of Tables

List of Symbols and Abbreviations

a	Acceleration (m/s^2) or Radius (m)
B	Plate bending stiffness (Nm)
c_B	Bending wave speed (m/s)
c_L	Longitudinal wave speed (m/s)
c_0	Speed of sound in air (343 m/s at 20°C)
c_T	Transverse wave speed (m/s)
C_g	Group velocity (m/s)
CLF	Coupling Loss Factor (dB re 10^{-12})
C(95%)	95% confidence intervals
C	WIA conversion matrix
d	Depth of cavity (m)
D	Longitudinal stiffness parameter (N/m^2)
$\mathbf{e}_D$	Energy vector
$\mathbf{e}_F$	Energy vector
E	Young's modulus (N/m^2) or energy (J)
E_ρ	Energy density (J/m^3)
E_{tot}	Sum of kinetic and potential energy (J)
E_{peak}	Peak kinetic energy (J/m^3)
E_n	Energy of subsystem n (J)
ELD	Energy Level Difference (dB)
f	Frequency (Hz)
f_n	n th natural Frequency (Hz)
f_c	Critical frequency (Hz)

f_R	Plain strain ring frequency of curved panel (Hz)
Δf	Average modal frequency spacing $=1/n$ (Hz)
F	Force (N)
F_x	Force in x direction (N)
$\mathbf{f}$	Force vector
g	Coupling parameter
$\langle g \rangle$	Average coupling parameter
G	Modulus of rigidity (N/m^2)
h	Thickness (m)
i	$\sqrt{-1}$
I	2^{nd} Moment of area (m^4)
ILF	Internal Loss Factor
k	Wave number (rad/m) or Spring stiffness (N/m)
k_x	Wave number component in x direction (rad/m)
k_B	Bending wave number (rad/m)
k_0	Wave number in air
l	Length (m)
$\mathbf{L}_D$	Power flow coefficient matrix
L_E	Energy Level (dB re 10^{-12} J)
L_v	Velocity level (dB re 10^{-6} m/s)
m	Mass (kg) or Mass per length (kg/m) or Surface density (kg/ m^2) or Correction factor or Any integer
$m^2_{v_2^2}$	Mean mean square velocity of an ensemble of subsystems similar to subsystem number two
M	Modal overlap factor or Bending moment (Nm)
n	Modal density (modes/Hz) or Any Integer
N	Number of resonant modes
p	Power flow (J/s)
P	Pressure (N/m^2)
$\hat{P}$	Magnitude of pressure (N/m^2)
$\langle p^2 \rangle$	Mean square pressure $(N/m^2)^2$
$\mathbf{p}_D$	Power vector

$\mathbf{p}_F$	Power vector
r_-	Complex magnitude of bending wave travelling in a -ve direction
r_+	Complex magnitude of bending wave travelling in a +ve direction
R	Mechanical Resistance (Ns/m)
S	Area (m^2)
SBA	Sound Barrier Assembly
SEA	Statistical Energy Analysis
SPL	Sound Pressure Level (dB re 20μ N/m^2)
t	Time (s) or Complex magnitude of transmitted bending wave
T	Time (s)
T_{60}	Reverberation time (s)
TL	Transmission Loss (dB)
TLF	Total Loss Factor (dB re 10^{-12})
$\langle v^2 \rangle$	Mean square velocity $(m/s)^2$
V	Volume (m^3)
v	Velocity (m/s)
$\|v\|$	Amplitude of velocity (m/s)
v^*	Complex conjugate of velocity
$\mathbf{v}$	Velocity vector
$\mathbf{v}^{*T}$	Transpose of complex conjugate of velocity vector
ω	Frequency (rad/s)
ω_n	n th natural Frequency (rad/s)
w	Angular velocity (rad/s)
W	Mechanical moment impedance (Nms)
x, y, z	Axes
Y	Mechanical mobility (m/Ns)
$\mathbf{Y}$	Mobility matrix
$\mathbf{Z}$	Impedance matrix
Z	Mechanical impedance (Ns/m)
ξ	Displacement (m)
ξ_α	Modal energy of mode α (J)

η	Displacement (m) or Damping loss factor
η_{rad}	Radiation loss factor
η_{12}	Coupling Loss Factor from subsystem 1 to 2
$\eta_{1,\,net}$	Net loss Factor of subsystem 1
$\hat{\eta}$	Amplitude of displacement (m)
n_-	Complex magnitude of bending near field decaying in a -ve direction
n_+	Complex magnitude of bending near field decaying in a +ve direction
μ	Poisson's ratio or Frequency ratio $\mu = (f / f_C)^{1/2}$
σ	Radiation efficiency
σ_x	Stress in the x direction (N/m^2)
$\sigma^2_{v_z^2}$	Standard deviation of temporal mean square velocity
λ_l	Longitudinal wavelength (m)
λ_B	Bending wavelength (m)
ε_z	Strain in the z direction
ρ	Density (kg/m^3)
Δ	Laplace differential operator
$\Delta\omega$	Half power or Resonant bandwidth (rad/s)
α	Surface acoustic absorption coefficient
$\phi_n(x,z)$	n the mode shape function of a panel
$\langle\psi^4\rangle / \langle\psi^2\rangle^2$	Modal shape factor
χ	Ratio of bending wave numbers
ψ	Ratio of bending wave impedance's
τ	Transmission coefficient
$\langle\tau\rangle$	Average transmission coefficient
Ψ	Wave heading (rad)
θ	Wave heading (rad)

Acknowledgements

I would like to acknowledge the advice and assistance of my supervisor Dr John Steel who could not have been more helpful during this project. A number of experimental apparatus were constructed during this work and I would like to thank David Calderwood for assisting me with this. I would also like to express my gratitude to the Nissan European Technology Centre, in particular Peter Sendall for arranging the loan of the Nissan Micra and technical advice given during this work. I am grateful to my family without who's support I could not have completed this thesis. Finally I would like to thank the Alexander Neilson Bequest for funding this research.

Abstract

This Thesis is about the application of Statistical Energy Analysis (SEA) to the study of noise and vibration in motor vehicles. Methods for predicting the transmission of structural waves between body panels in motor cars are given. A complex joint technique based on the wave dynamic stiffness approach is discussed in detail. This technique can account for the complexities of the joint structures found in motor vehicles.

Transmission of vibration energy between panels connected by a curved section of panel has been investigated using the complex joint modelling technique. Wave Intensity Analysis(WIA) and SEA were used to calculate the coupled panel vibration levels based on transmission coefficients calculated using the complex joint techniques. Energy Level Differences (ELDs) were measured for comparison with predicted results using laboratory models. SEA failed to accurately predict the ELDs except at low frequencies. However WIA was able to predicted the ELDs with reasonable accuracy using an existing expression for transmission at a panel corner joint.

Two SEA models of a small passenger car have also been constructed. One assumes simpler joint configurations when calculating transmission coefficients and the other uses the complex joint technique. Panel ELDs were measured using a small passenger car. The SEA model using the complex joint method gives better agreement with measured ELDs than did the model using the simpler joints. saloon Sound Pressure Level (SPL) as a result of engine noise was measured. Both SEA models of the vehicle gave good agreement between measured and predicted Saloon SPL. A noise problem associated with exhaust misalignment is also investigated.

Chapter 1

Introduction

1.1 General Introduction

Noise is a problem in cars. Damping treatments, sound barriers and absorbers are used to reduce the noise levels. Optimising these measures in terms of effectiveness, cost and weight requires measurement and/or prediction of their effects upon the noise levels. Predictive techniques have the advantage that they can be used with design drawings before a complete vehicle is constructed. Deterministic methods such as Boundary Element Methods (BEM) and Finite Element Methods (FEM) are currently used to predict noise levels below around 200Hz. At these frequencies resonant behaviour of the saloon volume, body and drive train often cause noise and vibration problems. At higher frequencies the number of structural and acoustic modes increase and deterministic methods require excessive computation. Statistical Energy Analysis (SEA) offers an alternative to deterministic methods for analysing complex structures at high frequencies. SEA requires typically only a small fraction of the computation needed for BEM of FEM. Car manufacturers have recently started using SEA to predict mid to high frequency (200-16000Hz) noise levels and the use of SEA in cars is currently an area of considerable research interest.

This chapter examines the existing literature concerning Statistical Energy Analysis and more specifically its use in quantifying the structural and acoustic response in modern motor vehicles. Many of the methods used to quantify the transmission of sound and vibration within an SEA framework pre date SEA itself. These methods and their more recent counterparts are reviewed before moving on to SEA itself. Transmission of structure borne vibration is covered first. When dealing with a mechanical structure in air it is often possible to ignore the effect of the air on the structure. Mid to high frequency vibrations are heard rather than felt in a motor vehicle, and airborne sound levels must be calculated. Work published on sound radiation and absorption by structures is reviewed in this chapter along with some of the more recent developments specifically relevant to the motor vehicle. A brief history of SEA is given followed by a review of some existing

studies on motor vehicles of which there are an ever increasing number. Some recent developments upon SEA are also discussed followed by an outline of the thesis.

1.2 Structure Borne Sound

Structural vibrations within the audible frequency range (16-16000Hz) are commonly referred to as structure borne sound. Cremer [1] presents a number of techniques developed for calculating structural response and transmission. Expressions for estimating wave transmission at joints between plates, beams and rods connected by various junction arrangements are given. The propagation of bending longitudinal and transverse waves on panels is examined. Transmission across panel junctions with beams or elastic layers along the length of the joint are also considered. Cremer [1] also gives mobility values for a number of structures such as infinite plates and beams. The real part of mechanical mobility is known as conductance. If the conductance matrix of a structure is known then the power flowing into it as a result of excitation can be calculated. Wave transmission between connected structures may often be calculated if the mobility of each structure is known.

The usefulness of expressions for structural mobility in calculating structural transmission and power inputs has encouraged work in this area. Eichler [2] calculated the plate edge admittance (mobility) matrix for two moments about in-plane axes and a transverse force. Unlike an infinite plate these moments and forces are coupled and applying transverse force will cause rotation at the edge.

Structures such as ships buildings and automobiles are often reinforced with built in beams. Machinery foundations in ships, buildings and engine mounting points in cars are typically constructed in this manner and knowledge of their impedance is useful in calculating vibration power flow into the structure. The impedance of plate beam assemblies have been examined by Lamb [3] for a transverse force and by Goyder&White [4] for forces and moments.

In many engineering structures vibration transmission is mainly between panels joined along a common boundary. This is also true of building structures and has encouraged the development of models for calculating wave transmission coefficients through various panel arrangements. A number of authors (for example [5,6,7]) have produced models for

panel junctions accounting for in-plane waves in some or all of the connected panels. These studies have all used similar methods to those described by Cremer [1].

Langley&Heron [8] have described a "wave dynamic stiffness matrix" technique to predict transmission of bending, longitudinal and transverse waves across junctions where an arbitrary number of flat panels meet at arbitrary angles. An optional beam stiffener with or without offset can be included at the joint. This work and the subsequent paper by Langley [9] which included the possibility of curvature of the panels represent one of the most flexible approaches to modelling complicated joints quickly and accurately.

Mees&Vermeir [10] considered panels joined by an elastic layer along the boundary. They improved upon Cremers [1] prediction for transmission in two ways. Oblique incidence of the waves was introduced and a more elaborate model of the elastic layer is presented. Cremer [1] modelled the elastic layer as a simple element with bending shear and longitudinal stiffness, this model is used by Mees&Vermeir [10] but another model which considers the elastic layer to be a wave baring structure is also given. The measured and predicted results for the wave bearing model show the presence of the first shear resonance of the interlayer. In calculating the stiffness of the elastic layer both Mees&Vermeir [10] and Cremer [1] made assumptions about the way it distorts under an applied load. Mees&Vermeir [10] stated that their original intention was to use a detailed FEM model of the layer for calculating the various stiffness terms required. They concluded however that the computation required was excessive because of the number of elements and the fact that the model would have to be re-run for every frequency/wave heading combination.

Bosmans,Mees&Vermeir [11] calculated bending wave transmission across a ridged 'L' junction between orthotropic plates. In the same paper they also calculated the structure borne sound by means of modal analysis of two finite orthotropic panels. In both cases they showed the results to be very similar to those for isotropic panels when the modulus of elasticity in the two principle directions are within a factor of two. This work was primarily aimed at building acoustics but some panels in motor vehicles are stiffened by slight corrugations which introduces orthotropic behaviour with increased bending stiffness about an axis perpendicular to the corrugation.

Fraser&Steel [12] describe a technique based on the wave dynamic stiffness approach of Langley&Heron [8], Langley [9] and Heron [93] for predicting wave transmission between panels connected by complex joint structures. The joint structure is built up from simple elements in a similar way to the FEM. This technique was used to predict transmission across the roof to windscreen joint of a small motor vehicle. Predicted Coupling Loss Factors (CLF) for the windscreen joint showed reasonable agreement with experimental results. Finite strip elements for flat and rounded panel sections were assembled to form the joint along with the simple elastic layer of Mees&Vermeir [10]. Complex joints of the sort found in modern motor vehicles which may exhibit resonant behaviour can be rapidly and easily modelled using this approach.

De Langhe *et al* [13,14,15] have demonstrated the use of Finite Element Analysis for calculating wave transmission coefficients between beams and plates. SEA CLFs may be calculated from these transmission coefficients. FEA has been used to calculate CLFs before [16, 17] usually to explain why measured results vary from or fluctuate about SEA predictions. The difference in this work is that only the joint structure need form part of the FEM. Wave absorbing elements were used to represent the boundaries of the subsystems into and out of which the waves flow. Only the joints between the SEA subsystems and not the subsystems themselves need appear in the FE model so a large reduction in computational expense is achieved. The advantage of this method over that described by Langley&Heron [8] is that joints of finite length and changing cross section can be modelled. A method of this sort would be well suited to modelling motor vehicle structures as they are complex in nature and the panel joint structures frequently change in cross section along their length.

1.3 Sound Transmission

There exist several theories that predict the transmission of airborne sound through a thin panel of infinite extent. The first was advanced by Lord Rayliegh[18]. The most widely known are the various mass laws so called because they indicate that only the mass of the panel significantly affects the transmission. This is only valid well below the critical or coincidence frequency, defined as the frequency at which panel bending waves travel with the same velocity as the airborne sound. Normal incidence mass law, as the name suggests, calculates the wave transmission coefficient for waves incident normal to the panel. Diffuse field mass law gives an average over all angles of incidence. Field incidence law is an empirical adjustment to the diffuse field by assuming incidence

between 0 and 78° to normal. This was introduced as it generally gives better agreement with measured results and was justified by the assertion that near grazing incidence waves are unlikely to have a significant intensity in a real acoustic space. Cremer [19] (Also given by Fahy [20]) derived an expression for the diffuse field sound reduction index above the critical frequency which depends upon the panel damping as well as mass. This is because above the critical frequency transmission is predominantly as a result of resonant behaviour in the panel, the amplitude of which is partly limited by panel internal damping. Fahy [20] explains most of the sound transmission and radiation theories described above. Sewell [21] and Leppington *et al* [22] have calculated expressions for the diffuse field transmission through rectangular panels of finite size and have shown better agreement with measured data than the mass law predictions with no need for the "*ad-hoc*" assumption that there are no waves incident above 78° to normal.

In structures such as aircraft and cars weight is at a premium and methods of reducing transmission without incurring the mass law weight penalty have been developed. These include double panel construction and or the use of sound absorbing materials. Fibrous mineral wool or polyurethane foam are the most frequently used as sound absorbers in motor vehicles. Beranek&Work [23] presented a method for predicting the normal transmission of sound through multiple panel structures of infinite extent with "flexible blankets" and air spaces. They used results from an earlier paper by Beranek [24] which examined the properties of porous sound absorbing fibre blankets. Two longitudinal wave types were considered in the blanket one predominantly in the fibres of the blanket and the other mostly in the air between the fibres. Crocker&Price [25] have used SEA to predict transmission through double panel structures with sound absorbing materials in the cavity as have Craik&Wilson [26]. That work [25, 26] was primarily studying cavity walls in buildings. Bolton *et al* [27] have published the most complete theory to date for predicting sound transmission through infinite multi-panel structures lined with elastic porous material. In their theory oblique wave incidence is included so that three wave types exist in the foam, longitudinal and transverse waves propagate primarily in the solid skeleton and a longitudinal wave primarily in the air within the skeleton. The seven material parameters used to characterise the foam were estimated by matching measured and predicted impulse response as described in Bolton&Green[28]. Foam is frequently used in modern motor vehicles to attenuate engine noise passing through the bulkhead or

fire wall between the engine compartment and the passenger compartment. The techniques used by Bolton *et al* [27] are suitable for the analysis of this problem.

Wentzel&Saha[29] give an empirical method for calculating the transmission loss across the Sound Barrier Assembly (SBA) used in a car. These assembles consist of a foam or fibrous layer attached to a limp impervious sheet of PVC or similar material. Such an assembly is applied to the fire wall between the engine compartment and the saloon and sometimes to the inside floor of the vehicle. The foam or fibrous isolator is always towards the body of the car with the PVC barrier facing into the vehicle. In that paper only transmission below the critical frequency was modelled. The analysis does not concern its self with the detailed behaviour of the material and the waves travelling in it. Instead single and double panel mass law expressions are used below and above the double wall resonance frequency respectively. The double wall resonance frequency is calculated by modelling the double wall as a mass spring mass system with air between the walls acting as a spring. Three frequency regions are identified. The lowest frequency range is the coupled mass region in which the panel and the SBA move as one and mass law may be used. The upper frequency range is known as the Double Wall Decoupled (DWD) region. In the DWD region the transmission loss (TL) is assumed to be the sum of the mass law TL for the body panel and the barrier. In between the coupled mass region and the DWD region there is a transition region. Attenuating effects of the isolator material were included by measuring the insertion loss (IL) of several thickness' of material when attached to a steel panel. An insertion loss may then be extrapolated from the measured data and added to the predicted transmission loss for the DWD region. Transmission Loss was measured for 60 samples having different combinations of isolator material and thickness with barriers of various densities were measured between 125Hz and 5kHz. Predicted results showed good agreement with measured results but were consistently 5dB high in the DWD frequency region. This discrepancy was said to be due to resonance effects in the isolator which were not modelled and an empirical 5dB adjustment was introduced. Measured results showed good agreement with the adjusted predictions. The theory presented in that work is not detailed but the experimentally derived adjustment makes the results very useful for calculating transmission losses across similarly constructed sound barriers in cars.

1.4 Sound Radiation and Response

When a structure vibrates and is in contact with a fluid such as air sound can be radiated from the structure. In most thin, plate like, structures sound radiation is associated primarily with bending motion as this is perpendicular to the surface. Response in this section refers to structural vibration caused by acoustic excitation. Lord Rayleigh [18] was the first to calculate the radiation of sound from a flat rectangular plate. Radiation efficiency or radiation resistance are used to quantify the ease with which a structure radiates sound. A circular piston with circumference much less than the acoustic wave length has a radiation efficiency of one. Rayleigh addressed the response problem by reciprocity and showed that response can also be related to the radiation efficiency. Wallace [30] also used an integral given by Rayleigh[18] to give approximate expressions for the radiation efficiency of each mode of a flat simply supported rectangular panel. These methods are accurate but require excessive computation at high frequency where the number of radiating modes is large.

Statistical Energy Analysis deals with the radiation/absorption problem at high frequencies where the number of modes is two high for discrete modal methods to be practical. It does so by assuming that the modes of the panel have equal modal energy in a given frequency band and that the modes are uncorrelated so that the average modal radiation efficiency can be used rather than calculating discreet values for each mode. Some of the early SEA studies included calculation of average radiation resistance for rectangular plates (Maidanik [31]) and beams (Lyon&Maidanik [32]), these are discussed below in Section 1.4. Crocker[25] gives the corrected radiation efficiency derived by Maidanik as his original paper [31] contained an error below the critical frequency. Leppington *et al* [33] produced a more complete analysis of the plate radiation efficiency. Maidanik[31] and Leppington *et al* [34] have both investigated the effects of changing the panel boundary conditions. Leppington *et al* [34] show that below the critical frequency the predicted radiation efficiency of a panel with clamped boundaries is approximately twice that of the simply supported case. These studies [31,33,34] all assume the plates were set in an infinite rigid baffle which is in the same plane as the plate, this is not normally representative of real situations. Panels in motor vehicles join at a range of angles in the region of 90°. Leppington [35] showed that the effect of a 90° baffle is to increase the radiation efficiency by approximately a further factor of two.

1.5 Statistical Energy Analysis (SEA)

SEA was developed in the early 1960s for predicting high frequency response of space vehicles during launch and re-entry. R. H. Lyon amongst others is credited with its development and the fullest account of the SEA approach is given in Lyon&DeJong [36]. The past 30 years has seen SEA used to study structural vibration and acoustic noise transmission in a wide variety of situations. It has been successfully applied in buildings, ships, aircraft, cars and rail vehicles. Commercial application is growing and there exist many SEA computer software packages at least two of which are commercially available at present.

SEA is based on the assumption that vibration power flow from one set of modes to those of another coupled set is proportional to the difference between the average modal energies of the two sets and will flow from the high to the low energy set. This proportionality was established by Lyon&Maidanik [32] using the assumption that the coupling is weak and the excitation of each mode is uncorrelated. Lyon &Maidanik [32] showed the importance of modal density, damping and coupling loss factor in transmission and response prediction.

Statistical in SEA refers to the fact that the predicted response is the average of an ensemble of structures with the same average modal density, mass and damping. Energy is the variable used to describe the response and is assumed equally distributed within the modes of each subsystem. The energy in each part of a structure is predicted by constructing a matrix of energy balance equations from the coupling between and the damping of each subsystem. A subsystem is a set of similar modes for example the bending modes of a plate or the acoustic modes in a room. Finally Analysis was chosen in the name so as not to be restrictive as SEA is used as a framework for analysing experimental results and carrying out measurements as well as predicting response and transmission. A certain amount of terminology has developed with SEA some of which is summarised as follows. Coupling strength in SEA is given in terms of a Coupling Loss Factor (CLF) which relates the power flowing between two subsystems to the energy of the transmitting subsystem. Power losses from a subsystem which are not transmitted to other subsystems in the model are included using the Internal Loss Factor (ILF). The ILF is often dominated by internal damping. Total power flow out of a subsystem is related to subsystem energy by the Total Loss Factor(TLF) which is given by summing the ILF and

all the CLFs out of the subsystem. The TLF does not necessarily relate the net power flowing out of the a subsystem to its energy as some may flow back from connected subsystems (See Lyon&DeJong [36]).

SEA is based on the assumption that resonant damping controlled response occurs in each subsystem. The modal overlap factor is a widely used parameter for measuring the degree to which resonant behaviour dominates response. Davies[37] examined two coupled beams and rods using analytical models and recovered the SEA power flow relationship assuming that the modal overlap factor exceeded unity in both subsystems. Fahy&Mohammed [38] showed using deterministic numerical models that CLFs calculated using wave transmission coefficients are generally to high when the modal overlap factor is much less than unity. They considered models of two coupled plates and two coupled beams. Fahy&Mohammed [38] observed that only the higher of the two subsystem modal overlap factors need exceed unity. Craik *et al* [39] established that 0.25 is an acceptable lower limit for the modal overlap in buildings and this is only required of the receiving subsystem. In general, for many engineering structures, the modal overlap factor increases with frequency and a required minimum modal overlap will impose a low frequency limit on the analysis. Lyon&DeJong [36] give a low frequency correction factor which reduces the predicted CLF when the lowest modal overlap is much below unity. Predicted energy levels in SEA are usually the mean response but several authors have attempted to calculate the response variance [36,38,39,40,41,42].

As the modal overlap factor increases the response variance reduces. Broadening the frequency bands considered will also reduce variance as the number of resonance's contained within each band increases. If the excitation is applied over a number of positions on the source subsystem this will also reduce the variance in the response as will averaging the response measurement over a number of positions. There is no universally accepted procedure however for predicting the variance or confidence limits and this is an area of current research.

Smith [43] derived the response of a resonant structural mode to acoustic excitation in terms of the radiation resistance and internal loss factor (ILF). He predicted that maximum response occurs when the radiation damping of the structural mode is much larger than its internal damping. When this is the case he calculated that the average vibration energy of the mode in the structure approaches that of the modes in the fluid. This limit is known as equipartition of modal energy.

Maidanik [31] calculated approximations for the radiation efficiency of a simply supported baffled rectangular panel and used it with Smiths [43] formulation to predict the mean square vibration level when the panel is immersed in a reverberant acoustic field. He showed reasonable agreement with experimental results. A number of studies [44,45,46,47] have used SEA to successfully predict structural response to acoustic excitation. The same radiation efficiencies used in calculating the response of structures to acoustic fields have also been used in SEA models to predict radiation from panels subject to mechanical excitation [47,48].

Energy is not usually the variable that an engineer requires from a model. Pressure, velocity and stress are more generally useful. Spatial distributions of response have been developed for a variety of systems [36,49,50] and may be used to predict the temporal mean square velocity from which the maximum expected stress and other variables may be calculated.

Theoretical studies of coupled multi modal structures such as plates and rods have been used to investigated the effect of strong coupling upon the accuracy of SEA power flow calculations [41,51,52,59,53,54]. Sharton&Lyon [55] have shown the power flow energy difference proportionality to be true for both weak and strong coupling provided the subsystem energies are taken as those of the blocked modes. The blocked modes are those which occur when connected subsystems are constrained not to move. Remington&Manning [51] performed an exact analysis of point coupled rods and compared the results with an SEA prediction using ordinary "weak coupling" coupling loss factors. They concluded that SEA predictions showed good agreement for both strong and weak coupling particularly as the modal overlap increases. Smith [54] suggested that the coupling is weak if it is significantly less than the damping of the coupled subsystems, this is the simplest criterion to apply in practice although how much of a difference is significant is not defined. Excessive damping will prevent reverberant behaviour and invalidate SEA predictions as the coupling loss factors are usually calculated assuming the subsystems are reverberant. Langley [56] used the requirement that the Greens function of the uncoupled structure does not change significantly when it is coupled weakly. Heron [57] has suggested that weak coupling is not essential if wave methods are used to calculate the Coupling Loss Factors.

Building acoustics has seen extensive use of SEA in prediction of response and transmission [58,59,60]. Indeed there exists a text book dedicated to the subject, Craik

[61]. Modal density in rooms and walls are usually high enough to sustain at least one resonant mode per 1/3 octave frequency band in each subsystem over the frequency range of interest and Craik *et al* [39] have shown good agreement when this is the case. Damping is typically high enough to give good modal overlap but not so high as to prevent reverberant behaviour.

SEA has proved a useful tool for analysing Ships: Trach [62], submarines and aircraft: Lyon&DeJong [36] as well as many other engineering structures including automobiles.

1.5.1 SEA in Motor Vehicles

DeJong [63] was the first to publish an SEA study of a complete motor vehicle. He modelled a "mid sized front wheel drive station wagon with an automatic transmission". The vehicle was assumed symmetric and only half was modelled using 36 subsystems consisting of panels, beams, cylinders and acoustic volumes. Structural and acoustic power inputs were considered from engine, tyre and aerodynamic sources. Measured noise and vibration levels were taken at three running conditions chosen to emphasise these three causes of noise and vibration in turn. Engine noise and vibration was emphasised by driving the car in 2nd gear up hill at 30mph on a smooth road. Tyre noise was examined by driving in 3rd gear at 30mph on a level coarse road. Aerodynamic noise was measured at 55mph in 3rd gear on a smooth down hill road. Power inputs to the model were calculated by matching measured and predicted energy levels in the source subsystems. Measured and predicted saloon SPLs show generally good agreement across the frequency range (63Hz -2kHz) for the three running conditions. It is unclear from this paper how accurately structure borne sound transmission was predicted by the model as the dominant saloon power inputs in each running condition came from acoustic transmission through panels or holes in the dash.

Cimerman *et al* [64] have predicted the transmission loss through the floor panels for motor vehicles which were trimmed with layered acoustic materials similar to that in Wentzel&Saha [29]. In the paper by Cimerman *et al* [64] methods for calculating Transmission Loss through multi panel structures described in Beranek&Ver [65] are used within the frame work of an SEA model. A more complete SEA model of the car is used and power inputs to the saloon for a constant 55mph journey are given for engine, road and wind noise. It is shown that above 800Hz power from airborne engine noise exceeds that from airborne tyre noise under the vehicle, which is why heavier insulation of the floor has no effect above this frequency. Prioritising power sources is one of the

most useful techniques within SEA for selecting the most effective noise countermeasures.

Steel [66] has examined structural sound transmission in a motor vehicle using SEA. His paper presents details of the panels and beams and the joints between them used to model the motorvehicle. All 83 subsystems are modelled as flat panels. Bending wave transmission was calculated assuming inline or 90° line joints after Cremer [1]. Joints around the windows with elastic layers were modelled as described by Mees&Vermeir [10]. Beams are included along some of the panel joints and transmission is then calculated after Steel [67]. Door hinges are represented in the model as pin connections between panels and transmission is calculated using theory developed for building wall ties by Craik&Wilson [26]. Transmission was measured in the vehicle by tapping a source subsystem with a hammer randomly over the surface to give uncorrelated "rain on the roof " excitation while measuring the acceleration levels of the source and receiving subsystems. This procedure was repeated several times so as to get a spatially averaged result for each subsystem. Measured and predicted results were presented in the form of Acceleration Level Differences (ALDs) and showed good agreement. It was concluded that the elastic joints and the door hinges required further examination. This work gives more detail of how the structure was modelled than most of the material published on this subject. The vehicle used in this study was a glass fibre reinforced composite kit car which differs in construction from more typical vehicles which are constructed of steel panels spot welded together. Damping in untreated GRP is higher than in untreated steel and the joints between the GRP panels are generally simpler than in a mass manufactured vehicle. Both these factors increase the likelihood that SEA will produce accurate answers. This work suggests that the increasing use of GRP in mass manufactured vehicles should make SEA more applicable.

Dong *et al* [68] have modelled the effect of road noise using SEA. A coarse rolling road was used to collect SPLs, acceleration levels and suspension power inputs to a vehicle. They considered both structural and acoustic excitation and concluded that for the car tested structure borne paths dominate below 400Hz with transmission due to mass law and air gaps generally dominating above 400Hz. Between 2.5 - 3.1 kHz the model predicted that radiation from the windscreen and door glass became the dominant power input to the saloon because of wave number coincidence. This would suggest that

between 2.5 - 3.1 kHz and below 400Hz, accurate modelling of structural transmission is important. Measured and predicted SPL in the front of the saloon showed very good agreement. A number of noise reducing modifications were tested experimentally and by using an SEA model. Measured improvements in SPL between 12% and 45% agreed well with the predicted values.

X. Huang *et al* [69] Used an analytical SEA model to guide the development of the sound package for a light truck. First the model was built and "validated" against a series of three experimental measurements. Airborne engine noise was simulated in the experiment by replacing the engine with a box of approximately the same size with a speaker on each face. A Similar experimental technique was used for exhaust noise. Tyre noise tests were conducted on a rolling road where the SPL in the wheel-well was measured. The "baseline validation" of the model would seem to consist of checking the results against measurements and adjusting the model to match although this is not made clear. A number of noise countermeasures were tested by modelling and measurements with general very good agreement between the two. In this study the acoustic trim i.e. the Sound Barrier Assembly (SBA) as described in Wentzel&Saha [29] were treated as SEA subsystems after Powell [70] rather than calculating transmission and insertion loss as in Cimerman [64]. This approach is only valid when there is significant resonant response in the SBA its self. The analytical SEA approach was chosen partly because noise level predictions can be made before any car parts are constructed. This reduces the time required to complete the design of the vehicle sound package allowing shorter "design cycle times" which is important to manufacturers.

1.6 Inverse or Test Based SEA(EFA)

Analytical SEA is easily applied in complex assemblies of simple substructures such as plates and beams. Expressions for the modal densities of such structures exist as do techniques for calculating Coupling Loss Factors for simple connections between them. When the substructures them selves are complex in shape with unevenly distributed mass or they are joined by complex joints it is more difficult to predict CLFs and modal densities. These concerns as well as uncertainty about the weak coupling and other assumptions made by analytical SEA models have led to the development of test based or inverse SEA other wise known as Energy Flow Analysis (EFA). Inverse or test based SEA allows the calculation of response based on CLFs and ILFs determined by experimental measurements in the hope that these will be more accurate.

Bies&Hamid [71] describe the experimental measurement of ILFs and CLFs for two coupled plates. This involves inverting a matrix of measured energy levels. SEA reciprocity relations were used to reduce the number of unknown CLFs allowing the use of a least squares approach to minimise numerical errors. Use of reciprocity required the calculation of modal densities for the panels using the flat thin plate expression given by Cremer [1]. Averages were taken over at least three positions when measuring panel velocity, so as to ascertain their energy levels accurately. Power inputs were applied at a similar number of points on each panel so as to excite all the modes equally on average. Power injection measurements of ILFs were compared with those taken using reverberation techniques and found to be higher. This was explained by the fact that more lightly damped modes will reverberate longer and dominate the decay in the reverberant technique. The matrix inversion method can require a very large number of measurements, N^2 where N is the number of subsystems, not accounting for multiple measurements for space averaging. Accuracy has consistently been a problem using methods of this sort, particularly in measuring the CLFs and especially when coupling is strong in relation to damping.

Woodhouse [72] and Hodges *et al* [73] suggested a technique using the requirement that all loss factors be positive to "massage" the measured data. Clarkson&Rankey [74] used an iteration scheme to tackle accuracy difficulties. They also agree with Bies&Hamid's [71] assertion that the reverberation technique is unsuitable for measuring plate ILFs in most cases. Lalor[75] simplified the matrix algebra required to calculate loss factors, separating the calculation of the ILFs from the CLFs. In a later paper, [76] he use the SEA assumption that subsystems which are not directly attached have CLFs of zero to introduce more redundancy and greater accuracy where this assumption is true.

Carr&Lalor [77] introduced the concept of equivalent subsystem mass. They measured the response of diesel engine components to power injected using a shaker. The damping loss factors of the components were also measured using reverberation time techniques. Predicted response to power injection using these damping values did not agree with the measured response. Response was given in the form of mean square velocities averaged over many locations on the component surface. The components were not of an even mass distribution, this would explain a discrepancy between the results. Two additional

reasons for the difference were suggested, firstly the number of measured velocities was insufficient for accurate measurement of the energy level and secondly non resonant behaviour resulting in an inequality between average kinetic and potential energy. Equivalent mass was defined to correct the discrepancy and is defined by the requirement that the total energy of the subsystem is equal to the mean square velocity times the equivalent mass.

Wu *et al* [78,79] have also used experimental SEA to model the structure of a diesel engine. They also used the equivalent mass concept. Whether SEA with or without equivalent mass is likely to be a suitable way to deal with complex non uniform structures such as engine blocks is still a matter of debate.

Plunt *et al* [80] published a discussion paper entitled "On the use and Misuse of Statistical Energy Analysis for Vehicle Noise Control". In it they present some data from a successful application of analytical SEA to the study of SPL in a city bus and a military tracked vehicle. CLFs calculated using a FEM of a two plate assembly are presented. The dimensions of the model are altered slightly to produce an ensemble average of 50 results. Even at high frequencies where the modal overlap was high the variance of the CLF distribution was $\pm$ 3-4 dB. It was suggested that an EFA measurement on one example of a structure would not represent the ensemble average. Given the large number of measurements discussed above by Bies&Hamid [71] for one measurement it was concluded that it is "entirely unrealistic" to accurately measure the ensemble average. The paper concludes that SEA is useful for predictions of interior noise in vans, buses and trucks but less so for passenger cars.

Chen *et al* [81] compared an analytical and a test based SEA model of a "Light Truck". The equivalent mass concept (Carr&Lalor [77]) is used in this paper. Both the analytical and the test based models are used to predict the SPL in the cabin as a result of engine noise at 5000rpm. It was concluded that the test based model was no more accurate for predicting SPL in the cabin than the analytical model. This was credited to the fact that much of the time the predicted SPL is dominated by non resonant transmission which is reasonably accurately modelled analytically. Predictions of SPL as a result of purely structural power inputs were more accurate from the test based model. It was further

concluded that measured damping was essential for accuracy as part of either analytical or test based models.

1.7 Advances on SEA

SEA has been used to accurately predict sound transmission within various complex structures [59,60,62,66]. However SEA has not always been accurate in predicting structural transmission even when modal overlap is high. Guyader *et al* [82] showed using a deterministic model, that SEA can severely over predict transmission between two rectangular panels joined at 90°. These factors and uncertainty over the effect of assumptions made during SEA modelling have led to the development of two methods which attempt to keep the simplicity of SEA but improve its accuracy.

ASEA or Advanced SEA was proposed by Heron [83], he states that SEA often exhibits errors when predicting structural transmission. Heron [83] suggests that these errors are not due to strong coupling but rather the inability of SEA to model the "tunnelling" effect in which coupling occurs between subsystems which are separated by other subsystems. Ray theory is used to track power flowing around the model and conventional SEA is used to deal with the remaining power. Subsystem energy is split into that available for transfer to another subsystem and that dissipated by damping which is not. The "level number" is the number of reflections of power across a subsystem before the ray tracing is truncated and SEA takes over. ASEA level zero is conventional SEA with the answer approaching a high frequency asymptote as the level is increased. The theory was explained for plates and rods and compared with analytical results for a line of six different coupled rods one end of which is driven. This example was chosen to demonstrate the "tunnelling" phenomenon where coupling exists between rods that are not directly connected. This is not reflected in the SEA model which assumes no coupling between non directly connected subsystems. ASEA showed very good agreement with the fully analytical results as the "level number" was increased but SEA produced errors of up to 60dB in the furthest rod from the source. One peculiar feature of the results presented was that SEA over predicted the response even in the furthest rod from the source. Tunnelling is usually associated with the under prediction of response in a remote SEA subsystem e.g. mass law transmission between rooms.

Wave Intensity Analysis (WIA) which was developed by Langley [84] is another development upon SEA. The diffuse field assumption of SEA is dropped and the directional dependence of intensity in each subsystem described by a truncated Fourier series. When there is only one Fourier term (a constant) the field is diffuse and the result reduces to SEA, as the number of terms increase the answer approaches a high frequency asymptote. The answer is presumably very similar in most cases to ASEA[83] but not necessarily identical. The analysis was explained in general terms then in more detail for panel subsystems. Three rectangular plate assemblies were modelled using WIA and an exact method (given by Langley [85]) for comparison. The panels were reverberant with high modal density and modal overlap which would suggest that SEA is suitable. One panel of a two panel L-structure was driven, SEA over predicted the response of the other panel, this observation which had been made previously [82,86]. WIA on the other hand converged upon the exact answer. Three and four panel arrays were also investigated with the source panel on the end. The "tunnelling" phenomenon was evident in the four panel array where SEA under predicted the response in the furthest panel from the source, WIA converged close to the exact result..

1.8 Aims of Thesis

Modern motor vehicles are constructed of complex sheet metal pressings spot welded together. Some form of stiffening arrangement is usually included by welding small additional pressed panels into joints. It would seem that existing SEA studies which deal with the structure borne sound in cars do not model the complex nature of the joints in motor vehicles other than perhaps by the inclusion of a simple beam or elastic layer within the joint (Steel [66]). The methods described in [8,9,12] would at least in part allow the inclusion of the joint complexity when calculating CLFs. It would represent a significant step to use these methods in an SEA model of a modern motor vehicle and this is the primary objective of the thesis. A more detailed experimental and theoretical examination of some particular complex joints type would also be worthwhile. Transmission between panels connected by a curved corner joint has been calculated by ignoring the curved section and treating the joint as a sharp corner. A further objective of the thesis is therefor to investigate the transmission across a curved corner joint. The aims of the thesis are listed below.

- To develop a general theoretical model for the prediction of vibration transmission at complex joints in motor-vehicle structures.

- To study vibration transmission in a motor vehicle using SEA.
- Identify the important mechanisms of sound transmission in a vehicle structure.
- To demonstrate the ability of SEA to identify important transmission paths and power inputs associated with a real noise problem in a motor-vehicle.

1.9 Outline of Thesis

Chapter 2: Background Theory

An overview of the fundamental theory is given in Chapter 2. The subjects covered include:- Structure borne waves, Modal density, Damping, Modal overlap, Structural Transmission coefficients, Transmission Loss, Radiation efficiency, Statistical Energy Analysis and Wave Intensity Analysis.

Chapter 3: Complex Joints

In this Chapter the theoretical development of the Wave Dynamic Stiffness matrix method of predicting wave transmission is presented. The derivation of two node elements for curved and flat panels as well as elastic layers is presented. Element assembly methods are briefly described. Chapter 3 contains a numerical investigation of a curved corner panel joint where the various wave types on the curved section are identified and their influence demonstrated.

Chapter 4: Measurement Procedures

Experimental transducers and instrumentation used to measure response and transmission in laboratory models of curved corner joints and in a Nissan Micra motor vehicle are discussed. Measurements described in this chapter are:- Acceleration Level Difference (ALD), Structural Mobility, Structural and Acoustic damping (Reverberation time) and Sound Pressure Levels(SPL). Chapter 4 concludes with discussion of the measurements and their statistics.

Chapter 5: Curved Corner Joint

In this Chapter measured and predicted results for transmission of vibration at rounded corner panel joints are presented. SEA and WIA predictions with transmission coefficients from the Complex joint model described in Chapter 3 are shown. Results are compared and discussed.

Chapter 6: SEA Study of Small Motor vehicle

Vibration transmission in a Nissan Micra motorcar is studied using SEA. This Chapter starts with a description of the car itself and the methods used to construct it. Two SEA models are developed, one using simpler predictions for vibration transmission at panel boundaries and another the Complex joint model using the theories given in Chapter 3. Predicted structural sound transmission is compared to measured data. SPL due to engine noise is also measured and predicted. Results for the two models are compared with each other and the measured data. The effect of exhaust misalignment is used to demonstrate the ability of SEA to rank the relative importance of each power input throughout the frequency range of interest. The chapter ends with the discussion and conclusions of this study.

Chapter 7: Discussion and Conclusions

The most important results and conclusions of the work are summarised in this Chapter. Chapter 7 concludes with an outline of some areas where future research would be useful.

Chapter 2

Background Theory

2.1 Introduction

This chapter describes some of the terminology and methods used in the study of acoustic and structure borne sound at audible frequencies (16-16kHz). Areas covered include structural wave types found in beams plates and rods, natural vibrations in finite structures and statistical parameters such as modal density and modal overlap. Statistical Energy Analysis is introduced and methods for calculating structural and acoustic Coupling Loss Factors are given. The chapter concludes with a description of Wave Intensity Analysis.

2.2 Longitudinal Waves

Particle motion in longitudinal waves is parallel to the direction in which the wave travels. The wave equation for plane longitudinal motion is given by Cremer *et al* [1] for a wave travelling in the x direction as,

$$D\frac{\partial^2 \xi}{\partial x^2} = \rho\frac{\partial^2 \xi}{\partial t^2} \tag{2.1}$$

where ξ represents displacement in the x direction and ρ is the material density. D is a longitudinal stiffness parameter which depends on the material and the dimensions of the structure. For propagation along a rod constructed of elastic isotropic material $D = E$, where E is Young's modulus. This assumes plain stress in the z and y axes which are perpendicular to the direction of propagation. A rod in this context is defined as having a cross section with depth and breadth much less than the longitudinal wavelength, λ_l. The longitudinal stiffness, D for a plate is given is given by Equation (2.2) where the thickness of the plate in the y direction is $h << \lambda_l$.

$$D = \frac{\sigma_x}{\varepsilon_x} = \frac{E}{1-\mu^2}, \quad (\sigma_y = 0, \varepsilon_z = 0) \tag{2.2}$$

where σ_y is the stress in the y (plate thickness) direction and ε_z is the strain in the z direction. Equation (2.2) assumes plane stress in the y direction $(\sigma_y = 0)$ and plain strain

in the z direction ($\varepsilon_z = 0$). Longitudinal waves propagating in rods and plates are termed quasi-longitudinal waves because the plain stress assumptions mean there is some motion perpendicular to the direction of propagation. Pure longitudinal waves occur only in solids where dimensions in all directions are much larger than λ_l. Under these circumstances plain strain assumptions can be made in z and y resulting in

$$D = \frac{\sigma_x}{\varepsilon_x} = \frac{E(1-\mu)}{(1+\mu)(1-2\mu)} \quad , \quad (\varepsilon_z = 0, \varepsilon_y = 0) \tag{2.3}$$

The longitudinal wave equation (2.1) is satisfied by any function, f such that $\xi = f(c_L t \pm x)$, where c_L is the longitudinal wave speed given by.

$$c_L = \sqrt{\frac{D}{\rho}} \tag{2.4}$$

This solution indicates non dispersive behaviour where the wave "shape" remains constant as it travels through the medium or equivalently that all frequency components of the wave travel at the same speed, c_L.

The Energy a wave carries travels at the group velocity C_g which is defined in Cremer *et al* [1] as.

$$C_g = \frac{\partial \omega}{\partial k} \tag{2.5}$$

The group velocity of non dispersive waves such as longitudinal waves is equal to the phase velocity. Therefore the power, p flowing in a longitudinal wave on a rod is given by

$$p = E_\rho c_L S \tag{2.6}$$

where E_ρ is the sum of kinetic and potential energy density (J/m^3) and S is cross sectional area. Average power flow during one cycle can be expressed in terms of complex force, F and velocity, v as.

$$p = \frac{1}{2}\mathrm{Re}\{Fv^*\} \tag{2.7}$$

where Re{} indicates the real part and v^* is the complex conjugate of velocity. Using Cremer's [1] expression for longitudinal wave impedance, $Z = S\rho\ c_L$ this can be written in terms of velocity amplitude, $|v|$ in (2.8)

$$p = \frac{c_L \rho S}{2}|v|^2 \tag{2.8}$$

2.3 Transverse Waves

Transverse irotational motion of planes perpendicular to the direction of propagation characterise this type of wave. The wave equation for free propagation of plane transverse waves is given by,

$$G\frac{\partial^2\eta}{\partial x^2} = \rho\frac{\partial^2\eta}{\partial t^2} \tag{2.9}$$

where G is the modulus of rigidity and η is displacement perpendicular to x which is the direction of propagation. This equation is identical in form to the longitudinal wave equation (2.1) and is also non dispersive. Transverse wave speed c_T is given by.

$$c_T = \sqrt{\frac{G}{\rho}} \tag{2.10}$$

Unlike longitudinal waves transverse waves can be polarised because particle motion may be in any direction on the plane perpendicular to the direction of travel. This means that two separate transverse waves can travel in the same (say x) direction in a solid, one causing motion in the y direction and the other in the z direction. Transverse waves in thin plates are usually assumed to cause only in-plane motion. This is because out of plane displacements of plates are dominated by bending motions at lower frequencies as discussed in Section 2.3.

Transverse waves are non dispersive so their group velocity is equal to their phase velocity so that power flow, p as a result of a transverse wave is given by

$$p = E_\rho c_T S \tag{2.11}$$

Power flow in a sinusoidal wave with velocity amplitude $|v|$ is given by (2.12), this is the average over one cycle.

$$p = \frac{c_T \rho S}{2}|v|^2 \tag{2.12}$$

2.4 Bending Waves

Bending or flexural waves can occur on beams and plates. A beam in this context is defined as having a cross section with depth and breadth much less than the bending wavelength, λ_B. Bending waves are often the most important reservoir of vibrational energy in a structure because the transverse motion can lead to high sound radiation and

their low mechanical impedance promotes high energy levels. Dynamic flexural behaviour of beams is governed by Euler's equation.

$$B\frac{\partial^4\eta}{\partial x^4} = -m\frac{\partial^2\eta}{\partial t^2} \tag{2.13}$$

where x is the axis along the beam and η is a displacement perpendicular to x. S is cross sectional area and $m = \rho S$ is the mass per unit length of the beam. $B = EI$ is the bending stiffness for a beam. Strain energy in flexural and longitudinal waves is due to stresses normal to the direction of propagation. Equation (2.13) is of forth order in x and second order in t which means that bending waves are dispersive and solutions of the form of equation (2.4) are not applicable for all functions f. Solutions to (2.13) can be sought by assuming a harmonic time dependence i.e. solving for each Fourier component of the wave independently giving.

$$\eta(x,t) = e^{i\omega t}g(x) \tag{2.14}$$

This yields solutions of a form shown below.

$$g(x) = r_{-}e^{ik_B x} + r_{+}e^{-ik_B x} + n_{+}e^{k_B x} + n_{-}e^{-k_B x} \tag{2.15}$$

where $k_B = \sqrt[4]{m\omega^2 / B}$ is the bending wave number. r_{-} and r_{+} are the amplitudes of sinusoidal bending waves travelling in the negative and positive x direction respectively. n_{-} and n_{+} are nearfields or stationary waves. Nearfield waves decay exponentially away from structural discontinuities. Nearfield waves must be considered when calculating transmission of waves across structural discontinuities. The velocity with which bending waves propagate is a function of frequency and is given by,

$$c_B = \frac{\omega}{k_B} = \sqrt[4]{\frac{B}{m}}\sqrt{\omega} \tag{2.16}$$

The thin plate bending wave equation is presented in Cremer [1] as,

$$B\Delta\Delta\eta + m\frac{\partial^2\eta}{\partial^2 t} = 0 \tag{2.17}$$

where Δ is a differential operator known as the Laplace operator and is given by,

$$\Delta = \left(\frac{\partial^2}{\partial x^2} + \frac{\partial^2}{\partial z^2}\right) \tag{2.18}$$

B is the plate bending stiffness given by $B = Eh^3 / 12(1-\mu^2)$, $m = \rho h$ is the surface density. The out of plane deflection $\eta(x,z,t)$ is a function of panel position and time. The

plate lies in the x z plane and η is in the y direction. Travelling plane wave solutions can be found by replacing $\eta = \hat{\eta} e^{i\omega t} e^{i(k_z z + k_x x)}$ into (2.17) where k_z and k_x are the wave number components in the z and x direction respectively. This gives a relationship between k_z and k_x.

$$k_B^2 = k_x^2 + k_z^2 \tag{2.19}$$

where $k_B = \sqrt[4]{\rho h \omega^2 / B}$ is the panel wave number magnitude which is determined by the panel properties and frequency. The Bending wave may propagate in any direction on the panel.

Power flow in plate bending waves can be calculated using the group velocity C_g by using.

$$p = E_\rho C_g h \tag{2.20}$$

This is the power flow in the propagation direction per unit width of wave front where E_ρ is the sum of kinetic and potential energy density in the panel. Because bending waves are dispersive the group velocity for thin plates (2.5) does not equal the phase velocity, it is in fact twice the phase velocity. Using this fact and expressing E_{tot} in terms of wave amplitude gives

$$p = \hat{\eta}^2 B \omega k_B^3 = \hat{\eta}^2 \rho h \omega^3 / k_B \tag{2.21}$$

Thin plate theory has a high frequency limit beyond which shearing motion becomes significant and the waves become closer to transverse waves in character. Cremer *et al*[1] give a more accurate theory which includes the effect of shearing and inertia forces. At high frequency the phase velocity given by the more accurate thick plate theory is lower than that from the thin plate theory given by equation (2.16). Cremer *et al*[1] proposed a maximum error in the phase velocity of 10%, this gives a maximum frequency beyond which the thin beam and plate bending wave equations (2.13) and (2.17) becomes inaccurate. Using this criterion requires that the bending wavelength exceeds the panel thickness by at least a factor of six. The panels most likely to contravene this requirement in a motor vehicle are plastic trim. Using a longitudinal wave speed of 600 m/s and a thickness of 3mm gives an upper limit of 10kHz. The windows have the next highest limit of 50kHz and probably play a more important role in the transmission of sound in a vehicle. These observations would suggest that thin plate theory is adequate for the study of panel vibration over the audible frequency range in motor vehicles.

2.5 Mechanical Impedance and Mobility

The vibration energy of a linear, damped structure is proportional to the power input to the structure. Power inputs to a vehicle structure results from engine vibrations, aerodynamic noise and suspension vibration. Power inputs to a structure by a force or moment acting upon it are given by,

$$p = \frac{1}{2}|F|^2 \,\mathrm{Re}\{Y\},\ p = \frac{1}{2}|M|^2 \,\mathrm{Re}\left\{\frac{1}{W}\right\} \qquad (2.22), (2.23)$$

where Y is the mechanical point mobility of the structure at the point of application of the load and W is the moment impedance defined by,

$$Y = \frac{v}{F} = \frac{1}{Z},\ W = \frac{M}{w} \qquad (2.24),(2.25)$$

Z is the mechanical impedance of the structure which is the reciprocal of mobility. The power injected into a structure by a point force excitation may be expressed in terms of impedance and velocity or impedance and acceleration as follows,

$$p = \frac{1}{2}|v|^2 \,\mathrm{Re}\{Z\} = \frac{|a|^2}{2\omega^2}\mathrm{Re}\{Z\} \qquad (2.26)$$

where $|a|$ is the amplitude of acceleration. Cremer[1] calculated a number of impedance formulae for various structures. The point impedance on the interior of a thin infinite isotropic plate is given by,

$$Z = 8\sqrt{B\rho h} \qquad (2.27)$$

Point force and moment impedance on plate edges, beams, rods and cylinders are also given in [1]. Only equation (2.27) is used in this work so the other expressions are not presented here. At the interior of an infinite panel a force applied normal to the surface does not produce any deflection other than in the direction of the applied force, nor does it cause any rotation. In general however when a force is applied to a structure the response may involve rotations and displacement not in the direction of the applied force. The movement of the loading point as a result of applied forces may be calculated using the mobility matrix, **Y**.

$$\mathbf{v} = \mathbf{Y}\mathbf{f} \qquad (2.28)$$

where **v** is a vector of three linear and three angular velocities and **f** is the vector of corresponding forces and moments. **Y** is a skew-Hermitian matrices when the structure is finite and conservative. When the structure is damped or extends to infinity and can carry power away from the point of excitation the entries of **Y** are complex. The impedance matrix is the inverse of the mobility matrix.

$$\mathbf{f} = \mathbf{Z}\mathbf{v},\ \ \mathbf{Z} = \mathbf{Y}^{-1} \tag{2.29}$$

Reciprocity dictates that the mobility and impedance matrices are symmetric. Notice that the entries of the impedance matrix are not necessarily the reciprocal of the corresponding entries in the mobility matrix this is only the case where **Y** and **Z** are diagonal i.e. the degrees of freedom are uncoupled. To directly measure the entries of a non diagonal structural impedance matrix the structure would have to be restrained from moving in any direction other than the forcing direction. It is simpler to measure the mobility matrix entries directly as no restraint is required and the impedance matrix can be calculated by inversion. Power flow into a structure can be written in more general terms than (2.22) and (2.23) using the mobility and impedance matrices.

$$p = \frac{1}{2}\mathrm{Re}\{\mathbf{v}^{*\mathrm{T}}\mathbf{Z}\mathbf{v}\} = \frac{1}{2}\mathrm{Re}\{\mathbf{f}^{*\mathrm{T}}\mathbf{Y}\mathbf{f}\} \tag{2.30}$$

Because the mobility and impedance matrices are symmetric the imaginary parts of the entries have no effect on the power flow and **Z** in (2.30) may be replaced by the resistance matrix, **R** whose entries are the real part of the corresponding entries in **Z**. Similarly **Y** may be replaced by its real entries in the form of **G**, the conductance matrix so that (2.30) may be rewritten as,

$$p = \frac{1}{2}\mathbf{v}^{*\mathrm{T}}\mathbf{R}\mathbf{v} = \frac{1}{2}\mathbf{f}^{*\mathrm{T}}\mathbf{G}\mathbf{f} \tag{2.31}$$

There are 36 entries in a 6x6 mobility matrix, assuming the matrix is symmetric would require the measurement of 21 entries. Manning[87] suggests that the products involving off diagonal terms in (2.31) can be ignored. The total power injected into the structure is then the sum of the power injected into each degree of freedom. This requires 6 mobility measurements or only 3 if the moment contributions are insignificant giving,

$$p = \frac{1}{2}\left|F_x\right|^2 \mathrm{Re}\{Y_x\} + \frac{1}{2}\left|F_y\right|^2 \mathrm{Re}\{Y_y\} + \frac{1}{2}\left|F_z\right|^2 \mathrm{Re}\{Y_z\} \tag{2.32}$$

where the *x*,*y* and *z* subscripts indicate the direction in which the mobility and force are measured. Measuring the forces and moments applied to a structure at a point of excitation requires the insertion of a transducer between the source of excitation and the structure. It is often easier to measure the velocity of a structure at the point of excitation as this does not require that the source and structure be separated. Equation (2.26) may then be used for each axis instead of (2.22).

2.6 Damping

Damping is the mechanism by which kinetic and potential energy is converted to heat. Linear damping can be introduced by using a complex modulus $E(1+i\eta)$ where η quantifies the damping and is known as the loss coefficient or the Internal Loss Factor (ILF). The ILF is frequently written in dB re 10^{-12}.

$$\text{ILF} = 10\log(\eta) + 120 \tag{2.33}$$

Average power dissipated as heat over one cycle as a result of damping can be written as.

$$p = E_{tot}\omega\eta \tag{2.34}$$

where E_{tot} is the total vibration energy content which is the sum of kinetic and potential energy. If the power input to a resonant structure is stopped abruptly then E_{tot} decays exponentially with time. The rate of decay can be expressed as reverberation time, (T_{60}) which is the time required for the energy to reduce by 60 decibels. Reverberation time can be related to the loss coefficient by (2.35).

$$\eta = \frac{2.2}{f T_{60}} \tag{2.35}$$

Where f is the frequency of vibration. Reverberation time can be measured (as discussed in Chapter 4) and structural and acoustic damping calculated using equation (2.35). The damping of acoustic vibrations in a vehicle saloon is increased by absorption of the sound at interior surfaces. Damping caused by absorption can be written in terms of reverberation time using the Sabine equation which is given by Craik[61] as.

$$T_{60} = \frac{0.161V}{\sum S\alpha} \tag{2.36}$$

where V is the volume of the saloon and the numerator is the total absorption of the saloon equal to the sum of the products of surface areas and their absorption coefficients α.

Fig. 2.1 shows a one degree of freedom resonator with a mass m on a spring of stiffness k and a linear viscous damper with a rate R (Ns/m). A force F is applied to the mass and causes a response with displacement x and velocity v.

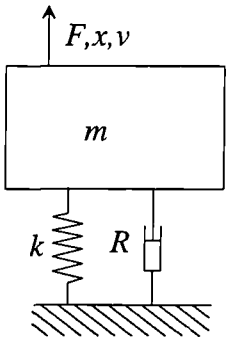

Figure 2.1: Mass spring resonator.

If a mass spring resonator with linear damping is excited by a harmonically fluctuating force, $F = \hat{F}\exp(i\omega t)$ the mobility is given by,

$$Y = \frac{1}{R - im\left(\frac{\omega_n^2 - \omega^2}{\omega}\right)} \tag{2.37}$$

where the undamped natural frequency is $\omega_n = \sqrt{k/m}$. Written in terms of the loss coefficient which in this case is given by $\eta \approx R/\omega_n m$ provided $\omega \approx \omega_n$, mobility is equal to,

$$Y = \frac{1}{\omega_n \eta m - i\left(\omega m - k/\omega\right)} \tag{2.38}$$

Mobility is highest at $\omega = \omega_n$. At this frequency the power fed into the oscillator by the applied force is given by equation (2.22) as $p = F^2/2\omega_n \eta m = F^2/R$ which is dependant only upon the damping. At frequencies either side of ω_n the power injected falls of reaching half the peak value at $\omega_n \pm \omega_n \eta/2$. The band between these two frequencies is known as the damping controlled region. The width of the damping controlled region, $\Delta\omega = \omega_n \eta$ (rad/s) or $f_n \eta$ (Hz) is known as the half power or resonant band width of the resonator. At lower frequencies the resonator response is stiffness controlled and at higher frequencies it is mass controlled.

2.7 Modal Resonators

Waves in finite structures such as plates and beams with low structural damping are reflected at boundaries. Incoming and reflected waves interfere to produce standing waves or modes on the structure. Each mode has a unique shape and an associated natural frequency or eigenfrequency which is not necessarily unique. The response of a particular mode peaks at its natural frequency. Modal response is determined by the location,

frequency and magnitude of exciting force and energy losses (such as damping). Modal analysis is useful because the response of each mode may be calculated individually and summed for the total response. Continuous systems such as beams and plates have an infinite number of modes, therefor the summation must be truncated and the response of the less influential modes ignored. Response of a plate can be calculated by summing the response of every mode as in equation (2.39).

$$v(x,z) = e^{i\omega t} \sum_{n=1}^{n=\infty} \frac{\phi_n(x,z)}{\Delta_n(\omega_n^2(1+i\eta)-\omega^2)} \int_S i\omega \hat{P}(x,z)\phi_n(x,z)dxdz \qquad (2.39)$$

where modal amplitude is normalised with Δ_n which is given by Cremer *et al* [1] as.

$$\Delta_n = \int_S m\phi_n^2(x,z)dxdz \qquad (2.40)$$

And $P(x,z) = \hat{P}(x,z)e^{i\omega t}$ is the pressure applied to the surface of the plate. $\phi_n(x,z)$ is the mode shape function of the n th mode and ω_n is the natural frequency of that mode. Each mode behaves like a mass spring resonator with natural frequency ω_n. Cremer *et al*[1] used these equations to calculate the point impedance of a rectangular panel. When no damping is present the response becomes infinite at the resonant frequencies and zero at anti-resonance which occurs between the resonant frequencies. When damping is introduced the response at resonance is finite and determined entirely by the magnitude and location of the force and the level of damping. Modal analysis can be used to calculate the response of any finite linear structure, ether by using analytical solutions such as (2.43) and (2.44) or semi analytical mode shapes and frequencies calculated using the Rayleigh-Ritz (See Thomson[88]) method. FE software packages can also perform modal analysis on almost any realistic structure. Many practical structures have tens of thousands of modes in the audible frequency range, this limits the practicality of modal analysis with current computer technology. Unless the analyst is prepared to use a very powerful computer for a long time only a small number of modes can be considered. Rayleigh-Rits and FE predictions require precise knowledge of structural details such as geometry and boundary conditions which may be difficult to obtain for a real structure such as a motor vehicle body. The response of higher order modes become increasingly sensitive to these structural details. This means that the response of higher order modes predicted using FE or Rayleigh-Rits may differ considerably from those of the structure being modelled.

2.7.1 Simply Supported Beams

A beam simply supported at each end has flexural modes shapes given by,

$$\phi_n = \sin\frac{n\pi x}{l} \tag{2.41}$$

where n is a positive integer and l is the length of the beam. The corresponding natural frequencies are given by,

$$\omega_n = \sqrt{\frac{B}{m}}\left(\frac{n\pi}{l}\right)^2 \tag{2.42}$$

This equation indicates that the natural frequencies of a simply supported beam become further apart as frequency increases.

2.7.2 Simply Supported Rectangular Panels

The mode shapes of a simply supported rectangular plate are given by Cremer *et al*[1] as,

$$\phi_n = \sin\frac{n_1\pi x}{l_1}\sin\frac{n_2\pi z}{l_2} \tag{2.43}$$

where n_1 and n_2 are positive integers, l_1 and l_2 are panel dimensions in x and z respectively. This equation is derived by solving equation (2.17) with products of separate functions of x and z then choosing those that will satisfy simply supported boundary conditions. The corresponding natural frequencies are given by,

$$\omega_n = \sqrt{\frac{B}{m}}\left(\left(\frac{n_1\pi}{l_1}\right)^2 + \left(\frac{n_2\pi}{l_2}\right)^2\right) \tag{2.44}$$

2.7.3 Modal density

Modal density, n can be defined as the average number of modes occurring in a one hertz frequency band. For simply supported beams is given by Cremer *et al*[1] as,

$$n(f) = \frac{l}{c_B} \tag{2.45}$$

Here n in (2.45) is not to be confused with n used previously as a positive integer. Average modal density of simply supported rectangular plates is given by Cremer *et al*[1] as,

$$n = \frac{\sqrt{3}S}{hc_L} \tag{2.46}$$

and is independent of frequency. Equations (2.45) and (2.46) were derived assuming simply supported boundary conditions. As frequency and the mode count rises the modal

density becomes less dependant upon the boundary conditions. It is therefor valid to use (2.45) and (2.46) as high frequency asymptotes even when the boundaries are not simply supported. Equation (2.46) may also be used at high frequencies for panels with non rectangular shape.

The modal density of an acoustic volume with ridged boundaries is given by Kuttruff[89] as,

$$n(f) = \frac{4\pi f^2 V}{c_0^3} + \frac{\pi f S}{2c_0^2} + \frac{L}{8c_0} \tag{2.47}$$

First, second and third terms are proportional to volume V, surface area S and total edge length L respectively. When one of the dimensions is small in relation to the wavelength and the volume represents that of a thin cavity between two panels (e.g. between the trim and body panels of a motor vehicle) then a two dimensional modal density expression given by Craik[61] may be used.

$$n(f) = \frac{2\pi f S}{c_0^2} \tag{2.48}$$

2.7.4 Modal Average Mobility

Lyon&DeJong[36] give the real part of the mobility of a multi modal structure averaged over a frequency band which contains a number of 'equivalent' modal bandwidths ($2.\pi\omega\eta/2$) as,

$$\mathrm{Re}\{Y\} = \frac{n}{4\mathrm{m}} = \frac{1}{4\mathrm{m}\Delta f} \qquad (\eta < 0.3) \tag{2.49}$$

where m in this equation is the total mass (not the surface density) and Δf is the average modal frequency spacing which is the reciprocal of modal density. Replacing n using equation (2.46) and putting $\mathrm{m} = \rho h S$ gives result for a infinite plate with the same thickness and material properties which is the reciprocal of equation (2.27). It is common when dealing with broad band excitation and or random excitation positions to use an infinite structural impedance when analysing a finite structure (See Lyon&DeJong[36]).

2.7.5 Mean Square Velocity and Sound Pressure Level

In undamped resonant vibrations the stored energy is converted from kinetic to potential and back twice every cycle. When the vibrations are damped some of this energy is converted into heat. The peak kinetic and potential energies in time are equal to the total

energy E_{tot}. The kinetic energy stored in out of plane motion of a panel with even mass distribution is given by Cremer *et al* [1] as,

$$E_{kin} = \frac{m}{2}\int_0^S v^2(x,z)ds \qquad (2.50)$$

If the velocity is varying in time as $v(x,z) = \hat{v}(x,z)\sin\omega t$ then the peak kinetic energy may be written as,

$$E_{peak} = E_{tot} = \frac{m}{2}\int_0^S \hat{v}^2(x,z)ds \qquad (2.51)$$

Cremer *et al* [1] define the mean square velocity, $\langle v^2 \rangle$ for a panel as averaged in both space and time which gives,

$$\langle v^2 \rangle = \frac{1}{ST}\int_0^T \int_0^S v^2(x,z)ds\,dt \qquad (2.52)$$

where T is the integration time and S is the surface area of the panel. Assuming sinusoidal time variation as before and integrating in time allows the peak kinetic energy and the total vibration energy to be written in terms of the mean square velocity,

$$E_{tot} = mS\langle v^2 \rangle \qquad (2.53)$$

This relationship is only valid for structures with uniformly distributed mass such as beams, cylinders and plates. Mean square velocity may be expressed in dB re 10^{-6} m/s giving velocity level, L_v as [61],

$$L_v = 10\log\left(\frac{\langle v^2 \rangle}{10^{-12}}\right) \qquad (2.54)$$

Energy may also be expressed as a level, L_E in dB re 10^{-12} Joules,

$$L_E = 10\log\left(\frac{E}{10^{-12}}\right) \qquad (2.55)$$

Vibration energy in acoustic spaces can be related to the mean square pressure, $\langle p^2 \rangle$ by,

$$E_{tot} = \frac{\langle p^2 \rangle V}{\rho_0 c_0^{\,2}} \qquad (2.56)$$

where the mean square pressure, $\langle p^2 \rangle$ has been averaged in both space and time. The density of air is ρ_0 and the speed of sound in air is c_0. Mean square pressure may be expressed as Sound Pressure Level, SPL in dB re 20μPa as given by Craik[61],

$$SPL = 10\log\left(\frac{\langle p^2 \rangle}{(2\times 10^{-5})^2}\right) \qquad (2.57)$$

2.8 Statistical Energy Analysis

When multi-modal structures such as plates and beams are in contact, the energy stored in the modes of one sub structure may flow to those of another. Power may also flow between different types of mode within the same structure e.g. from bending modes in a beam to longitudinal modes in the same beam. In SEA the entire structure is split into groups of similar modes known as subsystems. Lyon&Maidanik[32] deduced that the power flow from a mode α, of one subsystem to a mode β, of a connected subsystem is given by (2.58) when they are exited by independent white noise sources,

$$P_{\alpha\beta} = g(\xi_\alpha - \xi_\beta) \tag{2.58}$$

where ξ_α and ξ_β are the time averaged vibration energies of the two modes. The coupling parameter g is dependent upon the strength of mechanical coupling between the modes e.g. the stiffness of a spring connecting two structures, g also depends on the degree of spatial matching between the modes at the point, line or area of contact. The proximity of the natural frequencies of the two modes has a strong effect upon g which is large when the natural frequencies are within a resonant bandwidth and small otherwise. This relationship may be extended to give the total power flowing from all the modes of one subsystem to another in a frequency range $\Delta\omega$ (rad/s). If the power flow is summed for all the modes in one subsystem to all those in the other and the average coupling parameter $\langle g \rangle$ introduced then the total power flow from one subsystem to another is given by Lyon&DeJong[36] as,

$$P_{12} = \langle g \rangle N_1 N_2 \left(\frac{E_1}{N_1} - \frac{E_2}{N_2} \right) \tag{2.59}$$

where N_1 and N_2 are the number of modes of subsystem one and two respectively in the frequency interval $\Delta\omega$. Using the modal densities of the subsystems n_1 and n_2(modes/Hz) gives $N_1 = n_1 \Delta\omega / 2\pi$ and $N_2 = n_2 \Delta\omega / 2\pi$. E_1 and E_2 are the total energy of the modes in subsystems one and two respectively in the frequency range $\Delta\omega$. Two assumptions have been made in developing equation (2.59):

- The total energy of each subsystem is shared equally amongst all its modes within the frequency band $\Delta\omega$ and the modal amplitudes within a subsystem are incoherent. These conditions are best met when the coupling is light in relation to the damping and the damping of modes within a subsystem are similar. Modal incoherence is encouraged

by "rain on the roof" excitation, that is random impulsive excitation over the surface of the structure.

- Modal frequencies are randomly distributed with a uniform probability. Lyon&DeJong[36] use this assumption to produce the modal average coupling, $\langle g \rangle$ which is independent of the position of natural frequencies. It is this assumption that gives rise to the word "Statistical" in SEA.

The SEA power flow relations are usually written in terms of the Coupling Loss Factor (CLF). This gives equation (2.59) as,

$$P_{12} = E_1 \omega \eta_{12} - E_2 \omega \eta_{21} \tag{2.60}$$

where η_{12} and η_{21} are the CLFs which are given by,

$$\eta_{12} = \frac{\langle g \rangle N_2}{\omega}, \quad \eta_{21} = \frac{\langle g \rangle N_1}{\omega} \tag{2.61}$$

The CLFs are related by the reciprocity relationship which may be written as,

$$N_1 \eta_{12} = N_2 \eta_{21} \tag{2.62}$$

The reciprocity relationship between the CLFs may also be written in terms of the modal densities of the two subsystems, giving,

$$n_1 \eta_{12} = n_2 \eta_{21} \tag{2.63}$$

Power flowing between the two subsystems is illustrated in Fig. 2.2. The power flowing out of each subsystem as a result of damping has also been included using equation (2.34).

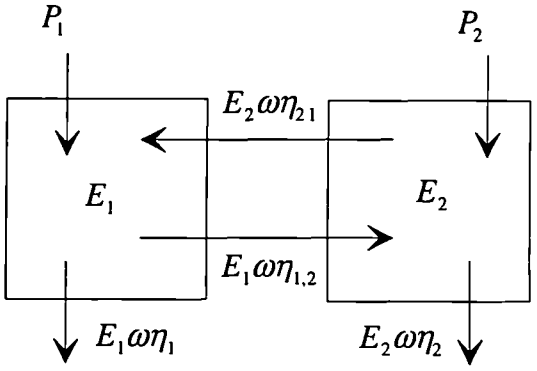

Figure 2.2: SEA subsystem power flow.

By conservation of energy the power entering a subsystem must either be fed to a connected subsystem or lost to the system. Energy may be lost to the system by

dissipation due to damping or by flow out of the system, e.g. radiation into a surrounding fluid. The Energy to power flow relationships shown in Fig. 2. can be expressed in matrix form,

$$\begin{pmatrix} (\eta_{12}+\eta_1) & -\eta_{21} \\ -\eta_{12} & (\eta_{21}+\eta_2) \end{pmatrix} \begin{pmatrix} E_1 \\ E_2 \end{pmatrix} = \begin{pmatrix} P_1/\omega \\ P_2/\omega \end{pmatrix} \tag{2.64}$$

This SEA model contains only two subsystems but the same principle can be applied to systems with hundreds. If the magnitudes of the power inputs can be estimated then (2.64) may be solved using Gaussian elimination, yielding the subsystem energy levels. Attenuation of vibration through the model may be evaluated for a given source location by setting the power input at this location to unity and all the others to zero. Energies are then expressed as ratios of the source sub system energy or in dB as an Energy Level Difference (ELD),

$$\mathrm{ELD}_{m,n} = 10\log\left(\frac{E_n}{E_m}\right) \tag{2.65}$$

where m is the source and n the receiving subsystem. When power flows into subsystem one only then E_2 / E_1 for the system shown in Fig. 2.2 is given by,

$$\frac{E_2}{E_1} = \frac{\eta_{12}}{\eta_2 + \eta_{21}} \tag{2.66}$$

where power is input to subsystem one only. The linear sum of the ILF and all the CLFs out of a subsystem is known as its Total Loss Factor (TLF). Both the CLF and TLF are frequently expressed in dB re 10^{-12} in the same way as the ILF in equation(2.33).

2.8.1 Modal Overlap Factor

The power flow relations given by Lyon&Maidanik[32] which form the basis of SEA assume that the interaction between coupled groups of modes are dominated by resonant behaviour. The modal overlap factor, M is a parameter which indicates what proportion of the frequency spectrum is likely to contain a resonant modal response and is given by Craik[61] as,

$$M = fn\eta \tag{2.67}$$

where η is the TLF of the subsystem. Modal overlap is also often given as $M = \omega n\eta$ (e.g. Fahy&Mohammed[38]) which is identical to equation (2.67) because n in that case is modes/rad rather than modes/Hz. When M =1 then the resonant bandwidth, $f\eta$ (Hz) is equal to the average modal frequency spacing, $1/n$ (Hz) and the subsystem response can

be expected to be resonant over most of the frequency range. This assumes that the modal resonance frequencies are uniformly distributed.

2.8.2 Predicted Response Variance

SEA energy level predictions are the mean energy of an ensemble of similar hypothetical systems. A laboratory model or manufactured product (e.g. a motorcar) constitutes one sample from an ensemble. Vibration or acoustic energies predicted using SEA are therefore no use to a design engineer without some idea of the likely deviation from the mean that could occur in one sample. Lyon&DeJong[36] have analysed the variance in SEA response predictions. They point to four important causes of variance:

a) Variation in the predicted power input. If power is injected into a subsystem at a discrete point then the magnitude of the power flowing into a particular mode of the structure will depend upon the modal displacement at the point where the load is applied.

b) Variation in the CLFs. The CLFs between connected subsystems will depend upon the modal displacements at the point, line or area of contact.

c) Modal displacement at the point where response is measured. If the response is measured near a node of a particular mode then contribution to the measured response from that mode will be small.

d) The number of resonant subsystem modes within a particular frequency band will vary from one sample of the ensemble to another.

Lyon&DeJong[36] have estimated the response variance for a two subsystem SEA model. They give the standard deviation of response normalised by the mean as,

$$\frac{\sigma^2_{v_2^2}}{m^2_{v_2^2}} = \left(n_1 n_2 \frac{\pi}{2} f(\eta_1 + \eta_2)\Delta f \right)^{-1} \left[\frac{\langle \psi_1^4 \rangle}{\langle \psi_1^2 \rangle^2} \right]^2 \left[\frac{\langle \psi_2^4 \rangle}{\langle \psi_2^2 \rangle^2} \right]^2 \qquad (2.68)$$

where Δf is the frequency band that is excited, $\sigma^2_{v_2^2}$ is the standard deviation of temporal mean square velocity at the measurement point on subsystem two. The mean square velocity of subsystem two is $m^2_{v_2^2}$. $\langle \psi^4 \rangle / \langle \psi^2 \rangle^2$ is a modal shape factor which is equal to 9/4 for a plate with sinusoidal mode shapes. Equation (2.68) is for a two subsystem model with a point load applied at a random position on the source subsystem, the response is at one randomly chosen point on subsystem. When the response of the receiving panel is averaged for a large number of loading and response positions the contributions to variance given in a) and c) become less important. This is the case when measuring

Energy Level Differences as described in Chapter 4. The largest contribution to variance in energy levels is from fluctuation of the CLF. Lyon&DeJong[36] give the normalised variance of the CLF between two SEA subsystems as,

$$\frac{\sigma^2_{\eta_{12}}}{\mathrm{m}^2_{\eta_{12}}} = \left(\Delta f\,(n_1+n_2) + \pi f\,(n_1\eta_{1,\,\mathrm{net}} + n_2\eta_{2,\,\mathrm{net}})\right)^{-1} \frac{\langle\psi_1^4\rangle}{\langle\psi_1^2\rangle^2}\frac{\langle\psi_2^4\rangle}{\langle\psi_2^2\rangle^2} \tag{2.69}$$

where $\mathrm{m}_{\eta_{12}}$ is the mean CLF. For plates with sinusoidal mode shapes the mode shape factors $\langle\psi^4\rangle/\langle\psi^2\rangle^2$ in equation (2.69) are equal to 3/2 if the panels are joined along a line boundary and 9/4 if they are connected at a single point. For a panel coupled to an acoustic volume the mode shape factor is 1 for the panel and 3/2 for the acoustic space. If the subsystems are irregular in shape then the mode shape factor is given by $\langle\psi^4\rangle/\langle\psi^2\rangle^2 = 3$ (See Lyon&DeJong[36]). $\eta_{1,\,\mathrm{net}}$ is the net effective loss factor of sub system one. The net effective loss factor lies between the internal loss factor and the TLF, it includes the effect of coupling to other subsystems. The net effective loss factors of the two subsystem SEA model shown in Fig. 2.2 are given by,

$$\eta_{1,\,\mathrm{net}} = \eta_1 + \eta_{12} - \frac{\eta_{12}\eta_{21}}{\eta_{21}+\eta_2}, \quad \eta_{2,\,\mathrm{net}} = \eta_2 + \eta_{21} - \frac{\eta_{12}\eta_{21}}{\eta_{12}+\eta_1} \tag{2.70}$$

Equations (2.68) and (2.69) show that variance reduces as the modal overlap factor, $M = fn\eta$ and the frequency interval Δf increase. In complex structures Lyon&DeJong[36] assume a log-normal distribution in energy levels. This means that energy levels expressed in dB are assumed normally distributed. Lyon&DeJong[36] give the relationship between variance of velocity level $\sigma^2_{L_v}$, (in dB) and the normalised linear variance as,

$$\sigma^2_{L_v} = 43\log\left(1+\frac{\sigma^2_{v^2}}{\mathrm{m}^2_{v^2}}\right) \tag{2.71}$$

Equation (2.71) can also be used for subsystem energy and ELD. The normalised variance of E_2/E_1 in a two subsystems model is at most equal to the normalised variance of the CLF because η_{12} and η_{21} (in equation (2.66)) are not independent variables. ELD variance may be calculated as follows. Normalised variance of the CLF and hence E_2/E_1 may be calculated using equations (2.69) and then converted into ELD variance using (2.71). Square rooting the variance then gives the standard deviation (σ). Taking an example of two coupled panels with $n_1 = n_2 = 0.2$ and $\eta_{1,\,\mathrm{net}} = \eta_{2,\,\mathrm{net}} = 0.01$,

this gives σ_{ELD}=2.3dB at 250Hz. For coupling between one of these panels and an acoustic space with $n_2 = 0.08$ at 250Hz and $\eta_{2,net} = 0.05$ the standard deviation is given by σ_{ELD}=2.5dB at 250Hz. In both these calculations the mode shape factors were assumed equal to 3 as the panels and acoustic volumes in motor-vehicles are normally irregular in shape. The panel and acoustic properties used in the examples above were taken from Chapter 6 and are typical of the body panels and saloon volume of a small passenger car. In a population with a normal distribution around 95% of the population lie within $\pm 2\sigma$ of the mean. In general the interval, mean $\pm$ C(95%) containing 95% of the population is known as the 95% confidence interval. In a normal distribution $C(95\%) = 2\sigma$. For the two panels given in the example above 95% of ELDs from an ensemble of similar coupled panels would be expected to lie within 4.6dB of the mean ELD value at 250Hz (C(95%) = 4.6dB). For an ELD between the panel and saloon, C(95%) = 5.0dB at 250Hz. The predicted confidence intervals reduce with frequency particularly for the saloon as its modal density increases with frequency. A number of approximations were made in order to derive equations (2.68) and (2.69) which are conservative and usually over estimate the variance. Procedures for measuring variance and calculating confidence in measured data are described in Chapter 4. Variance in the measurements discussed in Chapter 4 includes the effects of spatial fluctuation in response.

2.9 Evaluation of SEA Coupling Loss Factors

Several methods for calculating CLFs between connected subsystems have been developed. The methods used depend upon the nature of the subsystems and the type of coupling between them. Techniques for calculating CLFs are outlined below for point coupling, line coupling, panel-acoustic coupling and direct acoustic coupling.

2.9.1 Point coupling

Lyon&DeJong[36] used reciprocity relations to produce an expression relating the energy of two point coupled multi modal structures. The energy ratio is then given by,

$$\frac{E_2}{E_1} = \frac{4R_1R_2}{\eta_2 \omega n_1 |Z_1 + Z_2|^2} \tag{2.72}$$

Where R_1 and R_2 are the real parts of Z_1 and Z_2 respectively which are known as mechanical resistance's. η_2 is the ILF of subsystem 2. Using equations (2.66) and (2.63) allows the CLF to be written as,

$$\eta_{1,2} = \frac{1}{\frac{1}{a} - \frac{n_1}{n_2 \eta_2}} \text{, where } a = \frac{4R_1 R_2}{\omega n_1 |Z_1 + Z_2|^2} \tag{2.73}$$

When the connected subsystems are flat panels of the same material and thickness there impedances are real and equal i.e. $R_1 = R_2 = Z_1 = Z_2$. If this is the then case the CLF reduces to,

$$\eta_{12} = \frac{1}{\omega n_1 - \frac{n_1}{n_2 \eta_2}} \approx \frac{1}{\omega n_1} \qquad \omega\, n_2 \eta_2 >> 1 \tag{2.74}$$

if the inequality in equation (2.74) is true then the approximation is valid. Expressing the modal density in terms of mobility using (2.49) gives,

$$\eta_{12} = \frac{1}{4 m_1 \omega Y_1} \tag{2.75}$$

where m_1 is the total mass of the transmitting panel. A more general expression is given by Craik&Wilson[26] which accounts for the spring stiffness K of the element connecting the points on the two panels,

$$\eta_{1,2} = \frac{Y_2}{2\pi f\, m_1 \left((Y_1 + Y_2)^2 + (2\pi f / K)^2 \right)} \tag{2.76}$$

where Y_1 and Y_2 are the mobilities of the two panels at the point of coupling. If this expression is used for coupling between two identical panels connected near the centre of one and on the edge of the other the resulting CLFs will not be equal. The reciprocity relationship (2.63) requires that the CLFs are the same if the modal densities are equal. Equation (2.76) should therefor only be used edge to edge or middle to middle to preserve reciprocity. When the stiffness K is high enough such that $2\pi f / K << (Y_1 + Y_2)$ then the CLFs predicted by (2.76) for edge to edge and middle to middle are equal.

2.9.2 Structural acoustic coupling

In motor vehicles most of the surfaces which radiate are panels. The total power radiated from a panel is usually written in terms of the radiation efficiency, σ which is given by Fahy[20] as,

$$p = \sigma \rho_0 c_0 S \overline{\langle v^2 \rangle} \tag{2.77}$$

where the subscript 0 indicates the properties of air. For a baffled piston with radius a vibrating at a frequency such that the acoustic wavelength is much greater than the circumference (i.e. $ka >> 1$) the radiation efficiency is given by $\sigma = 1$. In most cases the

radiation efficiency is either below or very close to unity but there is no reason why it may not exceed this value. Radiated power may also be written in terms of the radiation loss factor, η_{rad} which is the CLF from the panel into the acoustic space,

$$p = E\omega\eta_{rad} \tag{2.78}$$

Using equation (2.53) allows the radiation loss factor to be related to the radiation efficiency by,

$$\eta_{rad} = \frac{\sigma\rho_0 c_0}{\omega m} \tag{2.79}$$

where m is the surface density of the plate material as before. Using the reciprocity relationship (2.63) the CLF from the acoustic space to the panel may be calculated from the radiation loss factor. The radiation efficiency of each mode of a rectangular simply supported panel surrounded in the same plane by a ridged baffle can be calculated using an integral expression given by Wallace[30]. As frequency rises and the modal overlap factor increases this approach becomes computationally expensive because of the large number of modes radiating significantly at each frequency. Under these conditions Maidanik[31] used a modal average radiation efficiency which is equivalent to assuming equipartition of modal energy within the panel. Leppington *et al*[33] give approximations to the average radiation efficiency of the same panel arrangement. For radiation from one side of a simply supported panel into an infinite acoustic volume Leppington *et al*[33] give the radiation efficiency as,

$$\sigma = \frac{Uc_0}{4\pi^2 f^{1/2} f_C^{1/2} S(\mu^2-1)^{1/2}}\left(\ln\left(\frac{\mu+1}{\mu-1}\right)+\frac{2\mu}{\mu^2-1}\right) \quad f < f_C,\ l_1(k_B - k_0) \text{ large} \tag{2.80}$$

$$\sigma = \left(\frac{2\pi f l_1}{c_0}\right)^{1/2} H\left(\frac{l_1}{l_2}\right) \quad f = f_C \tag{2.81}$$

$$\sigma = \left(1-\frac{f_C}{f}\right)^{-1/2} \quad f > f_C,\ l_1(k_0 - k_B) \text{ large} \tag{2.82}$$

$$f_C = c_0^2 / 1.8hc_L \tag{2.83}$$

where f_C is known as the critical frequency or the coincidence frequency, l_1 and l_2 are the dimensions of the panel chosen such that $l_1 \le l_2$. The perimeter length is $U = 2(l_1 + l_2)$ and here the variable $\mu = (f / f_C)^{1/2}$. H is a complicated function of the panel aspect ratio which is approximately $H(x) = 0.5 - 0.15x$. Maximum radiation occurs close to but not at the critical frequency, Leppington *et al*[33] suggests using $H(x) = 0.6 - 0.2x$

instead to give the maximum radiation. A bending wave at $f = f_c$ travels at the same speed as sound in air, above this frequency the bending wave travels faster than sound in air. This means that phase matching between a sound wave travelling from the panel and a bending wave is always possible above the critical frequency. Acoustic response from a bending wave on an infinite panel below the critical frequency is restricted to a near field or surface wave which decays exponentially away from the panel leading to a radiation efficiency of zero. Finite panels however do radiate power below the critical frequency but much less than above. Radiation below the critical frequency is from the panel boundaries and corners. Boundary radiation dominates equation(2.80) which is proportional to perimeter length. Leppington *et al's*[33] equations above are high frequency asymptotes derived under the assumption that acoustic wavelength is small in relation to the panel boundary lengths ($k_0 l_1 \rightarrow \infty$) . This is not the case at low frequencies for panels which radiate into a motor typical vehicle saloon, Fig. 2.3(a) and (b) show radiation efficiencies calculated by numerically integrating Walace's[30] integral for each mode of a window panel and modal average approximations calculated using Leppington *et al's*[33] equations.

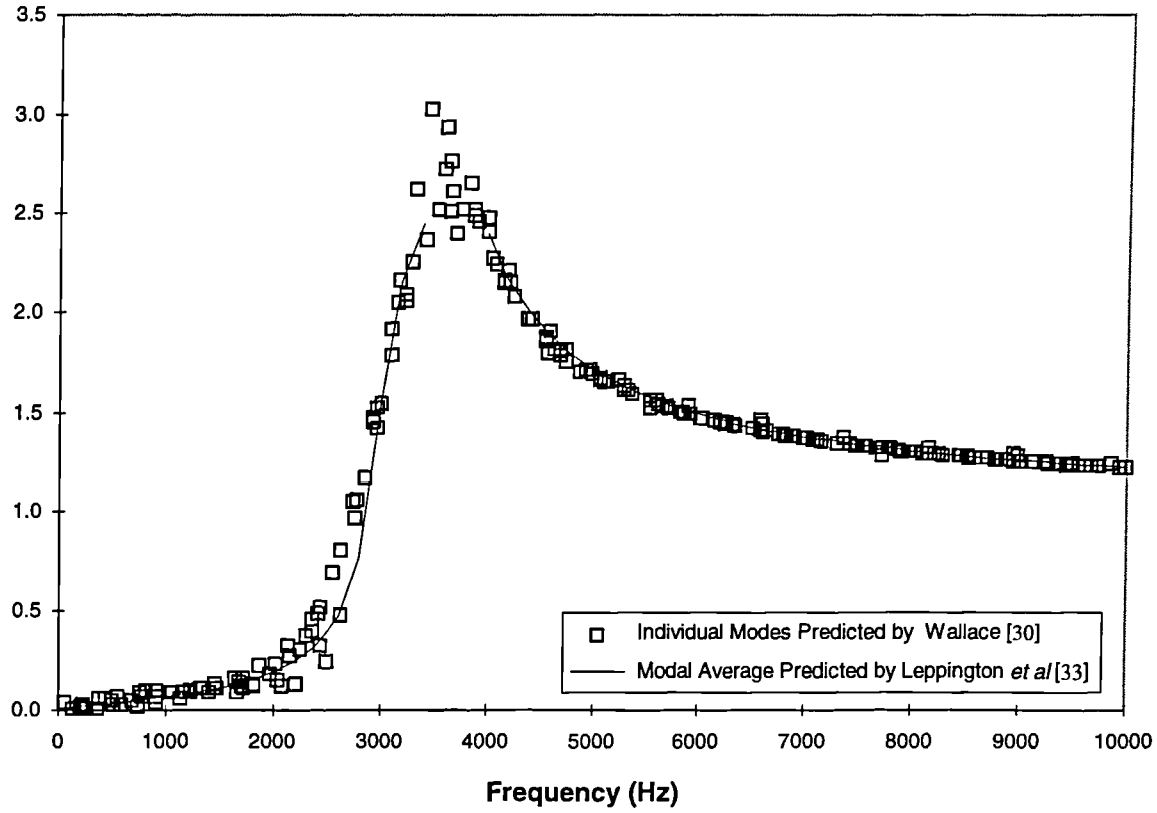

Figure 2.3(a): Radiation efficiency of a window panel, $h = 4$mm, c_L (plate) = 4900m/s, $\rho = 2500$ kg/m^3, μ =0.3, f_c = 3309 Hz and dimensions = (0.66×0.44)m.

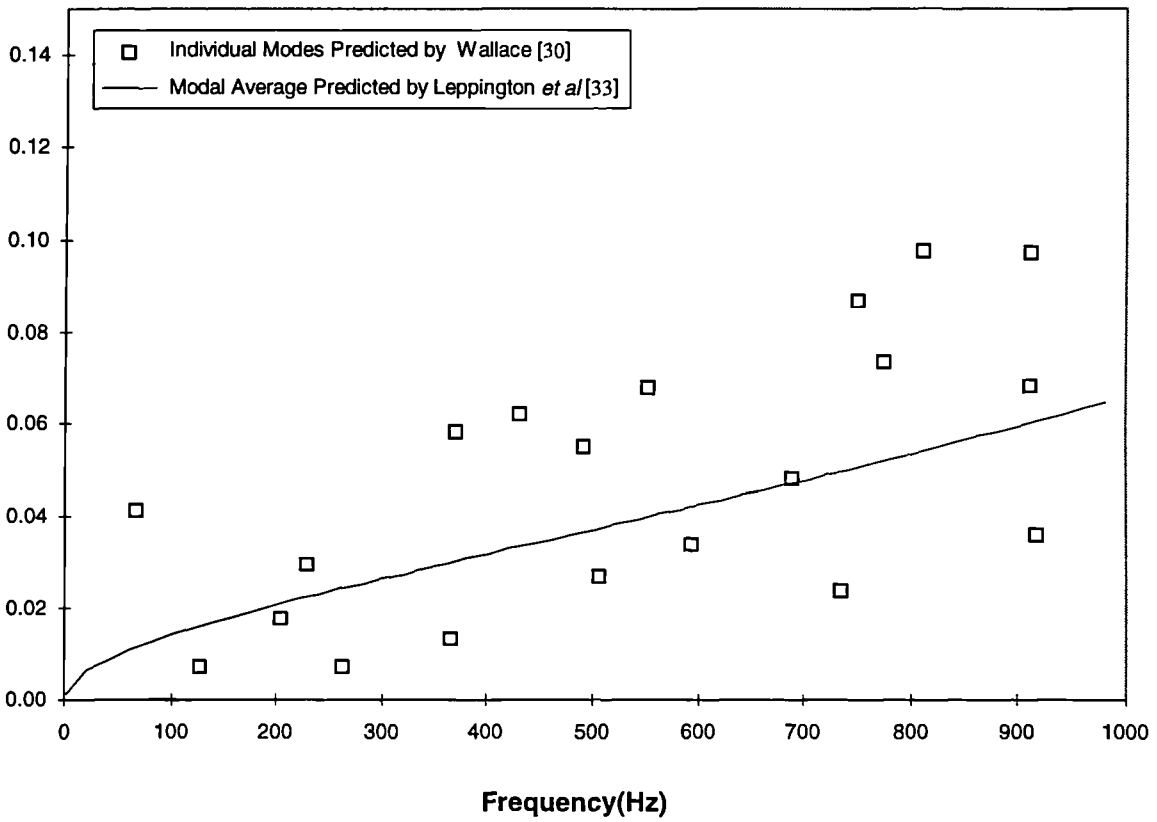

Figure 2.3 (b): As Fig. 2.3(a) above but 0-1000 Hz.

The approximate modal average values of radiation efficiency show good agreement with the numerically integrated ones over the entire frequency range. This suggests that equations (2.80)-(2.82) are applicable to panels of this size even at low frequencies provided there are sufficient panel modes for a modal average to be meaningful.

Real panels assembled in structures are not simply supported at their boundaries. In motor vehicles the body panels are usually spot welded into closed section beam arrangements along there boundaries. It is therefore probably a better approximation to assume that the body panels are clamped along there edges rather than simply supported. Leppington *et al*[34] showed that clamping the panel boundaries doubles the radiation efficiency below the critical frequency but has a negligible effect above the critical frequency. All the expressions discussed so far have been derived assuming the panels are surrounded by an infinite baffle in the same plane as the panel. The panels of a motor vehicle are joined at a variety of angles, but most frequently at around 90°. Leppington[35] showed that if the baffles surrounding the panel are at right angles to the panel surface then a further two-fold increase in radiation occurs below the critical frequency. Correction factors for boundary conditions and right angled baffles apply only below the critical frequency, to prevent discontinuity at the critical frequency Leppington *et al*[90] suggested multiplying by,

$$m-(m-1)\left(\frac{f}{f_c}\right)^4 \tag{2.84}$$

where m is the correction factor. Clamped boundaries and right angled baffles are probably the best approximation for the panels that radiate into the saloon of a motor vehicle giving $m = 4$.

When there is no baffle present the panel radiation efficiency below the critical frequency is less than from and otherwise identical panel with a baffle. This is because the waves radiated from the two sides of the panel partially cancel one another. Well above the critical frequency the radiation efficiency of an un-baffled panel is the same as that of a baffled one baring in mind that both sides of the panel radiate. Heron[91] has calculated an expression for the radiation efficiency of a rectangular free-free panel with no surrounding baffle. This is given below the critical frequency by,

$$\sigma = \frac{(l_1 + l_2)(3-2\sqrt{2})c_0}{4\pi f S \mu^3 \sqrt{\mu^2 - 1}}, \text{ where } \mu = \sqrt{\frac{f_C}{f}} \quad \text{and} \quad f < f_C \tag{2.85}$$

where l_1 and l_2 are the dimensions of the panel. It must be noted that the expressions for radiation efficiency given by Leppington *et al*[33,34,35,90] and Wallace[30] are for radiation into free space. If these expressions are to be used for radiation into a finite volume (Such as a vehicle saloon) then they must be regarded as an average over the modes of the volume in the frequency band of interest.(This is discussed by Fahy[20]).

2.9.3 Direct Non Resonant Coupling Across a Panel

When two acoustic volumes are separated by a panel with no holes one might expect the SEA model to be a simple chain of three subsystems. It is a well known fact however (See Leppington *et al*[22]) that this model significantly under predicts the coupling between the two acoustic volumes below the critical frequency of the panel. A correction in the form of a "direct" or non resonant coupling between the volumes is necessary. This direct coupling is shown in Fig. 2.4 by a dotted line.

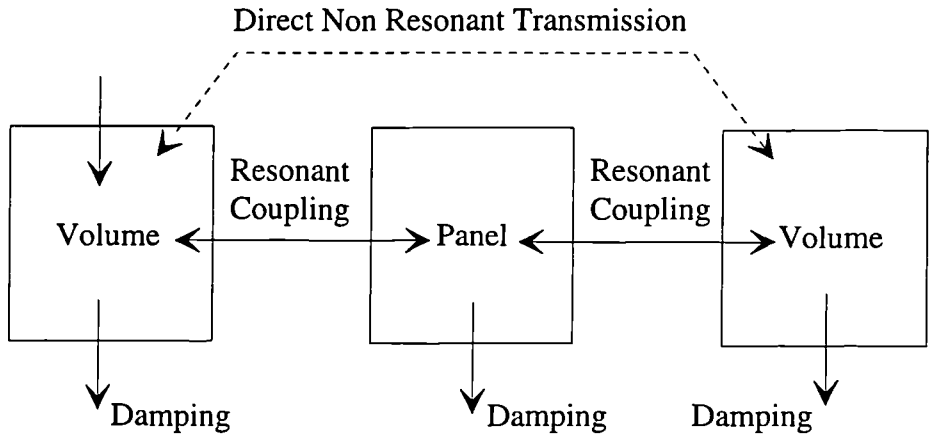

Figure 2.4: Direct non resonant coupling.

The direct coupling is necessary below the critical frequency because panel modes that are excited above there natural frequency are more efficient radiators than the resonant panel modes, so much so that the coupling between the acoustic volumes due to the structural modes excited above resonance is greater than that due to those excited close to resonance. Because the dominant coupling occurs through structural modes above resonance in their mass controlled region the coupling is strongly dependant upon the

surface density of the panel and very weekly dependant upon the stiffness or damping. Non resonant coupling can be calculated by wave methods and quantified by using a transmission coefficient, τ which is the proportion of energy incident upon the panel which is radiated on the other side. The transmission coefficient is a function of the angle at which the wave is incident to the panel. Fahy[20] gives the transmission coefficient for an infinite flat panel at frequencies well below the critical frequency as,

$$\tau(\phi) = \frac{1}{1 + (\omega m \cos\phi / 2\rho_0 c_0)^2} \tag{2.85}$$

where ϕ is the angle of incidence. The transmission coefficient may be averaged with respect to angle of incidence by using the equation (Beranek&Ver[65]),

$$\langle \tau \rangle = \frac{\int_0^{\theta} \tau(\phi) \sin 2\phi \; d\phi}{\int_0^{\theta} \sin 2\phi \; d\phi} \tag{2.86}$$

where θ is the maximum limiting angle of incidence which is taken as $\theta = \pi / 2$ for a diffuse wave field with random incidence. It is common to express acoustic transmission coefficients in dB using the Sound Reduction Index or Transmission Loss (TL),

$$\mathrm{TL} = 10 \log(1/\tau) \tag{2.87}$$

Averaging equation (2.85) using (2.86) with θ = 90° and expressing the result in dB using equation (2.87) gives a result which is known as the random incidence mass law. The field incidence mass law is an alternative which typically gives better agreement with experimentally measured Transmission Losses. Field incidence mass law TL may be calculated in the same way as the random incidence value except that equation (2.85) is averaged between 0 and 78° using (2.86). The Field incidence mass law is normally calculated using (Fahy[20]),

$$\mathrm{TL} = 20 \log(mf) - 47 \tag{2.88}$$

Leppington *et al*[22] have calculated an expression for the average transmission coefficient between two volumes which are separated by a finite rectangular panel in a ridged baffle. They give tne average non resonant transmission coefficient as,

$$\langle\tau\rangle=\left(\frac{\rho_0 c_0}{\pi f m\left(1-f^2/f_C^2\right)}\right)^2\left(\ln\left(\frac{2\pi f\sqrt{S}}{c_0}\right)+0.16+U(l_1/l_2)\right.$$
$$+\frac{1}{4\mu^6}\left[(2\mu^2-1)(\mu^2+1)\ln(\mu^2-1)+(2\mu^2+1)(\mu^2-1)\ln(\mu^2+1)\right. \quad (2.89)$$
$$\left.\left.-4\mu^2-8\mu^6\ln(\mu)\right]-\right)$$

where l_1 and l_2 are the dimensions of the panel. $U(l_1/l_2)$ is a function which becomes negligible in relation to the other terms for typical structures where $0.1 < l_1/l_2 < 10$. The parameter μ is given by $\mu=\left(f_C/f\right)^{1/2}$. The terms on the second and third lines can usually be ignored except close to the critical frequency. Leppington *et al's*[22] expression and the field incidence mass law gives similar results well below the critical frequency as shown by Craik[61].

The SEA CLF between to acoustic volumes due to direct transmission through a panel may be calculated from the transmission coefficient using,

$$\eta_{12}=\frac{c_0 S\langle\tau\rangle}{4\omega V_1} \quad (2.90)$$

where S is the area of the panel and V_1 the volume of the transmitting space.

2.9.4 Coupling Through Double Panels

Trim panels in motor vehicles separate the Body panels from the acoustic volume of the saloon and in doing so they form a narrow cavity between the panels. These cavities are typically 10-100mm in depth. Sound transmission through double panels with a cavity in between has been investigated using SEA by Price&Crocker[92]. A similar situation occurs in buildings with cavity walls which have a small gap between the two leaves of the wall. Craik&Wilson[26] have investigated sound transmission through cavity walls using SEA. Below the "mass-air-mass resonance frequency" the two panels move as one. The mass air mass resonance frequency is given by Fahy[20] as,

$$f_{dw}=\frac{1}{2\pi}\sqrt{\left(\frac{\rho_0 c_0^2}{d}\right)\left(\frac{1}{m_1}+\frac{1}{m_2}\right)} \quad (2.91)$$

where d is the depth of the cavity. For a typical light trim panel separated from the body panel by 10mm Equation (2.91) produces a value of around 590Hz. The "mass-air-mass resonance frequency" is also known as the Double Wall frequency which explains the *dw*

subscripts in equation (2.91). Above this frequency Craik&Wilson[26] treat the two panels as separate SEA subsystems which are coupled together as shown in Fig. 2.5

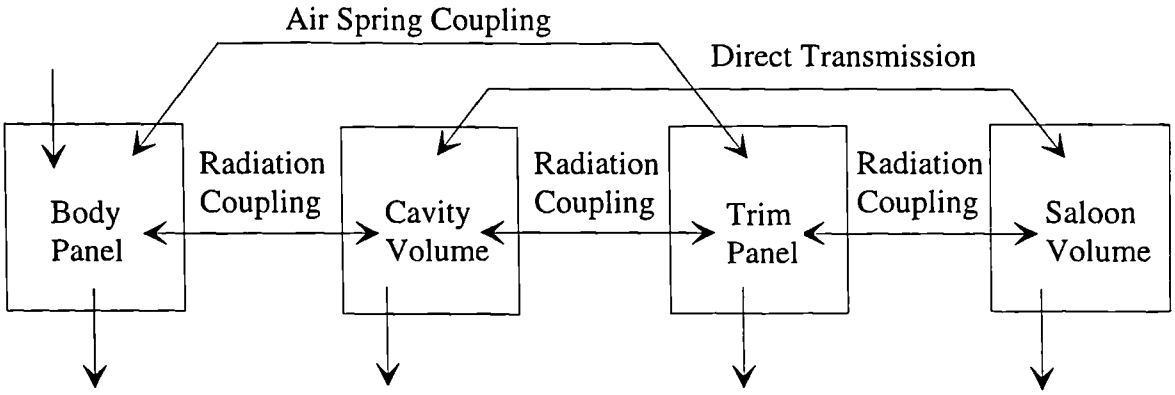

Figure 2.5: SEA model of trimmed panel with cavity and saloon volume.

In Craik&Wilson's[26] model the two panels are coupled by the air spring effect. They calculate the air spring coupling using equation (2.76) using the equivalent spring stiffness per square meter which is given by Cremer *et al*[1] as $K = 10^5 / d$. In addition to the non resonant coupling due to the air stiffness of the cavity the resonant coupling between the panels and the cavity is included using equation (2.79). When calculating the reciprocal coupling from the cavity to the panel the expression for the modal density of a narrow cavity (2.48) was used in place of the expression for a normal acoustic volume. The direct transmission between the cavity and the saloon volume through the trim panel was included using equation (2.90).Priece&Crocker's[92] model was very similar to Craik&Wilson's[26] except that the air spring coupling was not included.

Motor vehicle body panels are often fitted with what is known as a Sound Barrier Assembly (SBA) or sound package of the type described by Wentzel&Saha[29] and Powel *et al*[70]. A Sound Barrier Assembly consists of a foam isolator attached to a plastic barrier as shown in Fig. 2.6.

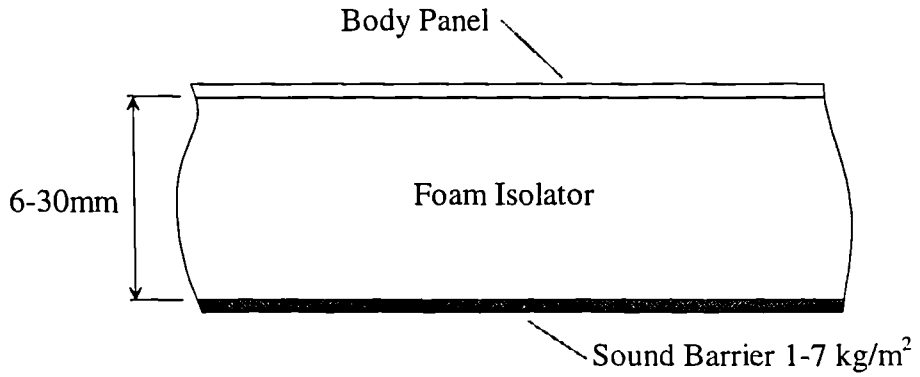

Figure 2.6: Sound Barrier Assembly with some typical dimensions and properties from Wentzel&Saha[29].

This assembly forms another double panel arrangement with the foam isolator in the cavity. The SBA used in the Nissan Micra motor vehicle is discussed in Chapter 6. Wentzel&Saha[29] measured the Transmission Loss of a number of motor vehicle SBAs and produced an empirical model for predicting it. Wentzel&Saha's[29] empirical model for predicting the Transmission Loss of motor vehicle Sound Barrier Assemblies is given by,

$$TL = 20\log(mf) - 47 \qquad f < f_{dw} \qquad (2.92)$$

$$TL = TL_1 + TL_2 + 20\log(fd) - 28.7 \qquad f_{dw} < f < f_{sw} \qquad (2.93)$$

$$TL = TL_1 + TL_2 + IL - 5 \qquad f_{sw} < f < f_c \qquad (2.94)$$

where $f_{sw} = c_0 / 12d$. Equation (2.92) assumes that the body panel and the SBA move as one and uses the field incidence mass law (2.88) to calculate the TL using m which is the combined surface density of both panels and the isolator. TL_1 and TL_2 are the individual Transmission Losses for the body panel and the barrier given by equation (2.88). IL is the Insertion Loss caused by the attenuating effects of the isolator foam. Wentzel&Saha[29] measured Insertion Loses for several isolators of different thickness.

2.9.5 Line coupling between panels

The most common type of structural coupling found in a motor vehicle is that across line boundaries between the panels that form the body of the vehicle. When the joint between the panels is longer than the wavelength of a bending wave travelling on the panels it is normal to treat it as a line contact. If the joint is much shorter than one wavelength it is usually treated as a point coupling. CLFs across line connections between panels may be

calculated from structural wave transmission coefficients which are defined as the proportion of the wave energy incident upon the junction that is transmitted to the other side. Bending longitudinal and Transverse waves can travel in panels so it is normal to specify the incident and transmitted wave types with subscripts (e.g. τ_{BL} is the proportion of bending wave energy from one panel that is converted into longitudinal wave energy on a connected panel). The transmission coefficient is a function of the angle at which the wave is incident but using the diffuse field assumption allows the transmitted power to be written in terms of the average transmission coefficient which is given by Cremer *et al*[1] as,

$$\langle \tau \rangle = \int_0^{\pi/2} \tau(\theta) \cos\theta \, d\theta \tag{2.95}$$

The CLF across the boundary is then calculated using,

$$\eta_{12} = \frac{C_g L}{\pi \omega S_1} \langle \tau \rangle \tag{2.96}$$

where L is the length of the boundary between the panels and C_g is the group velocity of the incident wave which is twice the phase velocity for bending waves.

There now follows an example given by Cremer *et al*[1] for calculating the bending wave transmission coefficient across a panel corner joint which is shown in Fig. 2.7 .

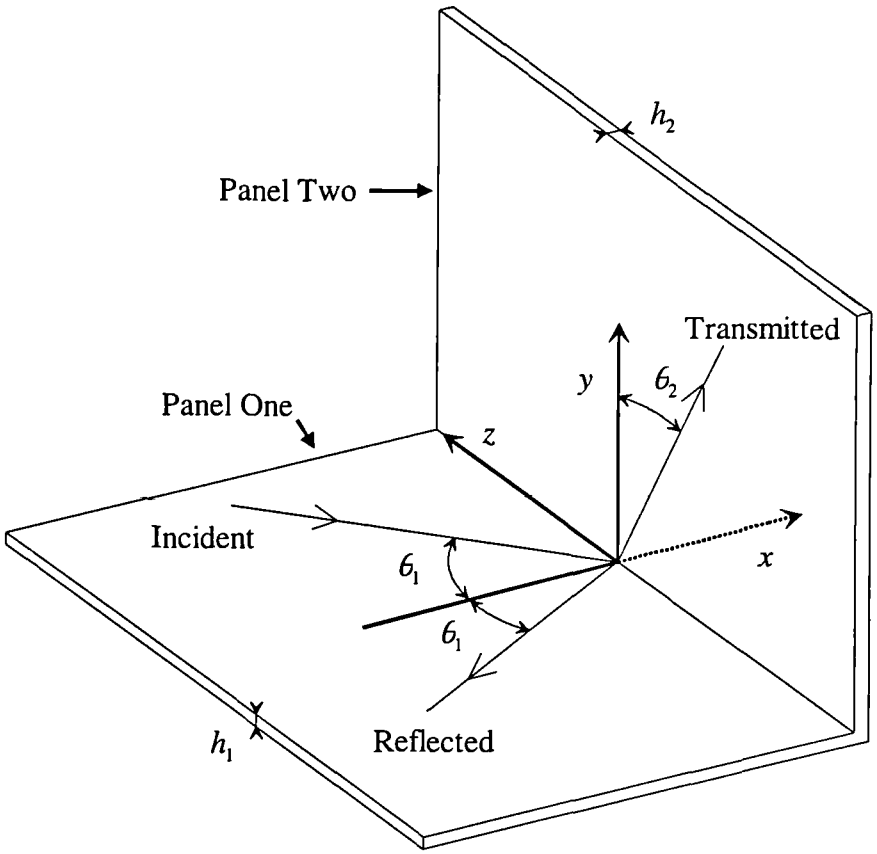

Figure 2.7: Right angled panel corner joint showing incident, reflected and transmitted bending waves.

In plane panel displacements are assumed to be zero so longitudinal and transverse waves are ignored in this analysis. The out of plane deflections of both panels are governed by the thin plate bending equation (2.17). The incoming wave is at a heading θ_1 to the x axis its displacement function is,

$$\eta = e^{i\omega t} e^{izk_1 \sin\theta_1} e^{-ixk_1 \cos\theta_1} \tag{2.97}$$

were the bending wave number on panel one is given by $k_1 = \sqrt[4]{\rho_1 h_1 \omega^2 / B_1}$ and the bending wave number on panel two is given by $k_2 = \sqrt[4]{\rho_2 h_2 \omega^2 / B_2}$. When a bending wave is incident on a boundary between two panels other waves are generated and together they fulfil the boundary conditions. It is assumed that the boundary lies along the z axis as shown in Fig. 2.7 and is infinite in length. No wave can assist in fulfilling the boundary conditions unless it has the same wave number in the z direction as the incoming wave. This dictates that all wave displacement functions must be of the form,

$$\eta_1(x,z) = f(x)e^{ik_z z}, \quad \eta_2(y,z) = f(y)e^{ik_z z}, \quad k_z = k_1 \sin\theta_1 \tag{2.98}$$

where displacement η (panel n) $= \eta_n$. The exponential function in time, $e^{i\omega t}$ is a common factor in all displacement functions and has been omitted. The plate equation (2.17) then relates the wave number in the z direction to that in the x direction on panel one, or y direction on two. There are four possible wave numbers in the x direction on plate one which gives,

$$f(x) = r\,e^{ixk_1\cos\theta_1} + n_1\,e^{x\sqrt{k_1^2+k_z^2}} + n_{1\_}\,e^{-x\sqrt{k_1^2+k_z^2}} + e^{-ixk_1\cos\theta_1} \tag{2.100}$$

where r, n and $n\_$ are the complex magnitudes of each wave. Note the last exponential in equation (2.100) is from the incoming bending wave which has unit magnitude. On plate two there are also four possible wave numbers such that,

$$f(y) = t\,e^{-y\sqrt{k_z^2-k_2^2}} + t\_\,e^{y\sqrt{k_z^2-k_2^2}} + n_2\,e^{-y\sqrt{k_2^2+k_z^2}} + n_{2\_}\,e^{y\sqrt{k_2^2+k_z^2}} \tag{2.101}$$

where t, $t\_$, n_2 and $n_{2\_}$ are the complex amplitudes of the waves on panel two. Because the panels extend an infinite distance from the joint exponential increase of deformation away from the joint is not a valid wave solution therefore $n_{2\_}$ must be zero. The bending wave with complex magnitude $t\_$ carries energy toward the joint and therefore cannot form part of the solution. This means that $t\_$ is also zero. Putting $n_{2\_}$ and $t\_$ equal to zero gives,

$$f(x) = r\,e^{ixk_1\cos\theta_1} + n_1\,e^{x\sqrt{k_1^2+k_z^2}} + e^{-ixk_1\cos\theta_1}$$

and on plate two,

$$f(y) = t\,e^{-y\sqrt{k_z^2-k_2^2}} + n_2\,e^{-y\sqrt{k_2^2+k_z^2}}$$

Putting $k_{n2} = -\sqrt{k_2^2+k_z^2}$, $k_{n1} = \sqrt{k_1^2+k_z^2}$, $k_{r1} = ik_1\cos\theta_1$ and $k_{t2} = -\sqrt{k_z^2-k_2^2}$ gives,

$$f(x) = r\,e^{k_{r1}x} + n_1\,e^{k_{n1}x} + e^{-k_{r1}x} \tag{2.102}$$

$$f(y) = t\,e^{k_{t2}y} + n_2\,e^{k_{n2}y} \tag{2.103}$$

The complex constants r, t, n_1 and n_2 represent the magnitude and phase of the reflected travelling wave, transmitted travelling wave and the nearfields on plate one and two respectively. k_{t2} is imaginary when $k_2 > k_z$ and gives rise to a travelling wave on panel two, when $k_z > k_2$, it is real, producing another nearfield and there is no transmission of bending wave energy onto panel two.

Boundary conditions

Inplane waves are not considered in this analysis and none of the wave displacement solutions above have any in-plane components. Assuming no in-plane motion implies that the out of plane deflection of both panels disappears along the z axis,

$$\eta_1(x=0,z)=0 \tag{2.103}$$

$$\eta_2(x=0,z)=0 \tag{2.104}$$

No external forces or moments are applied to the model so bending moments about the z axis must sum to zero at $x=0$,

$$M_{xz1}=M_{yz2}, \quad (x=0) \tag{2.105}$$

The panels are rigidly joined at the junction so the angular displacements of the panels must be equal along the z axis. For thin panel theory the angular displacement can be expressed as $\partial\eta_1/\partial x$ for panel one and $\partial\eta_2/\partial y$ for panel two which gives,

$$\frac{\partial\eta_1}{\partial x}=\frac{\partial\eta_2}{\partial y}, \quad (z=0) \tag{2.106}$$

Substituting equation (2.101) and (2.102) into equation (2.98) produces the displacement equations for both panels in terms of the wave amplitudes. Replacing the panel displacements into equations (2.103) and (2.104) gives,

$$1+r+n_1=0 \tag{2.107}$$

$$t+n_2=0 \tag{2.108}$$

Talking the derivative of the panel displacements with respect to x and y and replacing into equation (2.106) gives,

$$k_{r1}(r-1)+n_1k_{n1}=t\,k_{t2}+n_2\,k_{n2} \tag{2.109}$$

The bending moment boundary conditions (2.105) require the calculation of the moments in terms of the wave solutions. Bending moments are stress resultants which can be calculated if the stress distribution is known. Thin plate theory strain displacement relations are given by Cremer[1],

$$\varepsilon_x=-\frac{\partial^2\eta}{\partial x^2}r, \quad \varepsilon_z=-\frac{\partial^2\eta}{\partial z^2}r, \quad \gamma_{zx}=\gamma_{zx}=-2r\frac{\partial^2\eta}{\partial x\partial z} \tag{2.110}$$

where ε_x and ε_z are strain in the x and z directions respectively, γ_{zx} is the shear strain in the x-y plane in the x direction and r is the distance from the centroid of the panel. Linear, isotropic, elastic stress strain relations can then be used to calculate stress. Assuming plane stress in the y direction,

$$\begin{aligned}\sigma_x &= \varepsilon_x E + \mu\sigma_z, \quad (\sigma_y = 0)\\ \sigma_z &= \varepsilon_z E + \mu\sigma_x, \quad (\sigma_y = 0)\\ \tau_{zx} &= \tau_{xz} = G\gamma_{zx}\end{aligned} \tag{2.111}$$

where σ_x and σ_z are the stress in the x and z directions respectively, τ_{zx} is the shear stress in the x-y plane in the x direction. Substituting (2.110) into (2.111) for direct stress yields,

$$\begin{aligned}\sigma_x &= -\frac{Er}{1-\mu^2}\left(\frac{\partial^2\eta}{\partial x^2} + \mu\frac{\partial^2\eta}{\partial z^2}\right)\\ \sigma_z &= -\frac{Er}{1-\mu^2}\left(\frac{\partial^2\eta}{\partial z^2} + \mu\frac{\partial^2\eta}{\partial x^2}\right)\end{aligned} \tag{2.112}$$

Equations (2.110) to (2.112) refer to panel one but the same relations are used on panel two baring in mind the different orientation of the panel. Integrating $\sigma_x r$ with respect to r between $r = -h_1/2$ and $r = h_1/2$ produces an equation for the bending moment M_{xz1}, applying the same method to panel two yields the equivalent expression for M_{yz2},

$$\begin{aligned}M_{xz1} &= -B_1\left(\frac{\partial^2\eta}{\partial x^2} + \mu\frac{\partial^2\eta}{\partial z^2}\right)\\ M_{yz2} &= -B_2\left(\frac{\partial^2\eta}{\partial y^2} + \mu\frac{\partial^2\eta}{\partial z^2}\right)\end{aligned} \tag{2.113}$$

Substituting the panel displacements into (2.113) relates $\{r,t,n_1,n_2\}$ to the bending moments at the boundary,

$$M_{xz1} = -B_1\left((r+1)(k_{r1}^2 - \mu k_z^2) + n_1(k_{n1}^2 - \mu k_z^2)\right) \tag{2.114}$$

$$M_{yz2} = -B_2\left(t(k_{t2}^2 - \mu k_z^2) + n_2(k_{n2}^2 - \mu k_z^2)\right) \tag{2.115}$$

Equating (2.114) and (2.115) gives the final form of boundary condition (2.105),

$$\begin{aligned}&\left(t(k_{t2}^2 - \mu k_z^2) + n_2(k_{n2}^2 - \mu k_z^2)\right) =\\ &\frac{B_1}{B_2}\left((r+1)(k_{r1}^2 - \mu k_z^2) + n_1(k_{n1}^2 - \mu k_z^2)\right)\end{aligned} \tag{2.116}$$

Boundary conditions (2.107), (2.108), (2.109)and (2.116) can be simultaneously solved for $\{r,t,n_1,n_2\}$. The results for t and r respectively are then [1],

$$t = \frac{2i\cos(\theta_1)}{-\sqrt{\chi^2 + \sin^2\theta_1} - \psi\sqrt{1+\sin^2\theta_1} + i\left(\sqrt{\chi^2 - \sin^2\theta_1} + \psi\cos\theta_1\right)} \tag{2.117}$$

$$r = \frac{-\sqrt{\chi^2 + \sin^2\theta_1} - \psi\sqrt{1+\sin^2\theta_1} + i\left(\sqrt{\chi^2 - \sin^2\theta_1} - \psi\cos\theta_1\right)}{\sqrt{\chi^2 + \sin^2\theta_1} + \psi\sqrt{1+\sin^2\theta_1} - i\left(\sqrt{\chi^2 - \sin^2\theta_1} + \psi\cos\theta_1\right)} \tag{2.118}$$

where $\chi = k_2 / k_1$ is the ratio of the bending wave numbers in the two panels, $\psi = \sqrt{\rho_2 h_2 B_2} / \sqrt{\rho_1 h_1 B_1} = k_2^2 B_2 / k_1^2 B_1$ is defined by Cremer *et al*[1] as the ratio of the bending wave impedance's. The expression for *t* given by Cremer *et al*[1] has opposite sign to (2.117), this is because a different sign convention was used on panel two. Equation (2.118) for *r*, agrees with [1] as the sign convention on panel one was the same. Equation (2.119) relates *t* to $\tau_{BB}(\theta_1)$, the bending to bending wave transmission coefficient,

$$\tau_{BB}(\theta_1) = |t|^2 \frac{\rho_2 h_2 \cos\theta_2 k_1}{\rho_1 h_1 \cos\theta_1 k_2} = |t|^2 \frac{\psi\sqrt{\chi^2 - \sin^2\theta_1}}{\cos\theta_1} \tag{2.119}$$

Maximum transmission efficiency occurs when the two panels have identical properties i.e. $\psi = \chi = 1$. Under these circumstances τ_{BB} reduces to a very simple expression [1],

$$\tau_{BB} = \frac{\cos^2\theta_1}{2} \tag{2.120}$$

The assumption that there are no in-plane waves/deflections gives rise to equations (2.103) and (2.104). This is true for any corner angle except 180° (if the corner angle is 180° then a simple support must be included along the *z* axis to recover equations (2.103) and (2.104)). This means that if in-plane deflections are negligible then the transmission of bending waves across a corner joint between two panels is the same regardless of the corner angle. Panels in motor-vehicles are seldom joined at exactly 90° and the use of the same transmission coefficients for various joints at different angles would simplify the modelling process. Corner angle must be considered when in-plane waves are included as it effects the degree of coupling between in-plane and bending waves at the joint (this is explored in grater detail by Cremer *et al*[1]). Bending wave transmission is not function of frequency in this bending only model however Cremer *et al*[1] showed that when in-plane waves are included the transmission becomes a function of frequency. This is because the bending impedances of the two panels have the same frequency dependence, so there relative values are independent of frequency. When longitudinal waves are introduced the resulting impedances have a different frequency dependence to those caused by bending waves and there relative values change with frequency. Bending only models are valid at low frequencies, at higher frequencies longitudinal and transverse waves become significant. Bending wave transmission across a panel corner joint reduces at higher frequency as energy is transformed into Longitudinal and transverse waves. This is shown in Chapter 3 (Fig. 3.10).

2.10 Wave Intensity Analysis

Wave Intensity Analysis (WIA) which was first proposed by Langley[84] is a more recent development than SEA. It relaxes the SEA equipartition of modal energy assumption but maintains the assumed incoherence of modal amplitudes which means the total energy is still shared out amongst the modes. In wave terms, the diffuse field assumption is abandoned but the total energy is still the sum of the energy in each wave heading. The motivation for WIA was provided by studies (Guyader *et al*[82] and Boisson *et al*[86]) which showed that SEA over predicts the transmission of vibration in an L shaped plate structure. Langley[84] gives examples showing larger disagreement for a chain of line connected rectangular panels. WIA is applicable to one, two or three dimensional structures but is presented here in relation to two dimensional structures only. Fig. 2.8 shows the energy of random wave fields on two panels stored in waves flowing in eight discrete headings.

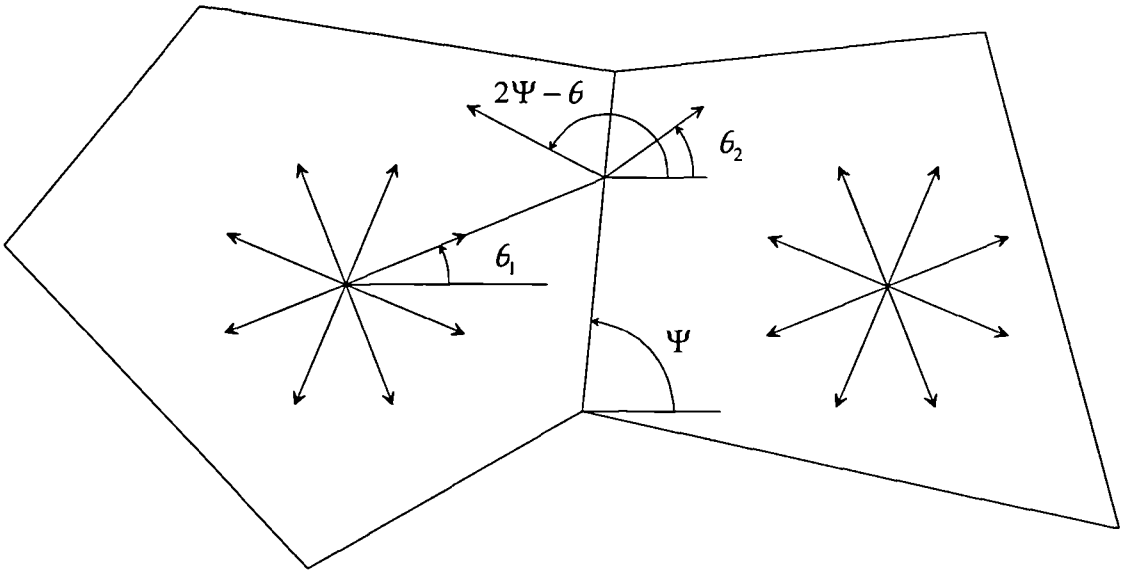

Figure 2.8: Energy stored in different wave headings on panels.

This arrangement may represent any random wave field to the required accuracy by varying the number of headings. The total energy at a given heading θ, on a particular panel j, of a wave type k (bending, longitudinal or transverse) may be written as $E_{\theta,j,k}$. For simplicity it will be assumed that only one wave type is present and k shall be dropped. When waves at a particular heading meet a boundary m, the incident power is given by,

$$p_{\theta,j,m} = E_{\theta,j}\frac{C_g L_m}{S_j}\cos(\theta - \Psi + \pi/2) \qquad (2.121)$$

Where Ψ is the orientation of boundary m as shown in Fig. 2.8 and $\theta - \Psi + \pi/2$ is the angle of incidence to the boundary. The constant, β which relates power flow, $p = E\beta$ to energy level E shall be referred to as the power flow coefficient for future reference. If the boundary is a connecting one between panels some of the power will be transmitted across the boundary into heading θ_2 on the second panel,

$$p_{1,2} = p_{\theta,1,m}\tau_{1,2,m}(\theta - \Psi + \pi/2) \tag{2.122}$$

Where $\tau_{1,2,m}$ is the transmission coefficient between the panels across boundary m. The receiving heading θ_2, on panel two may be calculated by using Snell's law,

$$\sin(\theta_2 - \Psi + \pi/2)c_2 = \sin(\theta - \Psi + \pi/2)c_1 \tag{2.123}$$

Some of the incident power will be reflected from the boundary into heading $2\Psi - \theta$ on the transmitting panel. If the boundary is not between panels and is completely reflective then all the incident power will flow into this heading. When splitting the field into discrete headings it is necessary round the receiving headings to the nearest discrete value. The only remaining cause of power flow is damping and external power input. Linear damping will cause power to flow out of the headings in proportion to there energy levels in accordance with (2.34). Using the conservation of energy and the power flow relations above, a loss factor matrix may be constructed which relates the energy levels of each heading to the external power inputs,

$$\mathbf{L}_D\mathbf{e}_D = \mathbf{p}_D \tag{2.124}$$

where $\mathbf{e}_D$ is a vector containing the energies in each heading on all panels and $\mathbf{p}_D$ contains the external power inputs to each heading on every panel. $\mathbf{L}_D$ may be systematically assembled by a computer program using three nested loops, the first loop is through each boundary the next through each panel connected to that boundary, the inner loop is through each wave heading on that panel. Within the inner loop the power flow coefficients for the heading in question are calculated for the relevant boundary, power incident to the boundary is lost to the transmitting heading so the coefficient from (2.121) is added to the relevant diagonal entry of $\mathbf{L}_D$. The coefficient from (2.122) and the equivalent for reflected power are subtracted from the appropriate off diagonal entry of $\mathbf{L}_D$. Once these loops have been completed all that remains is to add the power flow coefficient resulting from damping (which is given by $\omega\eta_j$ for the jth panel) to the corresponding diagonal entries of $\mathbf{L}_D$. Once $\mathbf{L}_D$ and the power inputs are known then Equation (2.124) may be solved for the energy levels, summing the energies for each

heading in a panel gives the total energy content of the panel. Assuming the power input is equal in each heading of the excited panel is reasonable if the excitation is of a "rain on the roof" nature.

Langley[84] did not solve for the panel energies in this way instead he expressed the energy in each panel as a truncated Fourier series in θ,

$$E(\theta) = E_{F1} + E_{F2}\sin\theta + E_{F3}\cos\theta + E_{F4}\sin 2\theta + E_{F5}\cos 2\theta ..... E_{F(2n+1)}\cos n\theta$$

(2.125)

where $E(\theta)$ is the energy per radian flowing in the panel at a heading θ and E_{Fn} is the nth Fourier coefficient. Using only the first term in the series (a constant) is equivalent to assuming a diffuse field and the result is SEA. Adding extra terms in the series increases the accuracy of the answer in the same way as increasing the number of headings and both methods converge to the same answer although not necessarily at the same rate. Langley[84] made the assumption that complete reflection at a boundary causes the wave intensity of incident and reflected waves to be equal over the entire surface of the panel. This requirement may be imposed by using only terms in the Fourier series that are symmetric about the axis parallel to the reflecting boundary. For a rectangular panel with only horizontal reflecting boundaries this requires there be only cosine terms in the series if $\theta = 0$ is horizontal as in Fig. 2.8. With horizontal and vertical reflective boundaries there are two axes of symmetry and only $\cos n\theta$ where n = 0,2,4... are appropriate terms. The intensity of an incoming and a reflected wave will be equal near a completely reflective boundary but not necessarily over the entire surface of the panel as damping will cause the waves to decay. It is interesting to examine the symmetry assumption for a one dimensional system with a reflecting boundary,

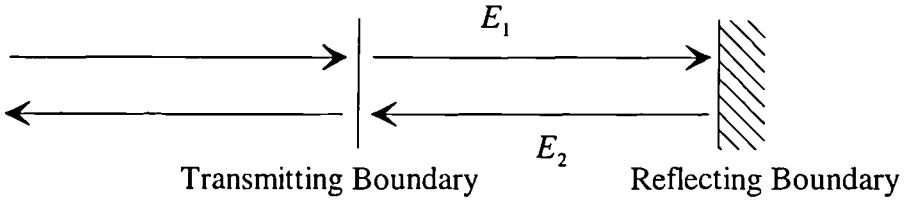

Figure 2.9: One dimensional system with reflecting boundary.

Fig. 2.9 is the simplest discrete wave heading model with only two for each substructure. Using this model it is possible to predict the ratio E_1 / E_2. The power flowing into heading two comes exclusively from heading one and is given by,

$$p_{1,2} = \frac{E_1 C_g}{L} \tag{2.126}$$

Power flows out of heading two at the transmitting boundary and also as a result of damping,

$$p_{2,\text{out}} = E_2\left(\frac{C_g}{L} + \omega\eta\right) \tag{2.127}$$

Equating the two power flows yields the predicted energy ratio as,

$$\frac{E_1}{E_2} = 1 + \frac{\eta L\omega}{C_g} \tag{2.128}$$

The energy ratio may also be predicted by considering a wave travelling from the transmitting boundary and its reflection in the opposite boundary . The energy of the wave decays exponentially in time such that,

$$\frac{E}{E_0} = e^{-t\omega\eta} \tag{2.129}$$

Where E_0 is the level at time $t = 0$. Energy travels at the group velocity C_g so the time required to travel the length of the structure is L / C_g. Replacing this time into (2.129) yields the ratio of the average energy levels in the two headings,

$$\frac{E_1}{E_2} = e^{\frac{\eta L\omega}{C_g}} \tag{2.130}$$

The wave decay answer approaches the power flow prediction provided $\eta L\omega / C_g$ is small,

$$\frac{E_1}{E_2} = e^{\frac{\eta L\omega}{C_g}} \approx 1 + \frac{\eta L\omega}{C_g}, \qquad \text{when}\left(\frac{\eta L\omega}{C_g} \to 0\right) \tag{2.131}$$

When $\eta L\omega / C_g > 0.5$ the error exceeds 10% above 0.5 the wave decay energy ratio is greater than predicted by (2.128). For bending waves on a steel panel 1mm thick and 1m in length with $\eta = 0.01$ and $c_L = 5200 m/s$ the predicted ratio using (2.128) is $E_1 / E_2 = 2.02$ at 10kHz which is 73% of the exact value from equation (2.130). Using the assumption that $E_1 = E_2$ causes a larger error which would suggest that the assumptions about the symmetry of the wave field are not necessary. It is possible to calculate the discrete heading energies and powers $(\mathbf{e}_D, \mathbf{p}_D)$ in terms of Langley's Fourier coefficients $(\mathbf{e}_F, \mathbf{p}_F)$ using a conversion matrix $\mathbf{C}$,

$$\mathbf{C}\mathbf{e}_F = \mathbf{e}_D\ , \quad \mathbf{C}\mathbf{p}_F = \mathbf{p}_D \tag{2.132}$$

The entries of **C** are calculated by integrating (2.125) with respect to θ over the range of each discrete heading. When there are a large number of headings the entries for a conversion matrix for one panel using only cosine terms approach the following,

$$\Delta\theta \begin{pmatrix} 1 & 1 & 1 & 1 & \cdots & 1 \\ 1 & \cos\Delta\theta & \cos 2\Delta\theta & \cos 3\Delta\theta & \cdots & \cos n\Delta\theta \\ 1 & \cos 2\Delta\theta & \cos 4\Delta\theta & \cos 6\Delta\theta & \cdots & \cos 2n\Delta\theta \\ 1 & \cos 3\Delta\theta & \cos 6\Delta\theta & \cos 9\Delta\theta & \cdots & \cos 3n\Delta\theta \\ \vdots & \vdots & \vdots & \vdots & \ddots & \vdots \\ 1 & \cos m\Delta\theta & \cos 2m\Delta\theta & \cos 3m\Delta\theta & \cdots & \cos mn\Delta\theta \end{pmatrix} \begin{pmatrix} E_{F1} \\ E_{F2} \\ E_{F3} \\ E_{F4} \\ \vdots \\ E_{Fn} \end{pmatrix} = \begin{pmatrix} E_0 \\ E_{\Delta\theta} \\ E_{2\Delta\theta} \\ E_{3\Delta\theta} \\ \vdots \\ E_{m\Delta\theta} \end{pmatrix} \quad (2.133)$$

where n is the number of terms in the Fourier series, $m+1$ is the number of discrete headings and $\Delta\theta = 2\pi/(m+1)$ is the range of angles that are lumped into a discrete heading. The matrices for each panel form the sub matrices of the global conversion matrix for the entire model,

$$\begin{pmatrix} \mathbf{C}_1 & \mathbf{0} & \mathbf{0} & \mathbf{0} & \mathbf{0} \\ \mathbf{0} & \mathbf{C}_2 & \mathbf{0} & \mathbf{0} & \mathbf{0} \\ \mathbf{0} & \mathbf{0} & \mathbf{C}_3 & \mathbf{0} & \mathbf{0} \\ \mathbf{0} & \mathbf{0} & \mathbf{0} & \ddots & \vdots \\ \mathbf{0} & \mathbf{0} & \mathbf{0} & \cdots & \mathbf{C}_i \end{pmatrix} \begin{pmatrix} \mathbf{e}_{F1} \\ \mathbf{e}_{F2} \\ \mathbf{e}_{F3} \\ \vdots \\ \mathbf{e}_{Fi} \end{pmatrix} = \begin{pmatrix} \mathbf{e}_{D1} \\ \mathbf{e}_{D2} \\ \mathbf{e}_{D3} \\ \vdots \\ \mathbf{e}_{Di} \end{pmatrix} \quad (2.134)$$

where i is the number of panels. The dimensions of the sub matrixes need not be identical for each panel as there may be different numbers of headings and Fourier terms on each panel. Equation (2.124) may be rewritten using **C** the global conversion matrix as,

$$\mathbf{C}^T\mathbf{L}_D\mathbf{C}\mathbf{e}_F = \mathbf{C}^T\mathbf{C}\mathbf{p}_F \quad (2.135)$$

The columns of **C** become orthogonal as the number of wave headings rises so that the off diagonal elements of $\mathbf{C}^T\mathbf{C}$ become zero and it may be inverted. Pre multiplying both sides by this inverse allows Langley's loss factor matrix $\mathbf{L}_F$ to be related to the discrete loss factor matrix $\mathbf{L}_D$ by,

$$\mathbf{L}_F\mathbf{e}_F = \mathbf{p}_F\,, \quad \mathbf{L}_F = (\mathbf{C}^T\mathbf{C})^{-1}\mathbf{C}^T\mathbf{L}_D\mathbf{C} \quad (2.136)$$

Panel boundaries couple energy in different wave headings together ether on the same or connected panels. Increasing the number of boundaries will tend to make the wave field more diffuse. This would suggest that SEA is more likely to give accurate results in panels with more complex shapes. Motor vehicles are constructed of panels with irregular shapes having a large number of connecting boundaries this favours an accurate result from an SEA model. A diffuse field is less probable when the transmission coefficient is a rapidly changing function of θ, especially in a chain of panels (as investigated by

Langley[84]) where wave filtering effect can have a large influence on transmission. Chapter 5 contains an examination of a rounded corner joint which has a marked wave filtering effect in θ, WIA has been used to for this reason.

2.11 Conclusions

A certain amount of explanation has been given in this Chapter but for the most part it is simply a source of equations for use in later Chapters and the author recommends the reader inspect the references for more detailed analysis. This chapter examines the back ground theory with particular concentration on those theories which are most likely to be useful in dealing with structure borne and acoustic noise in motor-vehicles. A number of conclusions regarding the suitability of certain theories to the study of structure borne and acoustic noise in motor-vehicles have been reached.

Thin plate theory is adequate through out the audible frequency range for the treatment of structure borne sound in car body panels.

Leppington *et al's*[33] equation produces an accurate estimate of the modal average radiation efficiency for panels with thickness and material properties typical of those found in motor-vehicles. For a modal average to be meaningful however the panel in question must have sufficient modes within the frequency band of interest.

C(95%) confidence intervals in SEA energy level predictions have been estimated using theory given by Lyon&DeJong[36]. With panel and saloon acoustic properties typical of those found in a motor-vehicle the structural and acoustic confidence intervals are around C(95%) =5dB at 250Hz. The confidence intervals reduce with frequency.

The investigation of Wave Intensity Analysis showed that SEA is more likely to accurately predict response when the subsystems are irregular in shape. The panels and acoustic spaces in motor-vehicles are irregular in shape and this should increase the accuracy of SEA predictions.

Chapter 3.

Wave Transmission at Complex Panel Joints.

3.1. Introduction

When a structural wave strikes an irregularity, such as a change in thickness, other waves may be generated. The energy carried by the incoming wave is carried away by the waves generated at the irregularity although some may be lost through damping. In this chapter we consider waves on flat and curved panels that have straight line boundaries, other panels may be joined along these boundaries. If a wave on one panel approaches the boundary then waves may be generated on all of the panels. The proportion of the incident energy to that carried away by a particular wave is known as a transmission coefficient. In the absence of damping at the boundary the sum of the transmission coefficients is unity by conservation of energy. Wave transmission coefficients across structural irregularities can be used to quantify the coupling between structures when used within a framework such as SEA, WIA, ASEA or Ray tracing. If the structural damping is known then these methods may be used to calculate the vibration levels within a structure subject to excitation. Methods for calculating transmission coefficients are therefore very valuable to the noise control engineer.

A large number of authors have calculated wave transmission coefficients between various types of panel connected together at line boundaries e.g. [1,6,8,10,11,67]. Joints with beams along the connecting boundary and or elastic layers between the panels have been modelled. Mass produced modern motor-vehicles are largely constructed of steel body panels spot welded together. Small additional pre-formed panel sections are welded into the joints between the panels to provide greater stiffness. Many of these stiffening sections may have resonances within the frequency range of interest. Each panel joint in a vehicle is typically different allowing for any left to right symmetry of a car. This variety and complexity means that none of the existing techniques described can adequately calculate the transmission coefficients for every line panel joint of a typical motor-vehicle.

This chapter describes a technique which can be used to more accurately calculate wave transmission at complex joints found in motor-vehicles. The method uses the "wave dynamic stiffness" approach described by Langley&Heron [8] and Langley [9]. It is easy to use and relatively rapid so that a large variety of joints can be quickly modelled. This Chapter starts with a derivation of the wave dynamic stiffness matrices for flat semi-infinite panels given by Langley&Heron [8] although the sign convention used in this work are different. A wave dynamic stiffness matrix is then derived for a strip of flat panel which is of finite width but still of infinite length as given by Heron [93]. This illustrates the ease with which the derivation of the semi-infinite panel matrix can be extended to give the finite strip matrix. Cylindrical panel sections are introduced and the wave types which can propagate on them are described. A derivation of the wave dynamic stiffness matrix for cylindrical panels is given as prescribed by Langley [9]. The extension to finite strip cylindrical panels is by the same approach as for the flat panels. A simple wave dynamic stiffness matrix is given for an elastic layer using a model given by Mees&Vermeir[10]. The methods by which the wave dynamic stiffness matrix of a complex joint may be assembled from those of its structural components is described with an example. None of these methods are in themselves new. The novelty comes in combining these techniques to calculate wave transmission at complex joint structures.

To demonstrate the usefulness of the method, transmission at a rounded corner joint is calculated and the mechanisms by which it occurs are studied. A more complex model of a joint between the roof and windscreen of a Nissan Micra motor-vehicle is also shown, this model forms part of the SEA study of that car in Chapter 6.

3.2. Wave Dynamic Stiffness

A dynamic stiffness matrix relates the displacements of a structure to the forces acting upon it, usually the forces are applied at one point on the structure. The problem addressed in this Chapter requires a stiffness matrix that relates displacement along an infinite panel boundary to the forces applied along that boundary. There are an infinite number of degrees of freedom along a line boundary; to deal with this a travelling wave motion with wave number k_z along the boundary is assumed. When the motions along the boundary are harmonic with wave number k_z then so are the resulting forces. This is only true when the boundary conditions do not change along its length and this is assumed to

be the case. Fig. 3.1 shows a section of semi-infinite panel which has one boundary. The boundary runs along the z axis. A plane wave incident at an angle θ gives rise to a projected wave number along the boundary of k_z which is determined by the incidence angle, θ and wave number, k_{INC} of the incoming wave.

$$k_Z = k_{INC} \sin\theta \tag{3.1}$$

When using thin plate theory there are four degrees of freedom along the panel boundary these are shown in Fig. 3.1.

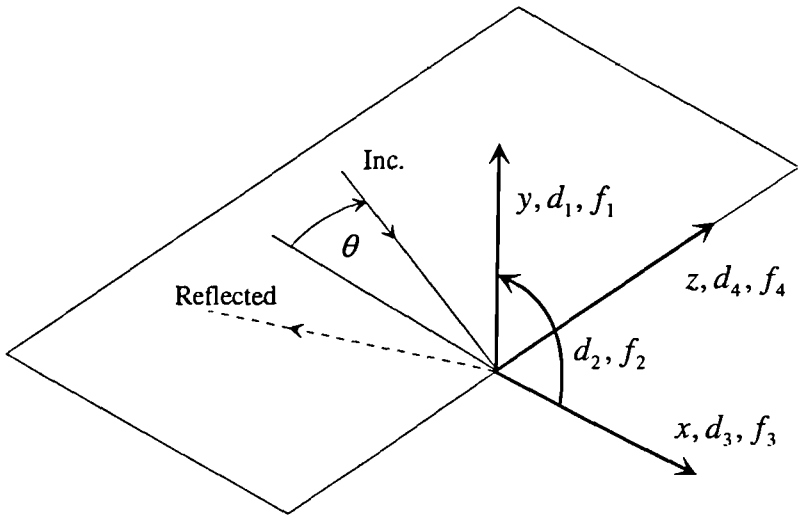

Figure 3.1: Boundary forces and displacements on semi-infinite panel also showing incoming and reflected waves.

The boundary lies along the z axis. Displacements at the boundary will be denoted using the vector $\mathbf{d} = (d_1, d_2, d_3, d_4)^T$ and force $\mathbf{f} = (f_1, f_2, f_3, f_4)^T$ where the displacement and force components are along the edge of the panel as shown in Fig. 3.1. The sign convention assumes forces act on an object attached to the panel. If the panels are assumed to be linear then equation (3.2) can be used to relate $\mathbf{d}$ and $\mathbf{f}$ where $\mathbf{A}$ is a 4x4 wave dynamic stiffness matrix.

$$\mathbf{A}\mathbf{d} = \mathbf{f} \tag{3.2}$$

Displacements and forces vary harmonically along the boundary and are given at any point along the boundary by equation (3.3).

$$\begin{aligned} \mathbf{d}(z,t) &= \mathbf{d}e^{ik_z z}e^{i\omega t} \\ \mathbf{f}(z,t) &= \mathbf{f}e^{ik_z z}e^{i\omega t} \end{aligned} \tag{3.3}$$

Henceforth the phrase stiffness matrix will be used in place of wave dynamic stiffness matrix. The stiffness matrix $\mathbf{A}$ is obtained by calculating two matrices, $\mathbf{B}$ and $\mathbf{C}$ which are

defined as follows. First solutions to the wave equations of the structure in question are sought in the form of (3.4).

$$s = |s| e^{k_x x} e^{ik_z z} e^{i\omega t} \tag{3.4}$$

The factor $e^{i\omega t}$ is omitted in subsequent expressions. Wave equations derived using thin plate theory will yield eight wave solutions, this assumes in-plane waves have been included. There are four types of wave on a flat thin panel these are bending, bending near field, longitudinal and transverse waves. Bending near field waves do not carry power away from the boundary, they have real k_x values and decay exponentially away from the boundary. Each of the four wave types give rise to two solutions in the form of (3.4) which have the same numerical value of k_x but with the sign swapped. One of these solutions is travelling towards the boundary like the incoming wave shown in Fig. 3.1 and the other is travelling away like the reflected wave. This is not the case for the near field wave, in the case of near fields the two solutions decay in different directions one decays in x direction and one in the -ve x direction. Only waves which either carry power away from the boundary or decay away from the boundary will result from excitation at the boundary in a semi-infinite panel and only these solutions are required. This means that any near field must decay in the -ve x direction if the panel is situated as shown in Fig. 3.1 which means k_x in this case must be positive. Using these solutions to the wave equations it is possible to calculate the entries of **B**. **B** relates the displacement vector along the boundary to the wave vector $\mathbf{w} = (r,n,l,t)^T$, where r,n,l and t are the complex amplitudes of each wave type.

$$\mathbf{B}\mathbf{w} = \mathbf{d} \tag{3.5}$$

Wave solutions may be used in conjunction with strain displacement relations and stress strain relations in order to relate the wave vector to the forces at the boundary.

$$\mathbf{C}\mathbf{w} = \mathbf{f} \tag{3.6}$$

The stiffness matrix of the panel may be calculated from **B** and **C** using (3.7).

$$\mathbf{A} = \mathbf{C}\mathbf{B}^{-1} \tag{3.7}$$

A, **B** and **C** have been defined here in connection with semi-infinite flat panels in which case they are 4x4 matrices. Semi-infinite panels are referred to as single node elements as they have only one connecting boundary or "node". Finite strip elements have two parallel boundaries and are therefor referred to as two node elements. The stiffness matrix **A** for a two node element is an 8x8 matrix as there are eight forces and eight displacements. **A** is calculated for two node flat and curved panel sections by first calculating **B** and **C** as

defined in (3.5) and (3.6), these matrices are also 8x8 in this case as there are eight waves on these elements. In sections 3.3 to 3.6 below the derivations of **B**, **C** and **A** are given for flat and curved panel elements.

3.3. Semi-infinite Flat Panels.

This section describes the calculation of **B** and **C** and thus **A** for flat thin semi-infinite panels. Flat panel in-plane and out of plane motions are uncoupled so 2x2 sub matrixes of **B**, **C** and thus **A** can be calculated and then assembled to produce the complete 4x4 matrices. Out of plane displacements η in thin panels are governed by the bending wave equation (2.17) solving for solutions in the form of equation (3.4) yields (3.8)

$$\eta = r e^{x\sqrt{k_z^2 - k_B^2}} + n e^{x\sqrt{k_B^2 + k_z^2}} \tag{3.8}$$

Where the square roots are positive. Here n is the complex amplitude for the bending near field and r is for the reflected bending wave when $k_B > k_Z$ or another near field when $k_Z > k_B$. Displacements d_1 and d_2 along the boundary are given by (3.9)

$$\begin{aligned} d_1 &= r + n \\ d_2 &= r\sqrt{k_z^2 - k_B^2} + n\sqrt{k_z^2 + k_B^2} \end{aligned} \tag{3.9}$$

d_2 is angular and is calculated by differentiating η with respect to x, then setting x=0 causing the exponent in x to become unity. $e^{ik_z z}e^{i\omega t}$ has been omitted. Expressed in matrix form (3.9) constitutes the top left (2x2) sub-matrix of **B**.

In-plane displacement is governed by two coupled differential equations in u and v Langley&Heron[8]

$$G(1+\gamma)\frac{\partial^2 u}{\partial x^2} + G\frac{\partial^2 u}{\partial z^2} + G\gamma\frac{\partial^2 v}{\partial x \partial z} - \frac{\partial^2 u}{\partial t^2}\rho = 0 \tag{3.10}$$

$$G(1+\gamma)\frac{\partial^2 v}{\partial z^2} + G\frac{\partial^2 v}{\partial x^2} + G\gamma\frac{\partial^2 u}{\partial x \partial z} - \frac{\partial^2 v}{\partial t^2}\rho = 0 \tag{3.11}$$

Where u is the in-plane deflection in the direction of d_3 and v is the in-plane deflection in the direction of d_4. $G = E/2(1+\mu)$ is the modulus of rigidity and $\gamma = (1+\mu)/(1-\mu)$. Equations (3.10) and (3.11) may be rewritten in matrix form assuming deflections proportional to $e^{ik_z z}e^{k_x x}$.

$$\begin{pmatrix} G(1+\gamma)k_x^2 - Gk_z^2 + \omega^2\rho & iG\gamma k_z k_x \\ iG\gamma k_z k_x & Gk_x^2 + \omega^2\rho - G(1+\gamma)k_z^2 \end{pmatrix}\begin{pmatrix} u \\ v \end{pmatrix} = \begin{pmatrix} 0 \\ 0 \end{pmatrix} \tag{3.12}$$

Langley&Heron[8] solved (3.12) as an eigen problem, setting the determinant =0 and solving for k_x yields .

$$k_x^2 = k_z^2 - k_s^2, \quad k_x^2 = k_z^2 - k_L^2 \tag{3.13}$$

Where $k_L^2 = \rho\omega^2(1-\mu^2)/E$ is the longitudinal wave number and $k_S^2 = 2\rho\omega^2(1+\mu)/E$ is the transverse wave number. Positive real and imaginary roots are the only acceptable solutions because the displacement must be finite at $x = -\infty$ and power must flow away from the boundary. Replacing these back into (3.12) and solving for the eigenvectors yields the mode shape of the relevant wave or near field. The shear solution, $k_{xS} = +\sqrt{k_Z^2 - k_S^2}$ has the shape vector $(u,v)^{\mathrm{T}} = (k_Z, ik_{xS})^{\mathrm{T}}$. Using the longitudinal solution $k_{xL} = +\sqrt{k_Z^2 - k_L^2}$ gives $(u,v)^{\mathrm{T}} = (-ik_{xL}, k_Z)^{\mathrm{T}}$. In-plane displacement in the panel can now be written in terms of the complex wave amplitudes as follows.

$$\begin{aligned} u &= -il\sqrt{k_Z^2 - k_L^2}\,e^{x\sqrt{k_Z^2-k_L^2}} + k_Z t e^{x\sqrt{k_Z^2-k_S^2}} \\ v &= k_Z l e^{x\sqrt{k_Z^2-k_L^2}} + it\sqrt{k_Z^2 - k_S^2}\,e^{x\sqrt{k_Z^2-k_S^2}} \end{aligned} \tag{3.14}$$

Where l is the complex amplitude of the longitudinal wave and t that of the of the transverse wave. When $k_L > k_Z$ l is the complex amplitude of a longitudinal travelling wave, if $k_Z > k_L$ then l is the complex amplitude of an in-plane near field or surface wave whose amplitude reduces exponentially away from the boundary. The same transition occurs to the transverse wave where t becomes the complex amplitude of a near field when $k_L > k_T$. Setting x=0 in (3.14) gives the displacement along the boundary as.

$$\begin{aligned} d_3 &= -il\sqrt{k_Z^2 - k_L^2} + k_Z t \\ d_4 &= k_Z l + it\sqrt{k_Z^2 - k_S^2} \end{aligned} \tag{3.15}$$

Equations (3.15) in matrix form constitute the lower right hand sub matrix of **B**. This along with (3.9) which gives the upper left hand sub matrix allows **B** to be written as.

$$\begin{pmatrix} 1 & 1 & 0 & 0 \\ \sqrt{k_Z^2 - k_B^2} & \sqrt{k_Z^2 + k_B^2} & 0 & 0 \\ 0 & 0 & -i\sqrt{k_Z^2 - k_L^2} & k_Z \\ 0 & 0 & k_Z & i\sqrt{k_Z^2 - k_S^2} \end{pmatrix} \begin{pmatrix} r \\ n \\ l \\ t \end{pmatrix} = \begin{pmatrix} d_1 \\ d_2 \\ d_3 \\ d_4 \end{pmatrix} \tag{3.16}$$

Matrix **C** as defined in (3.6) is calculated for flat panels by using the wave displacement relations (3.14) and (3.8) in conjunction with strain displacement and stress strain relations for the panel. Combining the strain displacement and stress strain relations gives the relationships between panel deflections and boundary forces.

$$f_1 = B\left(\frac{\partial^3 \eta}{\partial x^3} + (2-\mu)\frac{\partial^3 \eta}{\partial x \partial z^2}\right), \qquad (x=0) \quad (3.17)$$

$$f_2 = -B\left(\frac{\partial^2 \eta}{\partial x^2} + \mu\frac{\partial^2 \eta}{\partial z^2}\right), \qquad (x=0) \quad (3.18)$$

$$f_3 = -\frac{Eh}{1-\mu^2}\left(\frac{\partial u}{\partial x} + \mu\frac{\partial v}{\partial z}\right), \qquad (x=0) \quad (3.19)$$

$$f_4 = -Gh\left(\frac{\partial u}{\partial z} + \frac{\partial v}{\partial x}\right), \qquad (x=0) \quad (3.20)$$

Where B, the bending stiffness of the panel and not, **B** the matrix defined by equation (3.5). By replacing (3.8) into (3.17) and (3.18) out of plane forces f_1 and f_2 are given in terms of r and n. Replacing (3.14) into (3.19) and (3.20) relates the in-plane forces f_3 and f_4 to wave amplitudes l and t. These relations can be written in matrix form and combined to give **C**. Using **C** and **B** in (3.7) produces the panel stiffness matrix, the top left sub-matrix of which is given by.

$$\frac{B}{k_{xB}-k_{xN}}\begin{pmatrix} k_{xB}k_{xN}^3 - k_{xN}k_{xB}^3 & k_{xB}^3 - k_{xN}^3 + k_Z^2(\mu-2)(k_{xB}-k_{xN}) \\ \text{Symm.} & k_{xN}^2 - k_{xB}^2 \end{pmatrix}\begin{pmatrix} d_1 \\ d_2 \end{pmatrix} = \begin{pmatrix} f_1 \\ f_2 \end{pmatrix} \quad (3.21)$$

Wave numbers in the x direction have been abbreviated to $k_{xB} = +\sqrt{k_Z^2 - k_B^2}$ and $k_{xN} = +\sqrt{k_Z^2 + k_B^2}$. The bottom right sub-matrix of **A** which relates in-plane forces and displacements is given by.

$$\frac{Eh}{k_Z^2 - k_S k_L}\begin{pmatrix} \frac{(k_{xL}^2 - \mu k_Z^2)k_{xS}}{1-\mu^2} - \frac{k_Z^2 k_{xS}}{1+\mu} & \frac{i(k_L^2 - \mu k_Z^2)k_Z}{1-\mu^2} - \frac{ik_S k_L k_Z}{1+\mu} \\ -\frac{i(k_L^2 - \mu k_Z^2)k_Z}{1-\mu^2} + \frac{ik_S k_L k_Z}{1+\mu} & \frac{(k_S^2 - k_Z^2)k_{xL}}{2(1+\mu)} \end{pmatrix}\begin{pmatrix} d_3 \\ d_4 \end{pmatrix} = \begin{pmatrix} f_3 \\ f_4 \end{pmatrix}$$

(3.22)

The remaining elements of the stiffness matrix, **A** are zero as small in-plane and out of plane motions of a flat plate are uncoupled so that deflections d_1 and d_2 have no effect on forces f_3 and f_4 and deflections d_3 and d_4 have no effect on forces f_1 and f_2. Equation (3.21) is in agreement with equation (21) from Langley&Heron[8], allowing for the different sign conventions. Equation (28) from [8] is the corresponding equation to (3.22). Equation (28) from [8] and (3.22) do not agree completely even allowing for the differing sign conventions used here and in [8]. There is a misprint in the two of-diagonal terms in equation (28), [8] in that poissions ratio is squared when is should not be. This misprint

has been confirmed by the authors of [8]. If this misprint is corrected and equation (28) from[8] is altered to allow for the differing sign conventions then (3.22) and (28) from [8] agree.

3.3.1. Power Flow

The ultimate objective of this analysis is to calculate wave transmission coefficients. To do this it is necessary to relate the wave amplitudes to the amount of energy the waves carry. Power flow from the boundary per unit boundary length for bending longitudinal and transverse waves on a thin flat panel are given by (3.23), (3.24) and (3.25) respectively.

$$p = \mathrm{Im}\{k_{xB}\}\omega^3 \rho h |r|^2 / k_B \tag{3.23}$$

$$p = \frac{1}{2}\mathrm{Im}\{k_{xL}\}\omega^3 \rho h |l|^2 \tag{3.24}$$

$$p = \frac{1}{2}\mathrm{Im}\{k_{xS}\}\omega^3 \rho h |t|^2 \tag{3.25}$$

Power incident per unit boundary length as a result of an incoming wave can be calculated using (3.23), (3.24) or (3.25). These equations give power flowing from the boundary so the results for incoming waves will be negative because the x wave number will be negative.

3.4. Two Node Flat Panel Elements

Section 3.3 dealt with a semi-infinite panel having one line boundary. The same methods can be used to calculate a stiffness matrix for a finite strip of flat panel which has two parallel line boundaries separated by a distance b as shown in Fig. 3.2, see Heron [93].

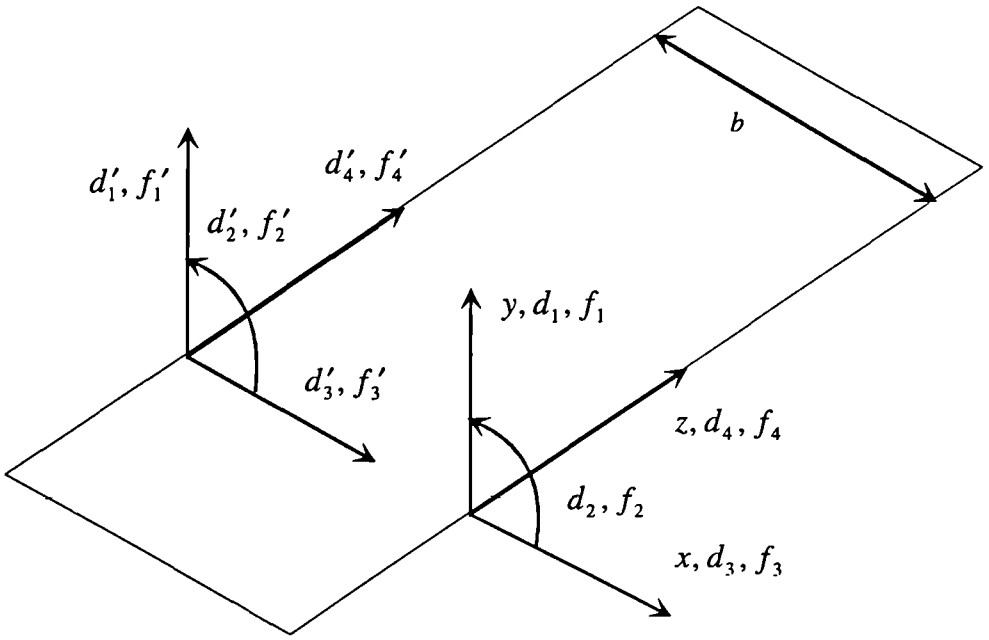

Figure 3.2: Boundary forces and displacements on finite width infinite length strip.

The panel in Fig. 3.2 is identical to that in Fig. 3.1 except for the additional boundary along the line x=-b. On this boundary the deflections and forces are again described as traveling waves with wave number k_z using (3.3). The deflection and force vectors along the boundary at x=-b are given by $\mathbf{d}' = (d_1', d_2', d_3', d_4')^{\mathrm{T}}$ and $\mathbf{f}' = (f_1', f_2', f_3', f_4')^{\mathrm{T}}$, the directions of these are shown in Fig. 3.2. As in the semi-infinite panel four waves/near fields travel from the boundary on the z axis, there complex amplitudes are (r,n,l,t). In addition to these waves four waves (r',n',l',t') travel from the boundary at x=-b towards the z axis. Because the finite strip has 8 degrees of freedom the stiffness matrix **A** is 8x8 as are the **B** and **C** matrices defined in (3.5) and (3.6). The displacement relations for the additional waves are given in (3.26) and (3.27).

$$\eta = r' e^{-(x+b)k_{xB}} + n' e^{-(x+b)k_{xN}} \tag{3.26}$$

$$\begin{aligned} u &= il' k_{xL} e^{-(x+b)k_{xL}} + k_z t' e^{-(x+b)k_{xS}} \\ v &= k_z l' e^{-(x+b)k_{xL}} - it' k_{xS} e^{-(x+b)k_{xS}} \end{aligned} \tag{3.27}$$

Using (3.8) and (3.26) and putting x=-b at the new boundary, the out of plane deflections are related to bending wave solutions in (3.28).

$$\begin{pmatrix} 1 & 1 & \frac{1}{\exp(k_{xB}b)} & \frac{1}{\exp(k_{xN}b)} \\ k_{xB} & k_{xN} & \frac{-k_{xB}}{\exp(k_{xB}b)} & \frac{-k_{xN}}{\exp(k_{xN}b)} \\ \frac{1}{\exp(k_{xB}b)} & \frac{1}{\exp(k_{xN}b)} & 1 & 1 \\ \frac{k_{xB}}{\exp(k_{xB}b)} & \frac{k_{xN}}{\exp(k_{xN}b)} & -k_{xB} & -k_{xN} \end{pmatrix} \begin{pmatrix} r \\ n \\ r' \\ n' \end{pmatrix} = \begin{pmatrix} d_1 \\ d_2 \\ d_1' \\ d_2' \end{pmatrix} \tag{3.28}$$

In plane waves and boundary deflections are related by (3.29).

$$\begin{pmatrix} -ik_{xL} & k_z & \frac{ik_{xL}}{\exp(k_{xL}b)} & \frac{k_Z}{\exp(k_{xS}b)} \\ k_Z & ik_{xS} & \frac{k_Z}{\exp(k_{xL}b)} & \frac{-ik_{xS}}{\exp(k_{xS}b)} \\ \frac{-ik_{xL}}{\exp(k_{xL}b)} & \frac{k_Z}{\exp(k_{xS}b)} & 1 & 1 \\ \frac{k_Z}{\exp(k_{xL}b)} & \frac{ik_{xS}}{\exp(k_{xS}b)} & -k_{xB} & -k_{xN} \end{pmatrix} \begin{pmatrix} l \\ t \\ l' \\ t' \end{pmatrix} = \begin{pmatrix} d_3 \\ d_4 \\ d_3' \\ d_4' \end{pmatrix} \tag{3.29}$$

B may be constructed from the two matrices in (3.28) and (3.29) given that the wave vector $\mathbf{w} = (r,n,l,t,r',n',l',t')^{\mathrm{T}}$ and $\mathbf{d} = (d_1,d_2,d_3,d_4,d_1',d_2',d_3',d_4')^{\mathrm{T}}$ is the displacement vector. Bending wave and near field amplitudes are related to boundary forces by (3.30) and (3.31).

$$\begin{pmatrix} f_{r1} & f_{n1} & -f_{r1}\exp(-k_{xB}b) & -f_{n1}\exp(-k_{xN}b) \\ f_{r2} & f_{n2} & f_{r2}\exp(-k_{xB}b) & f_{n2}\exp(-k_{xN}b) \\ -f_{r1}\exp(-k_{xB}b) & -f_{n1}\exp(-k_{xN}b) & f_{r1} & f_{n1} \\ -f_{r2}\exp(-k_{xB}b) & -f_{n2}\exp(-k_{xN}b) & -f_{r2} & -f_{n2} \end{pmatrix} \begin{pmatrix} r \\ n \\ r' \\ n' \end{pmatrix} = \begin{pmatrix} f_1 \\ f_2 \\ f_1' \\ f_2' \end{pmatrix} \tag{3.30}$$

$$\begin{aligned} f_{r1} &= Bk_{xB}(k_{xB}^2 + (\mu-2)k_Z^2), \quad f_{r2} = B(\mu k_Z^2 - k_{xB}^2) \\ f_{n1} &= Bk_{xN}(k_{xN}^2 + (\mu-2)k_Z^2), \quad f_{n2} = B(\mu k_Z^2 - k_{xN}^2) \end{aligned} \tag{3.31}$$

In plane wave amplitudes and boundary forces are related by (3.32) and (3.33).

$$\begin{pmatrix} -f_{l3} & f_{t3} & -f_{l3}\exp(-k_{xL}b) & -f_{t3}\exp(-k_{xS}b) \\ -f_{l4} & -f_{t4} & f_{l4}\exp(-k_{xL}b) & -f_{t4}\exp(-k_{xS}b) \\ f_{l3}\exp(-k_{xL}b) & -f_{t3}\exp(-k_{xS}b) & f_{l3} & f_{t3} \\ f_{l4}\exp(-k_{xL}b) & f_{t4}\exp(-k_{xS}b) & -f_{l4} & f_{t4} \end{pmatrix} \begin{pmatrix} l \\ t \\ l' \\ t' \end{pmatrix} = \begin{pmatrix} f_3 \\ f_4 \\ f_3' \\ f_4' \end{pmatrix} \tag{3.32}$$

$$\begin{aligned} f_{l3} &= \frac{iE}{1-\mu^2}(\mu k_Z^2 - k_{xL}^2), \quad f_{l4} = 2Ghk_Z k_{xL} \\ f_{t3} &= \frac{iE}{1-\mu^2}k_{xS}k_Z(\mu-1), \quad f_{t4} = iGh(k_Z^2 + k_{xS}^2) \end{aligned} \tag{3.33}$$

C may be assembled from (3.30) and (3.32) and used in conjunction with **B** to form the stiffness matrix.

3.5. Semi-Infinite Curved Panels

The analysis used to derive the wave dynamic stiffness matrix for semi-infinite curved panels follows the route prescribed in Langley[9]. The sign conventions used here are different to those used by Langley[9] they were changed in order to be consistent with other elements such as the flat panels shown in Figs. 3.1 and 3.2. The orientation of the curved panel is shown in Fig. 3.3.

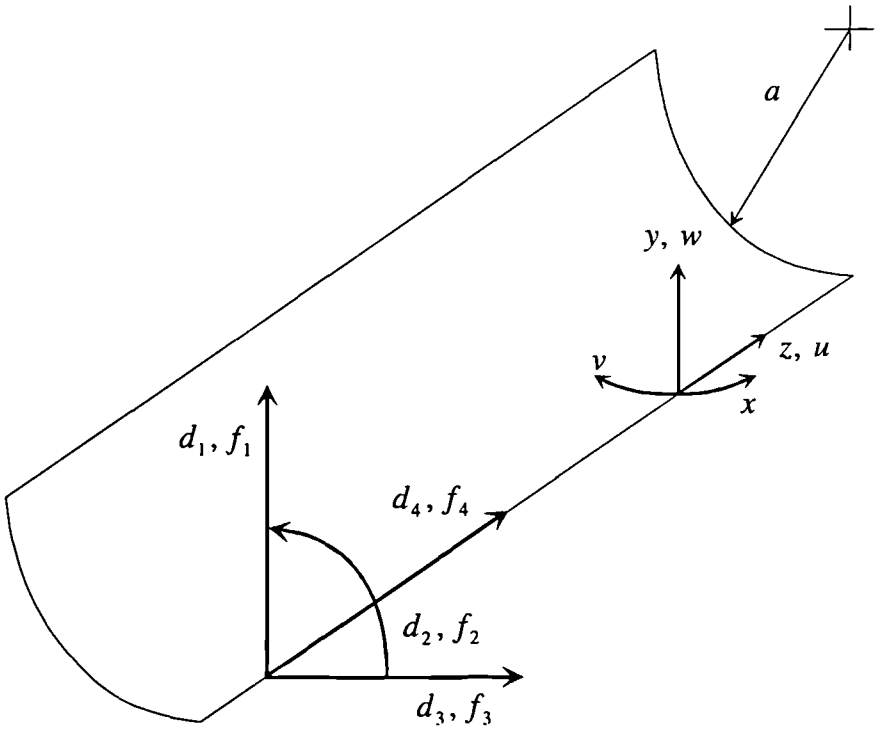

Figure 3.3: Boundary forces, displacements and co-ordinates for semi-infinite curved panels.

The radius of curvature of the panel is a. If the panel section in Fig. 3.3 extended away from the boundary an infinite distance it would loop back on its self, this is not what is intended by the name "semi-infinite curved panel". A semi-infinite curved panel section as shown Fig. 3.3. is one in which waves travelling away from the boundary along the z axis are not reflected back towards it.

Langley[9,94] used modified Love-Timoshenko[95] shell theory to solve for the wave types that may travel on the panel. On a curved panel in plane and out of plane

displacements are coupled together. The three coupled differential equations of Love-Timoshenco[95]shell theory can be written in matrix form.

$$\mathbf{Lu} = \mathbf{0} \tag{3.34}$$

Where $\mathbf{u} = (u, v, w)^T$ is the displacement vector which contains the three panel displacements shown in Fig. 3.3. $\mathbf{L}$ is a 3x3 differential operator. Solutions of (3.34) are sought in the form.

$$\mathbf{u} = \mathbf{c}\exp\left(k_x x + ik_z + i\omega t\right) \tag{3.35}$$

Where $\mathbf{c}$ is the wave shape vector. A non trivial solution to (3.34) is only possible where the determinant of $\mathbf{L}$ is zero. Replacing (3.35) into (3.34) and requiring the determinant to be zero gives rise to a quartic polynomial in k_x^2 which may be solved if k_z and ω are known. The four solutions correspond to the four types of wave which are possible on the panel. Square rooting for k_x gives eight complex values with one for each wave type travelling[1] in both the +ve and -ve x directions. Each valid solution for k_x may be replaced back into $\mathbf{L}$ and a corresponding eigenvector calculated which is the wave shape vector $\mathbf{c}$ for that particular wave. A dispersion curve for a curved panel is shown in Fig. 3.4 on which are plotted the k_x, k_z pairs for travelling waves. Only the magnitude of the pure imaginary solutions for k_x are shown on Fig. 3.4 as these represent travelling waves.

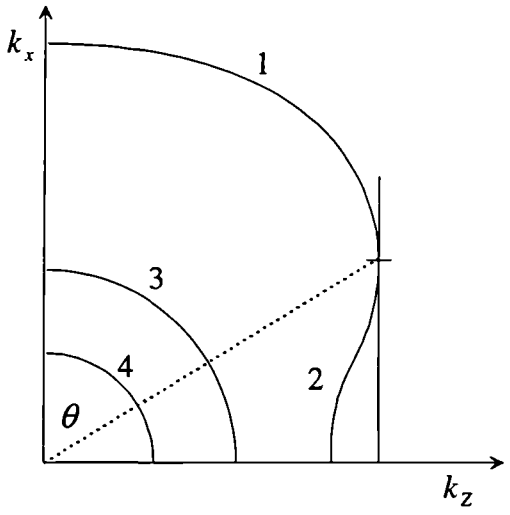

Figure 3.4: A dispersion curve for a curved panel showing the four travelling wave types.

Langley[9,94] identified four travelling wave types on this dispersion diagram, they are labelled 1,2,3 and 4 on Fig. 3.4. At a given frequency a maximum of three travelling waves may coexist on the panel with the same k_z. Panel motion in wave type 1 is normal

[1] Near fields do not travel but they do decay in either the +ve or -ve x direction.

to the panel surface with strain energy primarily due to bending. The angle θ on Fig. 3.4 is the limiting angle of incidence for wave type 1. As the frequency becomes higher in relation to the plain strain ring frequency ($\omega >> \omega_R$ where $\omega_R = \sqrt{E/\rho(1-\mu^2)a^2}$) wave type 1 becomes closer to a flat plate bending wave. Travelling wave type 4 occurs only at frequencies above ω_R and approaches a flat plate longitudinal wave as the frequency increases in relation to ω_R. Travelling wave type 3 is the curved panel equivalent to a flat plate transverse wave, when $k_x = 0$ it represents a pure torsional wave on the cylindrical section. Travelling wave type 2 does not have an equivalent on a flat panel and as the frequency rises such that $\omega >> \omega_R$ this wave type disappears from the dispersion curve. Langley [94] showed that the wave type labelled 2 on Fig. 3.4 has a negative group velocity in the x direction when the phase velocity is positive. This means that if the wave is to carry energy away from the z axis boundary then k_x must be imaginary and negative for this wave type. Wave types 1,3 and 4 must have a k_x which is imaginary and positive as is the case for a flat plate. The acceptable k_x values for near fields are ones which have a positive real part, that is they decay away from the z axis in Fig. 3.3. Wave type 3 and 2 result from the same root of the quartic equation in k_x^2 so there is another root which does no appear on Fig. 3.4. This root always gives rise to a near field wave, that is the real part of k_x is not zero. It is convenient to refer to the complex amplitudes of the four wave types on a curved panel as r,n,l and t in the same way as was done with the flat panel. Wave type 1 has complex amplitude r and type 4 has complex amplitude l . The complex amplitude t is that of type 3 or 2. The amplitude of the near field which doesn't appear on Fig. 3.4 is n.

Langley[9] defined a 4x3 differential operator **D** which relates the displacement vector $\mathbf{u} = (u,v,w)^T$ to the edge displacement vector $\mathbf{d} = (d_1,d_2,d_3,d_4)^T$ by,

$$\mathbf{d} = \mathbf{D}\mathbf{u} \tag{3.36}$$

D here is not exactly the same as Langley's[9] because of the different sign convention for **d**. The non zero entries of **D** are given by.

$$\mathbf{D}_{13} = \mathbf{D}_{41} = 1\,, \qquad \mathbf{D}_{22} = -1/a\,, \qquad \mathbf{D}_{23} = d_x\,, \qquad \mathbf{D}_{32} = -1 \tag{3.37}$$

Where d_x is the derivative with respect to x, this is given by k_x when the displacements are in the form of (3.35), once d_x has been replaced by k_x equation (3.36) represents simple matrix multiplication. If **u** in (3.36) is replaced by one of the eight eigenvectors (referred to as **c** above) then **d** becomes the wave displacement vector in the required co-

ordinates. The value of $d_x = k_x$ in **D** must be the value which corresponds to that particular eigenvector **c**. If the wave displacement vectors are calculated in this way for each of the four wave types which either carry power away from the boundary or decay exponentially away from the boundary (r,n,l and t) then they may be assembled together forming the columns of the matrix **B**, which is defined in equation (3.5). Note that the four wave types include the near field which is not shown on Fig. 3.4.

Langley[9] related the forces along the edge of the panel to the displacement vector **u** using another 4x3 differential operator, this time called **T**. Again the operator **T** given here is an altered version of Langleys[9] **T** to take account of the different sign conventions used in defining the edge force vector **f** which Langley [9] referred to as **t**.

$$\mathbf{f} = \mathbf{T}\mathbf{u} \tag{3.38}$$

The entries of the **T** operator may be calculated by assuming panel deflections in the form of (3.35) so that derivatives in the **T** operator may be replaced by the relevant wave number, $d_x = k_x$ and $d_z = ik_z$. Non zero entries of **T** are then given by.

$$\mathbf{T}_{12} = \frac{B(2(1-\mu)k_z^2 - k_r^2)}{a}\ ,\ \mathbf{T}_{13} = B(k_x^3 - k_x k_z^2(2-\mu))\ ,\ \mathbf{T}_{22} = \frac{Bk_x}{a} \tag{3.39}$$

$$\mathbf{T}_{23} = B(\mu k_z^2 - k_r^2)\ ,\ \mathbf{T}_{31} = -iGh\mu(1+\alpha)k_z\ ,\ \mathbf{T}_{32} = Gh(1+\alpha)k_x \tag{3.40}$$

$$\mathbf{T}_{33} = \frac{Gh(1+\alpha)}{a}\ ,\ \mathbf{T}_{41} = -Ghk_x\ ,\ \mathbf{T}_{42} = iGhk_z \tag{3.41}$$

Where $\alpha = (1+\mu)/(1-\mu)$. If **u** in (3.38) is replaced by an eigenvector **c** for a certain wave type and direction and k_r is the corresponding wave number in the x direction then **f** is the force produced at the boundary by a wave of that type with unit magnitude. Calculating **f** in this way for each of the four wave types which either carry power away from the boundary or decay exponentially away from the boundary gives four vectors which may be assembled to form the columns of the **C** matrix which is defined in (3.6). Note again that the four wave types include the near field which is not shown on Fig. 3.4. When **B** and **C** have been calculated as outlined above they may be used in (3.7) to give **A** the wave dynamic stiffness matrix.

The calculations above require knowledge of the power flow to or from the boundary along the z axis caused by a specific wave type. Power flow per unit boundary length is given by.

$$P_j = \frac{1}{2}\mathrm{Re}\{i\omega\, \mathbf{f}_j^{*\mathrm{T}}\mathbf{d}_j\} \tag{3.42}$$

Where the subscript j is to indicate which one of the eight waves is being considered , $\mathbf{f}_j$ is the force vector for the j th wave and $\mathbf{d}_j$ is the displacement vector for that wave. As the forces are defined here as being upon a line attached to the boundary then (3.42) will be positive when power flows out of the panel. This will occur when waves of type 1,3 and 4 approach the boundary and when waves of type 2 travel away from the boundary.

3.6. Curved Two Node Panels

A section of a curved strip of panel with infinite length is shown in Fig. 3.5, b is the circumferential breadth of the strip. Calculation of $\mathbf{A}$, the two node 8x8 stiffness matrix of this strip is described in this section. Extension of the analysis used to derive the stiffness matrix for the semi-infinite curved panel in section 3.5, to deal with an additional boundary is relatively straight forward. There are three new considerations.

- All eight of the waves referred to in section 3.5 must be included that is a wave of each of the four types travelling or decaying toward or away from the z axis.
- The effect of all the waves on both boundaries must be calculated, this will require the consideration of phase differences and or decay as the waves travel from one boundary to another.
- The displacements, $\mathbf{u} = (u, v, w)^{\mathrm{T}}$ describe the deflection of the panel in a co-ordinate system such that w is always perpendicular to the panel and v is always tangential to the panel. In order to produce a stiffness matrix using the co-ordinate system shown in Fig. 3.5 the displacements and forces at the boundary not along the z axis must be rotated to compensate for the curvature of the panel.

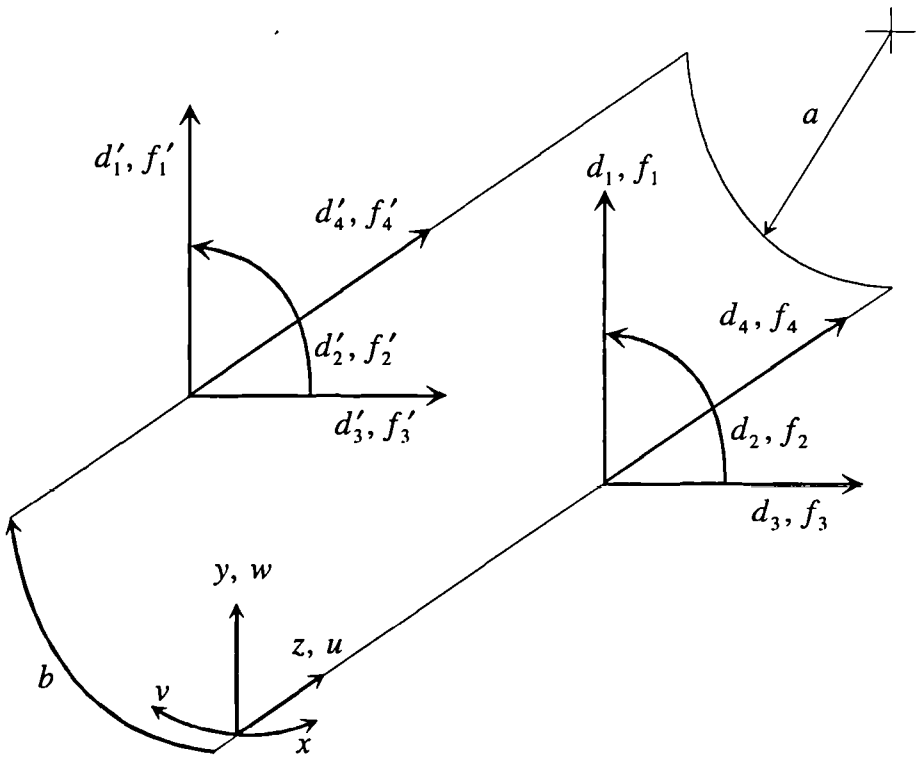

Figure 3.5: Boundary forces, displacements and co-ordinates for finite width, infinite length curved strip.

B, the 8x8 matrix relating the complex wave amplitudes to the boundary displacements was expressed in terms of four 4x4 sub matrices in order to calculate its entries.

$$\begin{pmatrix} \mathbf{B}_{11} & \mathbf{B}_{12} \\ \mathbf{B}_{21} & \mathbf{B}_{22} \end{pmatrix} \begin{pmatrix} \mathbf{w} \\ \mathbf{w}' \end{pmatrix} = \begin{pmatrix} \mathbf{d} \\ \mathbf{d}' \end{pmatrix} \tag{3.43}$$

Vector $\mathbf{d}' = (d_1', d_2', d_3', d_4')^{\mathrm{T}}$ contains the deflections of the boundary at x = -b and $\mathbf{d} = (d_1, d_2, d_3, d_4)^{\mathrm{T}}$ the deflections on the z axis boundary as shown in Fig. 3.5. Together **d** and **d′** make up the 8x1 displacement vector for the curved strip element. The 8x1 wave vector in (3.43) consists two smaller 4x1 wave sub vectors, $\mathbf{w} = (r, n, l, t)^{\mathrm{T}}$ contains the complex amplitudes of the waves which either carry power in the -ve x direction or decay in that direction, this is the same as for the semi-infinite curved panel. The wave sub vector $\mathbf{w}' = (r', n', l', t')^{\mathrm{T}}$ contains the complex amplitudes of the waves of the same types but which either carry power in the +ve x direction or decay in that direction, these were not applicable in the case of the semi-infinite panel but are necessary here. Together **w** and **w′** contain all eight waves which satisfy (3.35). The entries of the 4x4 sub-matrix $\mathbf{B}_{11}$ are identical to the entries of **B** for a semi-infinite curved panel with the same

properties. Sub matrix $\mathbf{B}_{12}$ relates the complex amplitudes of the $\mathbf{w}'$ waves (r',n',l' and t') to the displacements at the boundary on the z axis. The entries of $\mathbf{B}_{12}$ are calculated by replacing k_x and $\mathbf{c}$ for the r',n',l' and t' wave types into equation (3.36) and using the resulting $\mathbf{d}$ vectors to form the columns of $\mathbf{B}_{12}$ i.e. the same method as was used for the semi-infinite panel. The origin of the $\mathbf{w}'$ waves was chosen to be the z axis, the same as the $\mathbf{w}$ waves. Since $\mathbf{B}_{12}$ relates $\mathbf{w}'$ and $\mathbf{d}$ which are both on the z axis no extra phase or decay terms due to the wave travelling across the strip are required in the entries of $\mathbf{B}_{12}$. $\mathbf{B}_{21}$ relates the wave vector $\mathbf{w}$ to the displacements on the second boundary at x = -b which are given in $\mathbf{d}'$. As the waves have there origin at the z axis boundary they must travel across the strip before they cause deflections at the other boundary, this means that complex factors must be introduced into the entries of $\mathbf{B}_{21}$ which account for the resultant phase changes and or attenuation. Entries of $\mathbf{B}_{21}$ are calculated using equation (3.44) below.

$$\mathbf{B}_{21} = \mathbf{R}\left(\mathbf{d}_r \exp(-bk_{xr}), \mathbf{d}_n \exp(-bk_{xn}), \mathbf{d}_l \exp(-bk_{xl}), \mathbf{d}_t \exp(-bk_{xt})\right) \qquad (3.44)$$

$\mathbf{R}$ in (3.44) is a rotation matrix which compensates for the fact that the co-ordinate system on which the deflections u,v and w are based rotates with the panel surface where as the deflections $\mathbf{d}' = (d_1', d_2', d_3', d_4')^{\mathrm{T}}$ are based on the same co-ordinate system as the deflections $\mathbf{d} = (d_1, d_2, d_3, d_4)^{\mathrm{T}}$ along the z axis as shown in Fig. 3.5. The angle of rotation is given by b/a in radians about the z axis. Rotation matrices are discussed in greater detail in Section 3.8. The bracketed term on the r.h.s. of (3.44) is a 4x4 matrix whose columns are formed by displacement vectors calculated using (3.36) in the same way as for $\mathbf{B}$ in the case of the semi-infinite curved panel, $\mathbf{B}_{11}$ and $\mathbf{B}_{12}$ except that in this case complex exponential factors are introduced to account for phase shifts and or attenuation as the waves travel across the strip. Subscripts r,n,l and t have been introduced to differentiate between wave numbers and between deflection vectors for different wave types. The bracketed term on the r.h.s. of (3.44) is identical to $\mathbf{B}$ for the semi-infinite panel and the $\mathbf{B}_{11}$ sub matrix apart from the exponential terms. $\mathbf{B}_{22}$ is calculated in the same way as $\mathbf{B}_{21}$ except that the displacement vectors are calculated using the r',n',l' and t' waves and wave numbers instead of r,n,l and t.

$$\mathbf{B}_{22} = \mathbf{R}\left(\mathbf{d}_{r'} \exp(bk_{xr}), \mathbf{d}_{n'} \exp(bk_{xn}), \mathbf{d}_{l'} \exp(bk_{xl}), \mathbf{d}_{t'} \exp(bk_{xt})\right) \qquad (3.45)$$

Note that the wave numbers are as in (3.44) but the negative sign has been omitted because $k_{xr} = -k_{xr'}$ and $k_{xn} = -k_{xn'}$ etc.

C the matrix defined in (3.6) which relates the wave amplitudes to the forces applied at the boundaries is also calculated by splitting it into 4x4 sub matrixes.

$$\begin{pmatrix} \mathbf{C}_{11} & \mathbf{C}_{12} \\ \mathbf{C}_{21} & \mathbf{C}_{22} \end{pmatrix} \begin{pmatrix} \mathbf{w} \\ \mathbf{w}' \end{pmatrix} = \begin{pmatrix} \mathbf{f} \\ \mathbf{f}' \end{pmatrix} \tag{3.46}$$

The wave vector is the same as in (3.43). The force vector consists of two smaller 4x1 vectors $\mathbf{f} = (f_1, f_2, f_3, f_4)^{\mathrm{T}}$ is the vector of forces per unit length applied to an object attached along the z axis and $\mathbf{f}' = (f_1', f_2', f_3', f_4')^{\mathrm{T}}$ which is the same but for an object attached along the axis at x = -b . $\mathbf{C}_{11}$ is identical to **C** for the semi-infinite curved panel. The columns of $\mathbf{C}_{12}$ are calculated using (3.38) by putting **u** equal to **c** for the r', n', l' and t' waves and replacing in the corresponding wave numbers into the entries of **T**. $\mathbf{C}_{12}$ is given by.

$$\mathbf{C}_{21} = \mathbf{R}\left(-\mathbf{f}_r \exp(-bk_{xr}), -\mathbf{f}_n \exp(-bk_{xn}), -\mathbf{f}_l \exp(-bk_{xl}), -\mathbf{f}_t \exp(-bk_{xt})\right) \tag{3.47}$$

Equation (3.47) is similar to (3.44) in that the rotation matrix **R** is identical as are the exponential factors. The subscripts r, n, l and t indicate the wave type for which **f,** the force vector was calculated. Finally the entries of $\mathbf{C}_{22}$ are given by.

$$\mathbf{C}_{22} = \mathbf{R}\left(-\mathbf{f}_{r'} \exp(bk_{xr}), -\mathbf{f}_{n'} \exp(bk_{xn}), -\mathbf{f}_{l'} \exp(bk_{xl}), -\mathbf{f}_{t'} \exp(bk_{xt})\right) \tag{3.48}$$

$\mathbf{C}_{21}$ and $\mathbf{C}_{22}$ have minus signs before the force vectors because they relate complex wave amplitudes to the forces on the x = -b boundary whereas (3.38) gives the force vectors for the boundary at x = 0.

When the 8x8 **B** and **C** matrices have been calculated as above the stiffness matrix of the curved strip may be calculated using (3.7).

3.7. Elastic Layers.

Elastic layers appear in motor vehicles around windows and doors so their transmission properties are of interest. A simple model was constructed which considered shearing, bending and stretching of the layer. This is identical to the simpler of the two elastic layers described in Mees&Vermeir[10]. No waves in the elastic layer were considered in this model and so the **B** and **C** matrices are irrelevant. The stiffness matrix is given below.

$$\mathbf{A} = \begin{pmatrix} -K_S & 0 & 0 & 0 & K_S & 0 & 0 & 0 \\ 0 & -K_M & 0 & 0 & 0 & K_M & 0 & 0 \\ 0 & 0 & -K_C & 0 & 0 & 0 & K_C & 0 \\ 0 & 0 & 0 & -K_M & 0 & 0 & 0 & K_S \\ K_S & 0 & 0 & 0 & -K_S & 0 & 0 & 0 \\ 0 & K_M & 0 & 0 & 0 & -K_M & 0 & 0 \\ 0 & 0 & K_C & 0 & 0 & 0 & -K_C & 0 \\ 0 & 0 & 0 & K_S & 0 & 0 & 0 & -K_S \end{pmatrix} \tag{3.49}$$

The stiffness terms K_S, K_M and K_C depend upon material properties, the geometry of the layer. Mees&Vermeir[10] describe two approximations for the stiffness terms, one which assumes plain strain in the y direction and one which assumes plain stress. The latter assumption is made in this case giving rise to the following expressions.

$$K_S = G(1+i\eta)\frac{h}{b}, \quad K_M = \frac{E(1+i\eta)h^3}{12(1-\mu^2)b}, \quad K_C = \frac{E(1+i\eta)h}{(1-\mu^2)b} \tag{3.50}$$

Where η is the loss coefficient which is typically 0.1 for rubber, Cremer *et al*[1]. Elastic layers like all two node elements use the displacement and force convention shown in Fig. 3.2, h is the thickness of the layer in the y direction.

3.8. Rotation.

Stiffness matrices described so far are local, but the elements are to be assembled at different orientations to form a global stiffness matrix. Multiplication by a rotation matrix **R** converts from local to global co-ordinates as shown in Fig. 3.6.

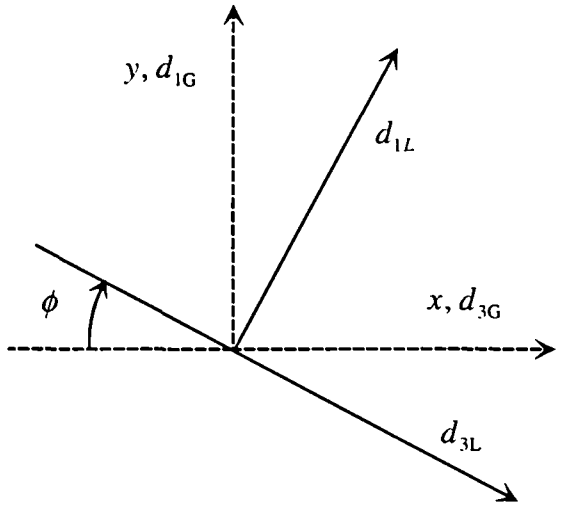

Figure 3.6: Local and global co-ordinates.

This is expressed algebraically in (3.51) by multiplying $\mathbf{d}_L$, the local displacement vector by **R**, the rotation matrix to get $\mathbf{d}_G$, the global displacement vector. For a one node element **R** is 4x4 and given by (3.52).

$$\mathbf{R}\mathbf{d}_L = \mathbf{d}_G \tag{3.51}$$

$$\mathbf{R} = \begin{pmatrix} \cos\phi & 0 & -\sin\phi & 0 \\ 0 & 1 & 0 & 0 \\ \sin\phi & 0 & \cos\phi & 0 \\ 0 & 0 & 0 & 1 \end{pmatrix} \tag{3.52}$$

Rotation about the z axis has no effect upon d_2 or d_4. Conversion from global to local co-ordinates is achieved by using $\mathbf{R}^{-1}$ in place of **R** in (3.51) or by using $-\theta$ in place of θ in (3.52). An element's global stiffness matrix may be calculated using

$$\mathbf{A}_G = \mathbf{R}\mathbf{A}_L\mathbf{R}^{-1} \tag{3.53}$$

Two node flat elements have an 8x8 rotation matrix consisting of a bottom right and a top left sub-matrix identical to (3.52), with zeros elsewhere. The number of zeros in this matrix make multiplying inefficient therefor a special procedure was written which skips the zeros.

3.9. Assembling Joint Stiffness Matrix

Once an element's global stiffness matrix has been calculated it may be assembled into the overall joint stiffness matrix. This is done using matrix assembly methods well known in Finite Element Analysis, see Thomson[88]. When two elements are joined at a node their global displacements at the node are constrained to be equal. The global force applied to the node by the elements is the sum of the global forces applied by each element. The matrix assembly method is illustrated below for the joint shown in Fig. 3.7.

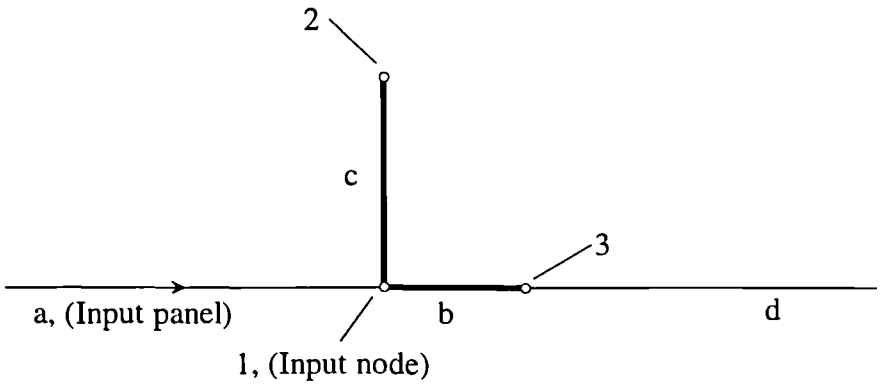

Figure 3.7: Assembled joint structure.

Fig. 3.7 shows a joint constructed of four elements, a, b, c and d. Elements a and d are semi-infinite flat panels, b and c are two node flat panel strip elements which form an "L" beam separating the two semi-infinite panels. The nodes of the model are labelled 1, 2 and 3. Assembling the joint stiffness matrix for this joint gives.

$$\begin{pmatrix} \mathbf{Aa} + \mathbf{Ac}_{11} + \mathbf{Ab}_{22} & \mathbf{Ac}_{12} & \mathbf{Ab}_{21} \\ \mathbf{Ac}_{21} & \mathbf{Ac}_{22} & \mathbf{0} \\ \mathbf{Ab}_{12} & \mathbf{0} & \mathbf{Ad} + \mathbf{Ab}_{11} \end{pmatrix} \begin{pmatrix} \mathbf{d}_{1G} \\ \mathbf{d}_{2G} \\ \mathbf{d}_{3G} \end{pmatrix} = \begin{pmatrix} \mathbf{f}_{1G} \\ \mathbf{f}_{2G} \\ \mathbf{f}_{3G} \end{pmatrix} \tag{3.54}$$

Each of the entries in the stiffness matrix in (3.54) are themselves 4x4 matrices. **Aa** is the global stiffness matrix of panel a and **Ad** is the global stiffness matrix of panel d. The 8x8 matrices **Ab** and **Ac** of elements b and c respectively have been split into four 4x4 sub matrices given by.

$$\mathbf{Ab} = \begin{pmatrix} \mathbf{Ab}_{11} & \mathbf{Ab}_{12} \\ \mathbf{Ab}_{21} & \mathbf{Ab}_{22} \end{pmatrix}, \ \mathbf{Ac} = \begin{pmatrix} \mathbf{Ac}_{11} & \mathbf{Ac}_{12} \\ \mathbf{Ac}_{21} & \mathbf{Ac}_{22} \end{pmatrix} \tag{3.55}$$

The location of the b and c element sub matrices within the overall joint matrix is determined by which node of each element is attached to which node of the overall model. For example the node of a, the first node of c and the second node of d are all connected to node one of the overall model giving a sub matrix of $\mathbf{Aa} + \mathbf{Ac}_{11} + \mathbf{Ab}_{22}$ which relates the displacements at node one of the model to the forces at node one. Summing the elements of the sub matrices is equivalent to summing the forces applied to the node by each element to give the total force.

3.10. Solving For Transmission Coefficients

So far we have described the calculation of the joint stiffness matrix. This section describes the way in which the stiffness matrices are used to calculate wave transmission coefficients.

The technique shall be illustrated by application to the joint shown in Fig. 3.7. In order to calculate the response of the joint structure to an incoming wave it is necessary to calculate the forces and deflections caused by the wave at the input panel boundary. In sections 3.2-3.6 it has been shown that the displacements and forces at panel boundaries caused by waves can be calculated in flat and curved panels. In the case of travelling waves on semi-infinite panels only those carrying power away from the boundary were considered. In this case however we must consider travelling waves which carry power towards the boundary. The local deflections caused along the z axis of a flat panel by an incoming wave are given by swapping the sign of the wave number in the x direction in

(3.9) for bending waves and (3.15) for longitudinal and transverse. These local deflections are converted into global co-ordinates by multiplying with **R** the rotation matrix for the input panel. This gives, $\mathbf{d}_{IN}$ the deflection of the input node caused by the incoming wave. $\mathbf{d}_{IN}$ is given for flat panels by (3.57) (3.56) and (3.58) for bending longitudinal and transverse waves (of unit magnitude) respectively.

$$\mathbf{d}_{IN} = \mathbf{R}\begin{pmatrix} 1 \\ -k_{xB} \\ 0 \\ 0 \end{pmatrix}, \quad \mathbf{d}_{IN} = \mathbf{R}\begin{pmatrix} 0 \\ 0 \\ ik_{xL} \\ k_Z \end{pmatrix}, \quad \mathbf{d}_{IN} = \mathbf{R}\begin{pmatrix} 0 \\ 0 \\ k_Z \\ -ik_{xS} \end{pmatrix}$$

(3.58) (3.57) (3.56)

The global displacement of the whole joint when considering only the incident wave is $\mathbf{d}_{INC}$, this takes no account of reflected waves or near fields and is zero every where except on the input node (Fig.7.). The model in Fig.7 has three nodes so that $\mathbf{d}_{INC}$ must be padded out with zeros in the second and third node entries as given below.

$$\mathbf{d}_{INC} = \begin{pmatrix} \mathbf{d}_{IN} \\ \mathbf{0} \\ \mathbf{0} \end{pmatrix} \tag{3.59}$$

The force on the input node resulting from the incoming wave shall be called $\mathbf{f}_{IN}$. For flat panels $\mathbf{f}_{IN}$ is given by (3.60), (3.61) and (3.62) for bending longitudinal and transverse waves respectively.

$$\mathbf{f}_{IN} = \mathbf{R}\begin{pmatrix} -B(k_{xB}^3 + (2-\mu)k_{xB}k_Z^2) \\ B(\mu k_Z^2 - k_{xB}^2) \\ 0 \\ 0 \end{pmatrix}, \quad \mathbf{f}_{IN} = \mathbf{R}\begin{pmatrix} 0 \\ 0 \\ \frac{iEh}{1-\mu^2}(k_{xL}^2 - \mu k_Z^2) \\ 2Ghk_Z k_{xL} \end{pmatrix}$$

(3.61) (3.60)

$$\mathbf{f}_{IN} = \mathbf{R}\begin{pmatrix} 0 \\ 0 \\ 2Ghk_{xS}k_Z \\ -iGh(k_{xS}^2 + k_Z^2) \end{pmatrix} \tag{3.62}$$

Again these vectors are derived using the same methods as were used in sections 3.2-3.4, except that forces due to waves carrying power toward the boundary rather than away

were considered. $\mathbf{f}_{INC}$ is defined as the force vector on the entire joint caused by the incoming wave alone. $\mathbf{f}_{INC}$ must be padded with zeros in the same way as $\mathbf{d}_{INC}$.

$$\mathbf{f}_{INC} = \begin{pmatrix} \mathbf{f}_{IN} \\ \mathbf{0} \\ \mathbf{0} \end{pmatrix} \tag{3.63}$$

The response of the joint to the incoming wave is calculated by superposition of two sets of forces upon the joint.

In the first loading scenario only the incoming wave is present on the input panel causing the input node to move but the other nodes are held stationary. The force vector applied to the nodes of the joint to impose these conditions is called $\mathbf{f}_{RES}$ and is given by equation (3.64).

$$\mathbf{f}_{RES} = -\mathbf{A}_{PAR}\mathbf{d}_{INC} - \mathbf{f}_{INC} \tag{3.64}$$

Where $\mathbf{A}_{PAR}$ is the partial joint stiffness matrix containing all the joint elements except the incoming panel as shown in Fig. 3.8.

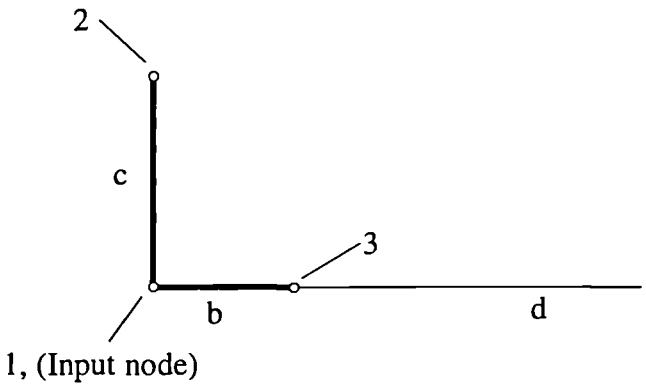

Figure 3.8: Partial joint structure (without input panel).

$\mathbf{A}_{PAR}$ is given by omitting the input panel stiffness matrix from **A** the joint stiffness matrix.

$$\mathbf{A}_{PAR} = \begin{pmatrix} Ac_{11} + Ab_{22} & Ac_{12} & Ab_{21} \\ Ac_{21} & Ac_{22} & \mathbf{0} \\ Ab_{12} & \mathbf{0} & Ad + Ab_{11} \end{pmatrix} \tag{3.65}$$

The input panel stiffness matrix is omitted because it was derived like all the others by assuming there are no incoming waves on the panel. $\mathbf{f}_{INC}$ is included in (3.64) to account for the force applied by the input panel.

In the second loading scenario the complete joint (Fig. 3.7) is displaced by $\mathbf{d}_{SOL}$ which is defined such that the joint structure applies $\mathbf{f}_{RES}$ to the nodes of the joint. Super position of the two motions results in a net force on the joint of zero which is what is required. Equation (3.66) is used to calculate $\mathbf{d}_{SOL}$ after adding the input panel to $\mathbf{A}_{PAR}$ giving the complete stiffness matrix **A**, given in equation (3.54).

$$\mathbf{A}\mathbf{d}_{SOL} = \mathbf{f}_{RES} \tag{3.66}$$

$\mathbf{d}_{SOL}$ contains the three nodal displacements which can be used to calculate the magnitude of the waves on each panel.

$$\mathbf{d}_{SOL} = \begin{pmatrix} \mathbf{d}_1 \\ \mathbf{d}_2 \\ \mathbf{d}_3 \end{pmatrix} \tag{3.67}$$

Where $\mathbf{d}_n$ is the 4x1 displacement vector for node *n*. $\mathbf{d}_{SOL}$ gives the total displacement of nodes 2 and 3 caused by the incoming wave because in the first loading scenario there displacements were zero so that superposition of the two displacements causes no change. In the first scenario node 1, (the input node) had displacement given by $\mathbf{d}_{IN}$ form equations (3.57-58), so this must be added to give the complete displacement of the input node.

$$\mathbf{d}_{INP} = \mathbf{d}_1 + \mathbf{d}_{IN} \tag{3.68}$$

The next step towards the wave transmission coefficients is to calculate the amplitudes of all the waves on the semi-infinite panels. For this we make use of the **B** matrix for the panel in question which was defined in (3.5). To calculate the complex amplitudes of the four waves on panel d in Fig. 3.7 we us equation

$$\mathbf{B}_d^{-1}\mathbf{R}_d^{-1}\mathbf{d}_3 = \mathbf{w} \tag{3.69}$$

Where $\mathbf{B}_d$ is the **B** matrix of panel d and $\mathbf{R}_d$ is the rotation matrix for panel d. Note that $\mathbf{d}_3$ gives the displacement of node 3 in global co-ordinates and $\mathbf{B}_d$ relates local displacements to the wave amplitudes in the wave vector **w** for panel d. The rotation matrix, $\mathbf{R}_d$ for panel d is included in (3.69) to convert the displacements into local co-ordinates. The wave vector on the input panel (a) is given below.

$$\mathbf{B}_a^{-1}\mathbf{R}_a^{-1}\mathbf{d}_1 = \mathbf{w} \tag{3.70}$$

$\mathbf{d}_1$ is used in (3.70) rather than the total input node displacement $\mathbf{d}_{INP}$ because $\mathbf{d}_{INP}$ contains deflections due to the incoming wave on the input panel where as **B** was derived assuming no incoming waves. If there were another semi-infinite panel attached to the

input node besides the input panel then $\mathbf{d}_{INP}$ would be used in place of $\mathbf{d}_1$ in (3.70) to calculate the wave vector for that panel as it wouldn't be carrying any incoming waves.

Once the amplitude of each wave type is known the power flowing in each can be calculated given the properties of the panels. Taking the ratios of these powers to the power of the incoming wave gives the transmission coefficients. Flat panel power flow is calculated using equations (3.23), (3.24) or (3.25) for bending, longitudinal and transverse waves respectively. This assumes that the waves are travelling waves and not near fields which carry no power away from the joint and give a transmission coefficient of zero. Bending longitudinal and transverse waves become near fields if k_x, the wave number in the x direction has a non zero real part.

In the joint from Fig. 3.7 both the semi-infinite panels were flat. If the joint contains any semi-infinite curved panels which are not the input panel then the same procedure is used to calculate the transmission coefficients except that equation (3.42) is used to calculate the power carried away by the waves on the curved panels. If the input panel is curved then the entries of the input panel displacement and force vectors $\mathbf{d}_{IN}$ and $\mathbf{f}_{IN}$ are not calculated using (3.57-58) and (3.60-62) as was the case with a flat input panel. $\mathbf{d}_{IN}$ with a curved input panel is calculated using (3.36) for the incoming wave in the same way as was used to calculate the columns of the $\mathbf{B}$ matrix for curved panels. $\mathbf{f}_{IN}$ with a curved input panel is calculated using (3.38) for the incoming wave in the same way as was used to calculate the columns of the $\mathbf{C}$ for curved panels . In a curved panel there are four types of incoming wave labelled 1,2,3 and 4 on Fig. 3.4, these were discussed in section 3.5. Wave types 1 and 2 only exist over limited angles of incidence and wave type 4 only occurs when the frequency is above the plain strain ring frequency ($\omega >> \omega_R$ where $\omega_R = \sqrt{E / \rho (1-\mu^2) a^2}$). Incident waves of type 1,3 and 4 have a phase velocity towards the boundary on the z axis as is the case with a flat input panel. An incoming wave of type 2 however must have a phase velocity away from the z axis boundary, where we have defined an incoming wave as one which carries power toward the joint. The reasons for this are discussed by Langley[9, 94].

3.11. Curved Corner Joint Example.

So as to illustrate the usefulness of this method the transmission properties of a rounded corner joint (Fig. 3.9) are investigated.

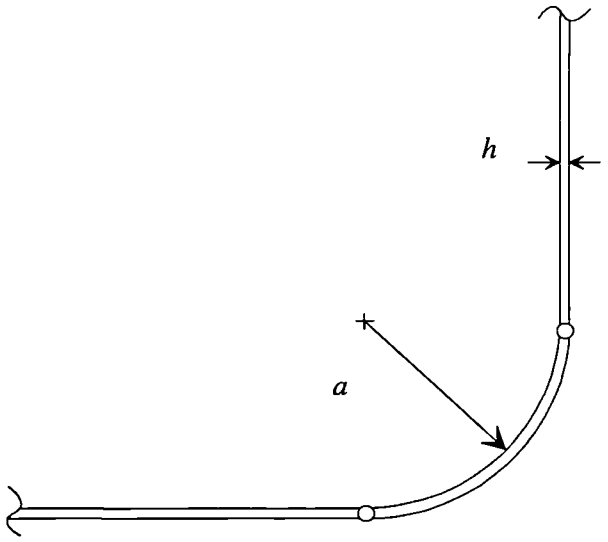

Figure 3.9: 90° Curved corner joint.

Very little published work (Fraser&Steel[12] and K. De Langhe *et al*[13])on the effect of rounding on the transmission of a corner joint has been found. Panel and beam connections of this sort are not uncommon in many structures such as motor-vehicles which makes this work of practical significance. The joint model in Fig. 3.9 is constructed by assembling two semi-infinite flat panels and a two node curved finite strip element all of which have thickness *h*. Bending wave transmission coefficients are shown in Fig. 3.10 which also contains sharp corner transmission coefficients calculated by joining the two flat semi-infinite panels directly. In this example h = 0.001m, a = 0.1m, $\mu = 0.3$ and plane strain longitudinal wave speed $c_L = 5200$ m/s.

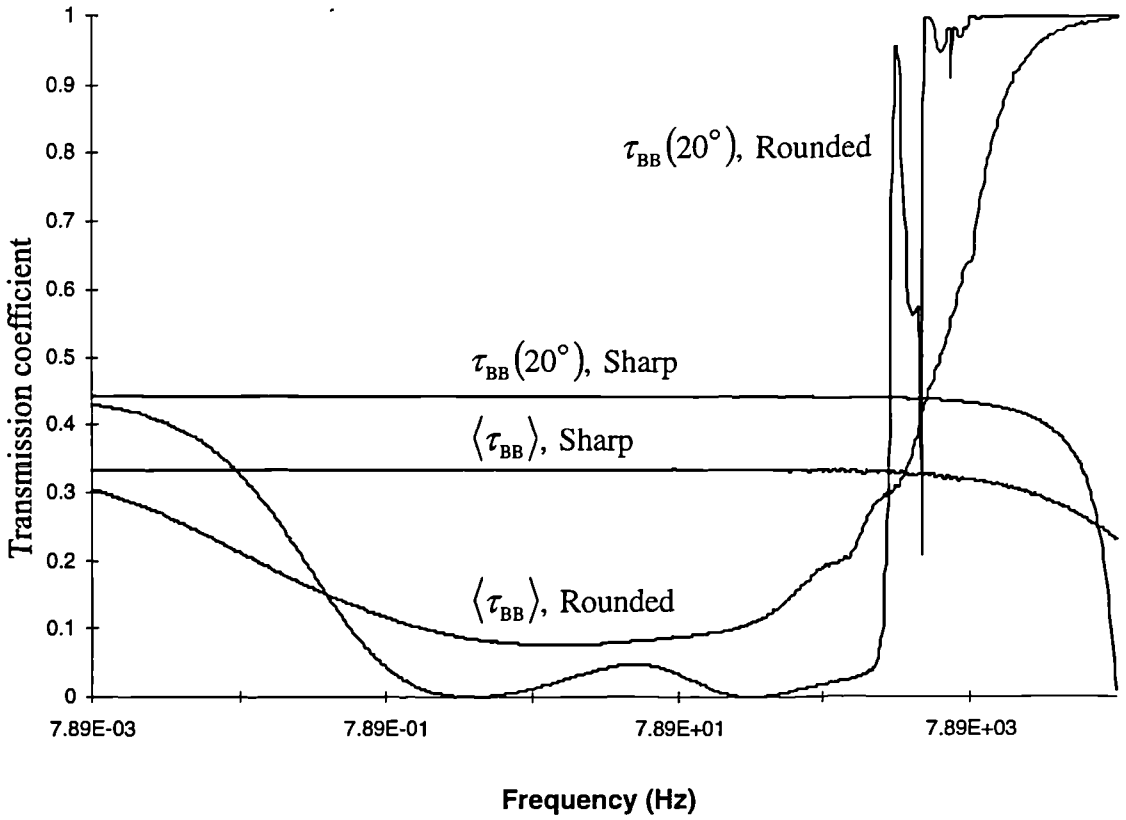

Figure 3.10: Bending wave transmission around curved and sharp corner joints.

h =0.001m, a = 0.1m, f_R = 7.895 kHz, μ = 0.3 and c_L(plate) = 5200 m/s.

Frequency is shown along the horizontal axis of Fig. 3.10 in hertz, each tick mark corresponds to a tenfold increase in frequency. The panel properties give a plain strain ring frequency f_R = 7.895 kHz for the curved section. Two sets of curves appear in the graph one for a bending wave incident at 20° and another of the diffuse field transmission coefficient calculated using equation (2.96) Both transmission coefficients are plotted for a sharp 90° corner joint along side the rounded values. Bending wave transmission at a corner joint was discussed in Section 2.9.5. The analysis in Section 2.9.5 considered bending waves only with no in-plane waves and predicted that transmission was constant with respect to frequency. The transmission coefficients in Fig 10 are constant at low frequencies with the same values that are predicted using the analysis in Section 2.9.5. Fig. 3.10 shows that the sharp transmission coefficients fall of at higher frequencies, this is due to the conversion of energy into in-plane waves at the junction. As the frequency approaches zero both the rounded corner transmission coefficients approach the relevant sharp corner joint value. Intuitively one would expect this to happen as the bending wavelength increases and the radius of curvature becomes small by comparison i.e. the corner becomes sharper. At $f = f_R \times 10^{-4}$ (0.79Hz) the 20° rounded value drops below

0.1 the curve stays below this value until $f_R > f > f_R \times 0.1$ where it oscillates violently until settling at 1.0. The rapid fluctuations were investigated to insure that they were a real phenomena and not due to numerical error. The transmission coefficients sum to one over this frequency range and closer inspection showed the curve to be smooth but rapidly changing function with peaks and sharp troughs over this range. The rounded section was replaced by a number of two node curved panels which gave identical results. Approximating the curved section by 30 two node flat plate elements gave very similar results which also oscillated violently before approaching complete transmission. These observations would suggest that the rapid variations in transmission with frequency are a real phenomenon and not due to numerical errors. It is probable that the rapid fluctuations are due to resonances in the curved section as it is of finite width. Woodhouse [72] has investigated coupling across resonant structures, his observations would suggest that when the transmission across the curved section is strong then it is close to a resonant frequency and when transmission is weak then it is close to an anti-resonance. Complete transmission at high frequency is not surprising as curved panels may be treated in some instances as flat plates of the same thickness, provided the frequency is above the ring frequency. For example Cremer *et al*[1], showed that the point impedance of a tube of infinite length approaches that of an infinite plate with the same thickness when the frequency rises above the ring frequency. Diffuse transmission also approaches 1.0 as the frequency rises but more gradually. This is because transmission coefficients for bending waves incident at different angles flip to complete transmission at different frequencies as shown in Fig. 3.11.

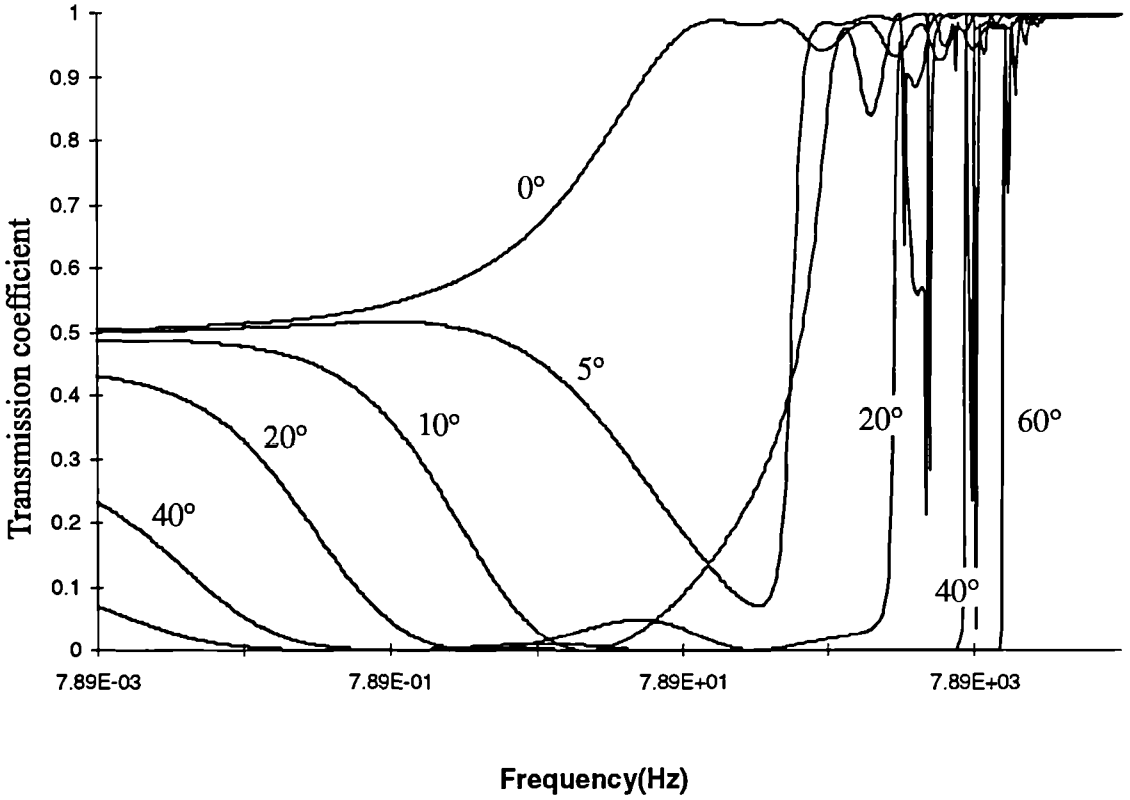

Figure 3.11: Bending wave transmission at a curved corner joint for various angles of incidence, h =0.001m, a = 0.1m, f_R = 7.895 kHz, μ = 0.3 and c_L (plate) = 5200 m/s.

Fig. 3.11 Shows the bending wave transmission of the rounded corner joint for waves incident at a number of angles. As the angle of incidence increases so does the frequency at which the curve approaches 1.0. There is no limiting frequency above which all curves have reached 1.0. By examining the dispersion curves of the curved and flat panels of the joint the location of the flip in transmission can be explained.

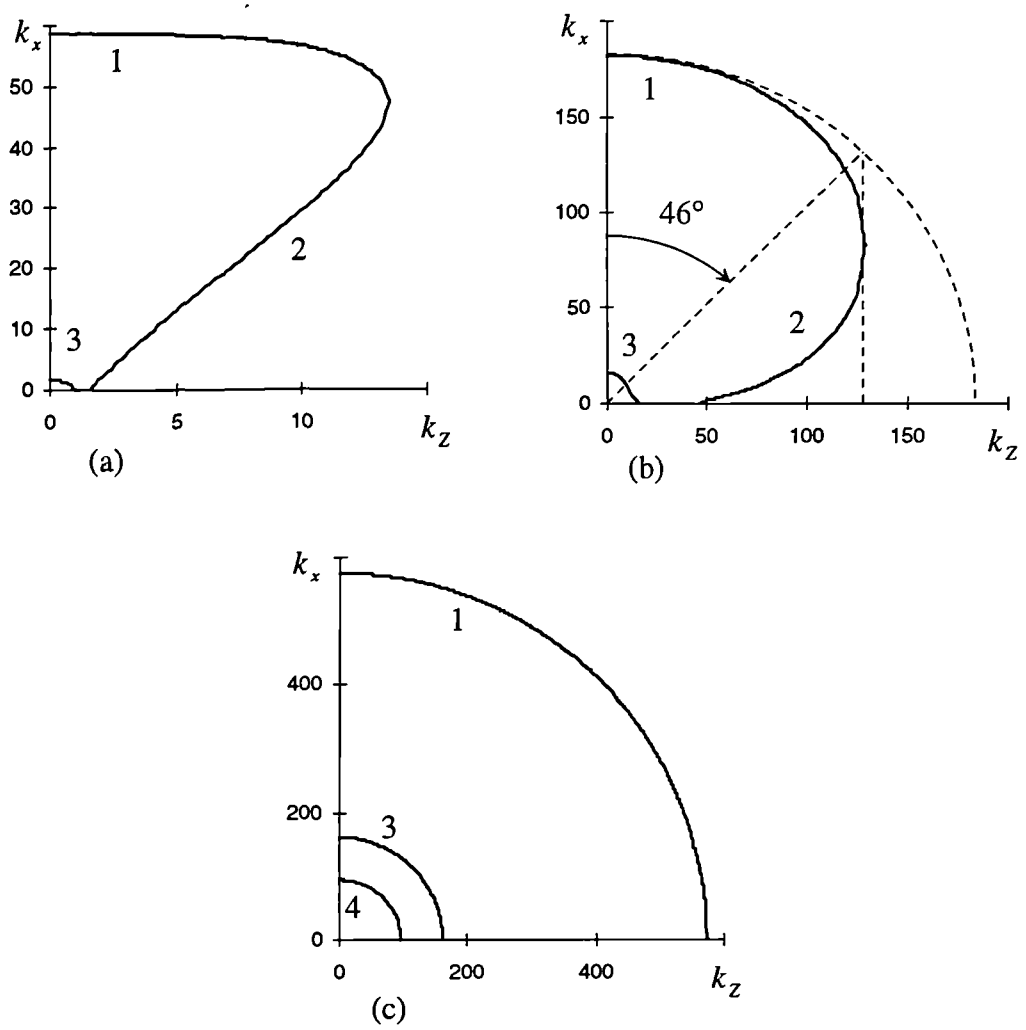

Figure 3.12: Dispersion diagrams for curved section with h = 0.001m, a = 0.1m and $\omega_R = 49600$ rad/s or $f_R = 7.89$ kHz. (a): $\omega = 0.1\,\omega_R$, (b): $\omega = \omega_R$ and (c): $\omega = 10\,\omega_R$.

Fig. 3.12 shows dispersion curves for the curved panel section at three frequencies. Fig. 3.12(b) which is the $\omega = \omega_R$ case also contains the dispersion curve for the bending wave on the flat panel which is the dotted line forming a quarter circle. The cut-off value of k_z for travelling waves in the curved panel is approximately 130 which is shown by the dotted vertical line, this corresponds to an incidence angle of 46° beyond which there is negligible transmission at this frequency as can be seen from Fig. 313

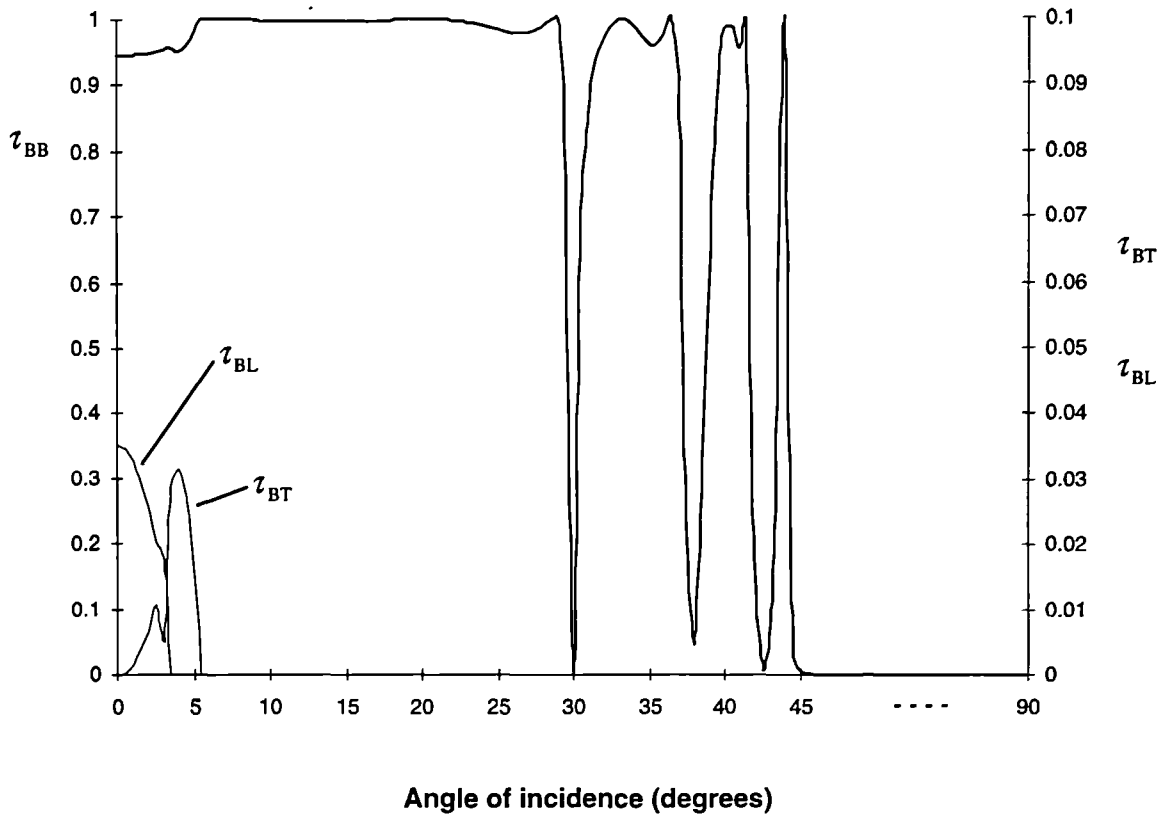

Figure 3.13: Wave transmission coefficients at the ring frequency $f_R = 7.89$ kHz for rounded corner versus angle of incidence in degrees, h =0.001m , $a = 0.1$ m.

Fig. 3.13 Contains all the transmission coefficients including those of the in-plane waves. In-plane waves are shown using a second (right hand side) scale which is a factor of ten smaller. The horizontal axis on this graph is bending wave incidence angle in degrees. Type 1 waves in the curved section are closest in character to flat plate bending waves, becoming asymptotically similar as frequency increases. This similarity would explain the high transmission when type 1 waves are present. Normal incidence transmission in Fig. 3.11 rises from the sharp corner value of 0.5 to 1.0 most rapidly without dropping first, this is because there is a type 1 travelling wave at $k_z = 0$, for all frequencies. The rise in normal transmission is presumably a result of the type 1 wave becoming closer in character to the flat plate bending wave as frequency increases. It is interesting to note that normal incidence transmission is greater than 0.9 at all frequencies above 79Hz which is only one hundredth of the ring frequency, a result which suggests that complete transmission is a better approximation than 0.5 for the equivalent beam structure. Transmission below the flip frequency at non normal incidence must be due to near field waves, this is possible as the curved section is of finite width and a near field originating from one boundary will cause deflection of the other. Wave number magnitude increase

with frequency which means less near field coupling would be expected as the frequency increases because the near field decays more rapidly in space and has less influence on the opposite boundary. This effect may be seen in Fig. 3.11 causing the non normal incidence curves to drop from the sharp corner values before reaching the flip frequency.

Prediction of the flip frequency for a given angle of incidence or flip angle for a given frequency requires considerably less computation than calculating the transmission coefficients. An approximate method based on the assumption that transmission is zero below the flip frequency and unity above would be quicker to calculate and fairly accurate over frequency ranges above the near field coupling region. Computation time was not a problem during this study and the approximate method was not used.

3.12. Roof to Windscreen Joint

In this section the joint structure connecting the roof and windscreen of a small passenger car has been modelled. The model is shown in Fig. 3.14 below, and the results are used amongst others in Chapter 6 as part of an SEA model of the car.

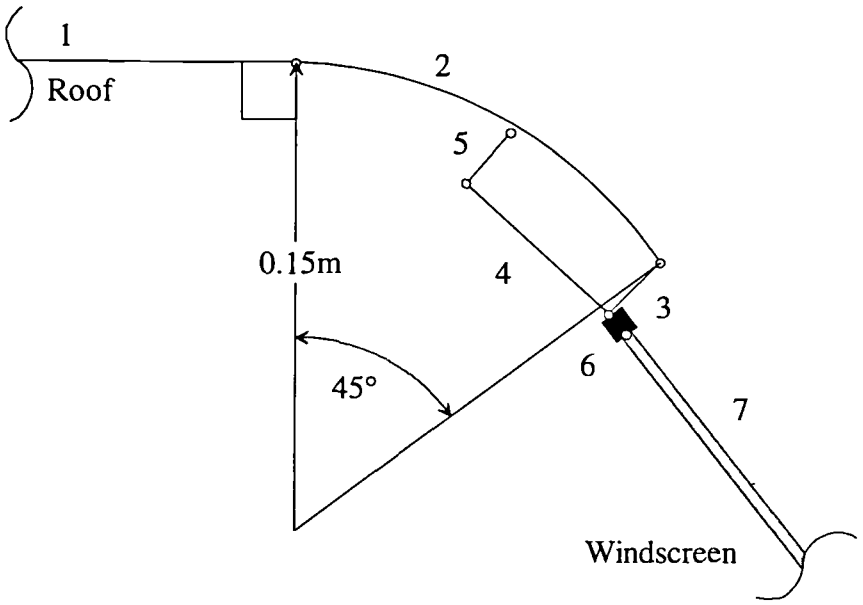

Figure 3.14: Roof to windscreen joint showing constituent elements.

The roof to windscreen model in Fig. 3.14 has six nodes, and consists of the following elements:

- The roof (labelled 1) is modelled as a flat semi-infinite panel of the type described in section 3.3. The roof panel is horizontal in Fig. 3.14 .
- The Windscreen panel (labelled 7) is also modelled as a flat semi-infinite panel which is 45° to horizontal.

- One two node curved panel element (labelled 2) of the type described in section 3.6.
- Three two node flat panel elements (labelled 3,4 and 5) of the type discussed in section 3.4. Panels 3 and 5 are o.o1m in width and 115.8° clock wise from horizontal. Panel 4 is 0.05m in width and 25.8° clock wise from horizontal.
- Element 6 is an elastic layer of the type discussed in section 3.7 which represents the sealant that holds the windscreen in place. The elastic layer is at 45° to horizontal.

Elements 1-5 are steel panels with plate longitudinal wave speed of c_L=5200m/s, density ρ = 7800 kg/m^3 , poissons ratio μ =0.3 and thickness of 0.7mm. The windscreen panel is 6mm thick, has a plate longitudinal wave speed of c_L=4900m/s , density ρ = 2500 kg/m^3 and poissons ratio of μ =0.3. The elastic layer (element 6) is 0.01x0.01m in size and made of rubber with the following properties: c_L= 68m/s, ρ = 1108 kg/m^3 , poissons ratio μ =0.5 and loss factor η =0.1. Bending wave transmission of this joint has been calculated using the methods described in this Chapter. The results are shown below.

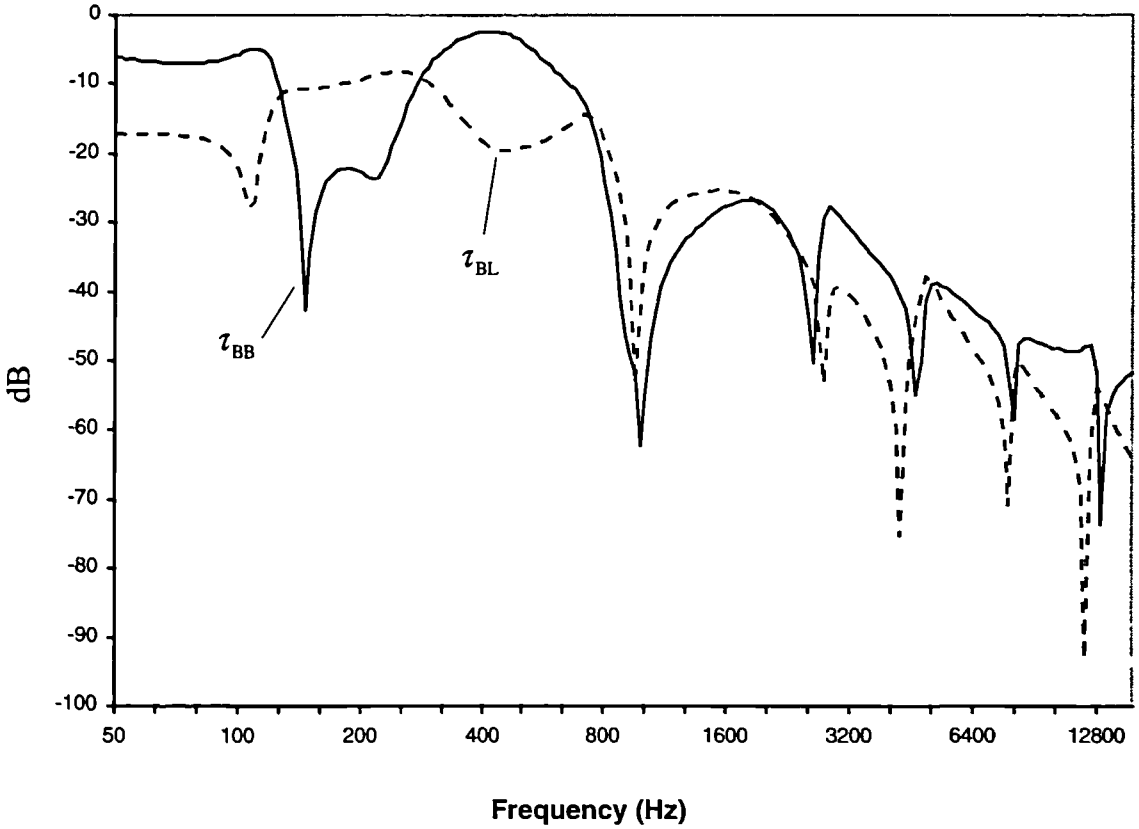

Figure 3.15: Roof to windscreen bending to bending and bending to longitudinal wave transmission coefficients for normal incidence.

Fig. 3.15 Shows the bending wave transmission coefficients across the roof to windscreen joint in dB versus frequency in Hz. Transverse waves are not generated as the incoming

bending wave in this case is incident normal to the joint. The effect of resonant behaviour within the joint structure is clearly evident in the peaks and troughs of the transmission curves in Fig. 3.15. If the joint structure was modelled as a simple beam then this resonant behaviour would not be correctly predicted because simple bending assumes that the cross section of the beam does not distort.

3.13. Validation

A number of mathematical and numerical checks were carried out in-order to validate the modelling software described in this Chapter. The code was checked mathematically against a number of existing references and a number of numerical checks were used.

The flat plate stiffness matrices agree with those given by Langley&Heron[8] allowing for a misprint discussed in Section 3.3 which they have pointed out in their paper. The curved panel stiffness matrices were calculated using the procedure given by Langleys[9], the differential equations given in that work were checked against other references i.e. Langley [93] and Mead&Bardell[96] In addition to mathematical checks a number of numerical tests were done in order to validate predicted transmission coefficients.

When all the elements of a joint model are conservative, i.e. there is no damping present in the joint then the transmission coefficients for all the wave types on all the panels must sum to one. When there is damping present in a joint then the sum of the transmission coefficients is less than one. The sum of the transmission coefficients can be used as a test of the validity of results although it is not a guarantee that they are correct. The transmission coefficients predicted using the complex joint modeller typically summed to one within at least five decimal places when no damping was present within the joint. When damping was present within the joint then they summed to less than one.

Conservation of energy dictates that the wave dynamic stiffness matrix of an undamped finite element should be Hermitian. Stiffness matrices calculated for the two node curved and flat panels were checked and found to be Hermitian to at least five significant figures, when using the dimensions, frequencies and material properties of the models given in this thesis.

The reciprocity of several joint models was checked by calculating transmission coefficients from one wave to another and then in the reverse direction, these should be equal provided the reverse transmission coefficient is for a wave incident at its original angle of transmission. That is: $\tau_{nm}(\theta_1) = \tau_{mn}(\theta_2)$ where θ_1 and θ_2 are related by Snell's law. Reciprocity was checked in this way for joints containing all the element types described in this Chapter.

A simple test of the two node flat panel elements is to join two semi-infinite panels together using a two node finite strip element with the same thickness and material properties, forming an infinite flat panel. Incident waves of any type should be completely transmitted across the two node element. A model of this sort was constructed and correctly predicted complete transmission of bending longitudinal and transverse waves with a variety of panel and strip properties and dimensions.

The semi-infinite and two node flat panel elements have been independently validated against other numerical models. Smith[97] constructed a model with four panels connected by a finite strip of panel, this gave excellent agreement with results from an identical model built using the complex joint modeller. Connelly[98] created a model for an "I" beam joining two semi-infinite panels in which the flanges of the beam were modelled as finite strips of plate. This also agreed with results from a complex joint model of the same beam.

The complex joint modeller output was checked against the numerical output for the three plate model presented by Langley&Heron[8]. All the transmission coefficients given were in excellent agreement with those predicted using the complex joint modeler. A two node flat panel element was introduced into the three plate model so as to test the two node element. The two node element was chosen to have the same thickness and material properties as one of the semi-infinite panels so that the transmission coefficients would be unaffected. The predicted results did not change which would suggest that the two node element was modelled correctly.

The curved panel stiffness matrices were calculated using a number of numerical procedures. The k_x wave numbers in equation (3.35) were calculated by solving a quartic

polynomial in k_x^2. The solutions calculated using the computer code were checked by solving the same polynomial using other mathematics software and were found to be accurate in all cases. The Eigen vectors **c** in (3.35) were calculated numerically using a reverse iteration technique with LU decomposition which is discussed in Press *et al*[99], These were also checked by comparing the results with output from independent mathematics and numerical software.

A complex joint model was used to replicate the numerical results for transmission coefficients between a curved and flat semi-infinite panel given by Langley[9]. The complex joint model agreed with the values in [9]. The model was then altered and a 90°section of the semi-infinite panel was replaced with two node flat panels joined to form a piecewise approximation to the curved section. With three flat sections the predicted transmission coefficients were generally not in very good agreement with those given by Langley[9]. As the number of flat two node panel sections was increased to better approximate the curved section the agreement improved. When the curved section was approximated by thirty flat panel segments the predicted transmission coefficients were generally within 10% of those given by Langley[9]. This gives greater confidence in both the curved and flat plate elements. This procedure was repeated using two node curved panel segments to replace a section of the semi-infinite curved panel. Using the two node curved panel elements gave identical results to the original model.

A complex joint model was constructed representing a corner joint between two panels and the resulting transmission coefficients compared with those given by a separate computer program using the model described by Craven&Gibbs[6] which includes in-plane waves on both panels. The complex joint model agreed very closely with this model. At low frequencies or with thin panels the complex joint results were very close to those given by Cremer *et al's*[1] bending only model which is given in Section 2.9.5. A model containing an elastic layer between the panels was also constructed and this gave very good agreement with results from a separate computer program using the bending shear and longitudinal stiffness elastic interlayer model described by Mees&Vermeir[10].

3.14. Discussion and Conclusions

A method for calculating wave transmission coefficients has been developed which is based on the wave dynamic stiffness approach proposed by Langley&Heron[8]. Langley&Heron's[8] and Langleys[9] work has been extended to include two node elements which may be assembled into complex joint structures. Resonant behaviour of the joint structure may be modelled using this approach. Treating the joint as a beam in simple bending will not reveal this resonant behaviour. Transmission of bending waves across a rounded corner joint has been investigated with a number of numerical experiments. Transmission of bending waves is predominantly by type 1 waves (See Fig. 3.4) on the curved section of panel. This is not surprising since these are the closest to flat panel bending waves. Transmission of bending waves is almost complete if the type 1 wave is present on the curved section. Type 1 waves are only the present below a certain angle of bending wave incidence. This angle is a function of frequency, getting larger at high frequencies. Waves incident at greater angles are almost entirely reflected in the examples investigated.

Computational efficiency was not the foremost objective when writing the computer code to implement the numerical procedures described in this chapter. None of the models used in this Chapter or Chapter 6 required an excessive time to compute the results. The joints constructed in this work were in many cases relatively simple representations of the actual joint structures. If larger more elaborate joints required analysis then it might be worth while optimising numerical efficiency of the code. A few alterations which may speed computation are given below.

In two node curved panels the waves travelling away from the z axis are the mirror images of those travelling towards it. This allows the calculation of one set of waves from the other without recalculating eigenvectors. The mirror image method was implemented in the final code.

Stiffness matrices must be calculated for every element in the model but if there are a number of identical elements in the model then the local stiffness matrix can be duplicated and then rotated to produce the global stiffness matrix using (3.53).

Rotation involves multiplication by rotation matrices which contain a large number of zeros. The 8x8 rotation matrices used with the two node elements contain a particularly large proportion of zeros. A dedicated procedure was written that skips the zeros thereby saving computation time. It is possible that the sophisticated optimisation algorithms used by the compiler may have already eliminated the unnecessary multiplication's from the code during compilation in which case the dedicated procedure is unnecessary.

Rotation of elements is not always necessary as some of the elements may already be aligned with the global co-ordinates. If a number of elements share the same orientation then the global co-ordinates could be rotated so as to align with these elements. This means that only the remaining elements need be rotated, thereby saving computation time.

Equation (3.7) was used to calculate matrix **A**, the element stiffness matrices. Inversion of the **B** matrix requires n Gaussian elimination's so that calculating **A** using (3.7) requires n Gaussian elimination's and one n x n multiplication. Where n x n are the dimensions of the **A**, **B** and **C** matrices. Equation (3.7) may be rewritten as.

$$\mathbf{B}^T\mathbf{A}^T = \mathbf{C}^T \tag{3.71}$$

Calculating the columns of $\mathbf{A}^T$ requires n Gaussian elimination's and we have saved an n x n multiplication. This method will be quicker than using (3.7) as transposition is computationally inexpensive.

There is great potential for future work modelling panel joints using the methods described in this chapter. Orthotropic panels possibly with "smeared" stiffening stringers or corrugation would be useful in treating aircraft, motor-vehicle and building structures. Corrected bending waves Cremer *et al*[1] taking into account out of plane shear deflections may be useful in certain building structures. Fluid loading effects on plate behaviour might be introduced for marine applications. A three or four node solid element could be formulated which would allow construction of more accurate models of rubber window seals, rather than making assumptions such as plane stress or strain. This would require models with a large number of nodes in which case the code may require optimisation to reduce processing time. Mees&Vermier's[10] wave baring elastic layer may be introduced for use in situations where the resonance of this part of the model is important.

The beauty of the wave dynamic stiffness technique is the ease with which elements based on different theory may be assembled together in one model much like FE methods.

Chapter 4

Measurement Procedures

4.1. Introduction

During the course of this work a number of sound and vibration measurements were carried out. The techniques used to take these measurements are presented in this chapter alongside statistical methods for calculating confidence intervals. The individual experiments and results are described in Chapters 5 and 6. The measurements covered in this chapter are panel damping, acoustic reverberation time, mechanical mobility, Acceleration Level, Acceleration Level Difference (ALD) and Sound Pressure Level (SPL).

4.2. Transducers and Instrumentation

Although several different types of measurements are discussed in this Chapter, many use the same transducers and instrumentation so these are described briefly first. Before shipping all the transducers are calibrated by the manufacturers who provide sensitivity factors. In all cases calibration resulted in only very small adjustments of these factors.

4.2.1. Acceleration

Three types of accelerometer were used during the work (B&K4500, B&K4393 and DJB Instruments A/23/E) all are around 2-3g in weight and have a flat frequency response over the measurement range (50-10000Hz). Beeswax was used to attach the accelerometers to the structure during measurement. Accelerometer signals were fed into a B&K2635 charge amplifier from which the signal was fed into the measuring instrument. A B&K4294 calibrator was used before each measurement, this provides a 10 m/s^2 reference acceleration in the 160 Hz $1/3^{rd}$ octave band. Acceleration levels are quoted as mean square acceleration in dB re 10^{-12} given by (4.1).

$$L_a = 10\log\left(\left\langle a^2 \right\rangle\right) + 120 \qquad (4.1)$$

Where $\langle a^2 \rangle$ is mean square acceleration. This gives the calibrator reference signal as 140dB re 10^{-12}.

4.2.2. Sound Pressure Level

Sound Pressure Level measurements were made using a B&K4133 microphone which has a flat frequency response within ± 1dB over the measurement range. The microphone was connected to a B&K2804 power supply and the output signal was fed into the measuring instrument. Calibration was carried out before each measurement using a B&K4231 calibrator which provided a root mean square pressure of 1 Pa in the 1kHz 1/3rd octave band or equivalently a Sound Pressure Level of 94dB re 2×10^{-5} N / m^2 given by,

$$\mathrm{SPL} = 10\log\left(\left\langle p^2\right\rangle\right)+94 \tag{4.2}$$

4.2.3. Mobility and Impedance

Structural impedance measurements were made using a B&K8001 impedance head which consists of two transducers built into one. An accelerometer measures the response of the structure and a piezoelectric transducer measures the force applied to it. Both these transducers have a flat frequency response over the measurement frequency range (50-10000Hz). B&K2635 charge amplifiers were used for both signals as with the acceleration measurements. Impedance was also measured using a B&K8202 force hammer and an accelerometer, the force transducer in the hammer has a flat frequency response across the frequency range. Calibration was checked for both methods by measuring the impedance of a known mass which is given by $Z = i\omega$ m.

4.2.4. Measuring Instruments

A Gould1421 two channel storage oscilloscope was used to inspect signals and for general fault finding.

B&K2032 [100]Narrow band dual channel Analyser: This instrument was used for measuring impedances, it is capable of time windowing the signals and has numerous other features the majority of which were not used. This analyser has a IEEE-488 bus which allowed the data to be transferred to a PC.

B&K2131 [101] Single channel 1/3rd octave band analyser: This instrument was used for recording ALD and SPL signals and is equipped with an IEEE-488 bus for transferring the data to a PC. The analyser can also be controlled by the PC over the bus. By controlling two of these analysers using a PC it was possible to take simultaneous level measurements of two signals.

B&K2148 [102] Portable two channel analyser: Used for damping, ELD and SPL signals. This analyser has a IEEE-488 bus but the software required to transfer data to the PC was not available so floppy disks were used instead.

IBM compatible PCs were used to down load and process data from the analysers. Statistical parameters such as standard deviation and confidence intervals were calculated using the PCs.

4.3. Statistics and Confidence Intervals

Whenever experimental measurements are made it is important to know how repeatable the results are. This knowledge is gained by experience of similar measurements or by repeating the measurement several times and examining the distribution of the results. There are two issues here, the first concerns the accuracy with which the required parameters can be measured and the second concerns the likely variance of the parameters which may be expected because SEA is a statistical theory. This Chapter is concerned with the accuracy of measurements, the accuracy or confidence in SEA predictions has already been discussed in Chapter 2.

SEA has been used in this work to predict energy levels and energy level differences in panels and acoustic subsystems. While it should be possible to compare measured and predicted variance and probability distributions only measured and predicted mean values are compared in this work. Without accurate knowledge of the mode shapes of a structure or acoustic space the vibration levels must be measured over many positions in order to calculate the energy level for a panel. In a panel with evenly distributed mass the energy is given by multiplying the mass by the mean square velocity as in (2.53). Mean square velocity is the mean of an underlying distribution which is sampled every time a measurement is taken. The sample mean $\bar{x}$ of n samples is given by,

$$\bar{x} = \frac{1}{n}\sum_{j=1}^{n} x_j \tag{4.3}$$

The variance of the underlying distribution is unknown but may be estimated by the sample variance, s^2 which is given by,

$$s^2 = \frac{1}{n-1}\sum_{j=1}^{n}\left(x_j - \bar{x}\right)^2 \tag{4.4}$$

Noise and vibration measurements within a subsystem were assumed to be normally distributed when expressed in dB after Lyon & DeJong[36]. C(95%) is known as the 95% confidence interval, it is defined such that there is a 95% chance that underlying mean is within ±C(95%) dB of the sample mean. If n samples of a normally distributed variable are taken then C(95%) is given by.

$$C(95\%) = \frac{s\, t(0.975,\, n-1)}{\sqrt{n}} \tag{4.5}$$

Where $t(0.975,\, n-1)$ is the value of the Student t-distribution function with degrees of freedom = n-1 (see Kreyszig[103]). As $n \to \infty$ $t(0.975,\, n-1) \to 1.96$ and the confidence intervals can be related to the sample variance by a simpler relationship, $C(95\%) = 1.96\, s / \sqrt{n}$. This expression indicates that the confidence limits reduce toward zero as the number of samples increase toward infinity. Confidence intervals were calculated for each 1/3rd octave frequency band as the data was being collected, generally sampling was continued until an acceptable 95% confidence interval was achieved in most frequency bands. When calculating ALDs and ELDs the difference in dB was calculated and its mean and confidence intervals then calculated as described. Some times acceleration or sound pressure levels in a few 1/3rd octave bands would fall outside the dynamic range of the analyser or below the back ground noise level. When this occurred the software used to process the results would ignore those frequency bands. The number of samples, n can therefore vary between 1/3rd octave bands.

4.4. Sound Pressure Level

During this work a Nissan Micra motor vehicle was studied, the results are presented in Chapter 6. SPLs resulting from engine noise were measured. SPLs were measured in the saloon, boot, engine compartment and underneath the vehicle. One occupant was inside the car to adjusted the engine speed to the required level using the accelerator while the measurements were taken. Tests were done at three engine speeds: 700, 3000 and 5700 rpm which were measured using the rev-counter provided with the vehicle. The microphone signals were linearly averaged for 16 seconds using a B&K2131 1/3rd octave band analyser. The analyser was controlled via the IEEE-488 bus by a PC which stored the data in 1/3rd octave frequency bands. The microphone was placed in a stand and positioned randomly in the cavity being measured. In the saloon SPLs measured at 6 microphone positions were averaged giving C(95%) intervals shown in Fig. 4.1.

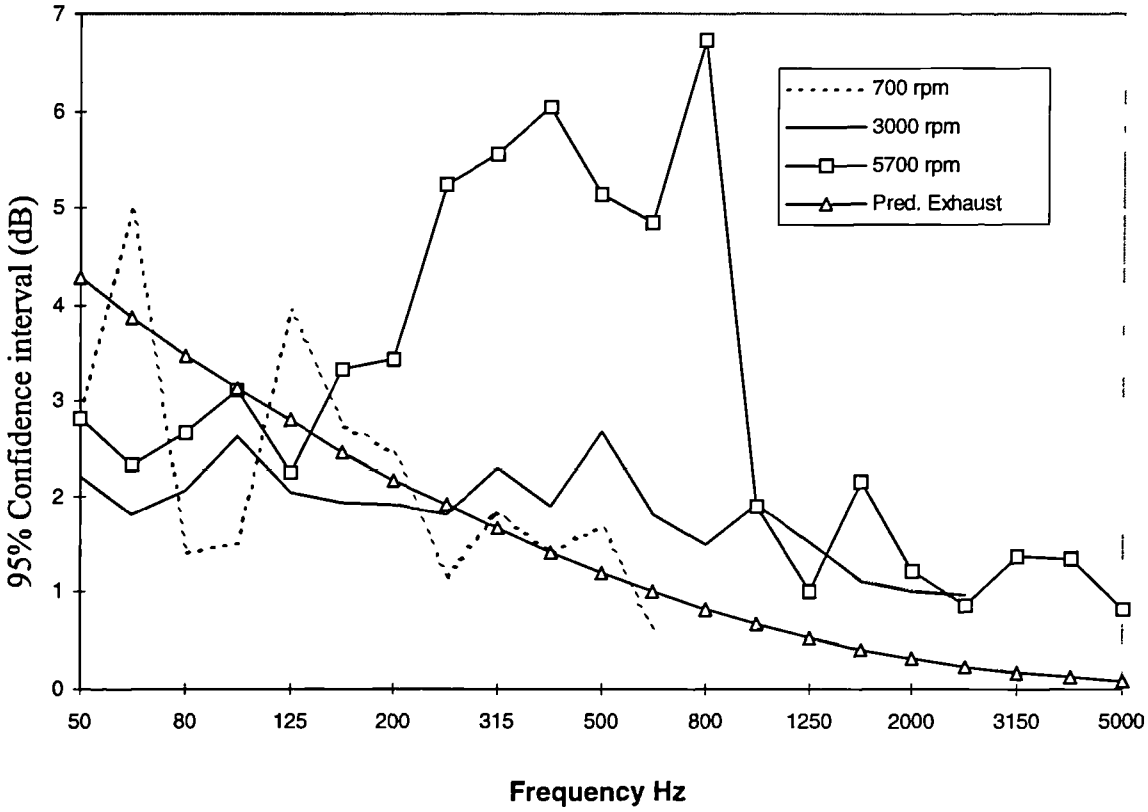

Figure 4.1: C(95%) confidence intervals for SPL measurements in the saloon of Nissan Micra with front exhaust mounts connected.

As can be seen from Fig. 4.1 most of the 95% confidence intervals are smaller than ± 4dB and ± 3dB for 700rpm, 3000rpm respectively. The confidence intervals for the SPLs measured at 5700rpm are larger than those measured at the lower engine speeds between 250Hz and 800Hz having an average value of ± 5.6dB within this range, outside this frequency range the average value is ± 2.0dB. The solid curve with triangular markers shown on Fig. 4.1 is the predicted C(95%) intervals for saloon SPL due to power injected at the front exhaust mounts into the floor panels. The contribution to the predicted saloon SPL variance from uncertainty in the power injected at the front exhaust mounts was neglected because power was calculated from the measured mobility and acceleration levels. Only the variance in the CLF between the floor panels and the saloon are included in the predicted C(95%) confidence intervals. SPL variance due to CLF fluctuation was calculated using equations (2.69) and (2.71) given that the saloon is irregular in shape and that the floor panels are nearly rectangular. This gives the modal shape factor, $\langle \psi^4 \rangle / \langle \psi^2 \rangle^2$ equal to 1 and 3 for the floor panels and the saloon respectively. The predicted confidence intervals shown in predicted Fig. 4.1 do not have the same meaning as those calculated from the measurements. If a large number of nominally similar Nisan

Micras had the same amount of power injected into the front exhaust mounts and the resulting saloon SPLs were averaged for a very large number of microphone positions in each car, then one would expect 95% of these average SPLs to lie within the SEA predicted SPL ± the predicted C(95%) intervals in Fig. 4.1. Naturally this assumes that the SEA model is a valid representation of the average car. In contrast the confidence intervals calculated from the measured data which are shown in this Chapter are an indication of how accurately a spatially averaged SPL or ALD has been measured in the particular vehicle or apparatus used in the test. Therefore it is best to regard the predicted confidence intervals as an indication of the certainty with which SEA can predict a particular SPL or ALD and the confidence intervals calculated from the measurements as an indication of how accurately a particular SPL or ALD has been measured. Saloon SPL was also measured with front exhaust mounts disconnected giving the C(95%) intervals shown in Fig. 4.2.

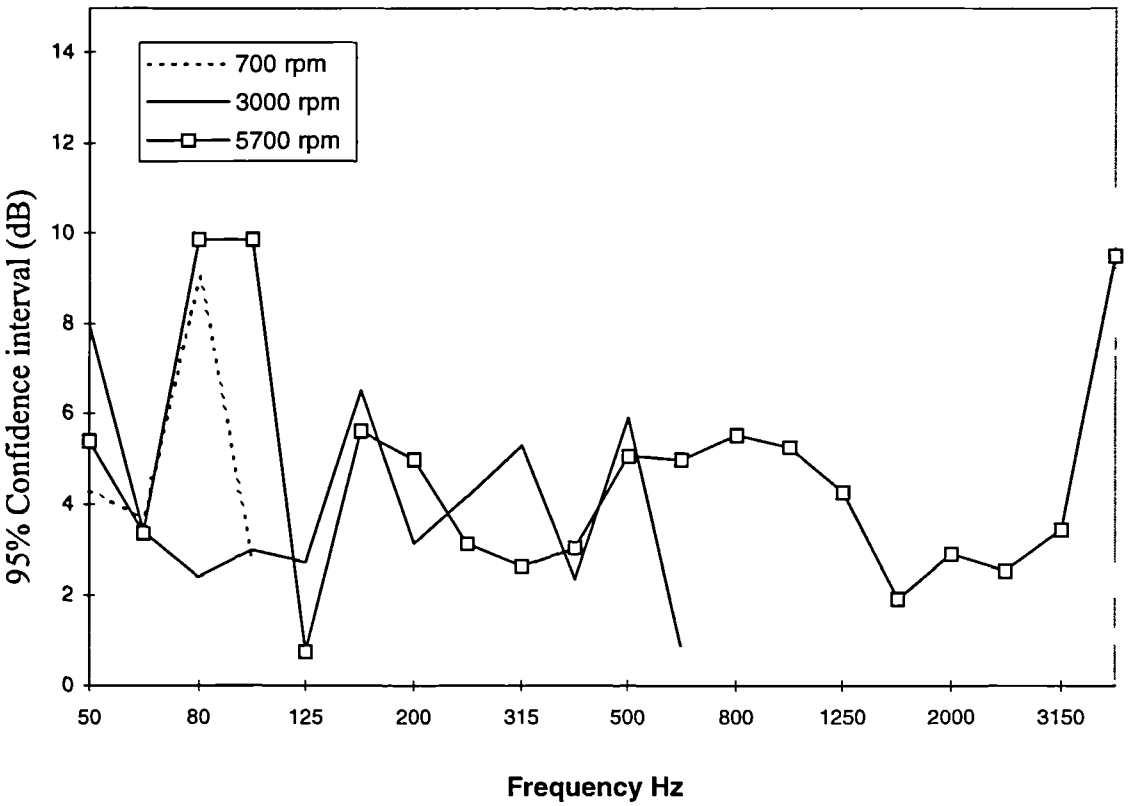

Figure 4.2: Micra saloon SPL C(95%) confidence intervals with front exhaust mounts disconnected.

Fig. 4.2 shows that the C(95%) intervals are usually smaller than ± 5dB for the three engine speeds. The C(95%) intervals for the Micra saloon SPL with the engine running at 3000rpm have been omitted from Fig. 4.2 above 630Hz because some of the values were

excessive. The large confidence intervals above 630Hz occurred because there were only two samples in each frequency band above this frequency. If there are only two good samples then $t(0.975, n-1)$ from the Student t-distribution function has a value of 12.7 which gives rise to very large confidence intervals from equation (4.5). The C(95%) confidence intervals with the front exhaust mounts disconnected are generally smaller than when they are connected between 125 and 800Hz if the engine is running at 5700rpm. This is the case despite the fact that more measurements were made with the mounts connected than with them disconnected. In Chapter 6 it is shown that between 250Hz and 1000Hz at 5700rpm the SPL in the saloon is caused primarily by the power injected into the floor of the vehicle at the front exhaust mounts. This means that the predicted confidence intervals shown in Fig. 4.1 by the triangular markers represent the predicted 95% confidence intervals in the total saloon SPL between 250Hz and 1000Hz when the engine speed is 5700rpm. Large confidence intervals suggest that the sound field caused by the excitation of the floor at the exhaust mounts could be of a direct non reverberant type. A direct non reverberant sound field would give rise to a high degree of variability in SPLs measured at different positions within the saloon and thereby produce large C(95%) intervals. If this were the case however one might expect all the noise sources to cause a non reverberant field in the saloon and therefore produce large confidence intervals but this was not the case. It is possible that the power injected into the front exhaust mounts causes radiation from a small area of the floor near the mounts which is why it produces higher variance in the saloon SPL than the other sources. Another possible cause of high variance in the saloon SPL resulting from the exhaust mount power input could be higher sensitivity to engine speed at 5700 rpm. If a distinct resonance or resonances in the exhaust system cause the increased saloon SPL at 5700 rpm then it could be that the level of this resonance is very sensitive to engine speed. The engine speed was manually controlled using the accelerator pedal and the rev-counter whilst measuring SPL at each microphone position.

In the engine compartment 8, 4 and 4 microphone positions were used at 700, 3000, 5700rpm respectively giving C(95%) intervals shown in Fig. 4.3.

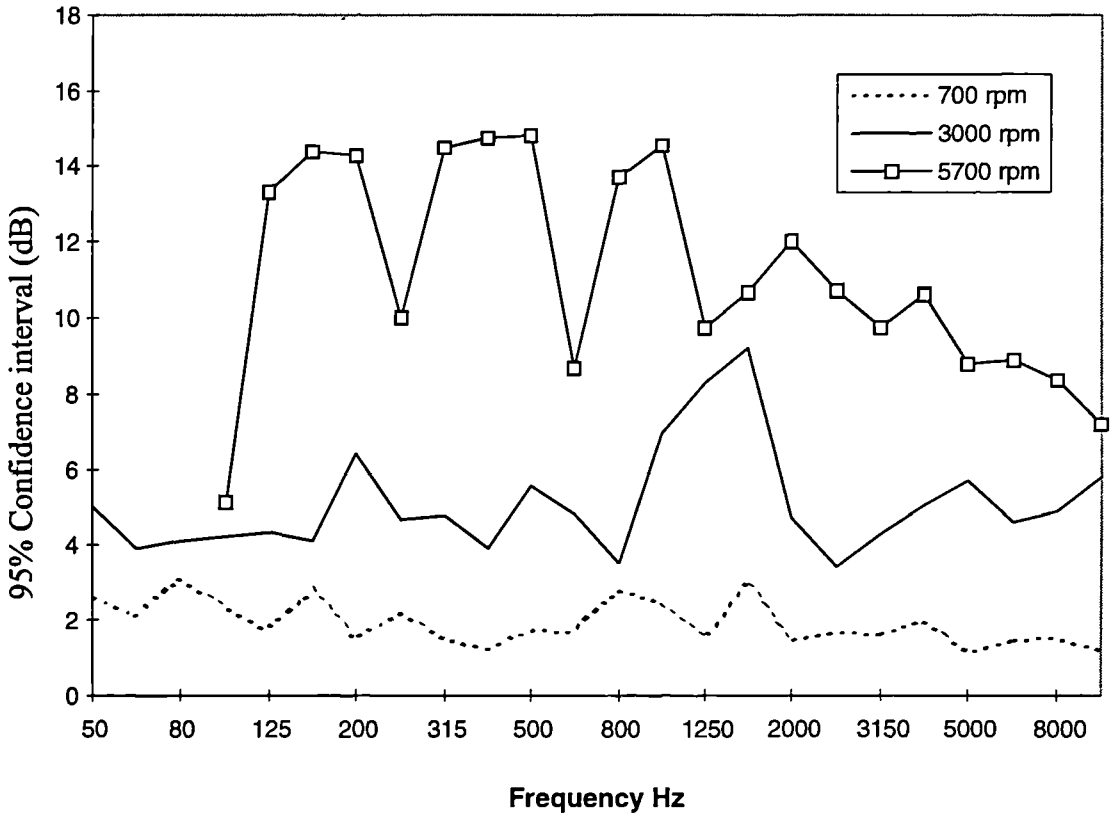

Figure 4.3: Micra engine compartment SPL C(95%) confidence intervals.

SPL C(95%) confidence intervals in the engine compartment are mostly less than ±3dB, ±5dB, ±11dB at 700, 3000 and 5700rpm respectively over the frequency range shown. Eight microphone positions were used at 700rpm, four were used at 3000 and 5700rpm. The sample variance and therefore the confidence intervals are larger when the engine is running at 5700rpm than 3000rpm or 700rpm. The engine is a complex system of moving parts and it is not clear why the spatial variance of SPL in the engine compartment is higher when the engine is running at 5700rpm than when it is running at 3000rpm. The high SPL variance with position in the engine compartment at 5700rpm may also be caused by an increased sensitivity to engine speed at 5700rpm as discussed in the paragraph above.

Acoustic subsystem energy may be calculated from the spatially averaged Sound Pressure Level using equation (2.56). Acceleration Levels were measured on various parts of the vehicle body at the same time as the SPLs. This was done by controlling two analysers with a PC via the IEEE-488 bus as shown in Fig. 4.4.

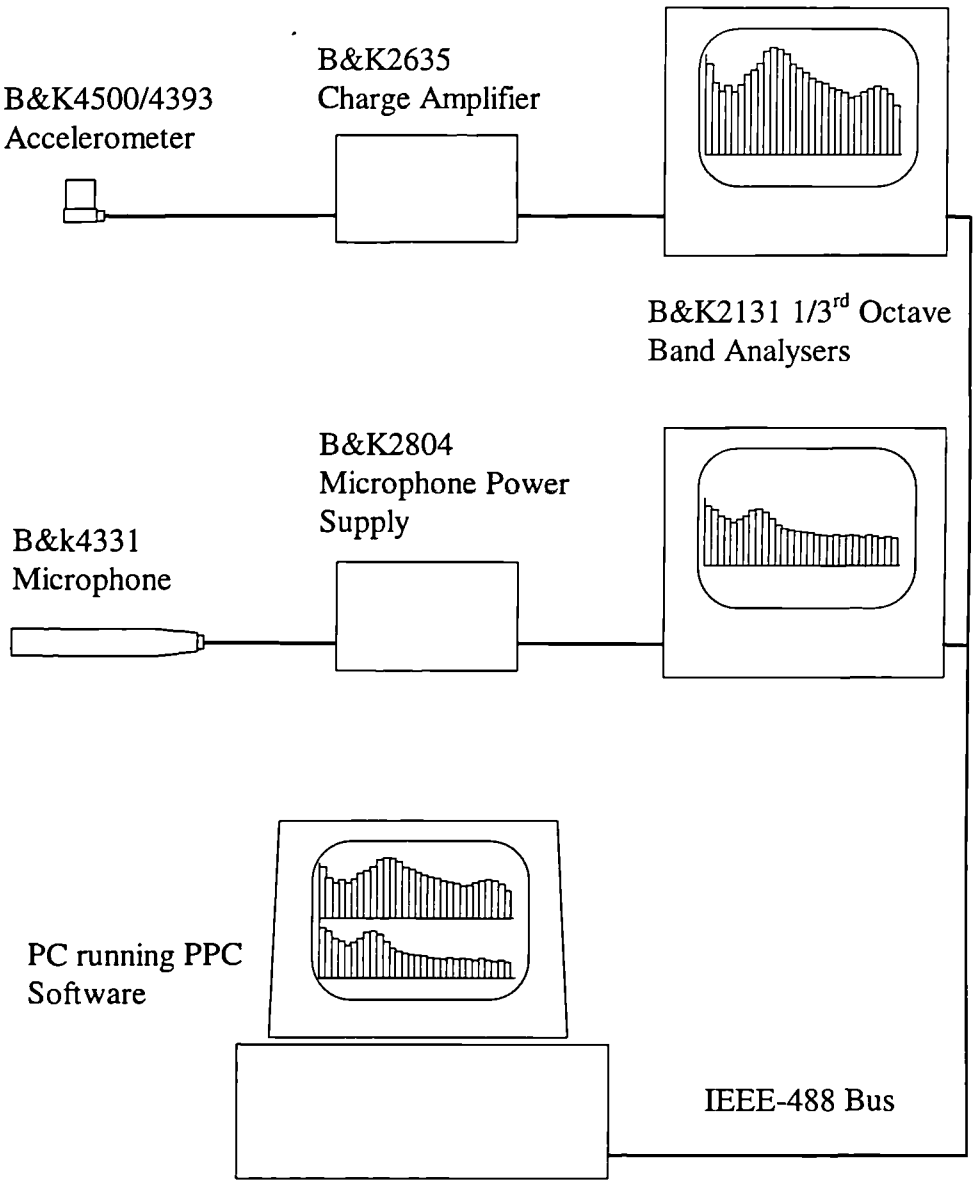

Figure 4.4: Transducers and instrumentation for measuring acceleration and SPL simultaneously: Two analysers controlled by a PC.

4.5. Acceleration Level

Acceleration levels of engine and exhaust mounts in the Micra were measured at the three engine speeds (700, 3000, 5700rpm). Accelerometers and charge amplifiers were used in place of microphones and pre amplifiers but the measurements were otherwise identical to those described above for SPL. Engine and exhaust mount acceleration are discrete point measurements and so space averaging is not relevant, linear time averaging was carried out by the analyser for 16 seconds. Mount acceleration levels were used in conjunction with the measured mobilities for predicting power inputs to the SEA models of the Micra

described in Chapter 6. These models were used to predict the saloon SPL so it is important that the measured mount accelerations are close to those that existed when the saloon SPLs were measured. The correspondence between acceleration and SPL was improved by measuring both simultaneously as shown in Fig. 4.4.

4.6. Damping

Damping measurements were carried out on panels and on acoustic spaces both using the reverberation time technique.

4.6.1. Acoustic Reverberation Time

In the Micra study of Chapter 6 a number of acoustic reverberation time (T_{60}) measurements were carried out. A microphone was used to measure the sound level with a microphone power supply. The signal was fed into a B&K2148 analyser which recorded a number of consecutive spectra and there by recorded the decay in each $1/3^{rd}$ octave frequency band. Excitation was provided by a speaker and a white noise source, the analyser was triggered to start recording after the source was stopped. The number of consecutive spectra recorded by the analyser could be adjusted as could the sampling interval for each spectra. There are two practical limits on the interval time. As the interval becomes shorter the lowest frequency that can be measured in each spectrum increases. The reciprocal of the time interval gives the approximate low frequency limit. It is not possible to accurately measure the decay if the time intervals are to large in relation to the duration of the decay. Typically 100 spectra were recorded for each decay and this gave sufficient resolution to determine the slope of the curve as shown in Fig. 4.5. In this case the time interval was 0.002 s.

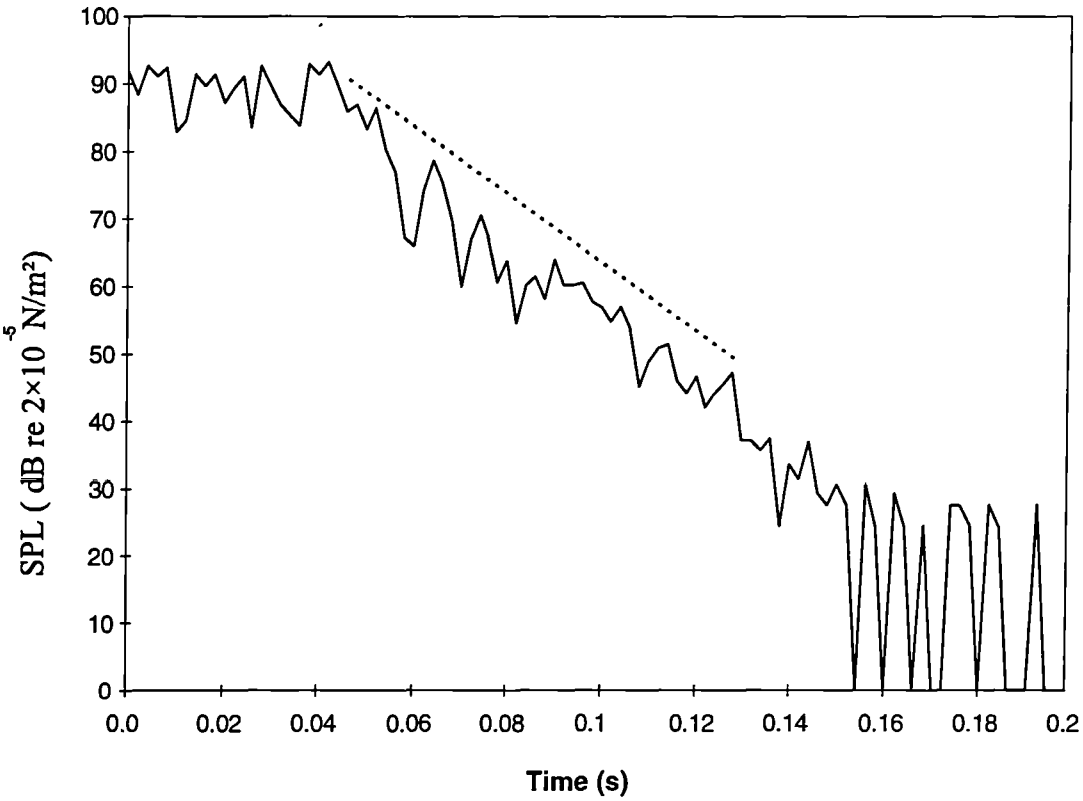

Figure 4.5: SPL decay in Micra saloon at 2500Hz also showing straight line fit.

Fig. 4.5 shows a SPL decay curve from the saloon of the Micra at 2.5kHz along side the straight line fit from a computer program for processing the results. The level is fairly constant until the source is stopped at around 0.04 seconds, it then decays linearly until reaching the back ground noise level. T_{60} for this curve is approximately 0.12s. It is common place to quantify the damping of acoustic spaces using the reverberation time but this may be converted into a loss factor using equation (2.35) giving a value of 0.0073 or 98.6 dB re 10^{-12} from equation (4.6).

$$\eta \text{ (dB)} = 10 \log\left(\frac{2.2}{f\, T_{60}}\right) + 120 \tag{4.6}$$

Acoustic damping was measured with a number of microphone and speaker positions to get a modal average. Eight microphone positions and eight speaker positions were used when measuring damping in the Micra saloon. C(95%) confidence intervals for saloon damping are shown in Fig. 4.6.

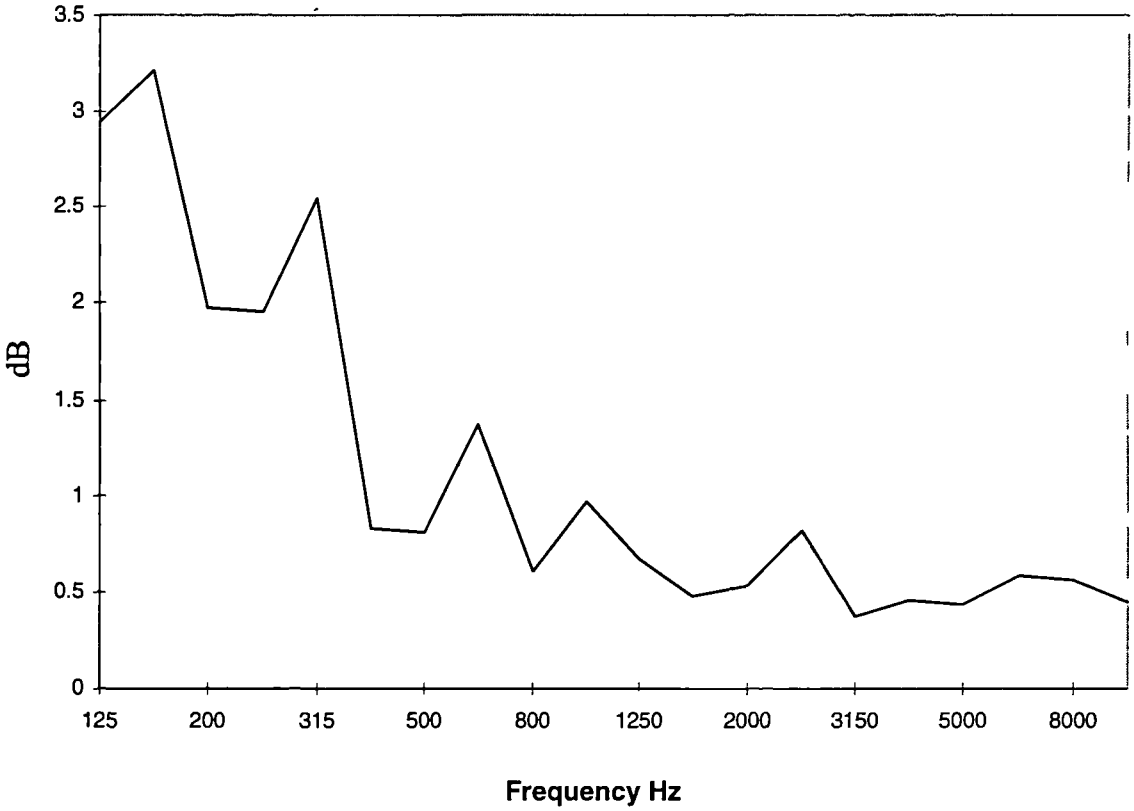

Figure 4.6: C(95%) confidence intervals for measured acoustic damping in the Micra saloon.

Over the majority of the frequency range the 95% confidence intervals for saloon damping are below ± 1dB.

4.6.2. Panel Damping

Panel damping was measured during the work on the Micra which is presented in Chapter 6 and also in the study of rounded corner joints in Chapter 5. A reverberation time technique was used as in the acoustic measurements. Mean square acceleration was measured using an accelerometer attached to the panel, excitation was provided by hitting the panel with a hammer. The signal was fed into the B&K2148 analyser which was set up in the same way as in the acoustic tests except for the triggering. When the acceleration level exceeded a selected level the analyser triggered, a certain "pre-trigger" was set so as to record a few spectra before the decay as can be seen in Fig. 4.7.

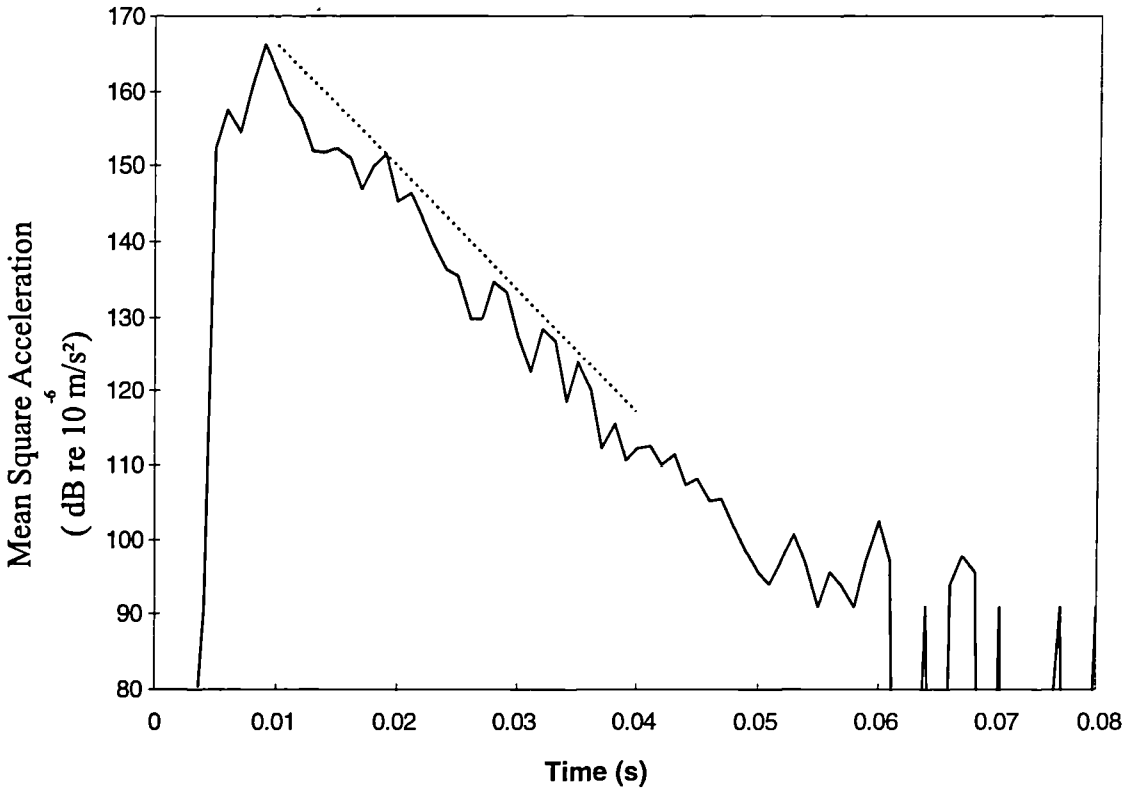

Figure 4.7: Acceleration level decay on damped 2mm steel panel at 2500Hz also showing straight line fit.

Fig. 4.7 shows the decay on a damped 2mm panel from the study in Chapter 5 the time interval is the lowest the analyser will allow at 0.001s. The level falls down into the background noise and the trace becomes intermittent because some of the spectra drop out of the dynamic range and the analyser sets them to zero. Panel damping is usually given as a loss factor which may be calculated from T_{60} using (2.35). It is also common to write the loss factor in dB re 10^{-12} using equation (4.6). The straight line approximation in Fig. 4.7 gives a value of 104dB. Decay measurements were taken at a number of randomly chosen accelerometer positions on each panel. The impulse position was also randomly applied at different positions on the panel. 20 measurement positions were used in the rounded corner joint study giving the C(95%) intervals shown in Fig. 4.8.

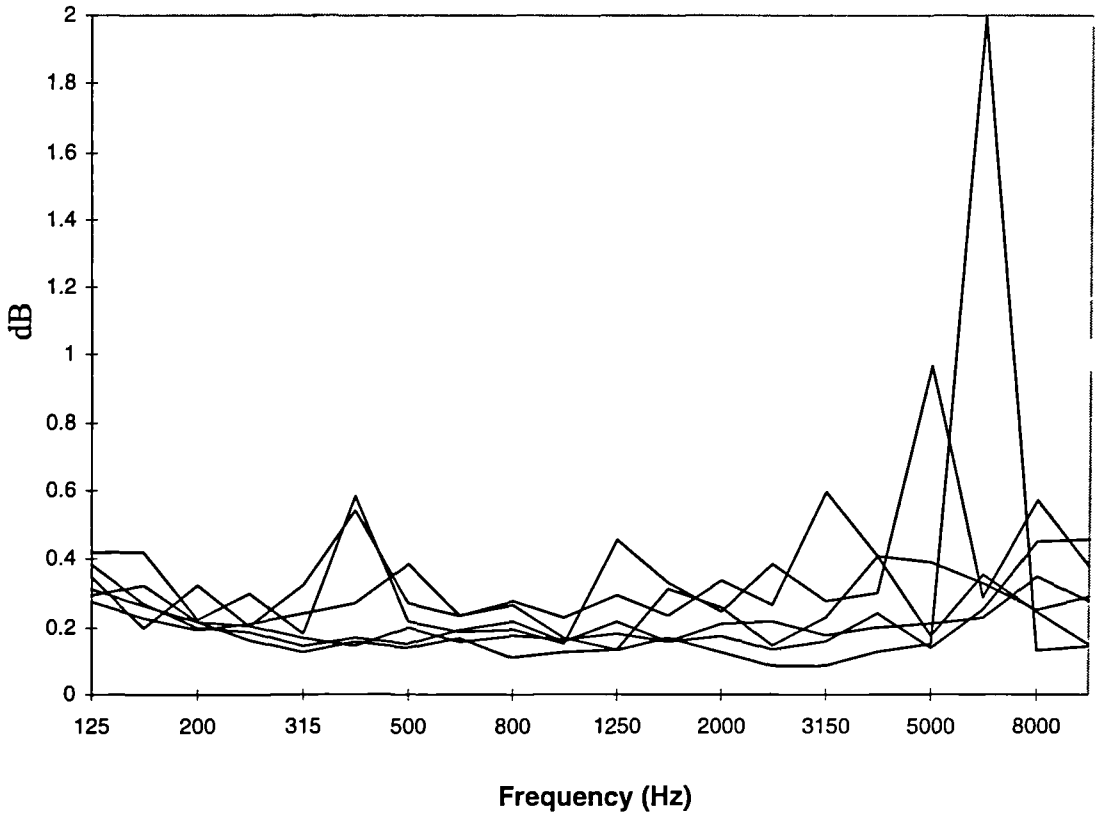

Figure 4.8: C(95%) intervals for panel damping measurements from curved panel joint study in Chapter 5.

The 95% confidence intervals for the damping of all the panels in the curved joint study (Chapter 5) are shown in Fig. 4.8, and are typically below ±0.4dB.

Panel vibration decay in the Micra study (Chapter 6) was measured at approximately 6-8 positions per panel. Fewer positions per panel were used in the Micra study than in the curved joint study because of the large number of panels in the Micra. This resulted in larger confidence intervals. A selection of typical 95% confidence intervals for Micra panel damping measurements are shown in Fig. 4.9.

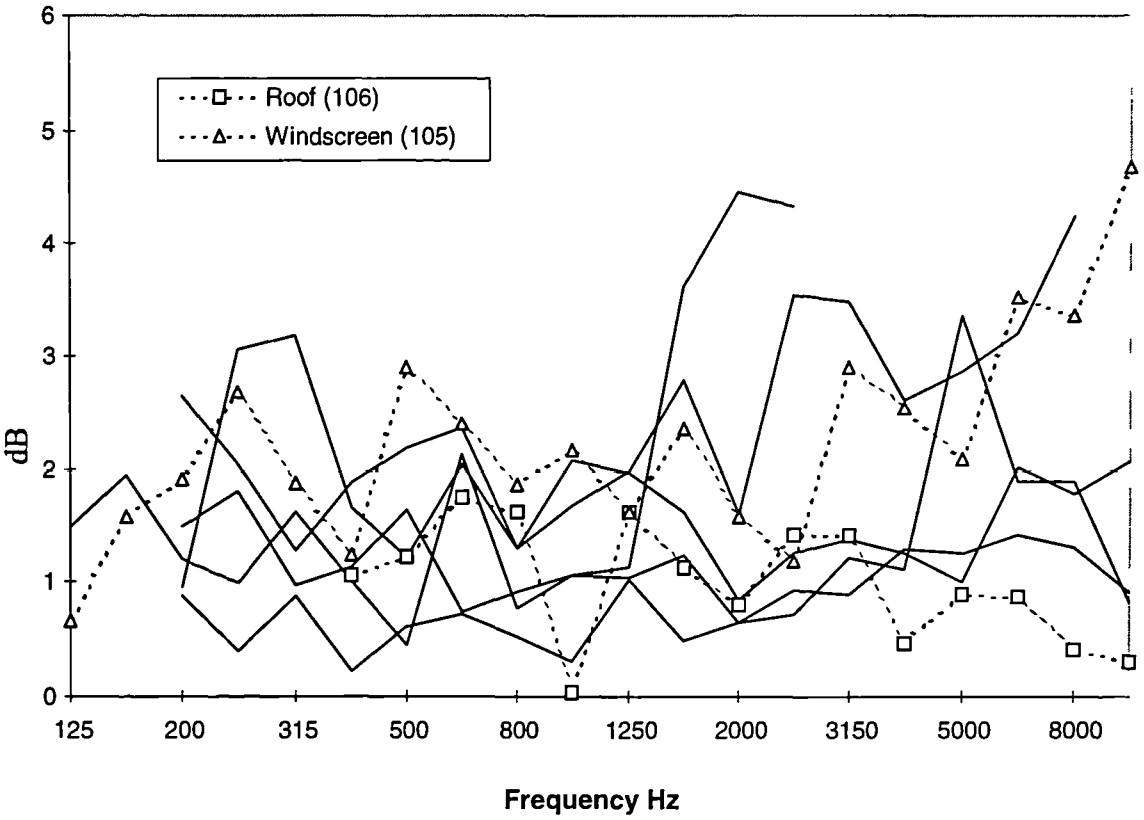

Figure 4.9: A selection of C(95%) confidence intervals for Micra panel damping measurements.

The 95% confidence intervals for the roof and windscreen of the Micra are identified on Fig. 4.9. by square and triangular markers respectively. Micra panel damping confidence intervals shown in Fig. 4.9. are typically less than ± 4dB. Three data points have been omitted from Fig. 4.9. because there values were excessive. The reason for these large confidence intervals stems from the methods used to process the decay results. A computer program was used to calculate the damping from the slope of the decay curves. When there was insufficient decay for the program to calculate damping it ignored the data from that measurement position. If, for example there are only two good samples then $t(0.975, n-1)$ from the Student t-distribution function has a value of 12.7 which gives rise to very large confidence intervals using equation (4.5).

4.7. Acceleration and Energy Level Difference

Panel acceleration level differences were measured by using an accelerometer on the source panel and one on the receiving panel. Two sets of instrumentation were used both linearly averaged the acceleration levels in $1/3^{rd}$ octave frequency bands for 16 seconds while the source panel was tapped randomly over its surface with a hammer. The first set-

up used two B&K2131 analysers and a PC. These analysers have only one channel so they were controlled via the IEEE-488 bus by the PC which synchronised the averaging and stored the data. This set-up is identical to that shown in Fig. 4.4 except that both channels were used to measure acceleration with one accelerometer on the source panel and the other on the receiving panel. A B&K2148 analyser was also used to record ALDs in 1/3rd octave frequency bands. This analyser has two channels so computer control was not necessary, in this case data was transferred to PC via floppy disk. The measurement procedure was as follows.

a) Randomly position the two accelerometers, one on the source panel and the other on the receiving panel. The accelerometers should be further than roughly ¼ of the bending wavelength from the nearest boundary, this reduces the contribution to the measured response from the bending near fields at the boundaries.

b) Start the analyser/s recording the two acceleration signals and tap the source panel randomly over its surface for around 15 seconds. The analysers were set to average the signals for 16 seconds which gives the vibrations a second or so to decay before the analysers stop. This reduces the errors from spectral leakage (See [100]). This method typically resulted in around 30-40 hammer excitation positions for each of the accelerometer positions. Whilst tapping the panel care was taken to avoid the accelerometer by a sufficient distance to prevent saturating the acceleration signal or measuring a significant contribution from the direct field close to the hammer. Typically this distance was around 100-150mm in the tests described in this Chapter.

c) Record the time averaged acceleration levels (L_a in equation (4.1)) from the source and receiver accelerometers and take the difference between the two. Add the acceleration level difference to the sum and recalculate the sample mean and sample variance for the ALDs using equations (4.3) and (4.4) respectively. Then calculate the 95% confidence intervals for the mean of the ALDs using (4.5). Repeat a), b) and c) until the required number of positions have been completed or until the desired statistical confidence has been achieved.

In the Micra study 10 accelerometer measurement positions were typically used per panel giving the C(95%) confidence intervals shown in Fig. 4.10. for the mean ALDs.

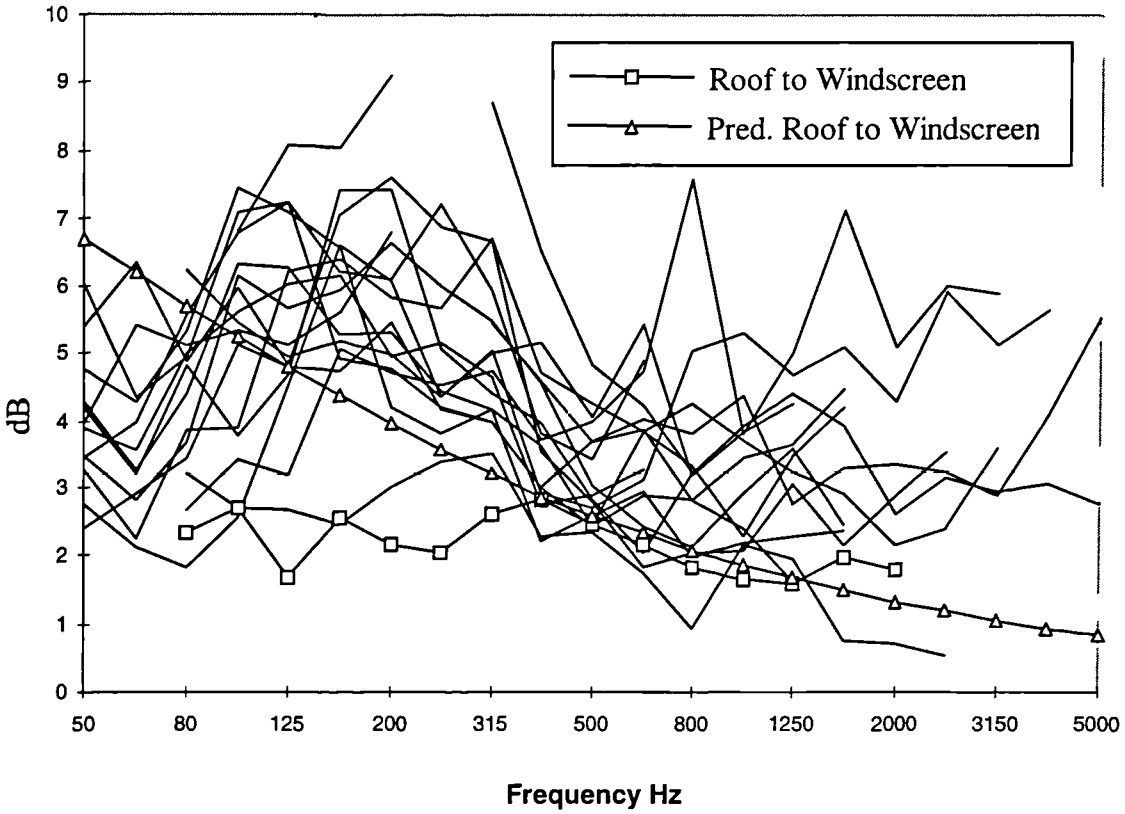

Figure 4.10: C(95%) confidence intervals for panel ALDs measured during the Micra study in Chapter 6, also showing predicted C(95%) confidence interval for roof to windscreen ALD.

Fig. 4.10 Shows the C(95%) intervals for all the panel ALDs measured during the Micra study (Chapter 6). The average starts at approximately ±4dB (50Hz) rising to around 6dB (125Hz) before falling to around ±3dB by 2kHz. The low level at 50Hz is probably due to the lack of resonant response in many of the panels at low frequency. Larger intervals at around 125Hz are probably the result of high variations in response with position because of the scarcity of resonant modes in each $1/3^{rd}$ octave band at these frequencies. As the modal overlap and number of modes in each band increase with frequency the response variance and the C(95%) intervals reduce. Fig. 4.10 also shows a line with square markers which is the curve for the roof to windscreen ALD confidence interval which is lower than average at around ± 2dB over the entire frequency range. Roof to windscreen ALD exhibits less variance with position, probably because of the high modal density of the roof and windscreen. The solid line with triangular markers shown on Fig. 4.10 is the predicted C(95%) confidence intervals for the SEA predicted ALD between the roof and the windscreen. These values were calculated using equations (2.69) and (2.71) assuming that the roof and windscreen panels are irregular in shape which gives modal shape factors

equal to 3 for both panels. The predicted curve has a different shape to most of the values calculated from the measurements at low frequencies. This is probably because the prediction assumes resonant response even at very low frequencies where as the real subsystems do not resonate significantly below there first natural frequency.

During the curved joint study (Chapter 5) structural attenuation was expressed as Energy Level Differences rather than ALDs. The ELD is given by adding ten times the logarithm of the panel mass ratios to the ALD as shown in (4.7).

$$\mathrm{ELD} = 10\log\left(\frac{\langle a_r^2\rangle m_r}{\langle a_s^2\rangle m_s}\right) = \mathrm{ALD} + 10\log\left(\frac{m_r}{m_s}\right) \tag{4.7}$$

From this equation we can see that the C(95%) confidence intervals for a measured ELD is equal to that of the ALD when expressed in dB provided the panel masses are regarded as constants rather than statistical variables. Panel ALDs were measured using 20 accelerometer positions during the curved joint study giving the C(95%) intervals shown in Fig. 4.11.

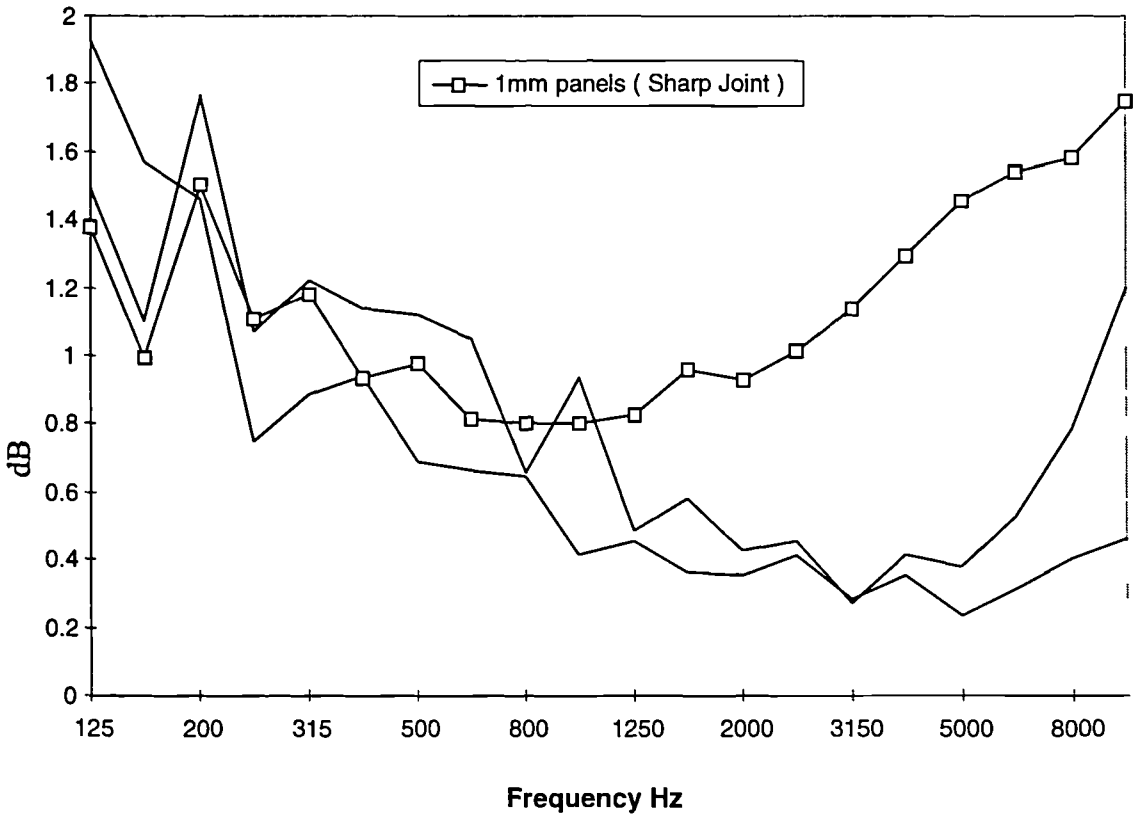

Figure 4.11: C(95%) confidence intervals for measured panel ELDs from curved joint study in Chapter 5.

Fig. 4.11 Shows that all the C(95%) confidence intervals are comfortably below ±2dB over the entire frequency range. The confidence intervals for the 1mm panels connected by a sharp corner joint are identified in Fig. 4.11 with square markers. These are roughly 1dB higher at high frequency than the intervals for the 2mm panels. It is possible that this is due to a less reverberant field in the more heavily damped 1mm panel which would cause a larger variation in measured acceleration with position.

4.8. Impedance/Mobility Measurements

During the Micra study structural mobility of engine and exhaust mounts were measured using an impedance head as shown in Fig. 4.12.

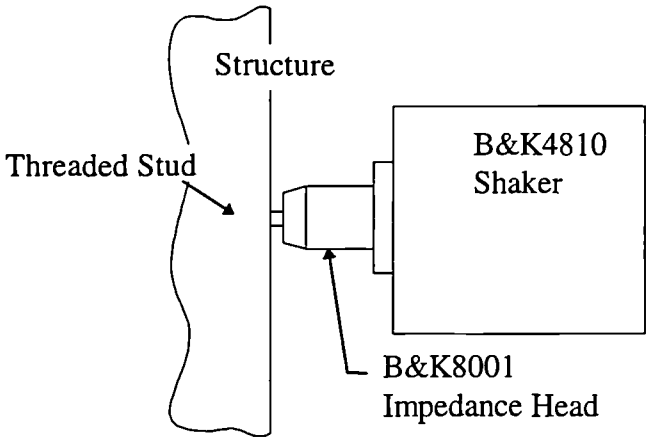

Figure 4.12: Impedance measurement.

Threaded studs were screwed into each end of the impedance head, a B&K4810 shaker was attached to one end. The shaker was held by hand and the stud in the other end of the impedance head pressed against the structure at the measuring point. This method does not damage the car and allows a larger number of measurements than would have been possible if the vehicle body had to be drilled and threaded for every measurement. The threaded stud in contact with the vehicle can loose contact if the force signal generated by the shaker exceeds the pressure applied to keep the stud in contact. Loss of contact was noticeable by a change in the sound emitted by the structure and an increase in the magnitude of the high frequency components of the force and acceleration spectrum. Loss of contact was therefore very noticeable and easily avoided by reducing the shaker signal amplitude. White noise was used to drive the shaker allowing the entire frequency spectrum to be measured at once. Force and acceleration signals were fed into the B&K2032 two channel narrow band analyser and linearly averaged for 16 seconds. The

analyser integrated the acceleration signal to give velocity and returned the mobility of the structure in each frequency band the equation,

$$Y = \frac{v}{F} = \frac{a}{i\omega F} \tag{4.8}$$

Where v, a and F are the complex velocity, acceleration and force. Mobility was measured at engine and exhaust mounts which are reinforced parts of the structure. The engine and exhaust are connected to the mounting brackets through rubber isolators which were left in place during impedance measurements. Forces resulting from engine and exhaust vibration are applied via brackets which spread the load on to the structure. The impedance measurements were taken on these brackets as close to the point of attachment as possible. As exhaust and engine mount mobilities were measured at discreet points averaging in space was not necessary, only in time which was carried out by the analyser. The impedance head was calibrated by attaching a known mass to the threaded stud labelled in Fig. 4.12 as discussed in Section 4.2.3. Impedance measurements were also conducted using a B&K8202 force hammer in conjunction with a separate accelerometer using the arrangement shown in Fig. 4.13.

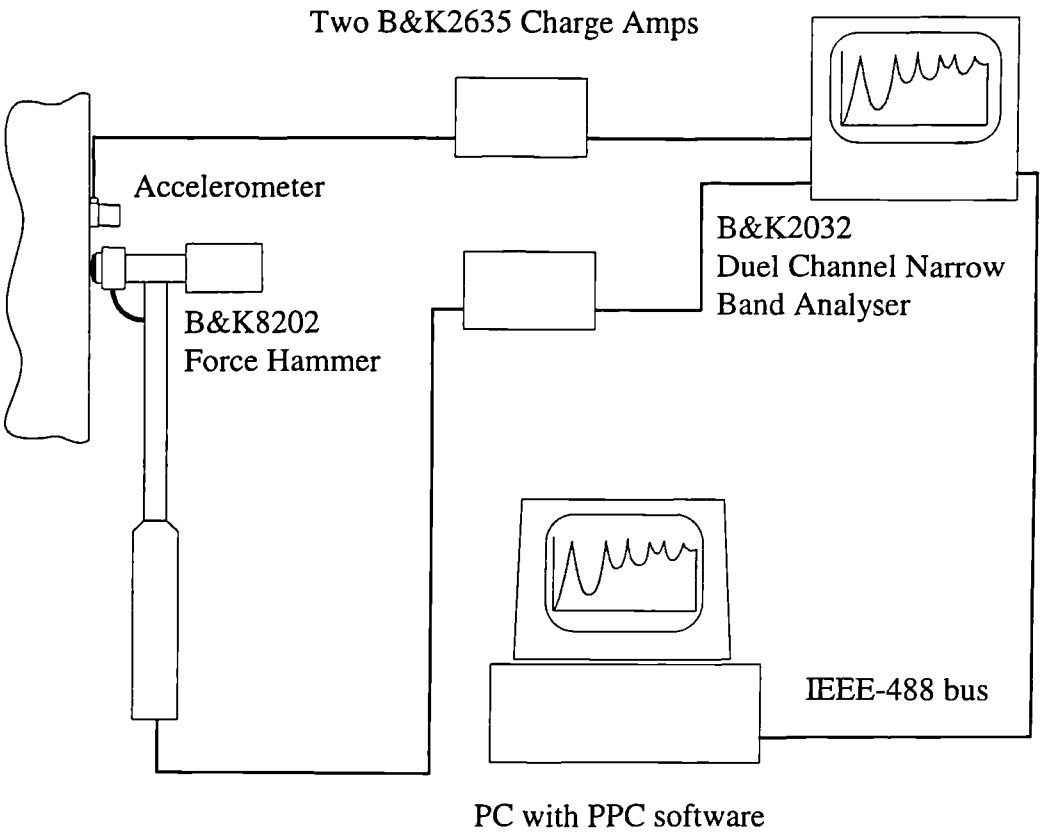

Figure 4.13: Transducers and instrumentation for measuring impedance with hammer.

The B&K2032 analyser allows time windowing of the signals before calculating the impedance. A rectangular time window was used with the force signal so as to cut the signal off when the hammer lost contact with the structure. An exponential window was used with the acceleration signal so as to reduce the magnitude of the signal at the end of the time record. This reduces the erroneous effects of a phenomenon known as spectral leakage (See [100]). The hammer tip may be changed to alter hardness and thereby the input force spectrum. The mass of the hammer may also be adjusted and the two adjustments together used to prevent a double bounce occurring. This arrangement may be calibrated by measuring the impedance of a known mass which is equal to $i\omega$ m, where m is the known mass. Fig 4.14 shows the real part of measured mobility for the roof panel (106) of the Micra motor-vehicle discussed in Chapter 6. The measured values are an average from six measurement positions on the panel made using the shaker method shown in Fig. 4.12.

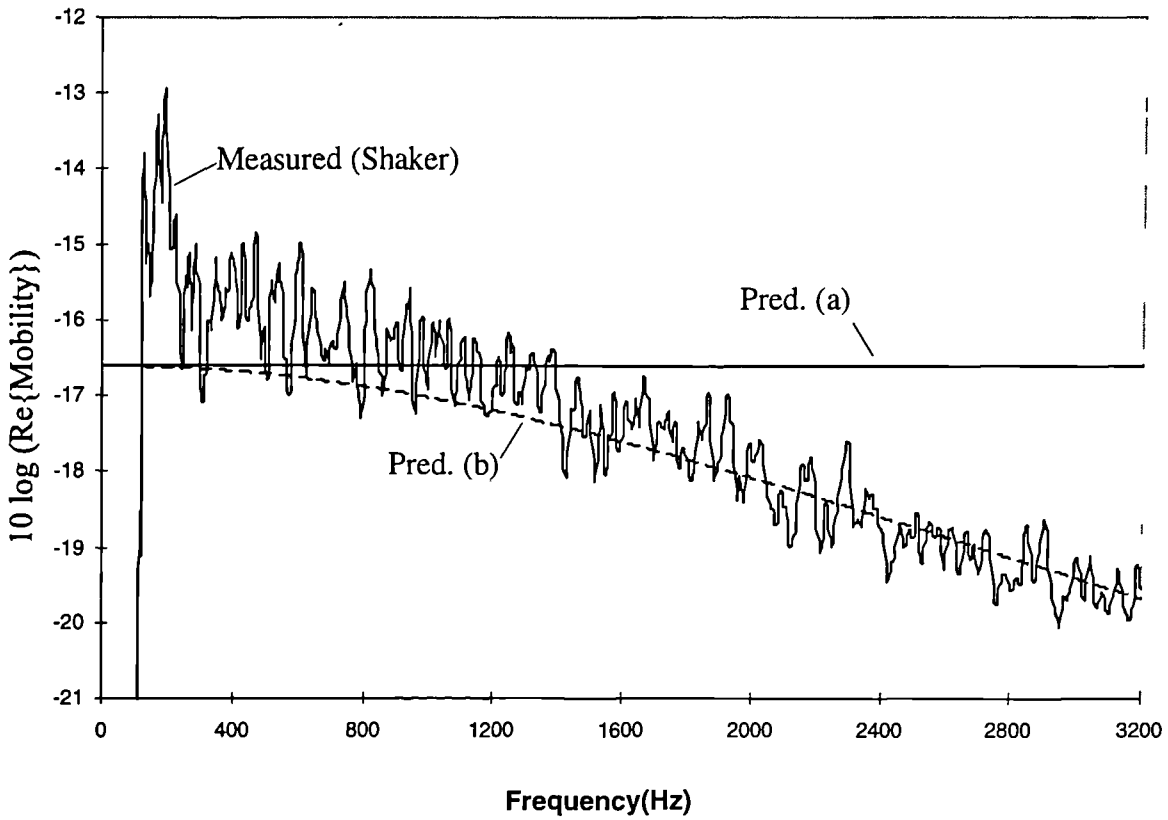

Figure 4.14: Real part of mobility of Micra roof measured using the shaker method plus two predictions. pred. (a): Infinite plate mobility from the reciprocal of Equation (2.27). pred. (b): As (a) but including a mass loading of 2.3g.

Fig. 4.14 shows the average measured mobility of the roof panel alongside two predicted values, all the values are in dB. Prediction (a) is the infinite flat plate mobility given by the reciprocal of Equation (2.27), this gives reasonable agreement (within 3dB) over the entire frequency range. Prediction (b) includes the effect of mass loading caused by the impedance head and the threaded stud used to connect it to the roof and is given by.

$$\mathrm{Re}\{Y_C\} = \frac{Y}{Y^2 + \omega^2 m^2} \tag{4.9}$$

Where Y_C is the predicted mobility of the roof with an additional mass m attached to the point of measurement. Y is the predicted mobility of an infinite flat panel given by equation (2.27) which is real. The size of the additional mass which gave the best match between the measured data and prediction (b) was 2.3g. The Mobility of the roof was also measured using the force hammer method which is shown in Fig. 4.13. Mobility measurements were carried out at six positions on the roof using the hammer and accelerometer, the real part of mobility was averaged and plotted in Fig. 4.15.

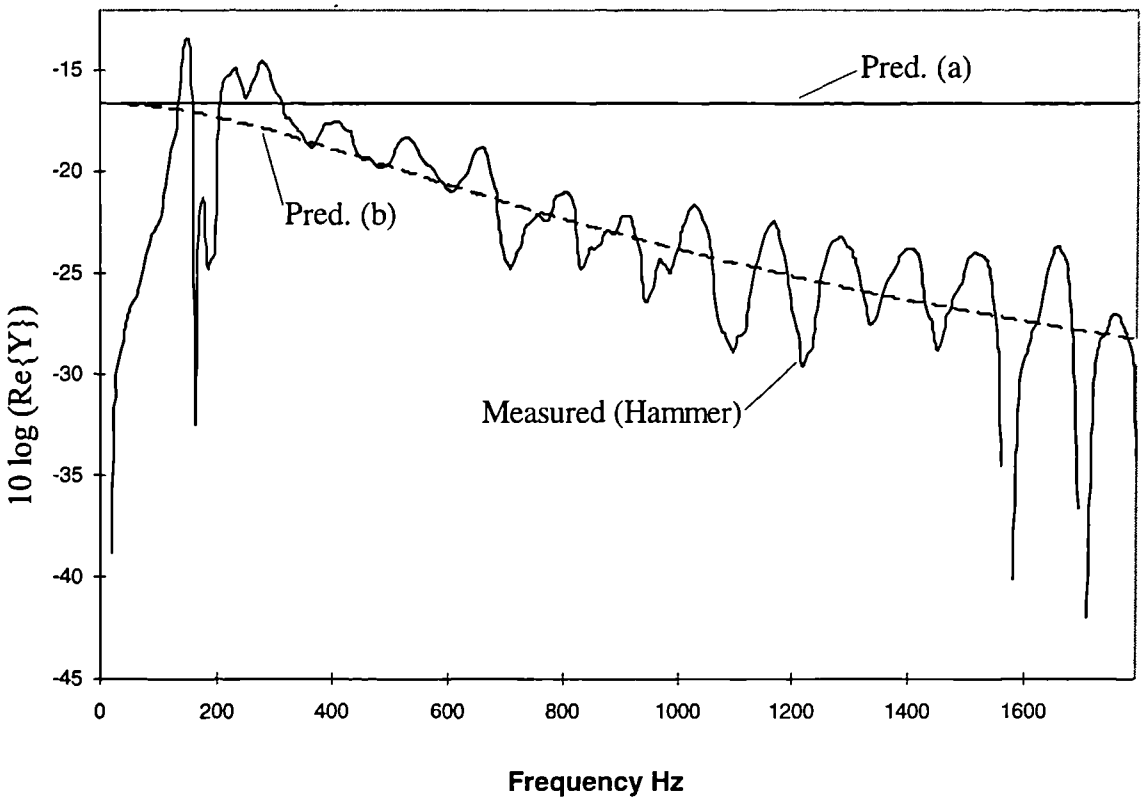

Figure 4.15: Real part of mobility of Micra roof measured using the force hammer method plus two predictions. pred. (a): Infinite plate mobility from reciprocal of Equation (2.27). pred. (b): As (a) but including a mass loading of 15g.

Measured data was only available up to around 2kHz because the force and acceleration signals were insufficient above this frequency. Prediction (a) is the infinite flat plate value and is identical to that shown on Fig. 4.14. Mobility measured using the hammer reduces by around 10dB between 200 and 2000Hz. This is a more rapid decrease than measured with the shaker. Prediction (b) is given by (4.9) with an additional mass of 15g. The mass of the hammer tip was 3.9g. The accelerometer which was attached to the roof had a mass of approximately 3g. Summing the tip and accelerometer mass gives 6.9g which is considerably less than 15g. Mass loading alone cannot explain the downward trend of mobility when measured using the hammer. The roof panel was 0.7mm thick and it was difficult to tap the roof without causing a small but noticeable local deflection of the roof panel. Infinite flat plate impedance given by equation (2.27) was derived assuming small deflections. It is possible that the large deflections caused by the hammer will significantly alter the measured impedance. When using the hammer method the response is not measured precisely where the load is applied. If the deflection of the panel reduces significantly between the loading point and the measuring point then mobilitiess measured

using the hammer will be smaller than the actual mobility. It is possible that one or both of these effects caused the mobility measured using the hammer to drop rapidly with frequency from the infinite plate value. Neither of these effects are likely to significantly influence impedance measurements carried out on engine and exhaust mounting points because these areas are heavily reinforced.

Fig. 4.16 shows the real part of impedance (in dB) measured using the force hammer method at the front right exhaust mount on the Micra.

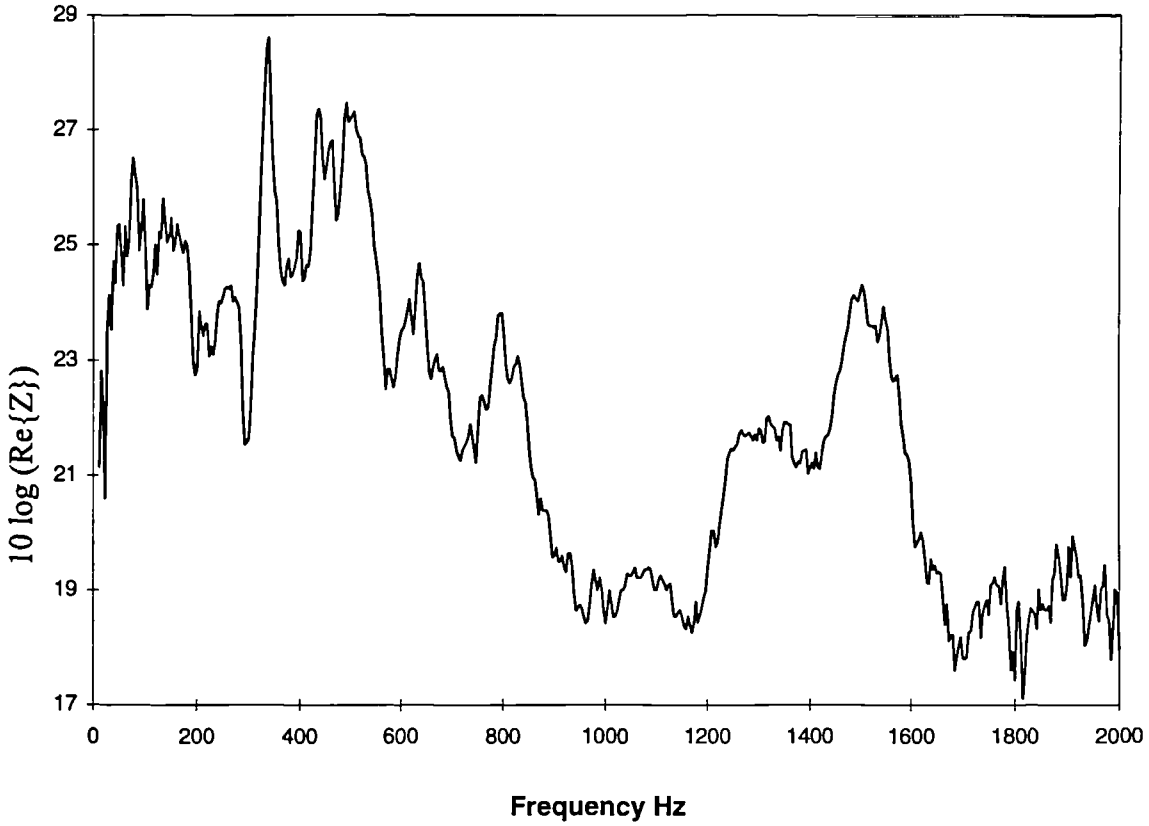

Figure 4.16: Real part of impedance for front right exhaust mount on the Micra. measured using the force hammer method.

This data was averaged in $1/3^{rd}$ octaves and used in equation (2.26) along with the measured acceleration level when the engine was running to calculate the power injected at the exhaust mount.

4.9. Conclusions

A number of measurements have been discussed in this chapter along with the statistical methods used to assess the confidence intervals for these measurements. All 95%

confidence intervals in this chapter have been calculated by assuming a normal distribution for whichever quantity is being measured.

Reverberation time methods for measuring structural and acoustic damping have been described in this chapter. C(95%) confidence intervals for damping measurements in steel panels were typically less than ±3dB for the Micra study in Chapter 6 and ±0.4dB for the curved joint study in Chapter5. Acoustic damping measurements in the saloon of the Micra motor-vehicle had C(95%) intervals of around ±3dB at 125 Hz falling sharply with frequency to around ±0.5dB at 10kHz.

Sound Pressure Level measurements were made in the saloon and engine compartments of the Micra motor-vehicle with the engine running. Measurements were made at three engine speeds (700, 3000, 5700rpm). Saloon SPL was measured with and without the front exhaust mounts connected. The C(95%) intervals for SPL in the saloon with the front exhaust mount disconnected are less than ±5dB over most of the frequency range for the three engine speeds. C(95%) intervals for saloon SPL at 700 and 3000rpm are less than ±3dB over most of the frequency range, this is because more measurements were taken with the exhaust connected.

At 5700rpm however the C(95%) intervals for saloon SPL are higher with the exhaust connected despite the larger number of measurements. C(95%) intervals at 5700rpm with the front exhaust mounts connected starts at around ±2dB below 125Hz at which point they rise to approximately ± 5.6dB and then fall off to around ±2dB at 5kHz. A possible reason for the increased variance in SPL with position in the saloon at 5700 rpm with the exhaust connected is that the excitation of the floor by the exhaust causes a direct rather than reverberant sound field in the saloon.

Acceleration Level Differences and Energy level differences may be measured using the techniques given in this chapter. C(95%) confidence intervals for ALDs measured during the Micra study of Chapter 6 are typically around ±6dB at 125Hz falling to around ±4dB at 1kHz. The C(95%) intervals for the roof to windscreen ALDs are below ±3dB over the entire frequency range. ELDs may be calculated from measured ALDs and the confidence

intervals are the same. ELD results from the curved joint study of Chapter 5 had C(95%) confidence intervals less than ±2dB over the entire frequency range.

Two methods for measuring structural impedance are discussed in this chapter. One method uses an impedance head and a shaker to provide excitation. The other method uses a force hammer to provide and measure excitation and an accelerometer to measure the structural response. Neither method caused any damage to the structure and both were quick and easy to use. Both methods could be accurately calibrated by measuring the impedance of a known mass. The mobility of the roof panel on the Micra motor-vehicle was measured using both methods. The shaker gave best agreement with a theoretical value for infinite plate mobility requiring only a small (3dB) adjustment for mass loading. Mobility measured using the force hammer method did not agree as well with the predicted value. Two possible reasons for this are the relatively large deflections caused by the hammer and the fact that the accelerometer could not be placed at the point of impact. Neither of these effects are likely to cause significant errors in the force hammer results for engine and exhaust mount impedance as these parts of the vehicle are reinforced.

Chapter 5

Curved Joints

5.1. Introduction

Wave transmission across a curved panel joint can be calculated using the complex joint techniques as described in Chapter 3. This Chapter describes experiments devised to test these predictions. The apparatus consisted of a steel panel bent to form two panels joined by the curved joint, an unconstrained layer of damping material was applied to one of the panels. Energy Level Differences between the two panels were measured as described in Chapter 4. Several methods exist for calculating the ELD based on transmission coefficients e.g. SEA[36], WIA[84], ASEA[83]. In Chapter 3 it is shown that the bending wave transmission coefficient across a curved panel joint can be very strongly dependant upon the angle of incidence to the boundary. This reduces the probability of a diffuse field in the panels. SEA assumes a diffuse field but ASEA and WIA do not. In this Chapter WIA and SEA are used for calculating the ELDs and measured results are compared with the two predictions.

5.2. Wave Intensity Analysis

Wave Intensity Analysis (WIA) was developed by Langley [84] and is a development upon SEA which discards the diffuse field assumption. WIA is discussed in Section 2.9. Two forms of WIA have been used to calculate the ELD predictions in this Chapter. The discrete wave heading approach and the Fourier series method. In the Fourier series method perfectly reflecting panel boundaries were assumed to cause symmetry of the field about a line parallel to the boundary. It is not a requirement of the Fourier series method that the wave fields be symmetric. Symmetry was not assumed to be the case in the discrete wave heading approach which required only the power balance equations to calculate intensity. In either case the predicted result converges as the number of Fourier coefficients or wave headings is increased. 100 headings per panel were used in the discrete wave heading model as the predicted ELDs had converged to within a fraction of a dB long before this point. 20 Fourier series terms were used on each panel to achieve a

similar degree of convergence which would suggest that the Fourier series method is potentially a more numerically efficient method.

A number of tests were carried out to check for errors in the computer code written to implement the WIA models. Langley's [84] two panel example was replicated using the program. The ELD predicted using the discrete wave heading model converge to within around 0.2 dB of the prediction given by Langley [84] but not to precisely the same values. The conversion matrix **C** (discussed in Section 2.10) was used to solve for the wave field in terms of Langley's Fourier coefficients. When the field symmetry assumptions were imposed as described by Langley [84] the 0.2dB discrepancy was eliminated and the predicted ELD converged to the result given in [84]. As a further test the WIA computer code was used to calculated ELDs between panels with only one Fourier coefficient in the wave field series on each panel. This gave the same ELDs as SEA which it the correct result.

Power input to the source panel was assumed to be equally distributed into each heading as might be expected from "rain on the roof" excitation. Measured ILFs were used in the models and the loss factors for each heading were assumed to be equal. The properties of the damped panels were calculated assuming that the applied damping layer contributed only extra mass to the panel and that any increase in bending stiffness was negligible.

5.3. Experimental Apparatus

Three apparatus were constructed each consisted of steel panels nominally 2m x 1m as shown in Figs.5.1-5.3. Two of the panels were bent in rollers to form curved joints of different curvature these panels were 2mm thick. For comparison, one panel (shown in Fig. 5.3) was folded to form a sharp corner joint (this panel was 1mm thick). Once the panels were bent damping material was applied on one side of the joint in order to increase the Energy Level Difference. An unconstrained bituminous damping material approximately 1 mm thick was attached to one side of the panel using a thin layer of adhesive. The surface density of the damping material was 2 kg / m^2.

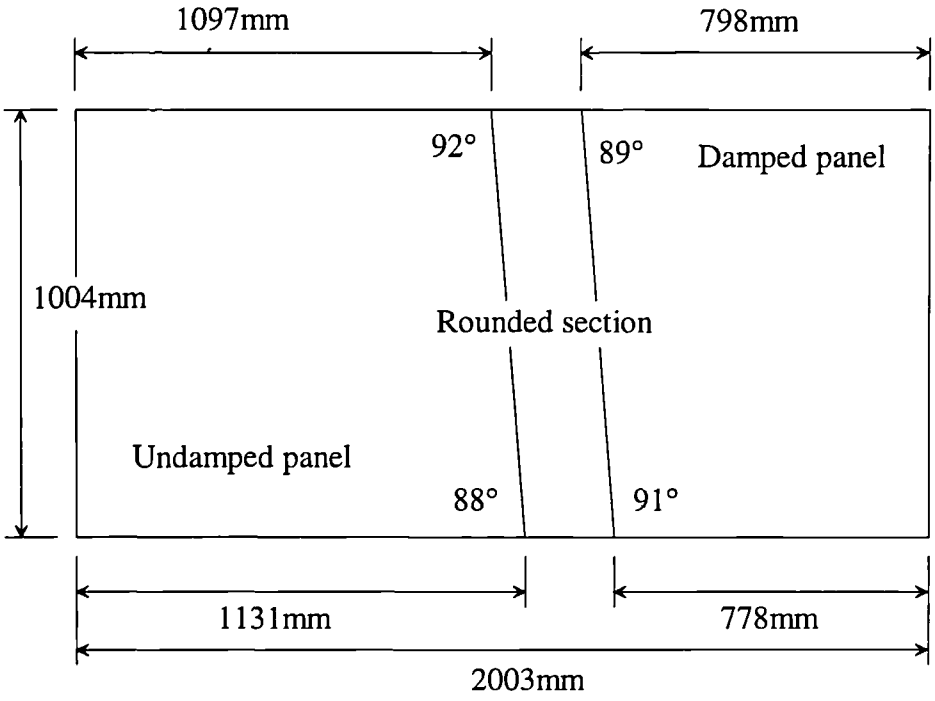

Figure 5.1: 2mm panel, 63mm radius joint with 87° bend.

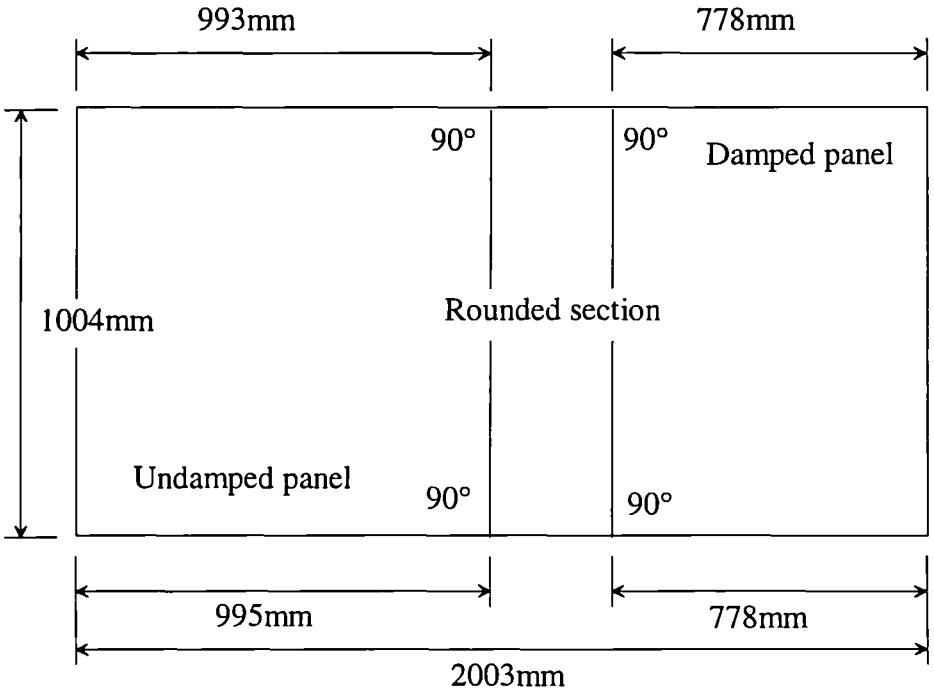

Figure 5.2: 2mm panel, 131mm radius joint with 103° bend.

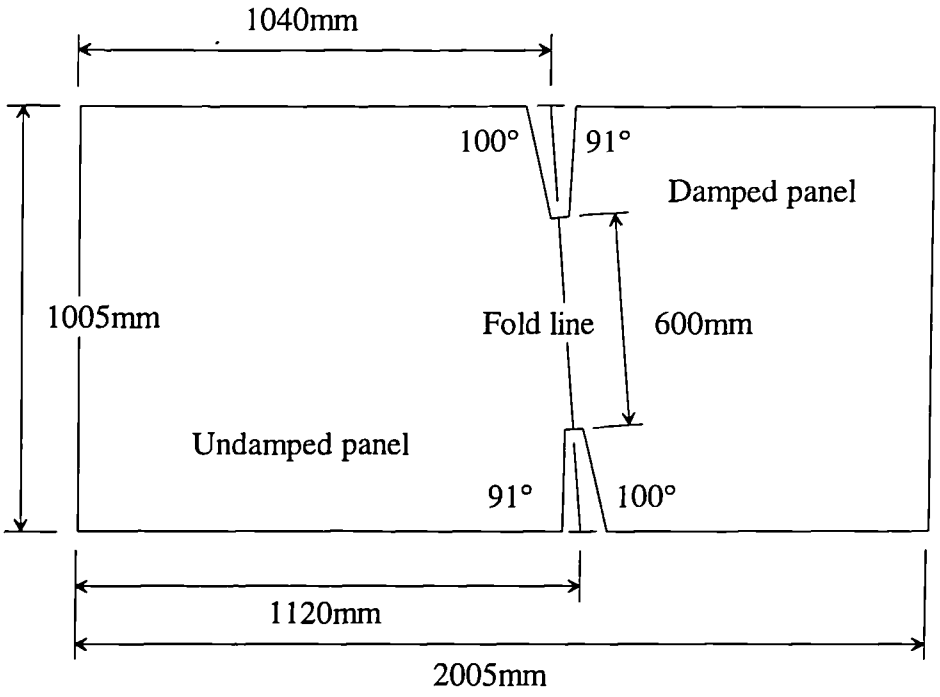

Figure 5.3: 1mm panel, sharp corner joint.

The plain strain ring frequencies of the curved panel sections are f_R=13.6kHz for the 63mm radius joint and f_R=6.6kHz for the 131mm radius joint. These values assume a plate longitudinal wave speed of 5400m/s for steel. Dimensions in Figs. 5.1-5.3 are within ±1mm and the angles indicated are accurate to within ±1°, panel corners shown as right angles were 90±1°. The Energy Level Difference was measured using two accelerometers (one on each panel) while tapping the source panel over its surface as described in Chapter 4. 20 measurement positions were used so as to bring the C95% confidence intervals within ± 2dB between 125 Hz and 10kHz as Shown in Fig. 4.11. During the measurements the panels were hung in frames from Nylon loops as shown in Fig. 5.4, this produced reflecting boundaries at the edges of the plates as assumed in the WIA model while still holding the panels in place.

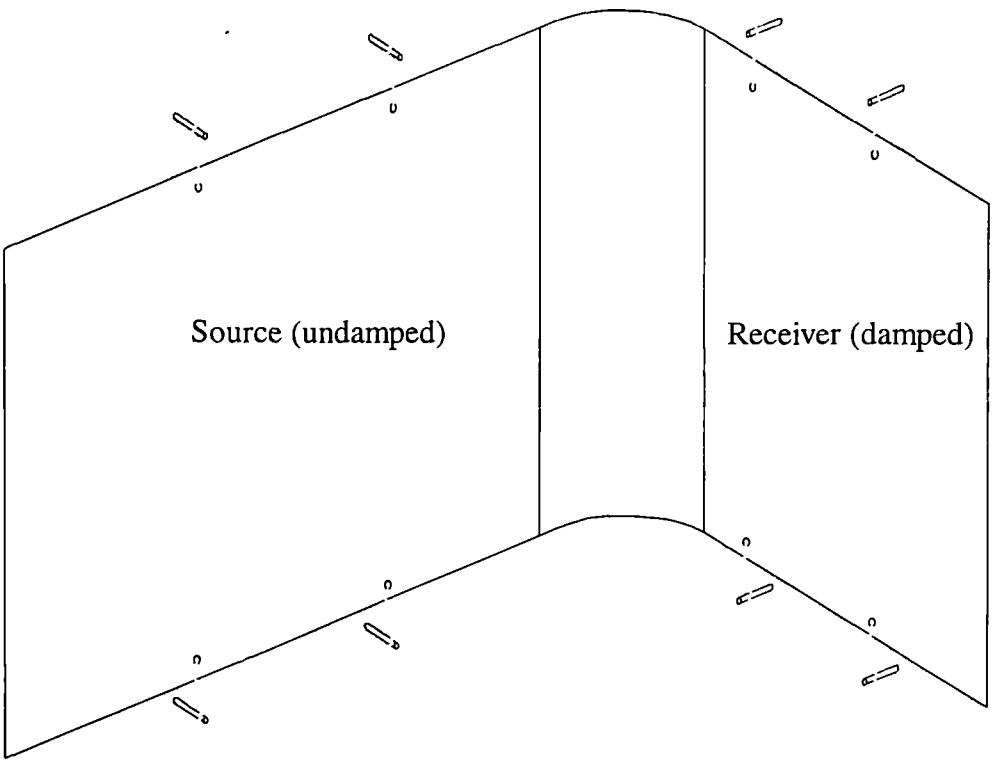

Figure 5.4: Panel held in frames for measurements.

Once the ELDs had been measured the panels were cut apart and their ILFs were measured using the reverberation time technique as described in Chapter 4. 20 measurement positions on each panel were used to average the ILF measurements bringing the C95% confidence intervals down to typically less than ±1dB as Shown in Fig. 4.8. During the ILF measurements the panels were hung in the frames as in the ELD measurements. All the losses except coupling at the corner joint are measured in this way. These losses include material damping, radiation damping and losses due to transmission at the nylon loops.

5.4. Measured and Predicted Damping of Unconnected Panels

The measured damping loss factor levels for the undamped panels are shown in Fig. 5.5. The results are given in dB re 10^{-12}. Measured results labelled 2/63mm are the values for the 2mm panel joined by the 63mm radius joint. Results labelled 2/131mm are for the two mm panel joined by the 131mm radius curved joint. Also shown are predicted values based on acoustic radiation and material damping. The radiation coupling is calculated using equation (2.85) given by Heron[91] which gives the radiation efficiency below the critical frequency for a free-free rectangular panel with no baffle. The critical frequency of

the damped panels are 6712Hz and 14390Hz for 2mm and 1mm respectively. The critical frequencies of the undamped panels are 6327Hz and 12634Hz for 2mm and 1mm respectively. Material damping levels were chosen to best match the measured data at low frequencies. A good straight line fit at low frequencies is given when the material damping loss is assumed to vary with the reciprocal of the square root of frequency i.e. approximately 1.5dB per octave. For the 2mm steel the best line fit is given by a damping loss factor of 0.00012 (1kHz) and for 1mm a value of 0.0005 (1kHz). These damping levels are reasonably consistent with steel loss factor values of around 0.0001 (80dB re 10^{-12}) given by Cremer *et al*[1]. The total predicted damping is shown in Fig. 5.5, it was calculated by adding the radiation damping and the best line fit for material damping.

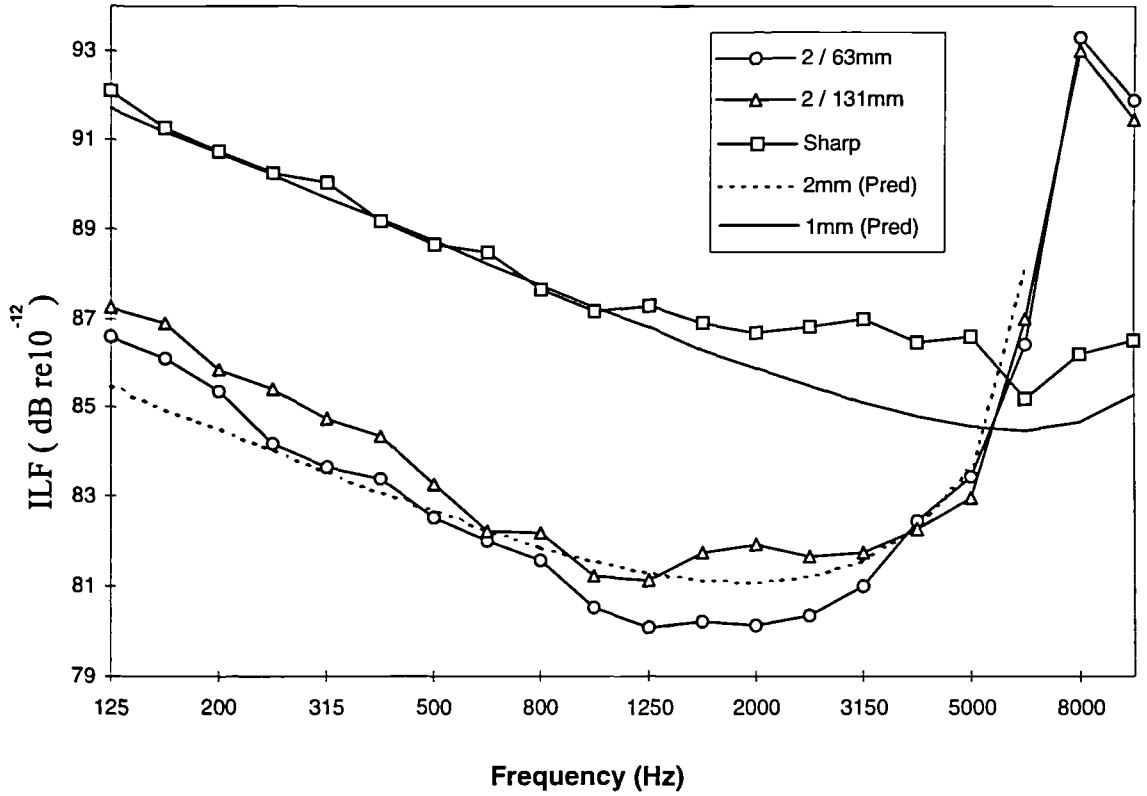

Figure 5.5: Measured ILF for undamped panels. Also shown are "predicted" damping curves based on predicted acoustic radiation given by Heron[91] plus material damping. The material damping was adjusted to give best line fit with measured data.

Fig. 5.5 shows that above 1kHz the predicted 2mm ILF is dominated by the acoustic radiation and shows good agreement with the measured result which clearly exhibits a peak near the critical frequency around 6.5kHz. This would suggest that the expression for radiation efficiency given by Heron[91] is accurate. As the critical frequency of the 1mm panels lies out side the measured frequency range the effect of acoustic radiation is

less obvious but it is still noticeable around 10kHz. Measured ILFs for the panels with a damping layer applied are shown in Fig. 5.6.

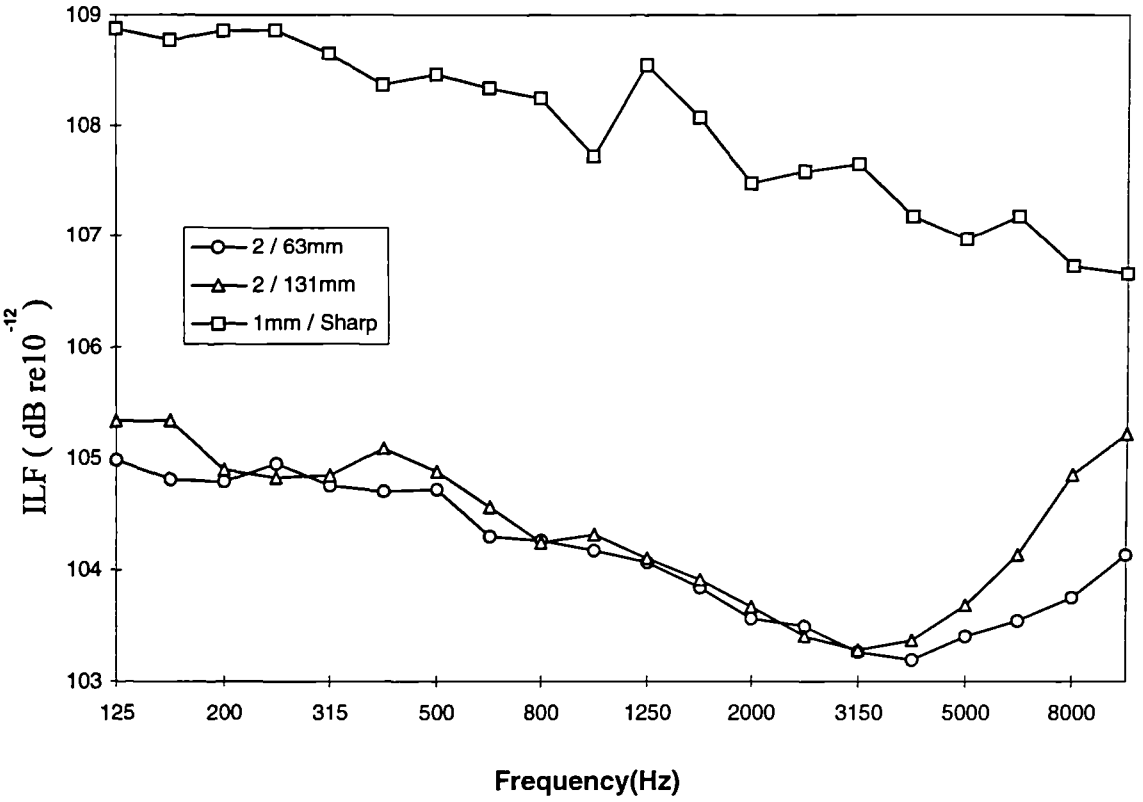

Figure 5.6: Measured ILF of damped panels.

Since the damping layer applied to all the panels was the same thickness it had a larger effect on the 1mm panel than the 2mm panels. The ILFs are at least 10dB higher for the damped panels than the undamped ones. 2mm panel ILFs increase near the critical frequency which is peculiar as the radiation loss should be much less than the internal damping. The damping material may have some frequency dependant property which causes this rise. The measured ILFs shown in Figs. 5.5 and 5.6. were used in the SEA and WIA models for predicting panel ELDs.

5.5. Energy Level Differences

Measured and predicted ELDs are given in this section, the vertical scale on the graphs are $\text{dB} = 10\log(E_2 / E_1)$ where E_2 is the energy level of the receiving panel and E_1 is the energy of the source. There were only three measured ELDs but several permutations of predicted results. These include two different WIA predictions, one using the discrete wave heading approach and the other the Fourier series approach. These methods are discussed in Section 2.10. The Fourier series method was used because it can be used to impose symmetry conditions upon the panel wave fields. Fig.5.7 shows a comparison

between some of the predicted ELDs with and without the field symmetry assumption. These predictions are not smooth curves because the predictions used the measured ILFs shown in Fig 5.5. and 5.6.

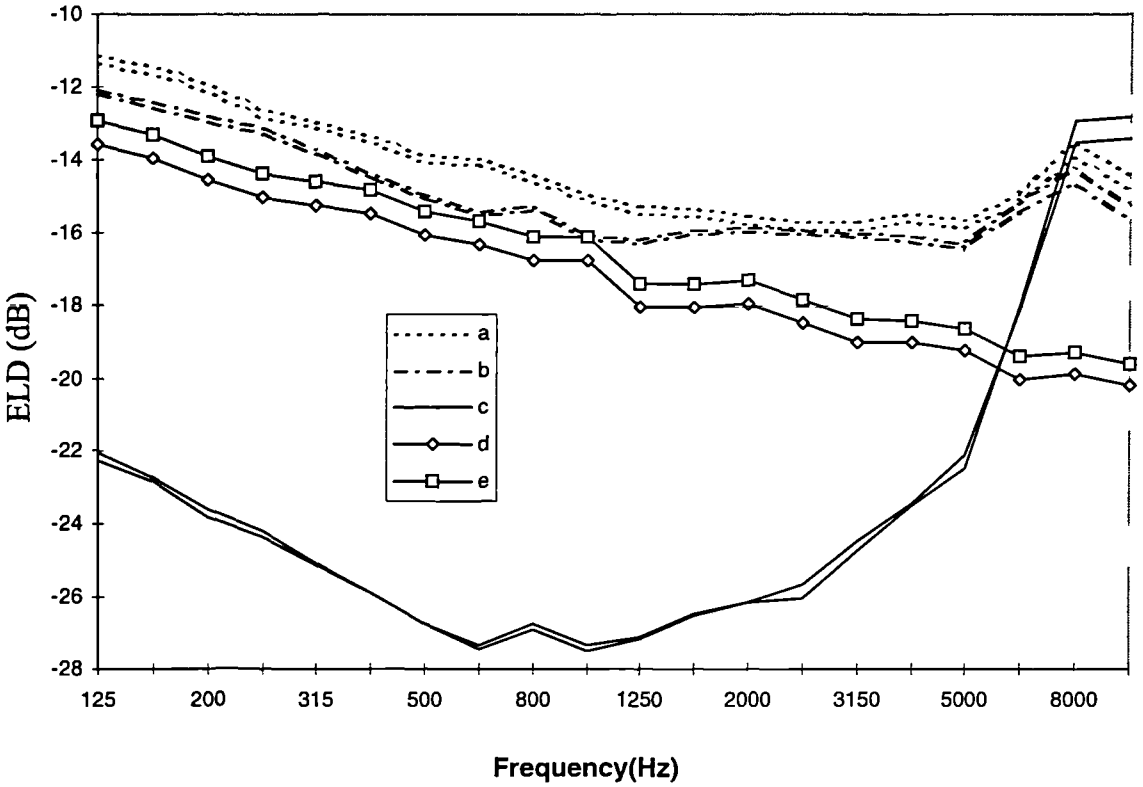

Figure 5.7: WAI predicted ELDs with and without field symmetry assumptions, a: 63mm joint (sharp), b: 131mm joint (sharp), c: 131mm joint (curved), d: sharp joint (symmetric field) , e: sharp joint (no assumed symmetry).

Fig. 5.7 shows some predictions for the curved joints and the sharp corner joint. The curved joints may be modelled using the complex joint modeller (curved) or simply treated as (sharp) corners with the same angle between the panels. Fig. 5.7 indicates that imposing symmetry about a line parallel to completely reflecting boundaries has a negligible effect on the predictions in these cases. For the curved joint the difference between the two predictions is typically less than 0.2dB whether it is modelled as a sharp or a curved joint. The 1mm panels which are joined by a sharp corner joint differ by a larger amount but still typically only 0.6dB. This is possibly due to the fact that the 1mm panels are more highly damped than the 2mm panels. In light of the small difference between the two WIA methods only the discreet wave heading predictions shall be shown in subsequent figures except for the sharp corner joint.

Predicted results for the sharp corner joint are in good agreement with the measured values as can be seen by Fig. 5.8.

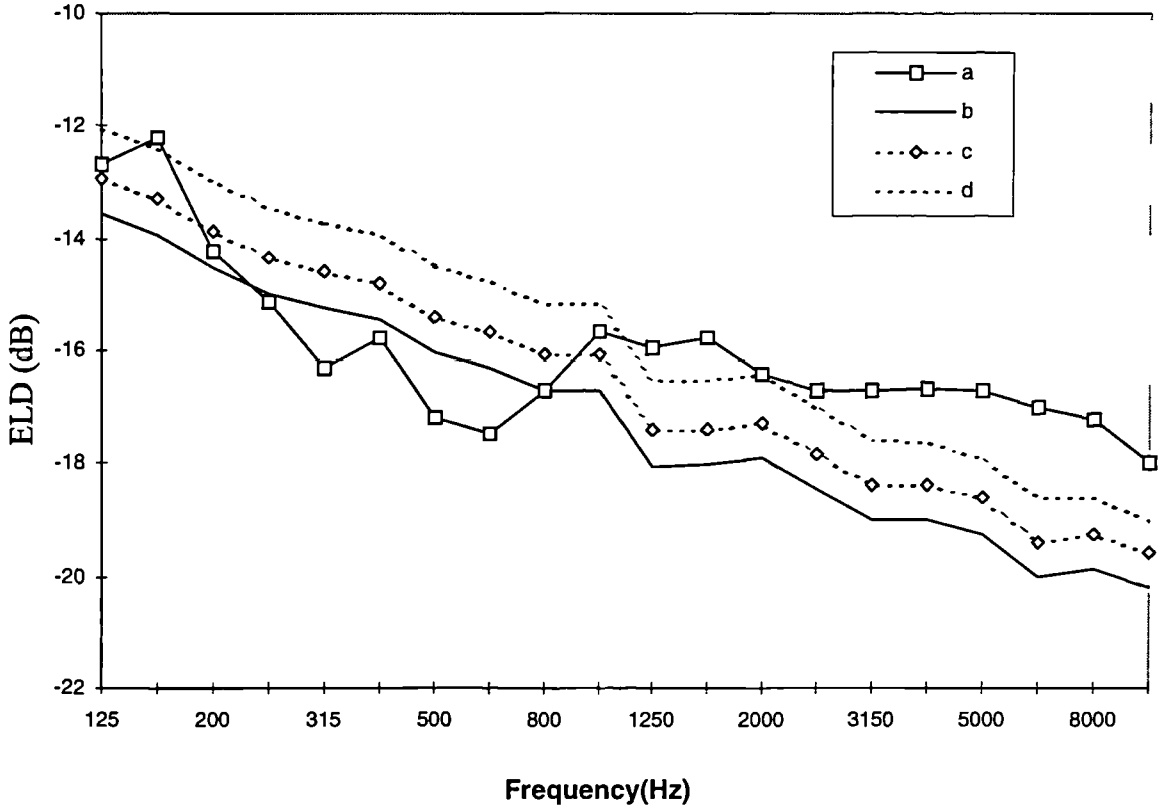

Figure 5.8: Measured and predicted ELDs for sharp corner joint, a: measured, b: WIA (symmetric field), c: WIA (no assumed symmetry), d: SEA.

WIA and SEA predictions are both typically within 2dB of the measured data over the entire frequency range. The reason for the closeness between SEA and WIA in this case is the complicated shape of the panels created by the notches cut into the joint (Fig. 5.3). This complexity mitigates towards a more diffuse field. The symmetry condition was not applied for the small boundaries that form the notches of Fig. 5.3. If they had been included one might have expected the WIA (symmetric field) prediction to be closer to SEA than the WIA (no assumed symmetry).

Measured and predicted ELDs are shown in Fig. 5.9 for the 63mm curved joint. ELDs are predicted with WIA and SEA using transmission coefficients assuming curved or sharp corner joint configurations.

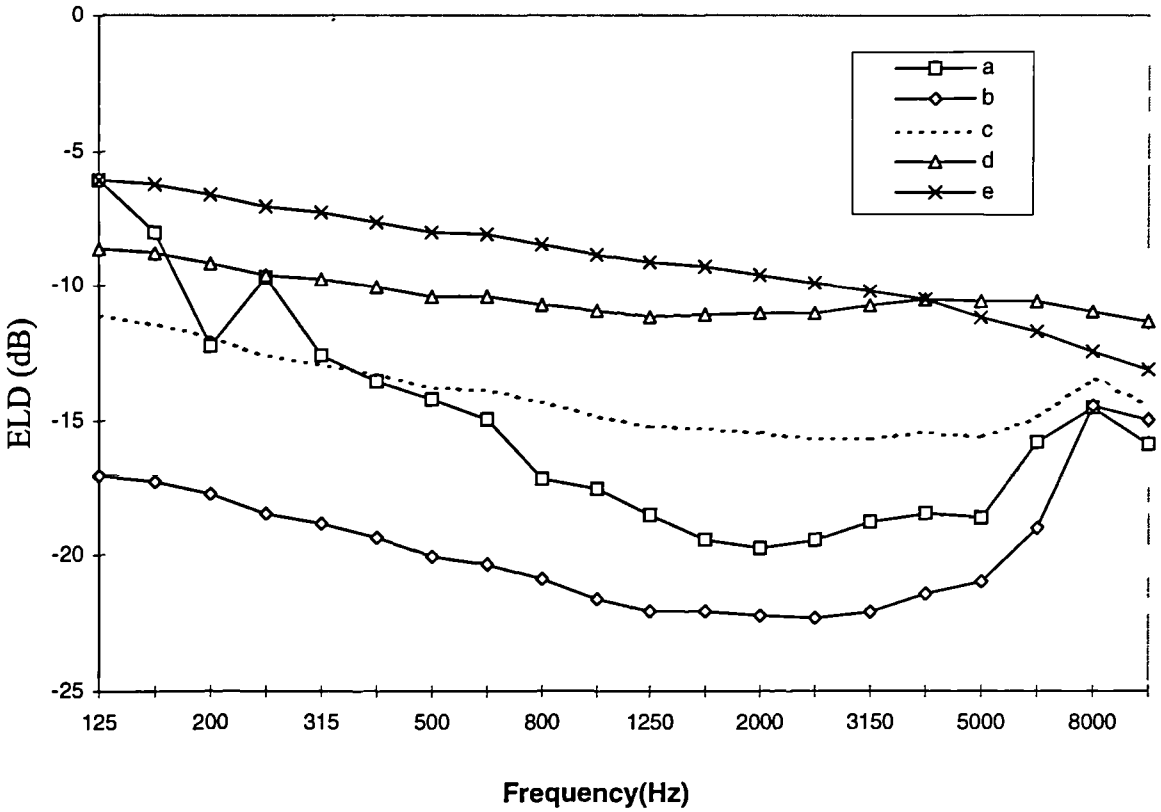

Figure 5.9: ELDs for 63mm radius joint (f_R=13.6kHz), a: Measured, b: WIA (curved), c: WIA (sharp), d: SEA (curved) , e: Sharp SEA.

Best agreement on average is with the WIA using the sharp transmission coefficients, WIA with curved transmission coefficients under predicts transmission. SEA generally over predicts transmission over most of the frequency range but gives good agreement below 315Hz when using the curved joint transmission coefficients. All predictions except SEA (sharp) predict the increase in transmission above 2000Hz.

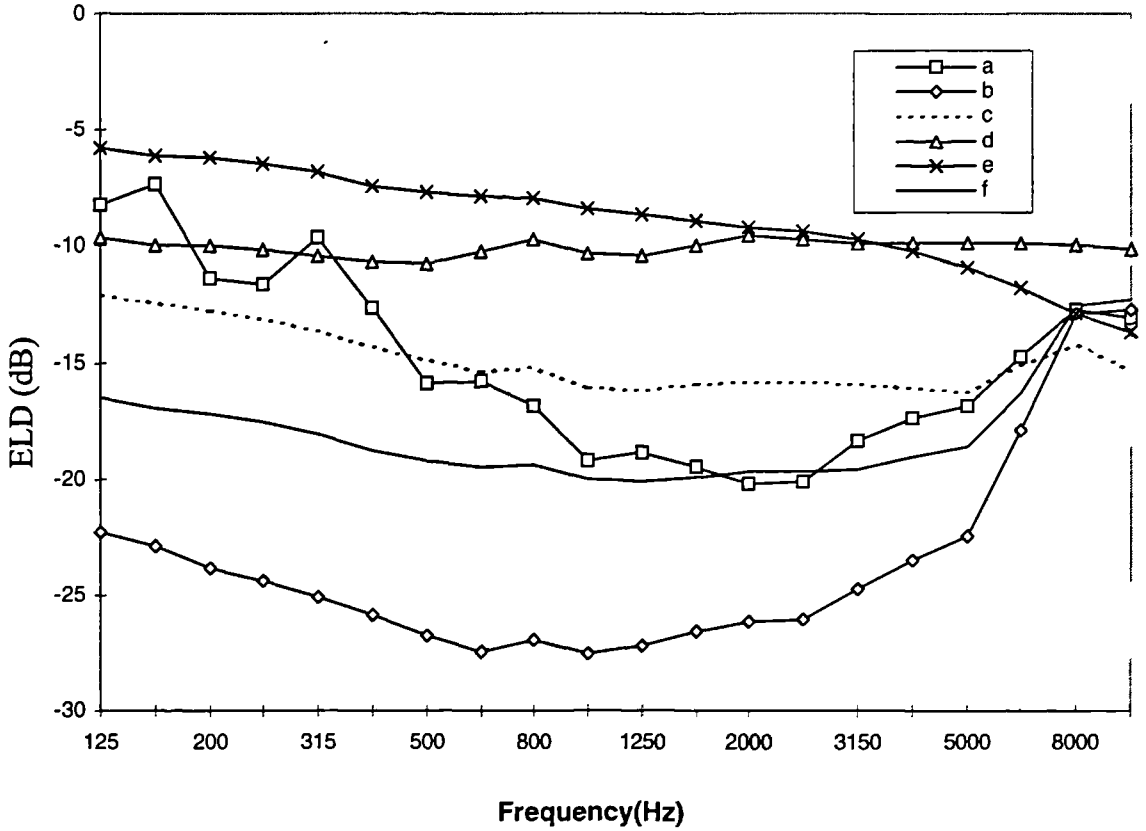

Figure 5.10: ELDs for 131mm radius joint (f_R=6.6kHz), a: measured, b: WIA (curved), c: WIA (sharp), d: SEA (curved) , e: SEA (sharp), f: WIA (curved 87°).

Fig. 5.10 shows the results for the 131mm radius joint. Again the closest agreement to the measured data is from WIA (sharp) with SEA predicting higher transmission and WIA (curved) lower.

Sensitivity of the predicted ELDs to fluctuations in dimensions and material properties was investigated by perturbing these parameters in the model. The damping, density, longitudinal wave speed and thickness of both panels in the WIA models were altered independently by up to around 50% either side of the original values. The sensitivity of the models to geometric errors was tested by altering the orientation of all the boundaries one at a time by a few degrees. The curvature and length of the rounded corner section were also altered. The findings of this sensitivity testing were that the angle of the joint between the panels was the most influential of the perturbed parameters in relation to the likely size of errors in its values. It was found that the WIA (curved) model was sensitive to the angle of the curved joint which was 90° as shown in Fig 5.2. This is illustrated by curve f (solid line) in Fig. 5.10 which is the prediction using WIA (curved) having changed the angle of the joint from 90° to 87°. The predicted ELD is also sensitive to

changes in the damping of the heavily damped (receiving) panel. A 1dB increase in the damping of the receiving panel causes a similar decrease(reduced transmission) in the ELD. The models were considerably less sensitive to the damping in the source panels. Changing the curvature and or length of the joint by an amount which was realistic in relation to the measurement errors had only a relatively small effect.

5.6. Discussion

SEA and WIA are only appropriate where the modal density is high enough that a number of modes are likely to resonate in each frequency band. The modal density for the panels may be calculated using Equation (2.46), for the smallest 2mm panels this gives a value of 0.13 modes per Hz. For the smallest 1mm panel the predicted modal density is 0.29 modes per Hz. In the 125Hz $1/3^{rd}$ octave band the expected number of resonant modes is therefor 3.9 (2mm) and 8.7 (1mm). As the width of the bands increase linearly with frequency so will the expected number of modes in each band. Modal overlap ($M=fn\eta$) factors calculated at 125Hz are 0.011 (2mm) and 0.072 (1mm) for the undamped panels and 0.51 (2mm) and 2.86 (1mm) for the damped panels. The modal overlap increases with frequency and the value for the damped 2mm panels exceeds one at around 250Hz. A two subsystem SEA model is most likely to produce accurate answers when one or both of the subsystems has a modal overlap exceeding one Lyon&Dejong [36], Fahy&Mohamed [47] which is the case here above 250Hz.

A widely used interpretation of the SEA weak coupling requirement is that the TLF of a subsystem must significantly exceed the individual CLFs out of the sub-system, Smith [54]. For a two subsystem model this means that the ILFs must exceed the CLFs. More recent work by Heron[57] has suggested that this requirement is unnecessary if wave methods are used to derive the CLFs and a number of theoretical studies have shown good agreement between SEA and deterministic models of strongly coupled multi modal structures (Remington&Manning[51] and Dimetriadis&Pierce [52]). Metal structures are often not sufficiently well damped to fulfil Smiths criterion but SEA has still predicted the transmission accurately in this type of structure (Trach [62], Steel [60]). In [60] a steel plate and beam were welded together, the plate was sufficiently damped to fulfil Smiths criterion but the beam was not. Bending waves on the beam and the plate constituted the subsystems. Equipartition was observed and predicted when the plate was the source. When the beam was the source then the ELD was equal to the CLF minus the TLF. This

situation is similar to the experimental set-up of the panels in Figs.5.1-5.3 in that one panel is highly damped and therefor fulfils Smiths[54] criterion but the source panel is not.

Damping levels in the treated panels are high (up to 109 dB for 1mm) and it is interesting to consider whether the damped panels will be reverberant or not. Equation (2.131) can be used to calculate the exponential decay of energy in space as it travels across the panel. Energy travelling as plane waves across the damped 2mm panels will typically decay to 52% in one meter at 1000Hz. The damped 1mm panel attenuates energy at a higher rate and plane wave energy will drop to 13% in one meter at 1000Hz. Attenuation of this magnitude would suggest that possibly the 1mm panels are not particularly reverberant. The high damping does not effect the relationship between the mean square velocity of the damped panel and the power dissipated within it provided the damping is linear. High attenuation will however effect the relationship between the damped panel energy and the power it feeds back to the source panel. When the damping is very high in relation to the coupling the power fed back is negligible in relation to the power supplied by the source panel. This is true whether the wave field in the damped panel is reverberant or not. This is probably why no significant error was observed between the measured and predicted results for the sharp corner (1mm) panels. Errors may have arisen if the panel was coupled to a third subsystem into which it fed power. When a panel is more heavily damped the relationship between panel energy and the power incident upon the boundaries of the panel differs from the reverberant case.

WIA differs from SEA only in that it does not assume a diffuse field within the panels. The boundaries of a panel couple the energy in different wave headings together. Panels with more boundaries and irregular shapes are more likely to support diffuse fields and give good agreement in an SEA model. This is why the SEA and WIA results for the sharp corner joint were typically within 2dB of each other and the measured ELD, Fig. 5.8 . Curved joint panels were left deliberately simple in shape so as to exaggerate the difference between WIA and SEA. In Chapter 3 numerically calculated transmission coefficients for the curved joint are discussed. In Fig (3.13) the transmission coefficients are shown for a curved joint, it can be seen that the transmission is extremely sensitive to the incidence angle. Below a certain angle of incidence there is almost complete transmission while at larger angles the incoming wave is almost completely reflected. The

angle at which the transmission flips increases with frequency. This behaviour was expected to further reduce the likelihood of a diffuse field and contribute to discrepancies between measured ELDs and those predicted using SEA. There are indeed large discrepancies between the SEA predictions and the measured ELDs above 300Hz but unfortunately the WIA (curved) models are also unable to accurately predict the ELDs except at high frequencies.

SEA over predicted the transmission above 300Hz in both curved joints (Figs. 5.9 and 5.10) using either the complex joint or the sharp corner transmission coefficients. This has been observed before for sharp corner joints between rectangular panels (Langley[84]). WIA gives the closest prediction when using sharp corner transmission coefficients but under predicts the transmission when using the curved joint coefficients. The error is particularly large with the 131mm radius joint Fig. 5.10. These findings would seem to suggest that curved joints are best modelled as sharp corners, ignoring the curvature. The fact that the measured ELDs for the 63mm and 131mm are almost identical where as the corresponding WIA(curved) predictions differ by 5dB at low frequencies (Fig. 5.11) adds more weight to this argument. The ELDs predicted using SEA and the curved joint transmission coefficients are also shown in Fig. 5.11.

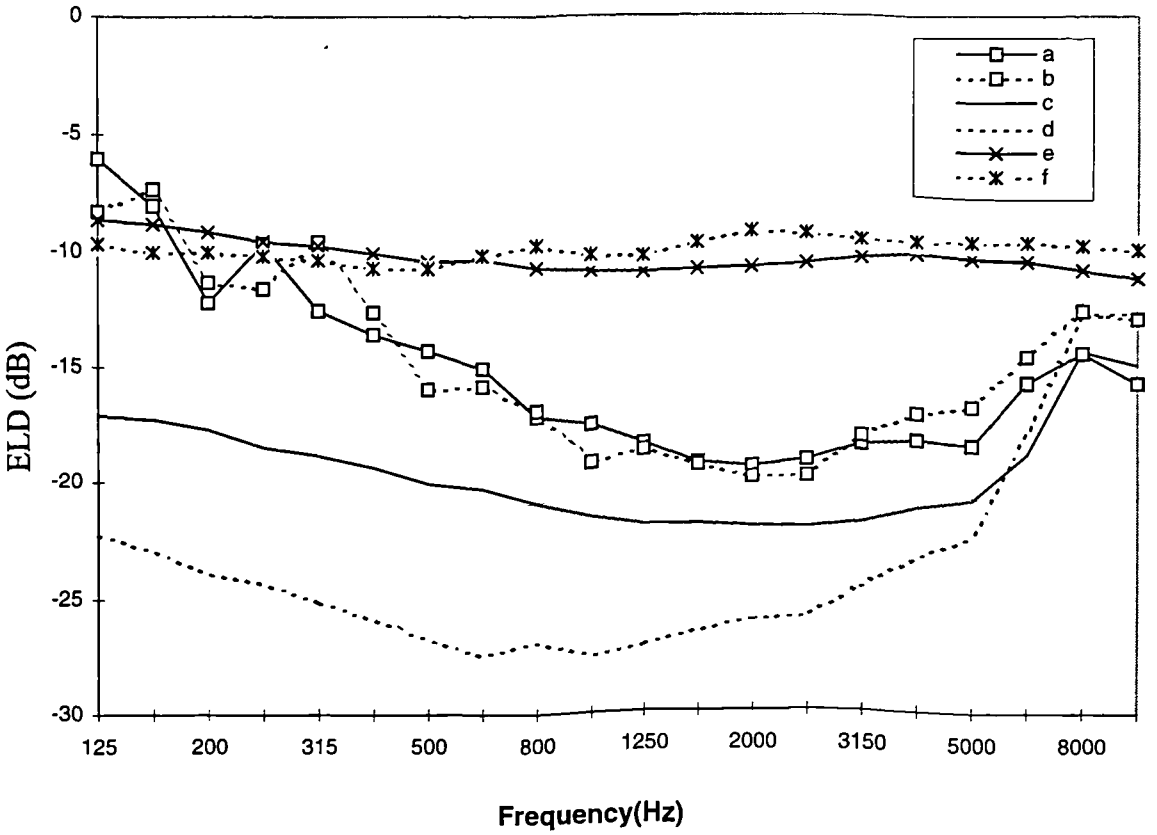

Figure 5.11: Measured and predicted ELDs, a: meas. (63mm, f_R=13.6kHz), b: meas. (131mm, f_R=6.6kHz), c: pred. WIA(curved 63mm), d: pred. WIA (curved 131mm), e: pred. SEA (curved 63mm), f: pred. SEA(curved 131mm).

The measured ELDs generally lie below the SEA(curved) predictions and above the WIA(curved) predictions. The SEA (curved) predictions are accurate below 300Hz and the WIA (curved) predictions are accurate above 6300Hz. The SEA and WIA predictions appear to form an upper and lower limit between which lie the measured results.

Fig. 5.11 shows that at frequencies above 3150Hz the measured ELD between the panels connected by the 63mm radius joint is slightly lower then that measured between the panels connected by the 131mm joint. The difference rises to roughly 3dB at 10kHz.. The 95% confidence intervals for the curved joint ELD measurements are shown in Fig. 4.11 and are between ± 0.5 and ± 1.2 dB in the frequency range (3150Hz-10kHz). This would suggest that the measured difference in ELD between the two joints is probably due to a systematic effect rather than random fluctuation. Fig. 5.6. shows that the measured ILF of the receiving panel which was connected to the 131mm radius joint is roughly 1dB higher than that which was connected by the 63mm radius joint at 10kHz. This would tend to

make the ELD between the panels connecting the 131mm joint smaller than the 63mm joint value rather than larger and therefor doesn't explain the difference between the measured ELDs at high frequencies. The ELDs predicted using the curved joint transmission coefficients with WIA show a similar trend at high frequencies. The WIA(curved) ELD prediction for the 131mm radius joint rises above that for the 63mm radius joint at around 6300Hz. In the 8kHz and 10kHz $1/3^{rd}$ octave bands both the 63mm and the 131mm WIA (curved) predictions are in very good agreement with the measured values.

Flanking transmission could cause the measured ELDs for the 63 and 131mm joints to be identical and stronger than predicted as seen in Fig 5.11. For this to be the case the flanking transmission would have to be stronger than the structural transmission across the curved joints. To eliminate this source of error the ELD measurements were repeated after the panels had been cut apart. These tests showed that there were no significant flanking paths.

The measured and predicted WIA (curved, 131mm) ELDs rise sharply in the region of the ring frequency for the 131mm joint (6.6kHz) and are in good agreement above this frequency. This would appear not to be strongly related to the ring frequency however because the 63mm results do the same despite the much higher ring frequency (13.6kHz) for the 63mm joint. The critical frequency of the undamped panel occurs at around 6.7kHz, the increased source panel damping caused by radiation might be the cause of the improved agreement between the WIA (curved) predictions and the measured results. Further tests with higher source panel damping would be required to confirm this.

WIA(sharp) accurately predicts the average level of the measured data but not the shape, the measured ELD for both joints drop more steeply than the prediction and then rises back up above 2000Hz. This shape is suspiciously similar to that of the ILF curve for the undamped 2mm panels shown in Fig. 5.5. It is not certain whether the shape is due to increased transmission at high frequencies as predicted by the curved joint model or some effect of the ILF. Prior to the experiments presented here a number of measurements were carried out on a 1mm curved joint connecting panels damped with a number of different damping treatments but the recorded ELDs exhibit a similar shape.

The high sensitivity of the WIA (curved) prediction to the angle of the joint is shown in Fig. 5.10. This sensitivity may explain some of the discrepancy between the predicted and the measured ELD. There was not a 3° error in the joint angle as this is outside the measurement tolerances so this is not the full explanation. The number of wave headings was increased to one per degree of arc but this made no significant difference to the sensitivity. Panel thickness was measured using a micrometer around the periphery. These measurements indicated that the 2mm panels were approximately 0.05mm (2.5%) thicker along a horizontal line through the centre than on the horizontal boundaries in Figs. 5.1 and 5.2. Thickness varied smoothly along the vertical boundaries. Bending wave speed is proportional to the square root of panel thickness and so the waves might be expected to travel approximately 1.25% faster along the centre of the panel than near the boundaries. Using this theory a plane wave travelling horizontally (Figs. 5.1 and 5.2.) along the panel for 1meter would be diffracted through roughly 1.4° downwards in the bottom half of the panel and upwards in the upper half. Given the sensitivity of the WIA(round) model to the wave headings the diffraction effect may explain some of the error in prediction.

The transmission characteristics of the curved joint model discussed at the end of Chapter 3 are similar in a sense to the acoustic radiation characteristics of an infinite panel. Bending waves on a infinite panel with a wave number less than the acoustic wave number can radiate into the acoustic space, where as those with a higher wave number cannot. In a similar way the trace wave number of the incident wave on the joint determines whether a wave is transmitted in to the connected panel or not. Trace wave numbers less than a certain value cause transmission where as those above do not. When a finite panel vibrates with modes having wave numbers greater in magnitude than the acoustic wave number, i.e. below the critical frequency it still radiates sound. This is because the waves are confined to a finite space which introduces other wave number components on either side of the peak in the wave number spectrum. Some of these components are below the acoustic wave number and give rise to radiation see Fahy [20]. The same sort of effect could occur in a finite panel joined by a curved joint which would increase transmission particularly at low frequencies which is what is required to better match the WIA (curved joint) predicted ELDs to the measured ELDs. Transmission of bending waves across a line joint between a thin panel and a thicker one made of the same material cuts of at a certain angle beyond which the incoming wave is reflected (see Cremer[1]). This angle is given by,

$$\sin\theta = \sqrt{\frac{h_{THIN}}{h_{THICK}}} \tag{5.1}$$

A realistic choice of thickness ratio of say 1/3 gives $\theta = 35°$. For a more extreme ratio of 1/10 the cut of angle is $\theta = 18°$. At 1000Hz the maximum transmission angle of the 63mm curved joint is approximately 14° which will reduce at lower frequencies. This shows that the transmission cut off effect is considerably more extreme in curved joints than in typical junctions between dissimilar plates. It is therefore still possible that this effect contributes significantly to the transmission at low frequencies across curved panel joints and yet is not a significant effect in the transmission between dissimilar plates connected at a sharp corner.

5.7. Conclusions

WIA and SEA ELD predictions for the panels joined by the sharp corner line joint were in good agreement with measured data. The panels were of an irregular shape which produces a more diffuse wave field and explains the closeness of the SEA and WIA predictions.

SEA over predicted the transmission across both the 63mm and the 131mm curved joints when using Cremers[1] sharp corner transmission coefficients or those calculated using the curved joint model.

WIA generally under predicted the transmission across both curved joints when using transmission coefficients from the curved joint model. The error reduces at high frequency. In the highest 1/3rd octave frequency bands measured (8kHz and 10kHz) the agreement between the measured ELDs and those predicted using WIA with the curved joint transmission coefficients was very good. The precise source of the error at lower frequencies is unknown.

WIA predictions showed best agreement with measured ELDs when the joint configuration was assumed to be sharp but did not exhibit precisely the correct trends with frequency.

The measured transmission across the two curved joints was very similar below around 3000Hz, above this frequency the transmission across the 131mm radius joint was slightly

stronger that that across the 63mm joint. The difference in transmission rose steadily to around 3dB at 10kHz.

The WIA field symmetry assumptions for reflecting boundaries had a negligible effect upon the panels modelled even though the damping was high. This may not be the case with more than two coupled panels.

The curved joint transmission coefficients have neither been validated nor invalidated by the results in this Chapter, more research is required in this area. Apparatus consisting of irregularly shaped reverberant panels joined by curved joints may produce more conclusive results. A numerical study of panels joined by a curved section using a technique such as FEM may eliminate some of the unknowns such as experimental error from the problem.

Chapter 6

The Nissan Micra

6.1. Introduction

The practical application of the theories presented in Chapters 2 and 3 are demonstrated in this Chapter. Sound Transmission in a Nissan Micra 1.3 CVT motor vehicle was studied. This work is primarily concerned with structure borne sound transmission but airborne sound transmission is also discussed in this Chapter. The objectives of this Chapter are to assess the accuracy and usefulness of SEA models of the Micra in light of the assumptions made and investigate any improvements in accuracy as a result of using the complex joint modelling techniques from Chapter 3. The Chapter starts by describing the materials and methods used to construct the Micra. A basic SEA model is then introduced with panel to panel line coupling calculated using 90° and inline joints, Cremer *et al* [1]. Some of the joints have elastic layers at the junction such as those around the windows. Point force coupling is used to model transmission across door hinges and acoustic coupling is included between panels and air spaces such as the saloon in the basic SEA model. A second, more refined SEA model is also considered. This model is identical to the basic SEA model except that most of the panel to panel line couplings are treated using the complex joint techniques of Chapter 3. Curvature and corrugation of body panels was ignored in the panel subsystems of the models but detailed joint construction was included in the complex joint SEA model. Experimental and predicted results from the two SEA models are then compared and the accuracy of the measured data discussed. Structural ALDs were measured over the vehicle and complex joint results showed improved agreement for transmission over most of the vehicle. Sound Pressure Levels (SPLs) were measured with the engine running. Saloon SPL predicted by both SEA models using measured power inputs were in good agreement with the measured values. The application of SEA to identify the effects of exhaust misalignment is also demonstrated. Construction methods and materials do not vary a great deal between mass

produced vehicles regardless of the cost. Thicker steel will usually be used in a larger car and more damping, sound absorbing and protective materials are likely to be applied. Quality of manufacture may vary significantly between manufacturers and models but if a Nissan Micra can be successfully modelled using SEA then so can almost any contemporary car on the road.

6.2. Construction

The Nissan Micra 'k10' was introduced in 1983, the New Micra or 'k11' with more rounded body panels was released in 1993. It is the 'k11' that is the subject of this chapter (Fig. 6.1). The Micra falls into the category known in the motor trade as the mini or super mini class which caters for the small economy car market. Most of the major competitors to Nissan produce a vehicle in this class and the majority are of the same format as the Micra with the engine in front driving the front wheels. Noise exposure is not a high priority in this market as it is in the executive car sector. Excessive use of vibration damping and sound absorbing materials increases the cost and weight of the vehicle. Increased weight has a detrimental effect on the all important fuel economy figures so there is a drive to reduce applied damping and sound insulation materials.

The body panels are steel mostly 0.7mm thick, pressed into the required shape. They are usually curved in two directions and or corrugated for improved rigidity. All mass produced cars are constructed on robot assembly lines where the panels are welded together. Micra body panels are spot welded together in common with the vast majority of modern motor vehicles although at least one manufacturer uses laser welding on some of its more expensive models. In order to prevent the ingress of salt and water, some of the joints contain a special mastic which doesn't interfere with the welding process. This method of construction produces a line of point contacts (usually approx. 30 mm apart) surrounded by a strip of mastic between the panels which cures to the consistency of a soft plastic. Thicker panel sections (approx. 1mm) are spot welded into the structure forming closed section beam arrangements that provide additional strength, rigidity and crash protection. Reinforcement is provided in this way around key areas such as suspension and engine mounts. Strengthened parts include the bottom of the firewall, around the front wheel arches, parts of the sills and around the rear of the vehicle. Some of the areas strengthened in this way are shown in Fig. 6.2 by the light grey shading.

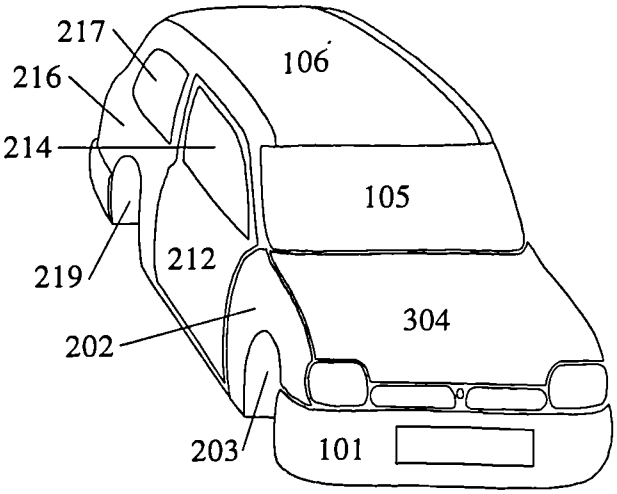

Right Side

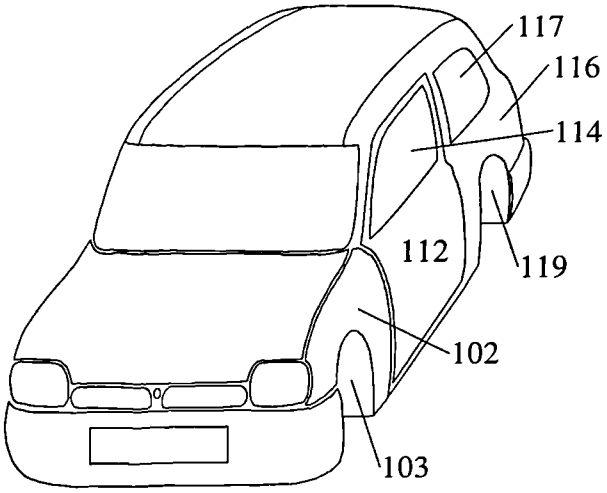

Left Side

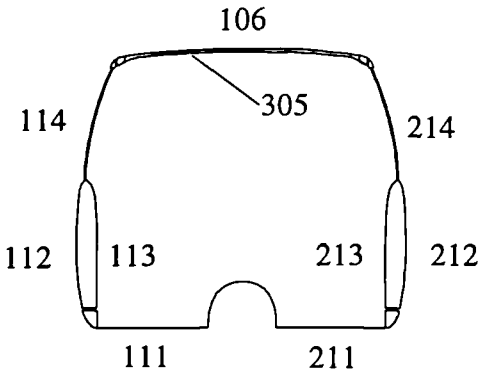

Front Seat Section

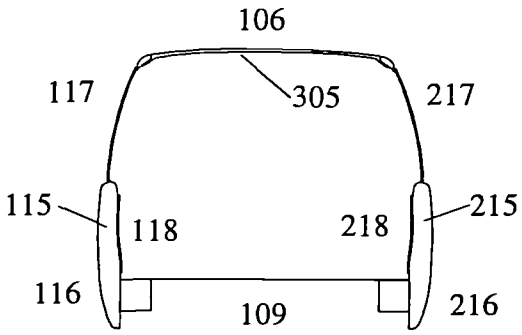

Rear Seat Section

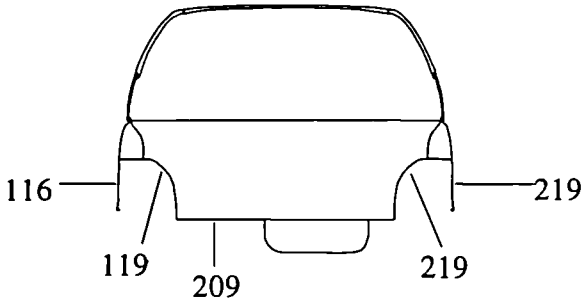

Boot Section

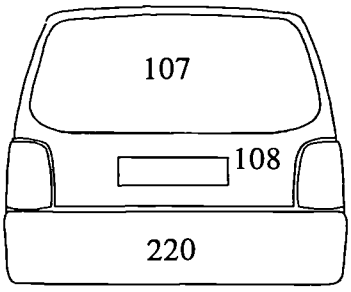

Rear View

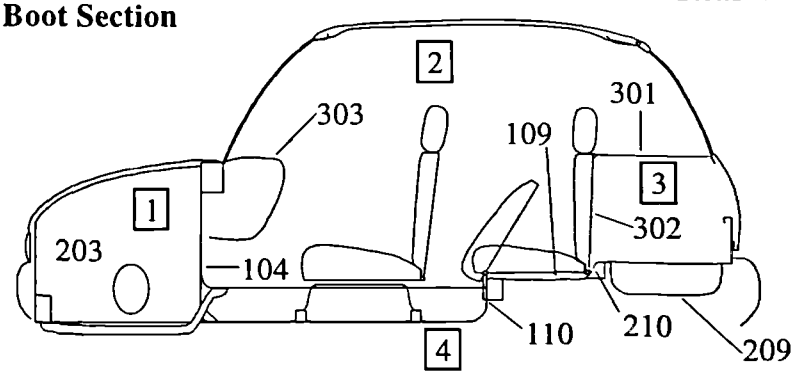

Longitudinal Section

Figure 6.1: Nissan Micra subsystems.

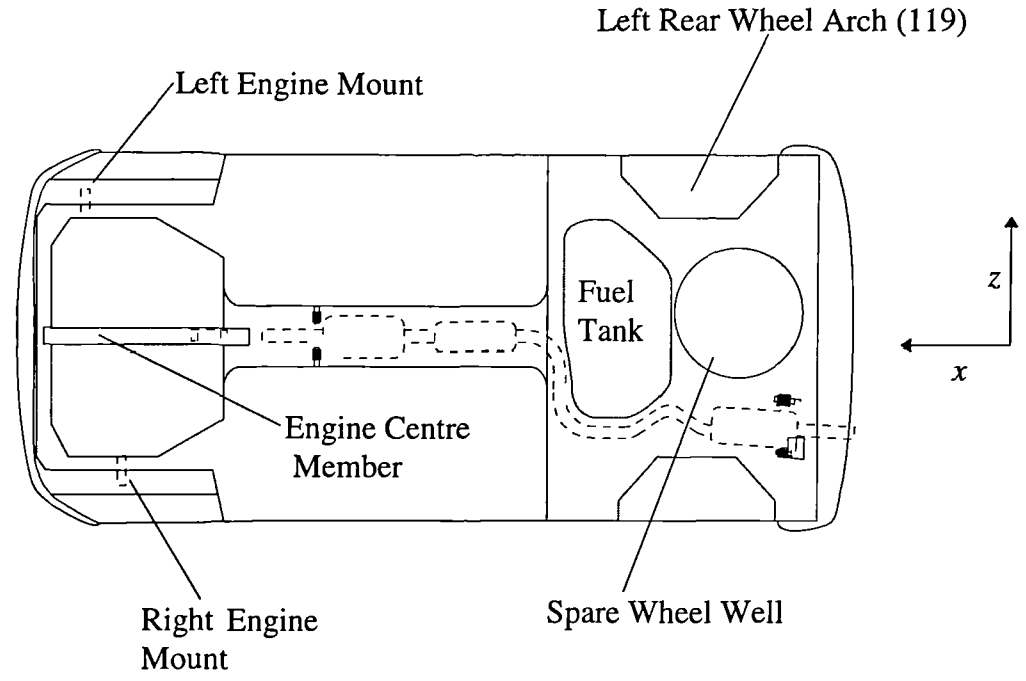

View of Underside

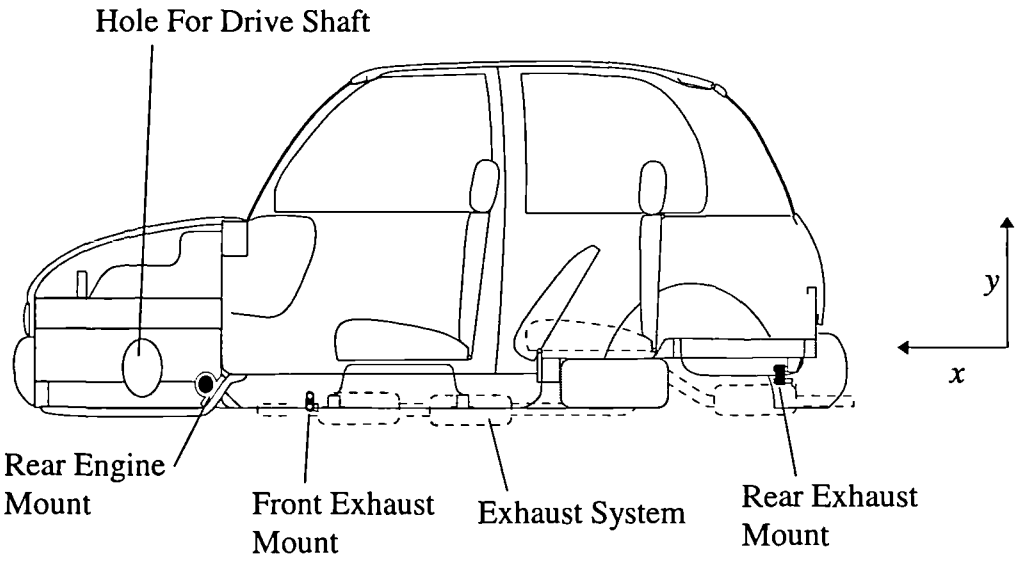

Longitudinal Section

Figure 6.2: Nissan Micra showing exhaust and engine mounts, light grey areas show reinforced parts of the body.

The front wings (102 and 202 of Fig. 6.1) are attached by 7 bolts to the front wheel arch assemblies for ease of replacement in the event of accident damage. Once the body of the

car is assembled it is painted and the underside sprayed with a protective plastic coating. Sheets of damping material approximately 1.5mm thick are applied to the interior of the vehicle on both sides of the floor (111, 211 Fig. 6.1) and to the floor under the rear seat (109). These sheets typically cover approximately two thirds of the panel in question. The windscreen (105) and the rear hatch window (107) are glued in place with an adhesive that sets to a rubber like consistency. Front door windows (114,214) are attached to the electric window mechanism and also guided by felt coated rubber weather strips which fasten around the window frame. Rear side windows are attached by a hinge at one end and a clip mechanism at the other, when closed the clip seals the window against the rubber strip which fits around the window frame. Carpet having a total mass of 4kg covers the floor of the vehicle and the lower part of the firewall (104). Carpet is also placed in the boot covering the spare wheel and the wheel arches. The rear seats consist of steel panels corrugated for rigidity with holes to save weight, they are upholstered with a thick layer of foam covered in velour. To minimise contact the horizontal rear seats (306) are attached to the vehicle by hinges along one edge and a supporting bracket at the other with a clearance to the panel below (109) of approximately 10mm. The vertical rear seat panel is attached at the rear of panel (109) by another hinge arrangement and to the parcel shelf (301) by a detachable hinge. Front seats are constructed of the same materials as the rear seats and are bolted into place. Interior trim is fitted over several areas, the roof is lined with a light composite panel which has a fine brushed finish. Plastic trim panels are attached beneath the rear side windows by snap in plastic fittings designed for rapid assembly. Panels of fibreboard trimmed with fabric are attached to the front doors again using rapid fit plastic studs.

The dash is a complex assembly of plastic mouldings with a layer of plastic coated foam (approx. 10mm thick on average) on the surfaces facing into the car. Into the dash are assembled storage drawers, the ventilation control panel with ventilation ducts and the drivers instrument panel. The total weight of this assembly is approximately 7kg. Further ventilation ducts and the electric fan/heater assembly are attached to the firewall behind the dash. The steering column passes through the firewall near the bottom and is attached at the top via a frame of welded steel tubing. The hole where the steering column passes through the firewall is sealed on either side by rubber boots. A number of cables (e.g. Speedometer, Clutch and Bonnet release cables) pass through holes in the firewall which are also sealed with rubber boots or grommets.

The engine and transmission are assembled into one unit which is connected to the vehicle by three rubber vibration isolators called engine mounts which are shown in Fig. 6.2. Left and right hand engine mounts are attached to reinforced box sections running along the front wheel arches. A 'U' section steel beam known as the engine centre member is connected front and rear across the engine compartment. The rear engine mount is attached to the engine centre member. The exhaust system runs underneath the engine and hangs below the vehicle on 4 rubber loops as shown in Fig. 6.2. these attach to brackets at the front on the left and right floor sections (111,211) and at the rear by brackets on the floor under the boot (209). Suspension components are attached at reinforced areas under the car through rubber bushes. The fuel tank is attached to the floor under the rear seat (109) by straps.

Material properties and dimensions for the Micra panels and compartments are given in Tables (6.1) and (6.2). Many of the panels are not rectangular and some are far from flat so the dimensions have been chosen such that they give approximately the correct surface area.

SUBSYSTEM NUMBER	DISCRIPTION	MATERIAL	DIMENSIONS (mm)	THICKNES (mm)
1	Engine Compartment Volume		900x320x1200 = 0.35m^3	
2	Saloon Volume		1700x1200x1100 = 2.24m^3	
3	Boot Volume		1100x450x600 = 0.3m^3	
4	Under Floor		300x1400x1230 = 0.52m^3	
5	Roof Cavity		1400x870x10 =0.012 m^3	
101	Front Bumper	Plastic	360x2110	3
102	Left Wing	Steel	900x372	0.7
103	Left Wheel Arch	Steel	560x590	0.6
104	Fire Wall	Steel	890x560	0.8/3/0.8/3
105	Wind Screen	Glass	1200x750	4.95
106	Roof	Steel	870x1400	0.65
107	Rear Window	Glass	1200x610	3.1
108	Rear Lower Door	Steel	1110x350	0.6
109	Floor Under Back Seat	Steel	1200x450	0.7
110	Step Floor to 109	Steel	220x1220	0.7
111	Floor Left Side	Steel	510x1230	0.7
112	Left Outer Door Panel	Steel	670x1240	0.7
113	Left Inner Door Trim	Composite	1010x560	3
114	Left Door Window	Glass	760x430	3
115	Left Latch Panel	Steel	430x150	0.7
116	Left Rear Wing	Steel	1060x515	0.7
117	Left Back Window	Glass	660x440	4
118	Left Back Seat Trim	Plastic	650x500	2.5
119	Left Rear Wheel Arch	Steel	620x440	0.65
122	Panel Above Left Rear Window	Steel	1100x100	0.7
123	Left Lower "A" pillar	Steel	100x450	0.7
124	Left Sill	Steel	200x1230	0.7
202	Right Wing	Steel	900x372	0.7
203	Right Wheel Arch	Steel	560x590	0.6
209	Floor of Boot	Steel	1200x450	0.7
210	Step 109 to 209	Steel	220x1220	0.7
211	Floor Right Side	Steel	510x1230	0.7
212	Right Outer Door Panel	Steel	670x1240	0.7
213	Right Inner Door Trim	Composite	1010x560	3
214	Right Door Window	Glass	760x430	3
215	Right Latch Panel ("B" pillar)	Steel	430x150	0.7
216	Right Rear Wing	Steel	1060x515	0.7
217	Right Back Window	Glass	660x440	4
218	Right Back Seat Trim	Plastic	650x500	2.5
219	Right Rear Wheel Arch	Steel	620x440	0.65
220	Rear Bumper	Plastic	1900x420	3
221	Rear Boot Panel	Steel	1200x160	0.7
301	Rear Parcel Shelf	Resin Board	1040x400	5
302	Back Seat Panel	Steel	1000x450	0.6
303	Dash Panels	Plastic		
304	Bonnet	Steel	1310x900	0.7
305	Roof Trim Panel	GRP	1470x1000	2

Table 6.1: Subsystem dimensions and materials.

MATERIAL	DENSITY (kg/m^3)	LONGITUDINAL WAVE SPEED (m/s)	YOUNG'S MODULUS (N/m^2)	POISSON'S RATIO
Steel	7800	5200	2×10^{11}	0.3
Plastic	900	605	3×10^{8}	0.3
Rubber	1180	68	5.5×10^{6}	0.5
Glass	2500	4900	6×10^{9}	0.3
Composite	600	3000	5.4×10^{9}	0.3
Resin Board	600	3000	5.4×10^{9}	0.3
GRP Roof Trim	600	3000	5.4×10^{9}	0.3
Carpet	245 (4mm)			

Table 6.2: Material properties.

6.3. Firewall and Sound Barrier Assembly

One part of the vehicle of particular interest from a noise and vibration point of view is the firewall (104) which separates the engine and passenger compartments. The firewall (104) is formed by a sandwich with two steel panels and two layers of bituminous damping material. A Sound Barrier Assembly (SBA) of the type described by Wentzel&Saha[29] and Powel *et al*[70] is placed against the firewall. The sound barrier assembly consists of a foam isolator attached to a plastic barrier. A section through the firewall and Sound Barrier Assembly is shown in Fig. 6.3.

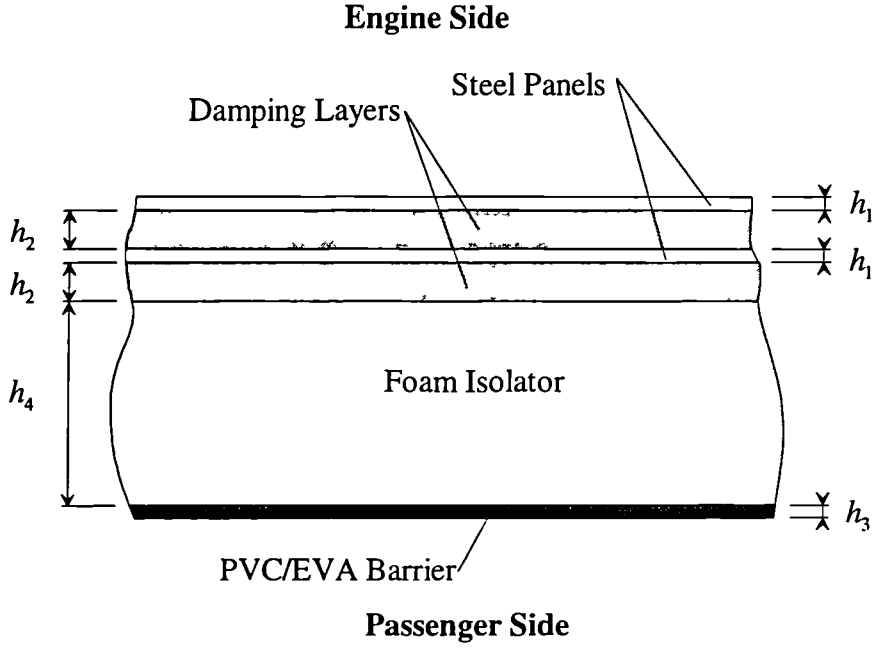

Figure 6.3: Firewall (104) and Sound Barrier Assembly, dimensions are, steel: $h_1 = 0.8\text{mm}$, bituminous damping material: $h_2 = 3\text{mm}$, sound barrier: $h_3 = 2.5\text{mm}$ and foam isolator: $h_4 = 30\text{mm}$.

The properties of the bituminous damping material in the sandwich were unknown. In order to calculate the effective bending stiffness of the composite panel certain assumptions were made. It was assumed that the modulus of rigidity of the filling was sufficiently high as to prevent significant shearing of this layer and maintain simple bending displacement assumptions throughout the composite panel. Using this assumption the bending stiffness due to the steel panels is given by.

$$B = \frac{E_1}{1-\mu_1^2}\left(\frac{h_1^3}{6} + \frac{h_1(h_1+h_2)^2}{2}\right) \tag{6.1}$$

It was assumed that the bending stiffness of the damping layers was negligible in comparison to the steel. The longitudinal stiffness of the composite panel was also assumed to be entirely due to the steel panels which is given by.

$$D = \frac{2\,E_1\,h_1}{1-\mu_1^2} \tag{6.2}$$

Surface density (m) of the composite panel can be calculated by summing the surface densities of the component layers. The contribution of the foam was ignored for this purpose as it was not firmly attached and is unlikely to move as a ridged layer with the panel. The shear stiffness of the composite panel was calculated by summing the shear stiffness of the two steel panels, this gives

$$K_S = \frac{E_1 h_1}{(1+\mu_1)} \tag{6.3}$$

The composite firewall panel was modelled as a single homogeneous panel with thickness h, Young's Modulus E, density ρ, and poisons ratio μ. These properties were calculated by equating surface density and the bending, longitudinal and shear stiffness of the composite and homogeneous panels. The stiffness terms and the surface density of the homogenous equivalent panel are given by.

$$B = \frac{Eh^3}{12(1-\mu^2)}\ ,\ D = \frac{Eh}{(1-\mu^2)}\ ,\ K_S = \frac{Eh}{2(1+\mu)},\ m = \rho h \tag{6.4}$$

Equating the calculated composite values to the homogeneous equations in (6.4) gives four equations in four unknowns which can be solved to give the properties of the equivalent homogeneous panel. poissons ratio for the homogeneous panel is equal to that of the steel panels ($\mu = 0.3$) because only the steel contributes to the stiffness terms. The equivalent homogeneous panel has the following properties: h = 3.87mm, E = 7.93×10^{10} N/m^2, ρ = 4818 m/s^2 and $\mu = 0.3$.

6.3.1. Sound Transmission Through the Firewall and Sound Barrier Assembly

Wentzel&Saha[29] produced an empirical model for predicting sound transmission through the firewall and SBA of motor-vehicles. This model is given in equations (2.93)-(2.95). The homogeneous equivalent panel properties for the Micra firewall were used in this model to predict the Sound Transmission Loss (TL) of the firewall and SBA which is shown in Fig. 6.4. by the dotted line.

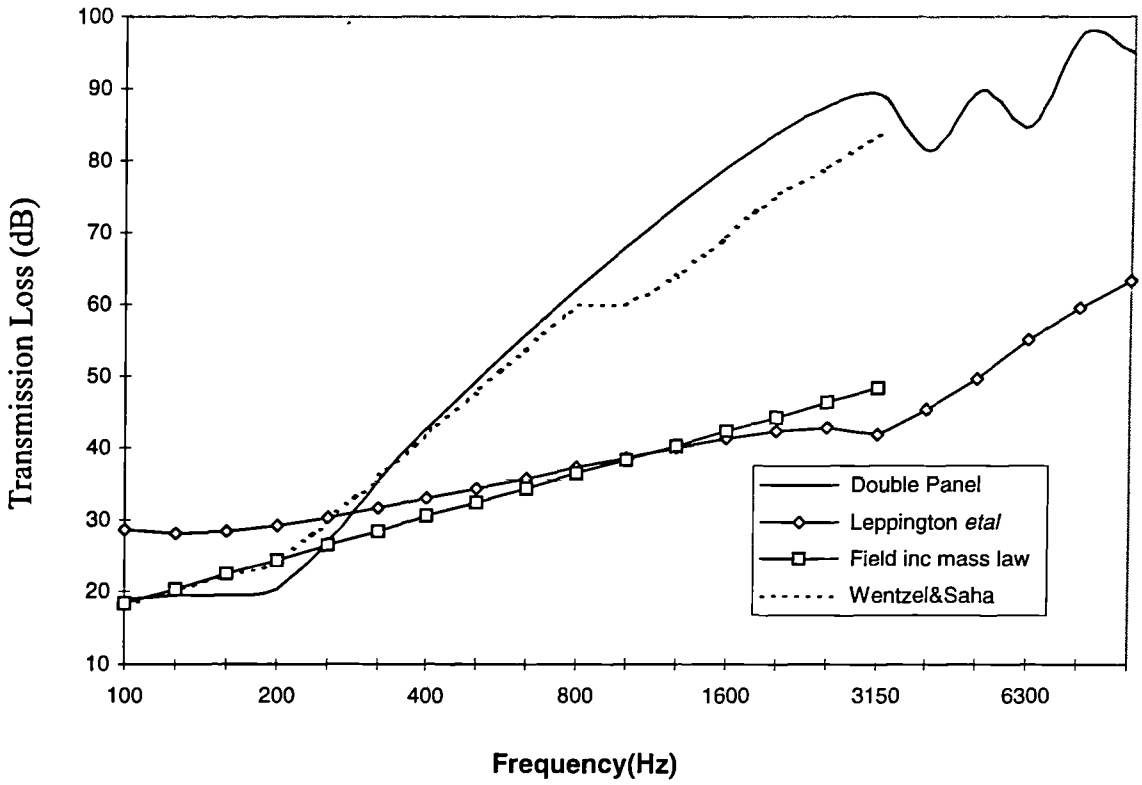

Figure 6.4: Predicted Sound Transmission Loss of firewall(104) and Sound Barrier Assembly.

Three curves are shown in Fig. 6.4 besides Wentzel&Saha's[29] empirical model. A Field incidence mass law prediction for the firewall panel without the SBA attached was calculated using equation (2.89) and is shown on Fig. 6.4 with square markers. Transmission Loss was also predicted for the bare firewall panel using the SEA model shown in Fig. 2.4 which uses equation (2.90) (given by Leppington *etal* [22]) for non resonant transmission and equations (2.80)-(2.82) (given by Leppington *etal* [33]) for resonant coupling. This prediction allows for the finite size of the panel. The solid line in Fig. 6.4 is the TL predicted using a double panel model which includes a finite thickness of elastic material in between the panels. The elastic material in the model joins the two panels, it is assumed homogeneous and can support longitudinal waves or near fields and transverse waves or near fields originating from both panels. This model is a greatly simplified version of one presented by Bolton *et al* [27]. They considered two longitudinal waves in the foam, one largely airborne and the other predominantly travelling in the solid structure of the foam its self. In the model presented here only one longitudinal wave can travel in the foam. The density of the elastic material between the panels in the model was set to 2.2 kg / m^2 and the plain stress longitudinal wave speed to 228 m/s. These values are within the range of those measured by Powel *etal*[70]. Poissons ratio for the elastic material was set to 0.3. These properties and the internal damping of

the elastic material were adjusted to give best agreement with measured Transmission Losses presented by Powel *etal*[70] who measured the TL for a SBA attached to a 0.7mm steel panel. The two panel model gave very good agreement with these results. The double panel model can be used to calculate the TL at frequencies higher than the critical frequency of the firewall panel (3941Hz) above which the empirical model of Wentzel&Saha[29] is not valid. The output from the double panel model is the most use full of the Transmission Losses shown in Fig. 6.4 because it is the only one which takes account of the effects of the SBA and is still valid above the critical frequency of the firewall. For this reason the double panel transmission losses were used in the SEA models. The model was used to calculate the wave transmission coefficient for plane acoustic waves incident upon the firewall panel at oblique angles. These transmission coefficients were numerically integrated from 0° to 78° using equation (2.87) to give the TL. Waves incident at angles greater than 78° are not included because it is assumed that predicted transmission will be more accurate if they are omitted as has been found for field incidence mass law calculations (this is discussed by Leppington *et al*[22]). Agreement between the empirical model and the two panel model was good up to 1kHz, above which the empirically predicted TL is approximately 10dB lower.

A number of tests were conducted to validate the double panel model. When the loss coefficient in the foam and the panels of the model were set to zero the acoustic transmission and reflection coefficients summed to one regardless of the other properties of the foam and panels. The SBA was removed from the double panel model and the TL calculated as described above, the TL matched the field incidence mass law given in equation (2.89) below the critical frequency. Above the critical frequency the TL from the altered model matched the diffuse field expression given by Cremer[19] and quoted by Fahy[20] provided the integration described above is between 0° and 90°. This would suggest that at least the panels in the model have been accurately modelled. Fig. 6.4 shows that the double panel model approaches the single panel field incidence mass law curve at frequencies below the mass-air-mass resonance frequency as it should. When the SBA was included but the foam given the density and longitudinal wave speed of air and the thickness of the panels reduced to an extremely small value the model predicted almost complete transmission as would be expected. The reciprocity of the model was checked by calculating transmission in opposite directions, this showed the transmission to be equal as it should be.

Holes in the firewall will increase sound transmission. There are holes in the firewall for the steering column etc. but as has been mentioned in Section 6.1 they are effectively sealed with rubber boots and grommets. Additional transmission through holes in the firewall was therefore ignored. The TL predictions in Fig. 6.4 do not account for the attenuating effects of the dash assembly (303) or the fans, ducts and steering column framework attached to the firewall. Therefore it is likely that they over predict the transmission between the engine compartment and the saloon. Structural vibration of the firewall will cause it to radiate sound into the dash cavity. The SBA and dash assembly will reduce the radiation into the saloon. There exists no simple method for calculating the effect of the dash assembly and SBA on the radiation efficiency of the firewall. In both the SEA models described in this chapter the radiation coupling from the firewall directly into the saloon was not included.

6.4. Basic SEA Model

Two SEA models of the Micra were constructed using the techniques described in Chapters 2 and 3. Both models had only acoustic and flat plate bending modes as subsystems, couplings were point, line and area (acoustic). The basic model described in this section contains only simple 90° line joints whereas the second model uses the more detailed joint modelling techniques described in Chapter3. Computer software called PPC was used to construct and analyse the SEA models, complex joint transmission was calculated using separate software and the results fed into PPC.

The basic model contained 48 subsystems 4 of which are acoustic volumes and 44 of which are flat thin panels. Although the vehicle exhibits a large degree of symmetry the power inputs are not necessarily symmetric therefore the whole vehicle was modelled. An SEA model of this size dose not represent a heavy computational burden on a modern PC. Only bending wave energy is considered in the structural subsystems.

The first and most important criterion that an SEA subsystem must satisfy is that there are resonant modes within the frequency range of interest. The modal density of all the panels listed in Table (6.1) are given using Equation (2.46) in Table (6.3) along with the

predicted first resonance frequency. Since some of the panels radiate into the acoustic spaces of the vehicle the critical frequencies are also given in Table (6.3). Where panels are mirrored left and right only left hand panels are listed as the properties of the right hand panels are identical.

SUBSYSTEM	MODAL DENSITY (1/HZ) $= 1/\Delta f$	FIRST NATURAL FREQUENCY (HZ)	CRITICAL FREQUENCY (HZ)	INTERNAL LOSS FACTOR
101	0.690 = 1/1.45	6.6	35724	0.03
102	0.159 = 1/6.29	14.0	17820	0.001
103	0.183 = 1/5.46	8.6	20790	0.02
104	0.104 = 1/9.62	16.8	3941	0.04
105	0.0636 = 1/15.7	27.5	2648	0.03
106	0.624 = 1/1.60	2.8	19190	0.001
107	0.0835 = 1/12.0	23.3	4270	0.03
108	0.216 = 1/4.63	12.7	20790	0.02
109	0.257 = 1/3.89	9.3	17820	0.02
110	0.128 = 1/7.81	35.2	17820	0.001
111	0.298 = 1/3.36	7.4	17820	0.02
112	0.395 = 1/2.53	4.8	17820	0.02
113	0.540 = 1/1.85	3.4	35724	0.03
114	0.0385 = 1/26.0	47.6	4413	0.02
115	0.0307 = 1/32.6	82.3	17820	0.001
116	0.260 = 1/3.85	7.69	17820	0.001
117	0.0503 = 1/19.9	33.8	6486	0.01
118	0.343 =1/2.92	4.7	42869	0.03
119	0.130 = 1/7.69	12.8	17820	0.02
122	0.0523 = 1/19.1	166.4	17820	0.001
123	0.0214 = 1/ 46.7	173.2	17820	0.001
124	0.117 = 1/8.54	42.4	17820	0.001
220	0.761 = 1/1.31	4.9	35724	0.03
301	0.0801 = 1/12.5	29.3	7207	0.01
302	0.214 = 1/4.67	9.8	17820	0.02
304	0.561 = 1/1.78	3.0	17820	0.02
305	0.424 = 1/2.36	4.0	10811	0.01
306	0.214 = 1/4.67	9.8	17820	0.02

Table 6.3: Properties of panel subsystems.

The majority of the panels have a first resonance below 50Hz and a modal density greater than 0.1 modes/Hz which means there will usually be more than 3 resonant modes in the 125Hz $1/3^{rd}$ octave band. Panel resonance frequencies are calculated using (2.44) which assumes simply supported flat rectangular panels. Many of the panels on the actual vehicle are curved, this will increase the first natural frequency and reduce the modal density below the ring frequency. Table (6.4) shows the approximate number of resonant modes within selected $1/3^{rd}$ octave frequency bands for a curved panel of radius 0.5m. The area of the curved plate was chosen so as to give a fat plate modal density of 0.1 modes/Hz because most of the panels in Table (6.3) have a higher value than this. A steel panel with a 0.5m radius of curvature has a plain strain ring frequency of around 1579Hz. At 250Hz the modal density of the curved panel is roughly one quarter that of a flat panel with the same area, thickness and material properties. At the ring frequency (1579Hz)

the modal density of the curved panel is approximately two thirds of the equivalent flat plate value.

1/3rd octave band	250 Hz	500 Hz	1000 Hz	1600 Hz
No of modes (Flat)	5.8	11.5	22.5	37.5
No of modes (0.5m)	1.4	3.8	11.3	25

Table 6.4: Number of resonant modes within selected 1/3rd octave bands for 0.5m radius steel panel and equivalent flat panel.

These values were calculated using the modal densities for curved panels given by Langley[104]. Most of the curved panels on the Micra have a higher radius of curvature than 0.5m so the reduction in modal density will be less than shown in Table (6.4). Modal density for the saloon volume, boot and the space under the car were calculated using (2.47) and are shown in Table (6.5). Also presented in Table (6.5) are predicted first resonance frequencies calculated as given by Craik[61]. Equation (2.48) was used to calculate the modal density of the cavity between the roof and the trim panel because the first cross resonance occurs outside the frequency range of interest at approximately 17kHz. The average modal density of an acoustic space is a function of frequency so values are given at three frequencies for modal densities of acoustic spaces in Table (6.5). Acoustic reverberation times used in the SEA models are also given in Table (6.5).

SUBSYSTEM.	MODAL DENSITY (1/Hz) = $1 / \Delta f$			f_1 (HZ)	T_{60} (S)
	125Hz	500Hz	2000Hz		
Saloon (2)	0.0342 = 1/ 29.2	0.250 = ¼.0	3.08= 1/0.325	100.9	0.05
Boot (3)	0.00934= 1/107	0.0453= ½2.08	0.449= 1/22.3	155.9	0.046
Under Car (4)	0.0152= 1/65.8	0.0780= 1/12.8	0.782= 1/1.28	122.5	0.05
Roof Cavity (5)	0.00009=1/11100	0.0208= ¼8.1	0.0848= 1/11.8	122.5	n/a

Table 6.5: Modal densities, first resonance frequencies and reverberation times for acoustic subsystems.

6.4.1. Standard Coupling Loss Factors

The Couplings Loss Factors for the basic model assumed relatively simple joint configurations. Structural coupling between the panels was treated either as point or line contacts. Hinges connecting doors etc. were treated as point force couplings as were some of the trim attachments. Equation (2.76) was used in conjunction with the impedance of the panels (given by equation(2.27)) to calculate the CLF. All but one of the line couplings were calculated using the configurations shown in Fig. 6.5.

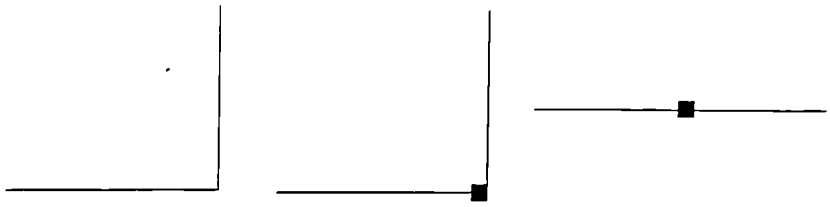

(a) Corner (b) Corner with elastic layer (c) Inline elastic layer

Figure 6.5: Basic SEA model line coupling.

Transmission coefficients for all the joints in Fig. 6.5 were calculated considering only bending wave transmission methods given by Cremer[1]. The simplest of these (Fig. 6.5 (a)) is described in Section 2.8.5 The elastic layers were assumed to be of square cross section, 10 x 10 mm in size which is reasonably representative of the real dimensions and likely to give bending longitudinal and shear stiffness similar to the actual window seals. Material properties for the rubber are given in Table (6.6).

Leppington *et al*'s[33] equations (2.80)-(2.82) for panel radiation were used to calculate the coupling between the panels and the acoustic volumes. The SEA reciprocity relation (2.63) was then used to calculate the coupling from the volumes back to the panels. Panel boundaries were assumed to be clamped when calculating there radiation efficiencies, this increases the radiation below the critical frequency by a factor of two as shown by Leppington *et al*[34] and discussed in Section 2.8.2. Radiation efficiencies were calculated assuming the panels were surrounded by perpendicular baffles, this introduces a further factor of two increase in the sub critical radiation as shown by Leppington *et al*[35]. The correction factors were introduced using equation (2.84). Subsystem five is a narrow cavity between the roof panel and the trim. Coupling across this cavity between the roof and the saloon is modelled as shown in Fig. (2.5) except that the air spring coupling was not included which gives Crocker&Price's[25] model. This includes non resonant transmission through the panels below there critical frequencies. The joint configurations in the basic model are given in Table (6.6), where a joint is duplicated left and right only the left hand joint is given.

SUBSYSTEMS	TYPE	DIMENSIONS. / NO OF POINTS
(106-105)roof - windscreen	Line(c)	L = 1.2m
(105-104)windscreen - Firewall	Line(b)	L = 0.89m
(108-107)Hatch - Hatch window	Line(c)	L = 1.2m
(116-117)LR wing - LR window	Line(c)	L = 0.66m
(117-122)	Line(c)	L = 0.66m
(111-110)L Floor - Step	Line(a)	L = 0.51m
(110-109)	Line(a)	L = 1.2m
(109-210)	Line(a)	L = 1.2m
(210-209)	Line(a)	L = 1.2m
(211-111)L Floor - R Floor	Line(a)	L = 1.0m
(111-104)L Floor - Firewall	Line(a)	L = 0.51m
(209-119)Boot floor - LR wheel arch	Line(a)	L = 0.62m
(109-116)	Line(a)	L = 0.45m
(122-106)	Line(a)	L = 0.66m
(112-113) L Door panel - Door trim	Line(a)	L = 1.0m
(116-115) LR Wing - L B-Pillar	Line(a)	L = 0.5m
(102-103) LF Wheel arch - LF Wing	Line(a)	L = 0.6m
(103-104) LF Wheel arch - Fire wall	Line(a)	L = 0.6m
(119-116) LR Wheel arch - LR Wing	Line(a)	L = 0.3m
(111-124) L Floor - L Sill	Line(a)	L = 1.23m
(124-116) L Sill - LR Wing	Line(a)	L = 0.15m
(111-123) L Floor - L A-Pillar	Line(a)	L = 0.15m
(124-115) L Sill - L B-Pillar	Line(a)	L = 0.05m
(124-123) L Sill - L A-Pillar	Line(a)	L = 0.1m
(111-116) L Floor - LR Wing	Line(a)	L = 0.15m
(116-110)	Line(a)	L = 0.22m
(116-122) LR Wing - Panel above LR window	Line $(\langle \tau \rangle = 1)$	L = 0.1
(104-103) Fire wall - Bonnet	Point	2
(118-116) LR Trim - LR Wing	Point	3
(118-115) LR Trim - L B-Pillar	Point	1
(102-101) LF Wing - Bumper	point	1
(104-303) Fire wall - Dash	Point	16
(306-210) R Seat - Step	Point	2
(123-112) L A-Pillar - L Door panel	Point	2
(115-112) L B-Pillar - L Door Panel	Point	1
(112-114) L Door - L Door window	point	2
(106-5) Roof - Cavity	Radiation	S = 1.218 m^2, U = 4.54m
(305-5) Roof trim - Cavity	Radiation	S = 1.47 m^2, U = 4.94m
(108-3) Hatch panel - Boot	Radiation	S = 0.388 m^2, U = 2.92m
(116-3) LR Wing - Boot	Radiation	S = 0.546 m^2, U = 3.15m
(119-3) LR Wheel arch - Boot	Radiation	S = 0.273 m^2, U = 2.12m
(209-3) Boot floor - Boot	Radiation	S = 0.549 m^2, U = 3.34m
(301-3) Parcel shelf - Boot	Radiation	S = 0.416 m^2, U = 2.88m
(302-3) Seat panel - Boot	Radiation	S = 0.45 m^2, U = 2.9m
(301-2) Parcel shelf - Saloon	Radiation	S = 0.416 m^2, U = 2.88m
(303-2) Dash - Saloon	Radiation	S = 1.156 m^2, U = 4.360m
(305-2) Roof trim - Saloon	Radiation	S = 1.47 m^2, U = 4.94m
(105-2) Windscreen - Saloon	Radiation	S = 0.9 m^2, U = 3.9m
(107-2) Hatch window - Saloon	Radiation	S = 0.732 m^2, U = 3.62m
(111-2) Floor - Saloon	Radiation	S = 0.627 m^2, U = 3.48m
(113-2) L inner door panel - Saloon	Radiation	S = 0.566 m^2, U = 3.14m
(114-2) L Door window - Saloon	Radiation	S = 0.327 m^2, U = 2.38m
(117-2) LR Window - Saloon	Radiation	S = 0.29 m^2, U = 2.2m
(118-2) LR Trim - Saloon	Radiation	S = 0.3 m^2, U = 2.2m
(2-301-3) Saloon - Boot via Parcel shelf	Non Resonant	S = 0.416 m^2
(2-305-5) Saloon - Cavity via Roof trim	Non Resonant	S = 1.47 m^2
Rubber in elastic layer 10 x 10mm, c_L=68 m/s, ρ =1180kg/m^3, μ = 0.3, η=0.0 in basic model, η=0.1 in complex joint model		

Table 6.6: Couplings for basic joint Micra SEA model.

6.4.2. Total Loss Factors

The TLF of a subsystem is equal to the ILF plus the sum of CLFs out of the subsystem. Internal Loss Factors are inputs to the SEA model. Panel ILFs were assumed constant across the frequency range. The values of panel ILFs were adjusted so as to give reasonable agreement between measured and predicted TLFs. This was done manually by trial and error taking care to keep the ILF values within realistic limits for the materials in question. TLFs for most of the panels and volumes were measured using the decay rate techniques described in Section 4.5. Some of the measured and predicted TLFs are shown in Figs.6.15-6.21. Different panels of the same material, thickness and level of damping treatment were assumed to have the same ILFs. Some of the ILFs have been categorised in Table (6.7), all the panel ILFs are given in Table (6.3) including those which do not fall into one of these categories.

PANEL TYPE	INTERNAL LOSS FACTOR
Untreated Steel	0.001
Steel - One unconstrained damping Layer	0.02
Plastics	0.03

Table 6.7: Panel types with the same Internal Loss Factors.

The reverberation time of the acoustic subsystems in the SEA model were assumed constant with respect to frequency. Reverberation time measurements were carried out in the saloon of the vehicle using the methods described in Section 4.5.1. Measured reverberation times were converted into TLFs using equation (2.35) which are shown in Fig. 6.6.

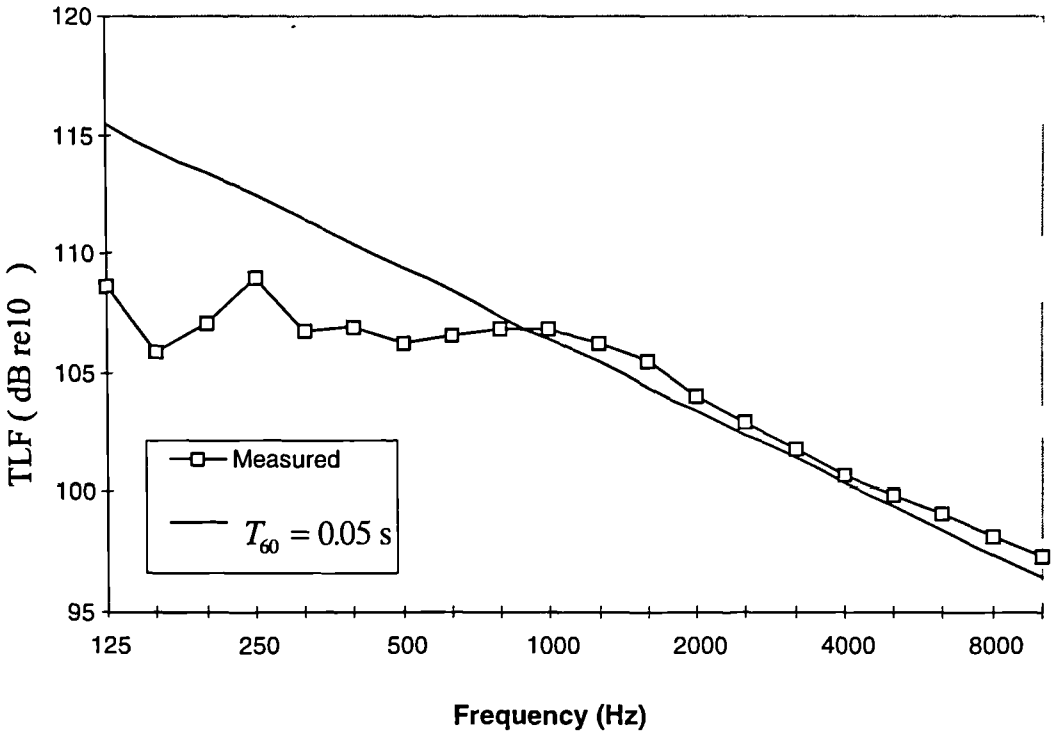

Figure 6.6: TLF of saloon (2).

Fig. 6.6 also shows the TLF corresponding to a reverberation time of 0.05 s which is the value used for the saloon in the SEA model. The constant reverberation time is a good approximation above 800Hz but would appear to over estimates the saloon damping below this frequency. Sound Pressure Levels predicted using this approximation would be around 7dB lower than they should be at 125Hz if the measured TLF is correct. The saloon reverberation damping measurements are only meaningful if there are modes present in the saloon. Table (6.5) gives the first natural frequency of the saloon as 101Hz based on the assumption that the saloon is a rectangular box with hard surfaces which has similar dimensions and the same volume as the actual saloon. This is a large approximation but it would certainly suggest that there will be resonant modes in the saloon well below 800Hz. Another possible cause of errors in saloon reverberation time damping measurements could result from body and trim panels which are coupled to the saloon. If a coupled panel is less heavily damped than the saloon then its vibration level will decay slower than the SPL in the saloon. The panel may then dominate the decay of saloon SPL by acoustic radiation. This would mean that the measured TLF would be that of the panel rather than the saloon. There are a number of panels such as the windscreen (Fig. 6.18) which have a TLF of around 107 dB which is approximately the measured saloon TLF below 800Hz. There is a degree of uncertainty therefore in the measured saloon TLF.

The reverberation time used in the SEA models for the other cavities were not based on direct measurements but rather calculated as described below. Equations (2.35) and (2.36) show that the ILF of an acoustic volume due to absorption at surfaces is proportional to surface area and inversely proportional to volume. Although the boot is smaller than the saloon it has a similar surface area to volume ratio. Using this fact and assuming that the average surface absorption coefficient in the saloon is the same as that of the boot infers that the ILF of the boot and saloon are equal. Adding the CLFs from the boot gives the boot TLF. Converting the boot TLF into a reverberation time gives a value of around 0.046 s over most of the frequency range and this is the value which was used in the SEA model. Equation (2.35) was used to calculate the reverberation time for the volume under the vehicle by assuming an absorption coefficient of 1 for the open sides and 0 for under side of the car and the ground. This gives T_{60}= 0.05 s. The TLF for the roof cavity was approximated by summing the CLFs and doubling this value. T_{60} reverberation times for the acoustic subsystems used in the Micra models are given in Table (6.5).

6.5. Complex Joint SEA Model

A second SEA model of the Nissan Micra was constructed where the joints were modelled using the theories described in Chapter 3. Two of the panel subsystems of the basic model are omitted from the complex joint model, these are the two small steps in the floor of the car labelled 110 and 210 in Fig. 6.1. The elastic layers in the complex joint model have an internal loss factor of 0.1 as opposed to zero in the basic model. The other subsystems are assumed to have the same dimensions and properties as those of the basic model which are given in Tables(6.1-6.5). Point coupling between panels and all the acoustic couplings were calculated in exactly the same way as in the basic model. Bending to bending wave transmission coefficients for both the complex joint model and the basic model were averaged using equation (2.96) and are shown in Figs. 6.7 -6.14 in dB. Also shown in these figures are diagrams of the complex joint models themselves.

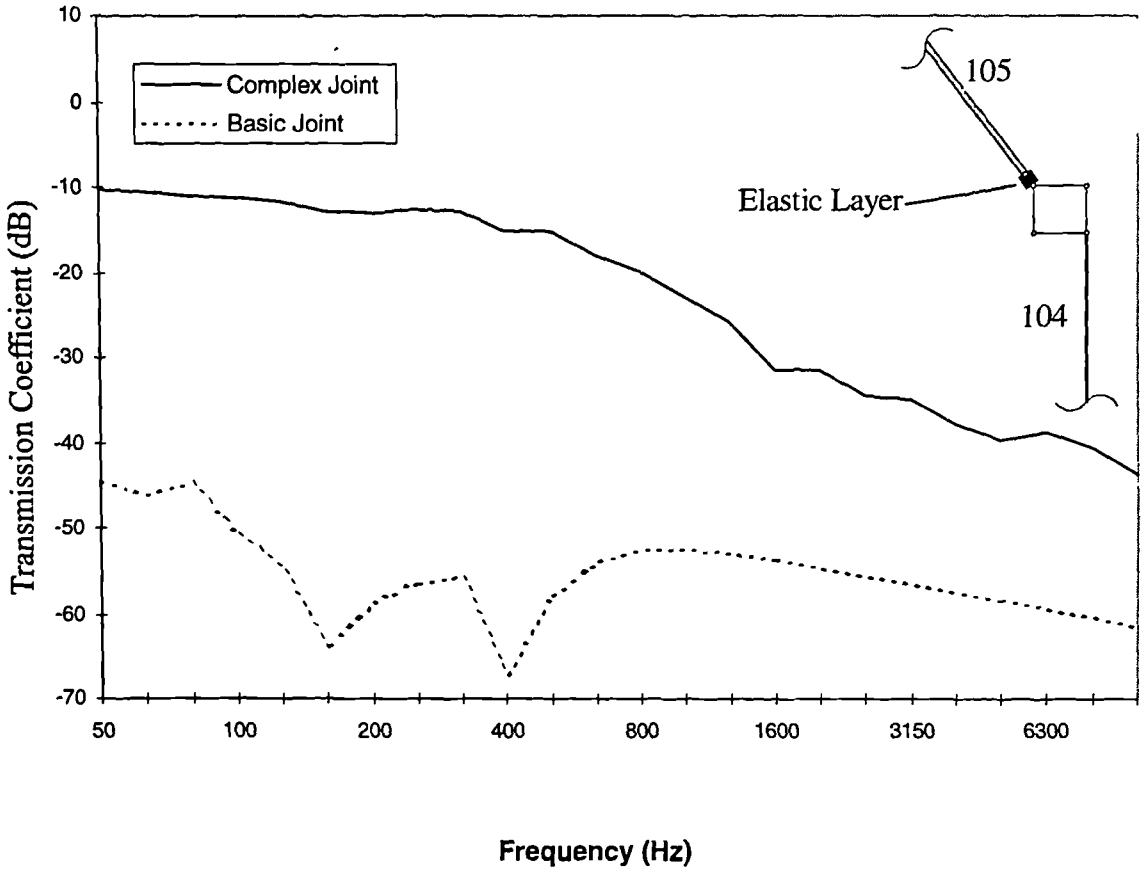

Figure 6.7: Average bending to bending wave transmission coefficient from firewall to windscreen (104-105)using the complex joint model and basic joint shown in Fig. 6.5(b).

The bending wave transmission from the firewall to the windscreen predicted using the complex joint model is higher than that given by the basic model particularly at low frequency. The transmission coefficients calculated using the complex joint models in Figs. 6.7 -6.14 produce jagged lines. This is because of the resonance effects present in the complex joint predictions, these can give rise to rapidly changing values even when transmission is averaged in 1/3rd octave bands. Complex joint transmission coefficients plotted in narrow frequency bands vary more smoothly with frequency as can be seen in Fig. 3.14 which shows the bending wave transmission across the roof to windscreen joint for a normally incident wave. Random incidence bending wave transmission in 1/3rd octaves for the roof to windscreen joint is shown below in Fig. 6.8.

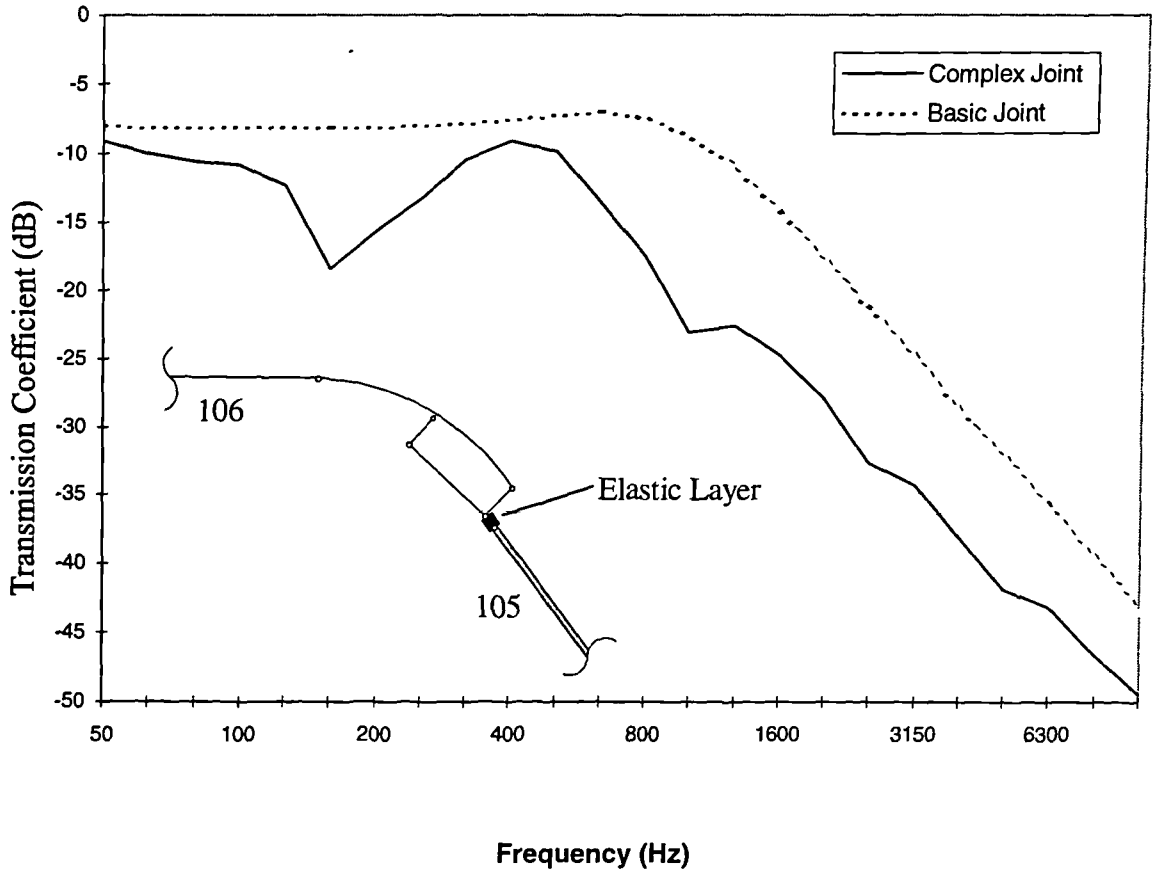

Figure 6.8: Average bending to bending wave transmission coefficient from roof to windscreen (106-105) using the complex joint model and basic joint shown in Fig. 6.5(c).

The dimensions and material properties of the roof to windscreen joint are given in Section 3.11. The bending wave transmission predicted between the roof and windscreen by the complex joint model is around 5-10 dB lower that that predicted by the basic joint model.

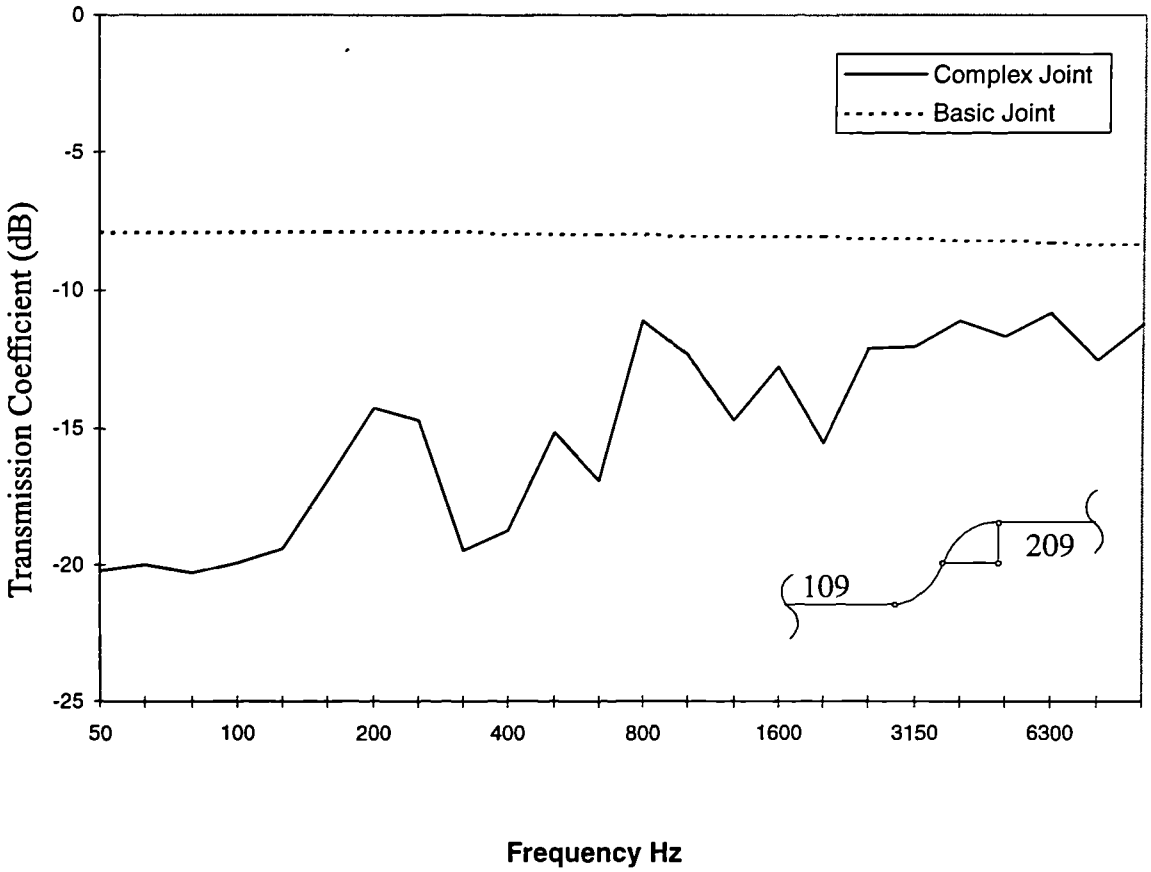

Figure 6.9: Average bending to bending wave transmission coefficient from floor under rear seat to boot floor panel (109-209) using the complex joint model and effective average transmission coefficient using simple joint SEA model.

In the basic model the transmission from the floor under the rear seat (109) to the boot floor panel (209) is via a small step panel (subsystem 210). The average transmission coefficient between (109 and 210) and between (210 and 209) is -4.8dB, which is the value for a corner joint between identical panels. SEA can be used to calculate the effective average transmission coefficient between (109 and 209), this is shown by the dotted line in Fig. 6.9. The effective transmission coefficient predicted using the basic SEA model varies slightly with frequency despite the fact that transmission into and out of (210) is constant with respect to frequency, this is because of damping in (210). Subsystem (210) was not required in the complex joint SEA model.

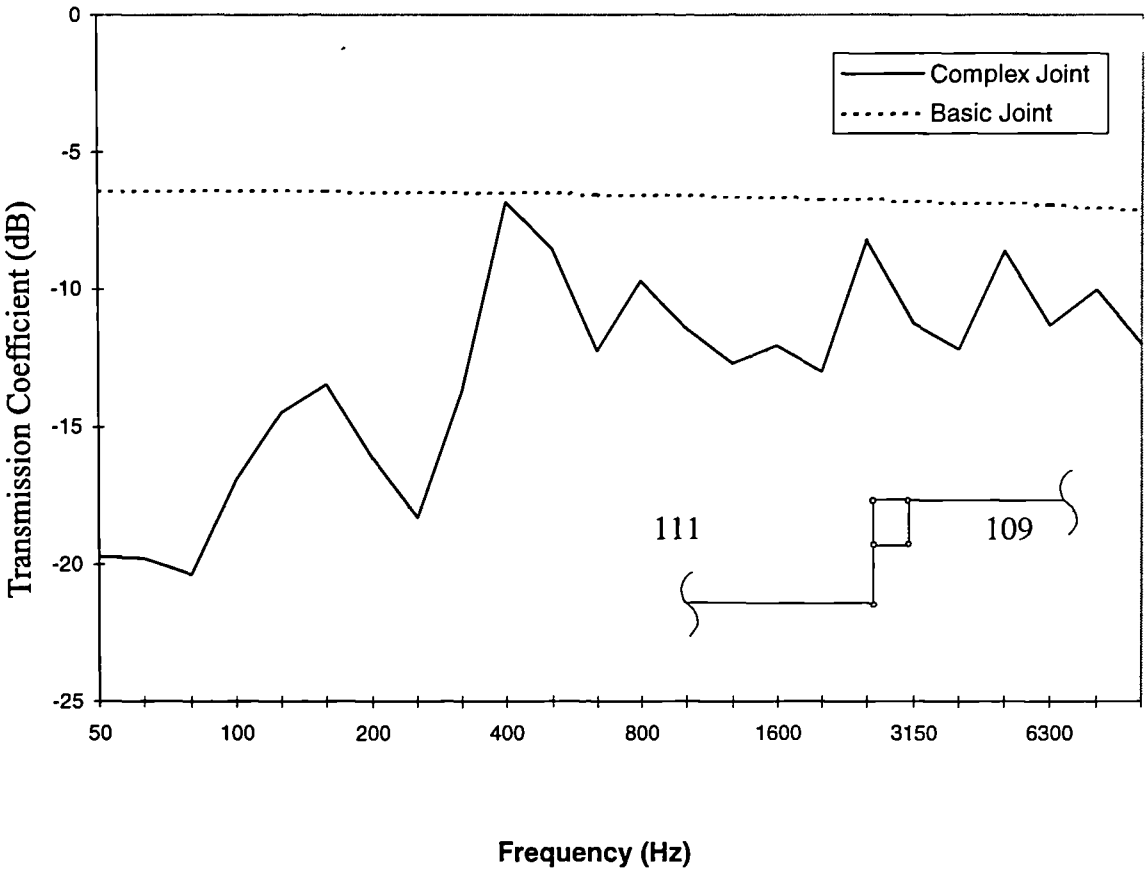

Figure 6.10: Average bending to bending wave transmission coefficient from floor to floor under rear seat (111-109) using the complex joint model and effective average transmission coefficient using simple joint SEA model.

Fig. 6.10 shows a diagram of the panel arrangement at the joint between the floor panels (111 and 211) and the floor under the rear seat (109). In the basic SEA model an extra panel is included (110) in order to calculate transmission. The same method was used to calculate the effective transmission between (111 and 109) as described above for (109 and 209).

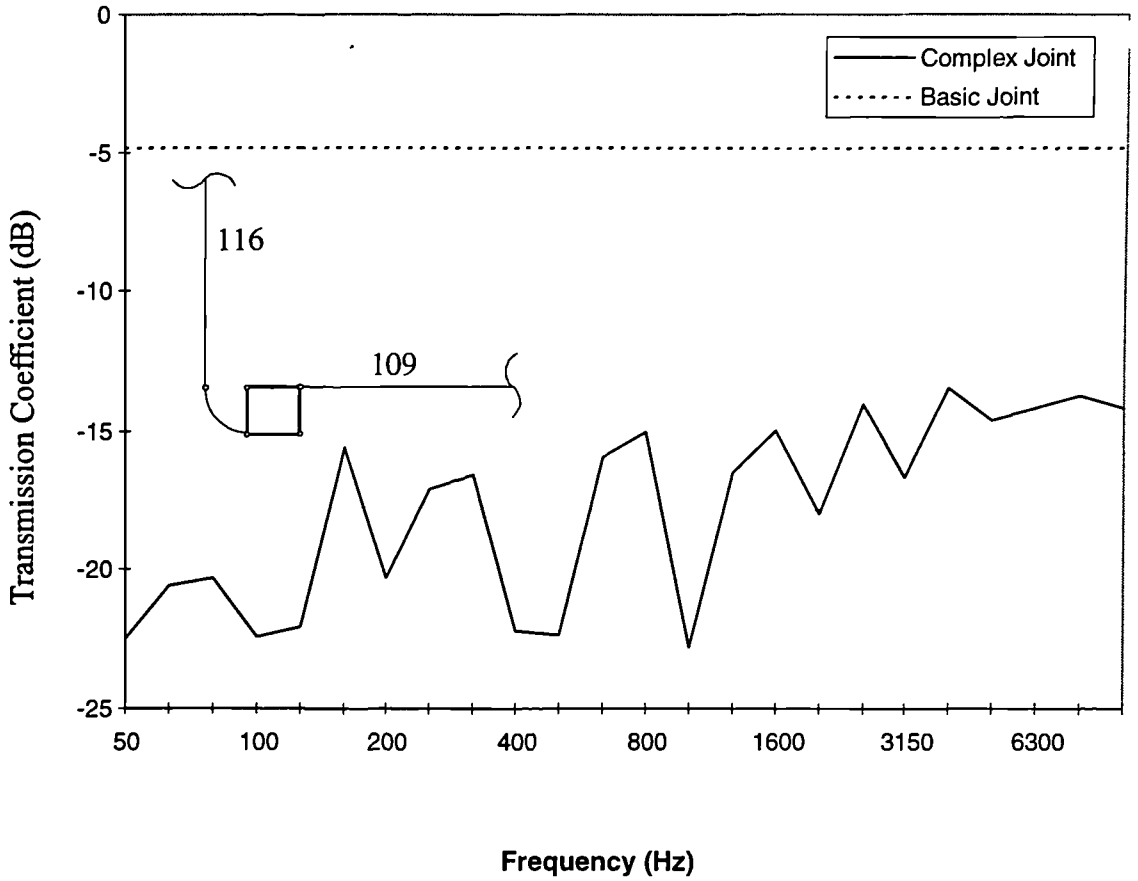

Figure 6.11: Average bending to bending wave transmission coefficient from floor under rear seat to rear wing (109-116) using the complex joint model and basic joint shown in Fig. 6.5(a).

Fig. 6.11 shows a diagram of the complex joint model used to calculate the bending wave transmission between the floor under the rear seat and the rear wing. This joint includes a box section which is used to reinforce the structure of the vehicle at the points where the rear suspension is attached. The box section is constructed of thicker (1.4mm) steel, this reduces the transmission which is around 10-15dB lower than that predicted by the simple joint shown in Fig. 6.5(a).

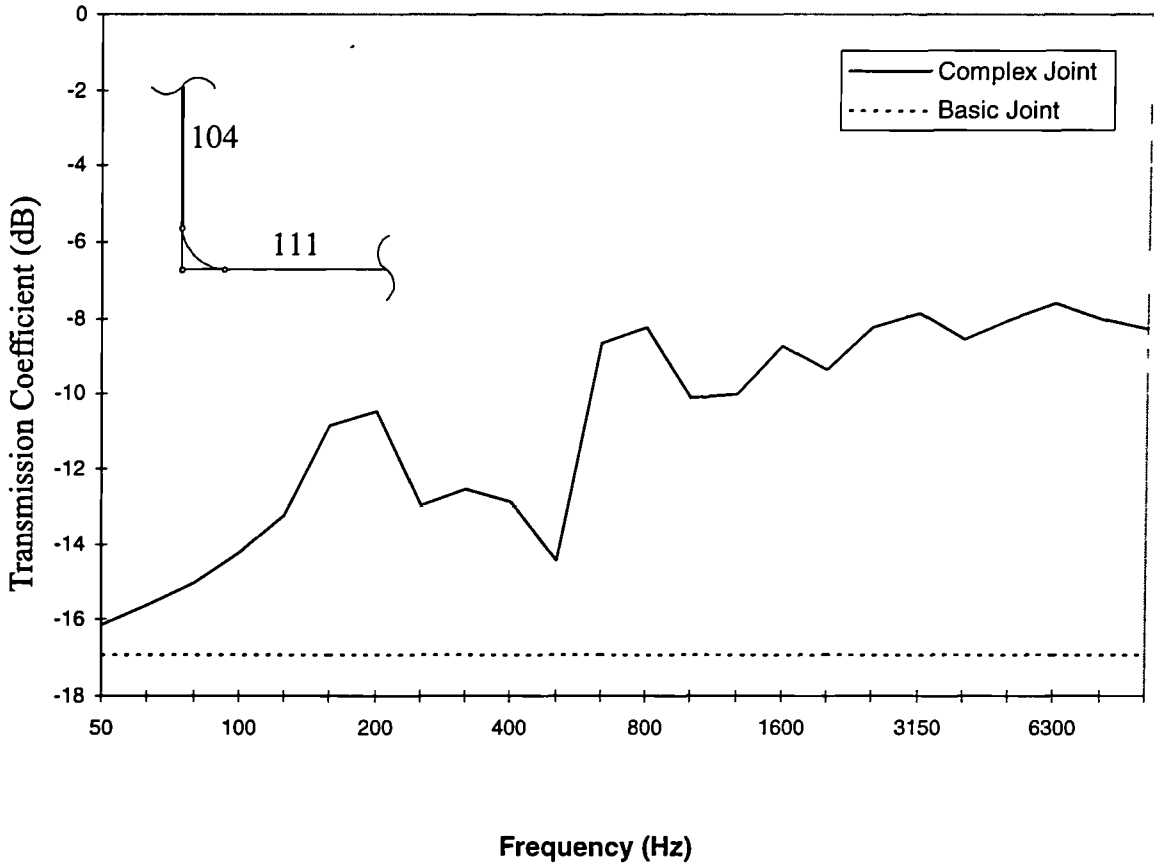

Figure 6.12: Average bending to bending wave transmission coefficient from floor to firewall (111-104) using the complex joint model and basic joint shown in Fig. 6.5(a).

Fig. 6.12 Shows that the complex joint model predicts stronger transmission than the simple corner joint. The firewall is of a sandwich construction as discussed in Section 6.2 this produces a large mismatch in wave impedance between the firewall and the floor panels which is why the simple corner joint transmission is low. This joint is important in the transmission of engine noise in the car as discussed later in Section 6.5.3.

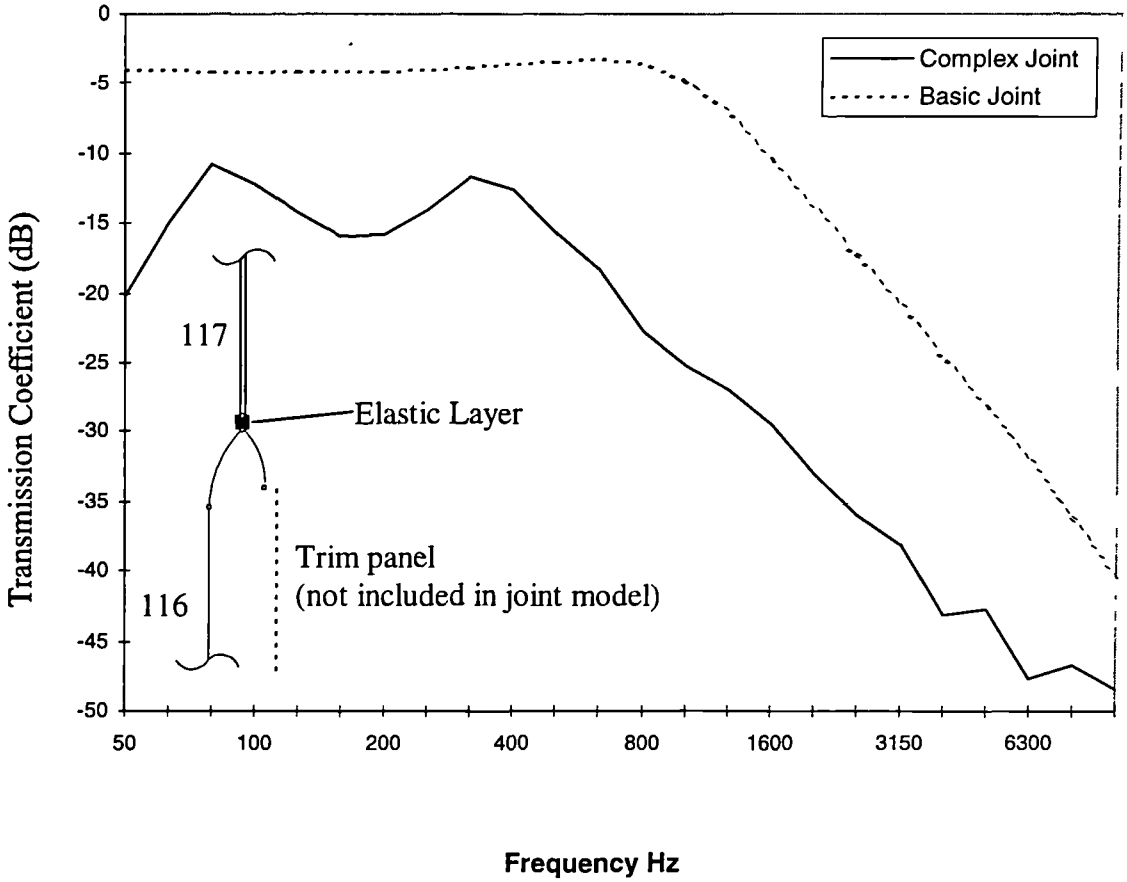

Figure 6.13: Average bending to bending wave transmission coefficient from rear wing to rear side window (116-117) using the complex joint model and basic joint shown in Fig. 6.5(c).

Fig. 6.13 shows that the complex joint model gives 10-20 dB lower transmission than the basic model between the rear wing panels and the rear side windows. The diagram of the complex joint model in Fig. 6.13 shows the rear side trim panel which is attached to the curved section of metal on the right hand side of the elastic layer by fastening studs in the car. This trim panel was not included in the complex joint model for calculating transmission between the rear wing and the rear side window.

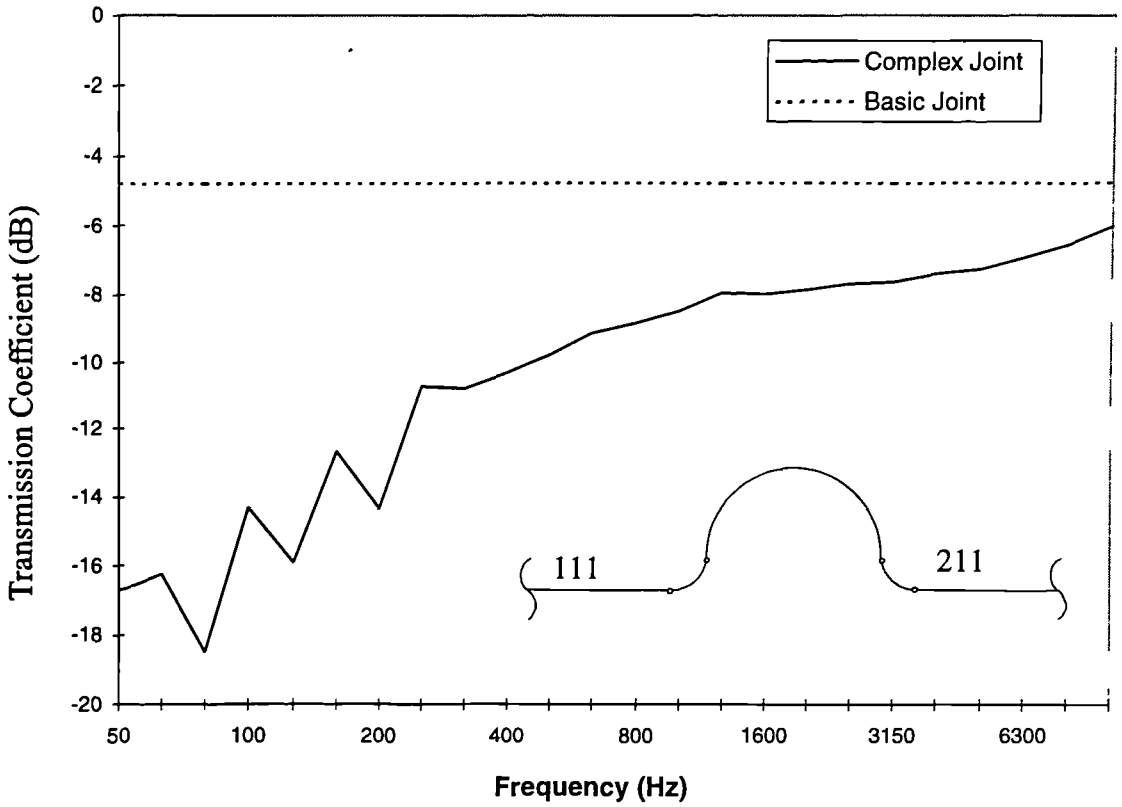

Figure 6.14: Average bending to bending wave transmission from left to right floor panels (111-211) using the complex joint model and basic joint shown in Fig. 6.5(a).

Predicted average bending to bending wave transmission coefficients between the left and right front floor panels (111-211) are shown in Fig. 6.14 . This joint will probably be less influential in predicting noise and vibration levels when the car is in operation as the power inputs will probably be relatively if not completely symmetric.

6.6. Results

The measured and predicted results in this section are of three types. Total Loss Factors of various body and trim panels were measured using the reverberation time technique described in Chapter 4, predicted TLFs from both SEA models are also presented. The TLF of the saloon has already been given in Fig. 6.6 Measured and predicted Acceleration Level Differences were measured by tapping the source panel with a hammer and measuring panel response with accelerometers as described in Chapter 4. Predicted ALDs are given for comparison from both the simple and complex joint SEA models. Finally measured and predicted Sound Pressure Levels in the saloon due to engine noise are presented.

6.6.1. Total Loss Factors

Measured and predicted TLFs for a selection of panel subsystems are shown in Figs. 6.15-6.21.

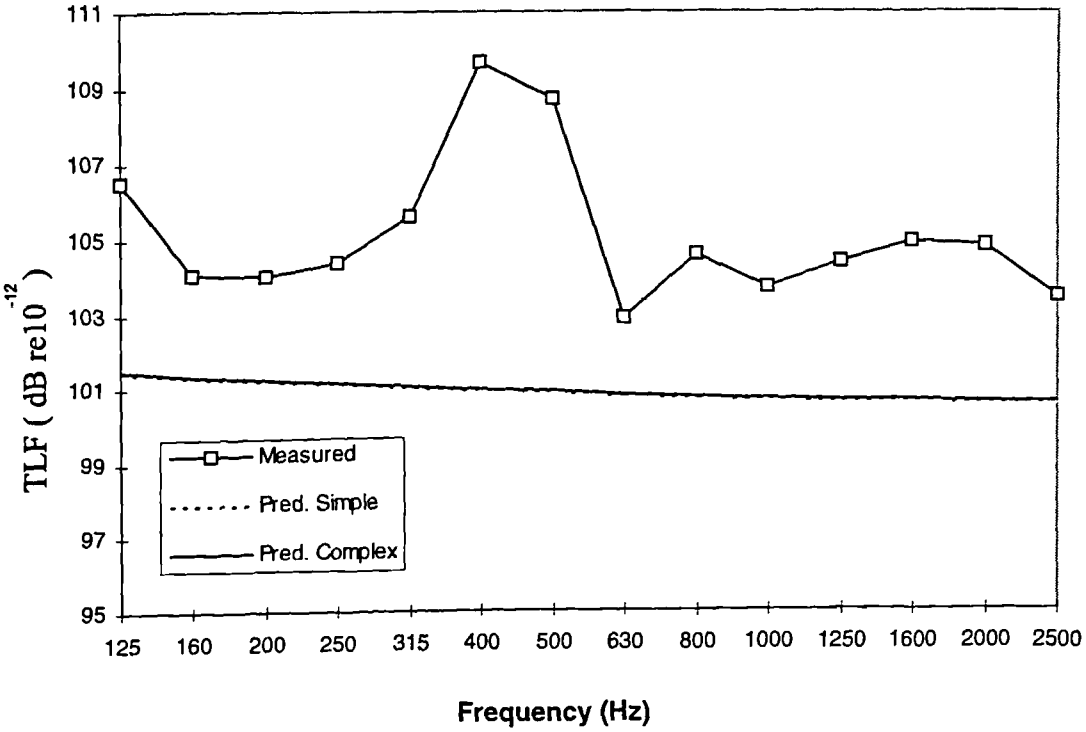

Figure 6.15: Measured and predicted TLF of roof trim (305).

The largest contribution to the predicted roof trim TLF is from the internal loss factor of 100dB re10^{-12}. The measured TLF is around 3dB higher than predicted but the frequency trends are similar except for a peak in the measured values around 400Hz.

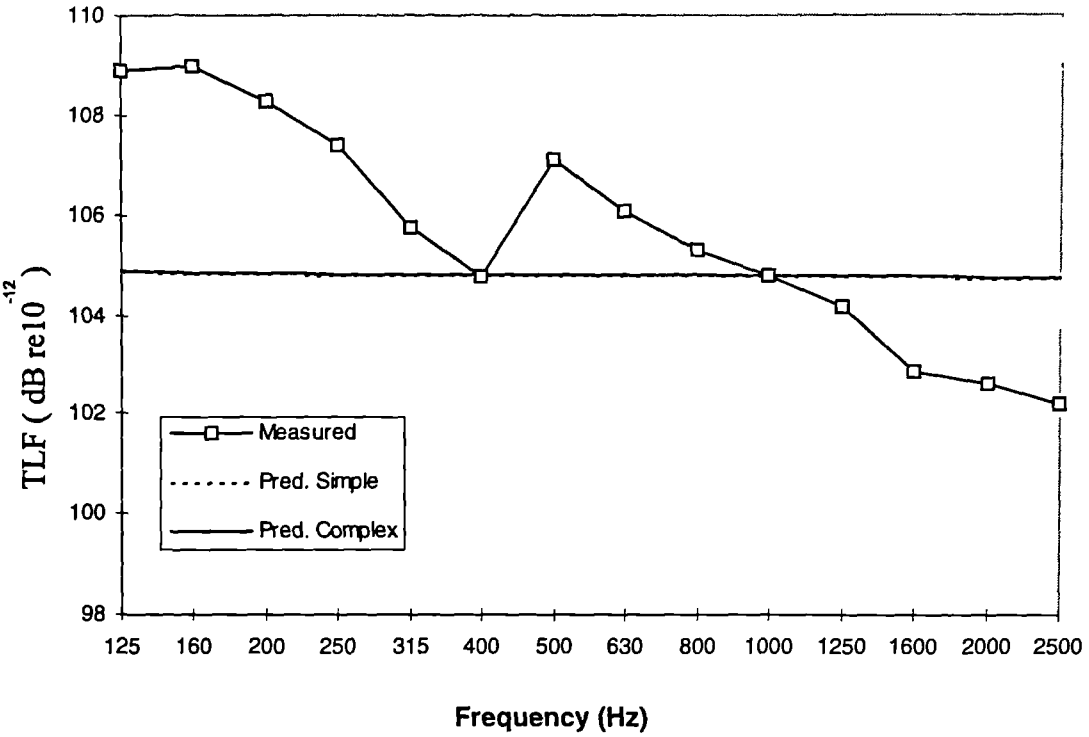

Figure 6.16: Measured and predicted TLF of dash panel (303).

The predicted TLF of the dash panel is dominated by the ILF. Measured and predicted TLF are within 3dB over most of the frequency range shown but there is a difference in trend with the measured value dropping of as frequency increases.

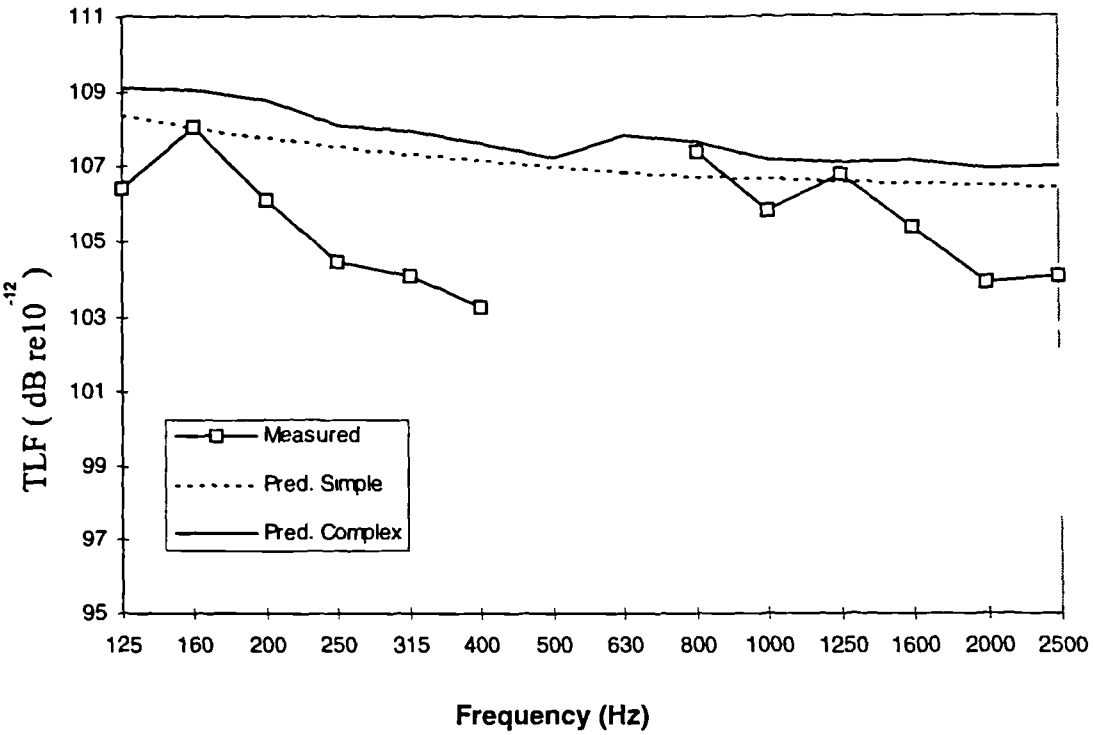

Figure 6.17: Measured and predicted TLF of firewall (104).

The firewall is coupled in the SEA models to 9 subsystems. Internal damping and coupling make a similar contribution to the TLF of the firewall. firewall couplings predicted by the complex joint model are stronger than the basic model so the TLF predicted by the complex joint model is roughly 1dB higher than the basic model.

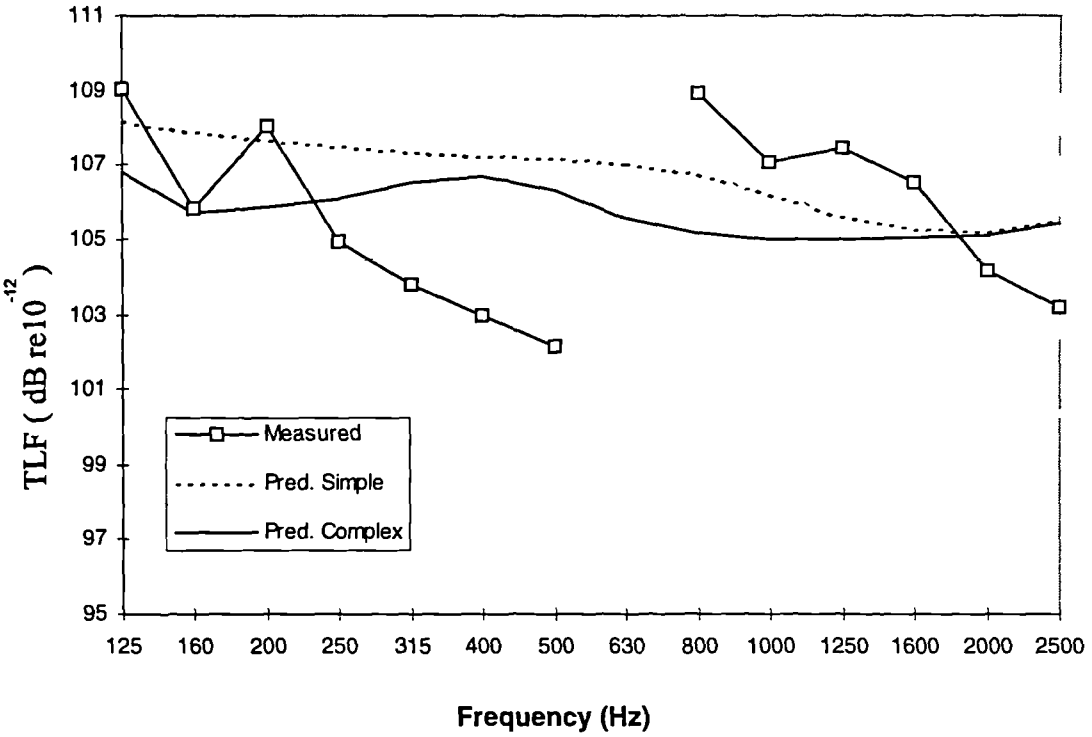

Figure 6.18: Measured and predicted TLF of windscreen (105).

The TLF of the windscreen predicted by the complex joint SEA model is dominated by the ILF (105dB re10^{-12}) with coupling to the firewall, roof and saloon compartment making a minor contribution. Coupling between the roof and windscreen predicted by the basic SEA model is greater than the complex joint model and this gives rise to a larger predicted TLF as shown in Fig. 6.18. Both predictions are typically within 3dB of the measured values.

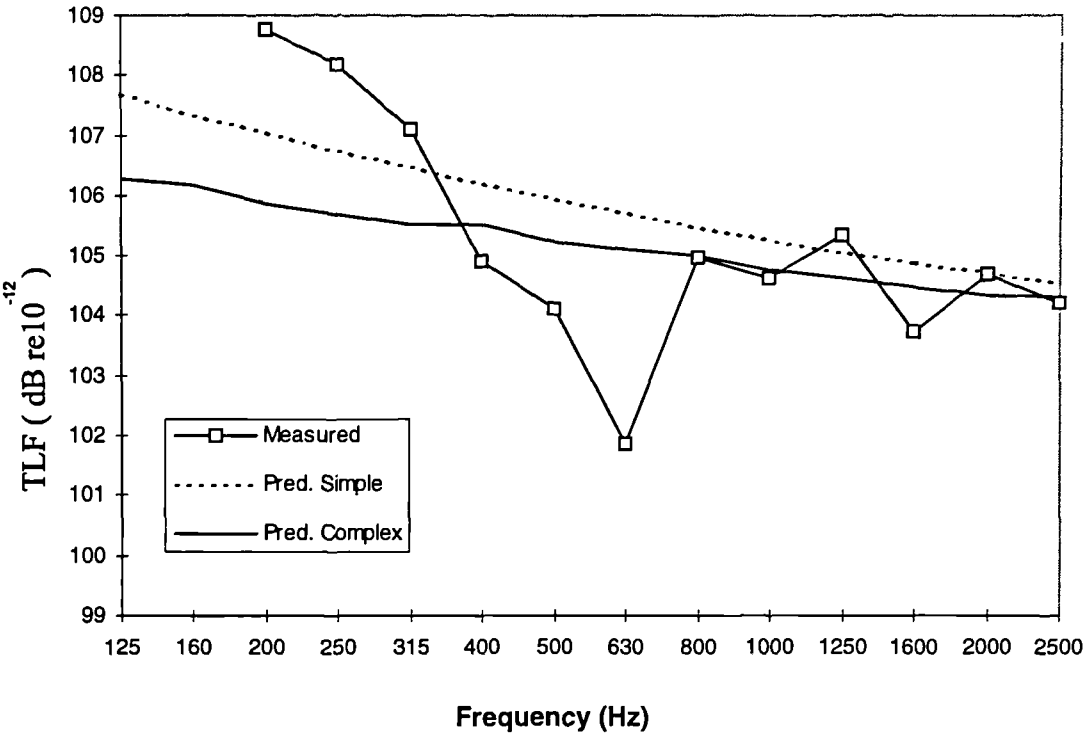

Figure 6.19: Measured and predicted TLF of left front floor (111).

Fig. 6.19 shows Front left (111) floor panel TLF predicted by the complex joint model. This is dominated by the ILF used (103dB re10^{-12}) over most of the frequency range. The TLF predicted by the basic model is higher because the CLFs from the floor panels are higher. Measured floor panel TLFs are generally within 3dB of both predictions.

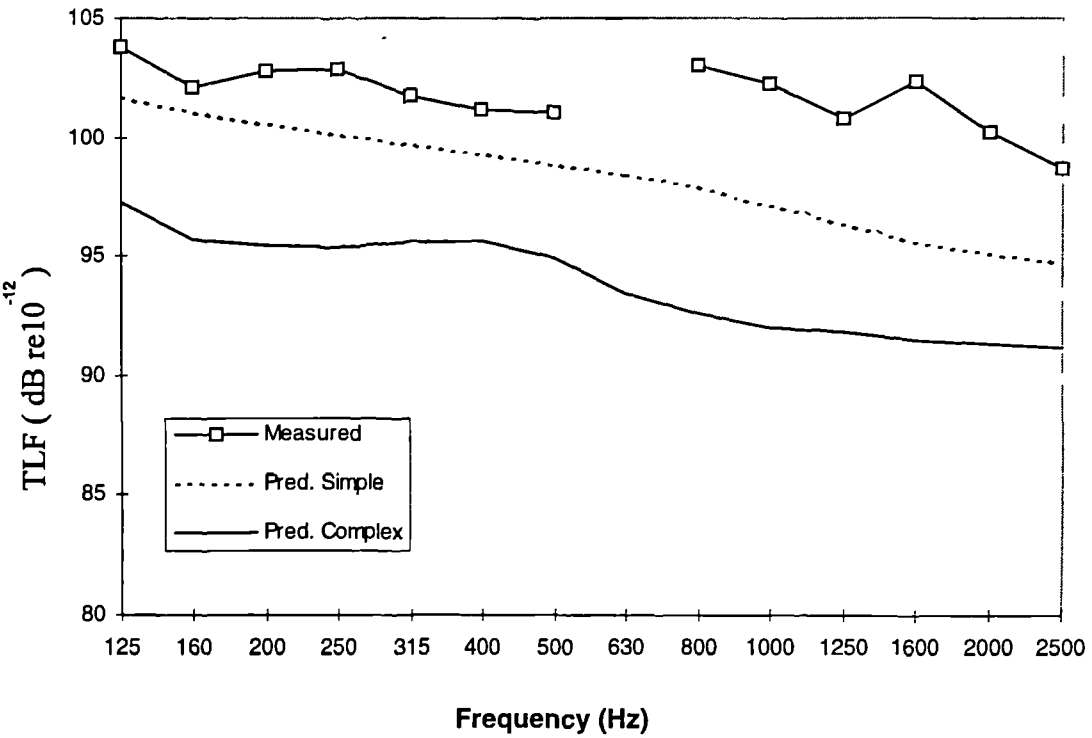

Figure 6.20: Measured and predicted TLF of roof (106).

The roof TLFs predicted by both complex and basic SEA models are dominated by the CLFs. The TLF predicted using the basic SEA model is approximately 5dB higher than the value predicted using the complex joint CLFs because of stronger coupling from the roof to the windscreen and the sides of the car predicted using the basic joints.

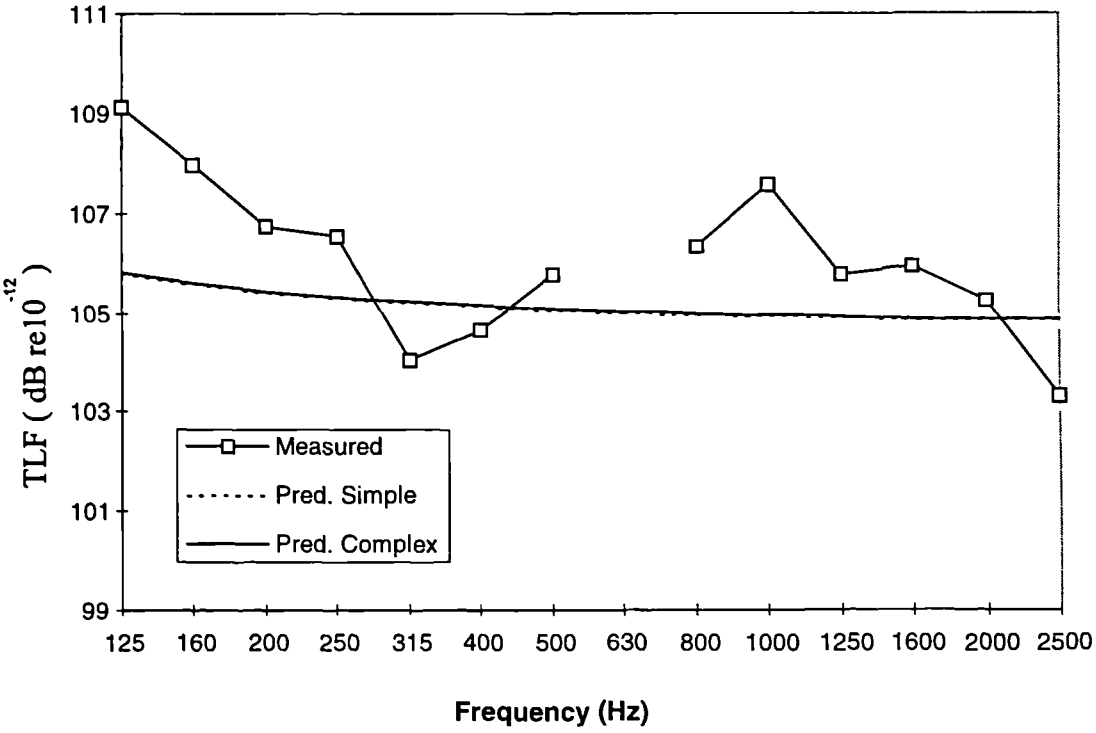

Figure 6.21: Measured and predicted TLF of right rear trim panel (218)

The right rear trim panel is made of plastic so a high ILF (105dB re10^{-12}) was assumed. The rear side trim panels are attached by rapid fix studs to the body of the car, the coupling effect of these studs was calculated using Equation (2.76). The predicted TLF shown in Fig. 6.21 is dominated by the ILF of the trim panel and are typically within 2dB of the measured values.

6.6.2. Energy Level Differences and Acceleration Level Differences

ALDs were measured and predicted in order to discover how accurately the models could predict the transmission of structural vibration from a source panel to other panels on the vehicle. ALD measurement was carried out on the vehicle using the techniques described in Chapter 3. One of two source panels were used in the tests. The right hand front floor panel (211) was used as the source for the bulk of the measurements because it is easily accessible, close to the sources of engine noise and large enough to sustain a number of resonant vibrations in each $1/3^{rd}$ octave band across the frequency range considered. Transmission across the roof (106) to windscreen (105) joint was investigated by making the roof the source and measuring the response of the windscreen. The measured and predicted ALD from the roof to windscreen is given in Fig. 6.22.

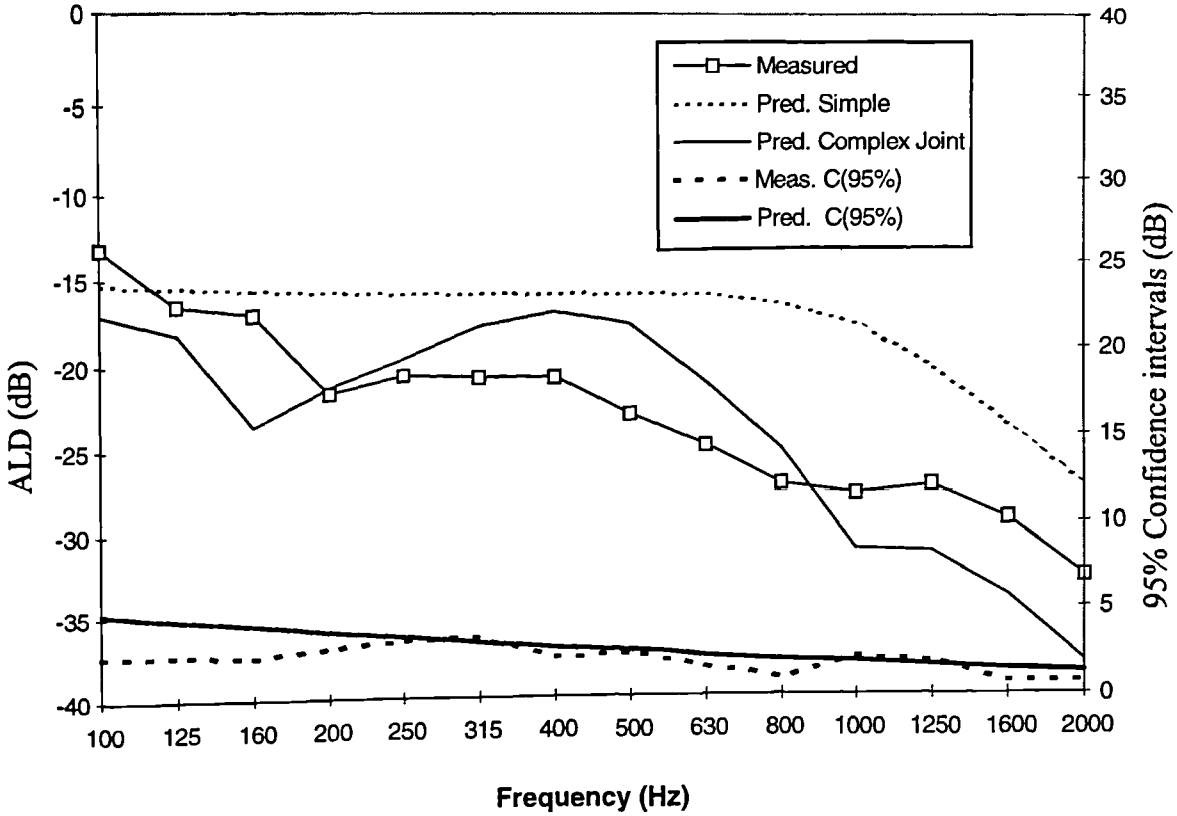

Figure 6.22:Measured and predicted ALD from roof (106) to windscreen (105), also showing measured and predicted 95% confidence intervals.

Both the roof and the windscreen are large and only slightly curved so the assumption that the panels are flat and have a resonant modes within each 1/3rd octave band are likely to be accurate. The windscreen is heavily damped which will help prevent equipartition of modal energy (See Lyon&DeJong [36]) so that the ELD/ALD will be sensitive to transmission across the joint shown in Fig. 6.8. The roof to windscreen joint is 1.2m in length, which is equal to the bending wave length in the windscreen at around 30Hz and in the roof at around 4Hz. Therefore above 30Hz the roof to windscreen joint can be treated as a line boundary. The joint cross section remains fairly constant along its length so that the joint model shown in Fig. 6.8. should be a good representation of the real joint. These factors make the roof to windscreen ALD a good indicator of the accuracy of the complex joint model and Fig. 6.22 shows good agreement between the measured results and the complex joint prediction but considerably poorer agreement with the simple joint model. Another factor which will strongly effect the roof to windscreen ALD is the TLF of the windscreen. Both SEA models predicted windscreen TLFs within 3dB as shown in Fig. 6.18 which would suggest that the ALD results in Fig. 6.22. give a valid comparison of the two joint models. Also shown in Fig. 6.22 are measured and predicted 95%

confidence intervals. The predicted confidence intervals were calculated using equations (2.69) and (2.71) and mode shape factors of 3 for both panels, these equations are known to produce conservative (large) confidence intervals. The measured 95% confidence intervals were calculated as described in Chapter 4. The predicted confidence intervals suggest that 95% of a population of similar vehicles would have roof to windscreen ALDs within less then ± 5dB of an accurate SEA prediction over most of the frequency range. The measured 95% confidence intervals show that there is a 95% chance that the underlying ALD in this particular vehicle lies within less than ± 5dB of the measured value over the frequency range.

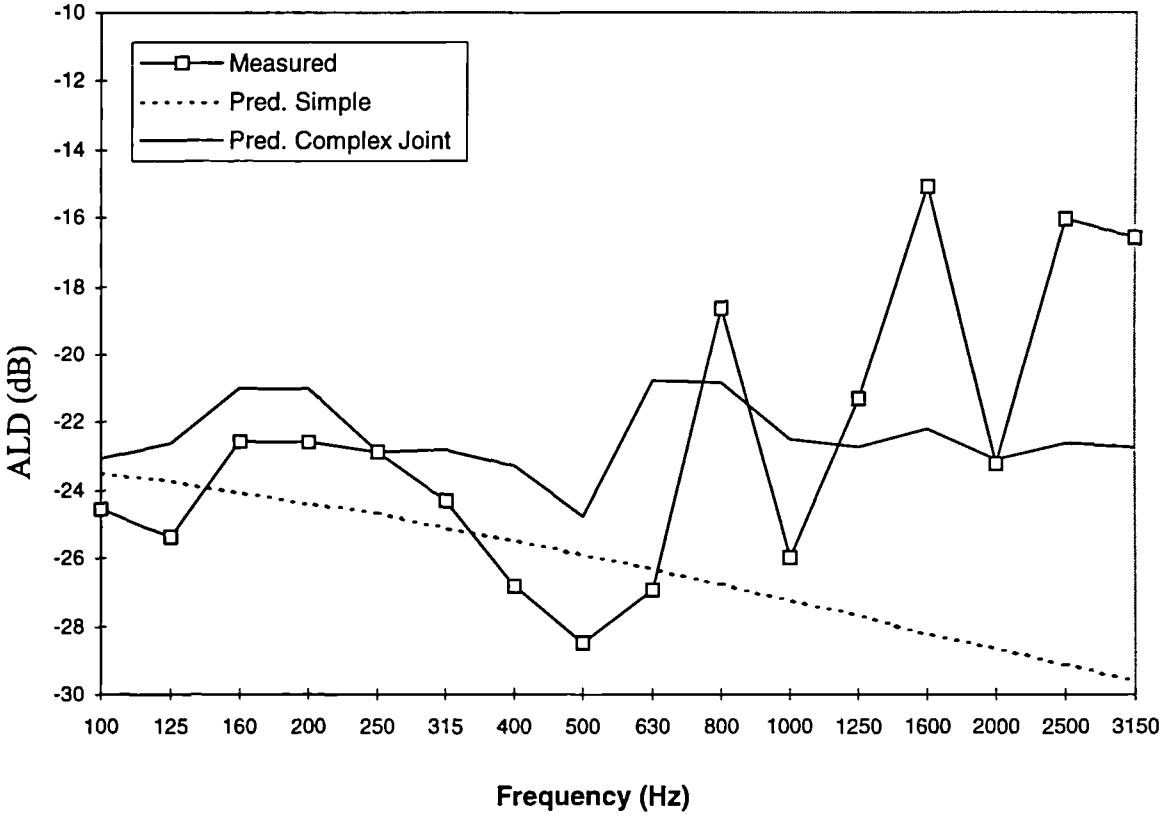

Figure 6.23: Measured and predicted ALD from right floor (211) to firewall (104).

Fig. 6.23 shows the measured and predicted ALDs from the floor to firewall. Both predicted ALDs between floor and firewall are dominated by the transmission across the line junction between the floor and the firewall. Bending wave transmission coefficients for this joint are shown in Fig. 6.12 The complex joint model predicts stronger transmission than the basic joint which gives better agreement with the measured ALD shown in Fig. 6.23. Above 500Hz the measured data has a high variance giving rise to large 95% confidence intervals of around ± 6dB. It was difficult to find randomly spread accelerometer measurement positions on the firewall because of the close proximity of the

engine and the number of items attached to the firewall. This may have contributed to the large variance in the measured results. The floor panel (211) and the firewall (104) are fairly flat on a large scale but contain small corrugations for increased stiffness the effect of the corrugations was not calculated in ether the basic or the complex joint model. The boundary between the right hand floor panel and the firewall is 0.51m which is longer than the bending wavelength in either the floor or the firewall at frequencies above 100Hz.

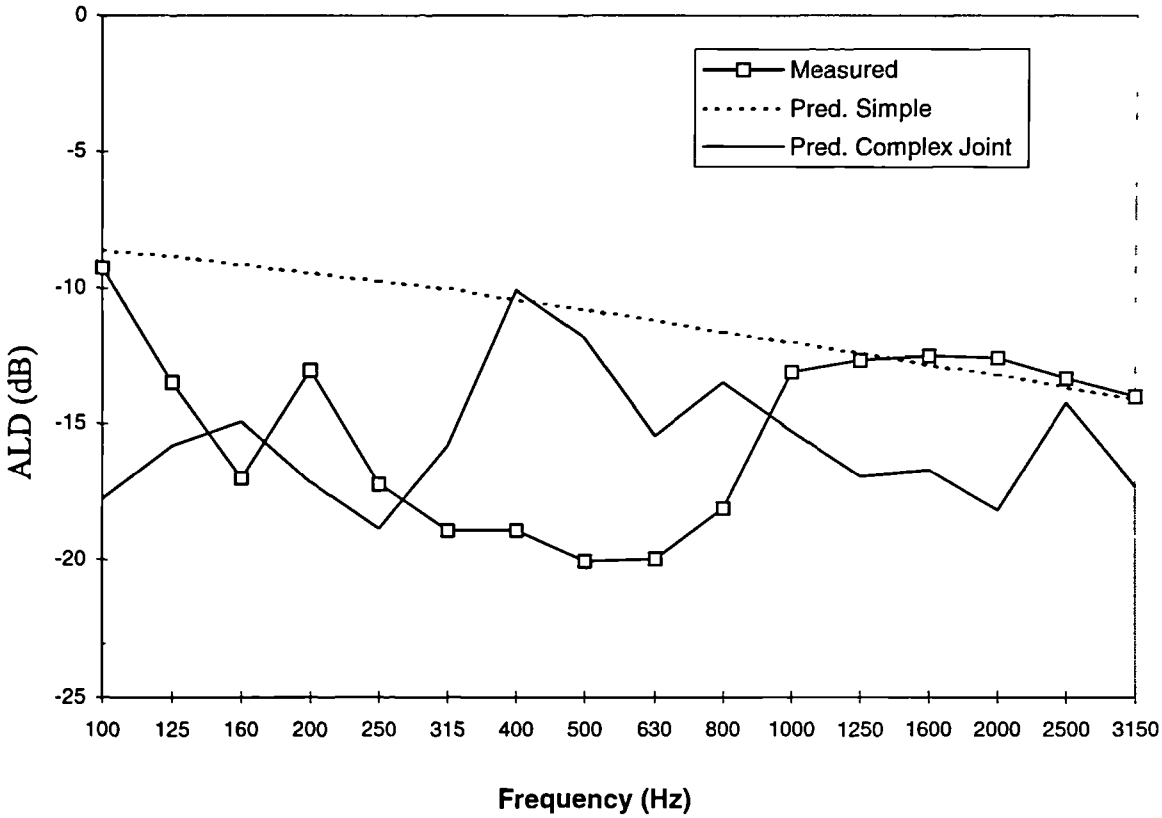

Figure 6.24: Measured and predicted ALD from right floor (211) to floor under rear seat (109).

Fig. 6.24 shows the measured and predicted ALD between the right floor panel (211) and the panel under the rear seat (109). The complex joint model prediction is within 5dB over most of the frequency range shown. ALDs predicted using the simple joint model are approximately 5dB lower than the measured values below 800Hz but are in very good agreement above 1000Hz. The simple joint SEA model assumes that the step between the floor and the floor under the rear seat is a plate subsystem (110). Treating the step as a panel subsystem assumes that its response is resonant and that it supports a diffuse wave field. These assumptions are unlikely to be valid at low frequencies in such a small panel. This is probably why the simple SEA model shows poorer agreement below 1000Hz and

good agreement above. The simple model gives good agreement above 1000Hz despite ignoring the effect of the box section which is included in the complex joint model shown in Fig. 6.10. The boundary between the floor and the floor under the rear seat is longer than the bending wavelength on the floor or floor under the rear seat at frequencies above 25Hz.

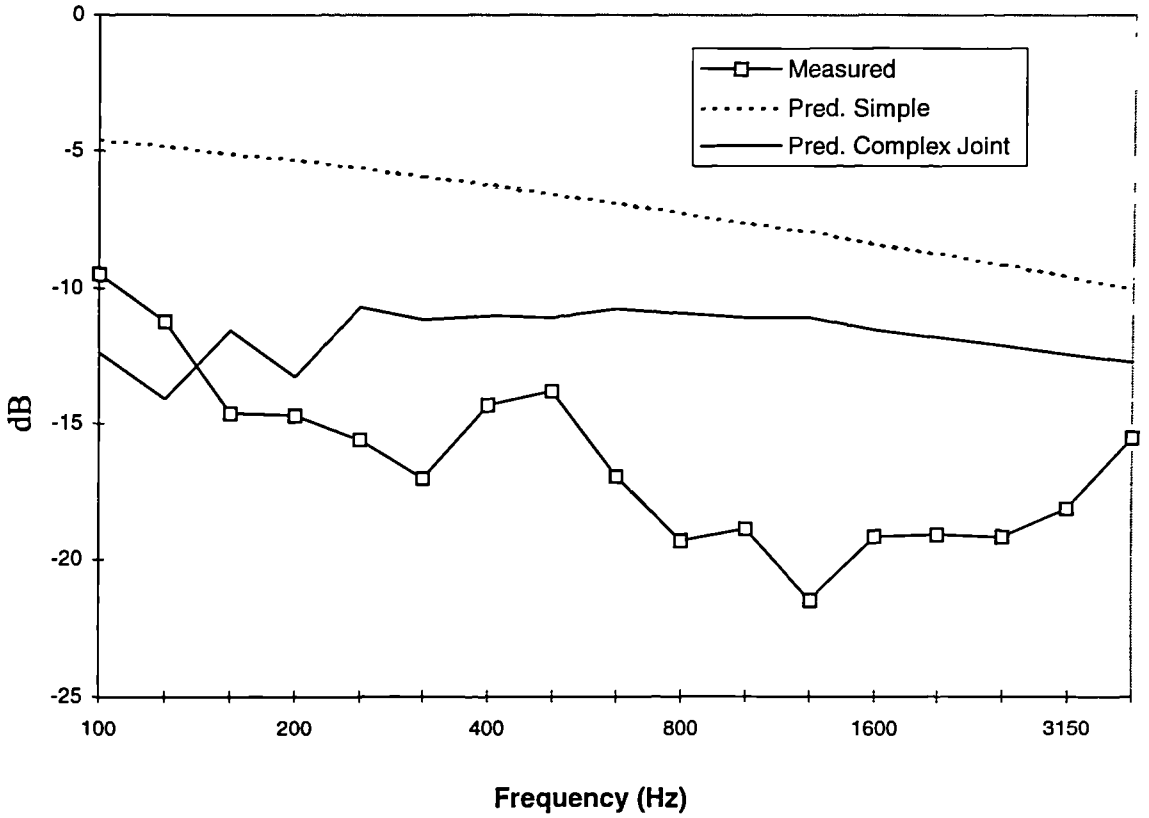

Figure 6.25: Measured and predicted ALD from right floor (211) to left floor (111).

Measured and predicted ALDs from the right to left floor panels are shown in Fig. 6.25. The transmission between the floor panels in both SEA models is dominated by the transmission across the exhaust channel in the floor with flanking transmission through the firewall and the floor under the rear seat playing only a very minor role. The complex joint and the simple joint transmission coefficients across the exhaust channel are given in Fig. 6.14. The complex joint model predicts the transmission accurately at around 100Hz but over predicts the transmission at higher frequencies. The simple joint over predicts the transmission by around 10dB over the entire frequency range. It is not surprising that the simple model of this joint fails to accurately predict transmission as it bears little resemblance to the real situation. The gear shift and hand break mechanism is attached to the underside of the exhaust channel also the shape of the exhaust channel was more complicated than that shown in Fig. 6.14 as it had small stiffening corrugations in the

panels. It is possible that these features reduces the transmission across the floor and may explain the discrepancy between the measured and predicted ALD at higher frequencies. Most power inputs to the vehicle resulting from engine, road and aerodynamic noise are likely to be fairly symmetric. Noise and vibration levels predicted using the SEA models with these power inputs will be extremely insensitive to transmission from left to right floor panels because the models are also symmetric. Therefore errors in predicted transmission across the floor will probably not cause large errors in predicted engine, aerodynamic and road noise and vibration levels. The nine ALDs which depended mainly upon transmission across point contacts such as door hinges do not show good agreement with either SEA model. The ALD between the right floor and the right outer door panel shown in Fig. 6.26 is an example of this.

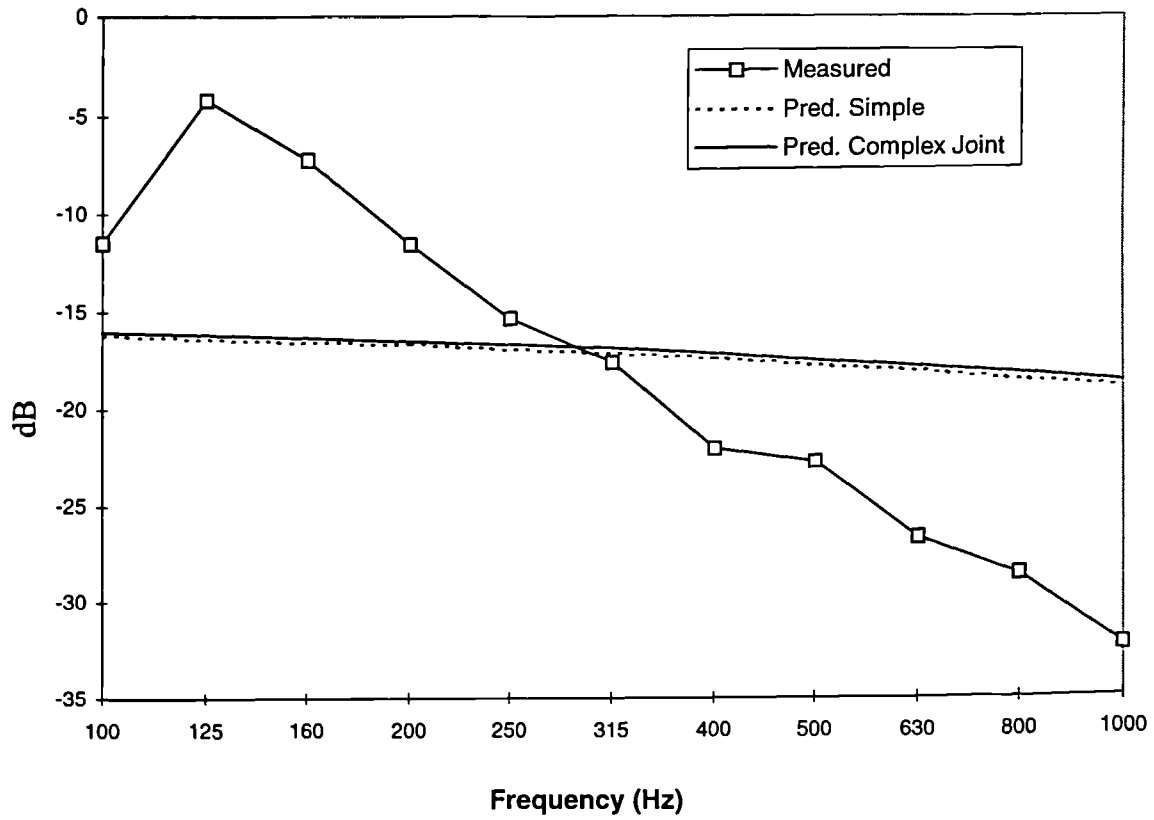

Figure 6.26:Measured and predicted ALD from right floor (211) to right outer door panel (212).

It is not surprising that measured ALDs strongly dependant upon transmission across door hinges do not agree well with predicted results as they were modelled as simple point contacts between panels and no attempt was made to account for the effect of reinforced areas around the hinges. Twelve ALDs were measured in addition to those shown in Figs. 6.22 to Fig. 6.26. Five ALDs including those shown in Figs. 6.22 to 6.25 are generally

within 5dB of the complex joint model predictions over most of the frequency range 100Hz-3150Hz. This reasonable level of agreement only occurs in ALDs which depended strongly upon transmission across line boundaries in the models. Three ALDs did not show good agreement with the complex joint model predictions despite being strongly influenced by transmission across line boundaries. These ALDs were those between the right floor panel (211) and the panels of the right rear wing (217), roof (106) and windscreen (105).This would suggest that the reasonable agreement found between the measured and predicted ALD for the floor (211) to right rear side window (217) is fortuitous as any structural path between the two subsystems must include either the roof or the right rear wing. Transmission from the right floor (211) to the right rear wing (216) is through a very complex interconnection of subsystems including the sill (224) and the B pillar (215) both of which are actually closed section beams formed of thin sheet metal. If the sill or B pillar were approximated as a cylinder the plain strain ring frequency (discussed by Langley[9]) would be in the region of 10kHz. Both the Sill (224) and the B pillar (215) were modelled as flat plates and since the frequency range is below 10kHz this will contribute to the error. The coupling boundaries between the structures joined at the junction between the floor and the right rear wing are often 0.15 m or less in length. This will cause errors as they were all treated as line coupling but the bending wave length only falls below 0.15m above 400 Hz. It is not particularly surprising then that the model failed to accurately predict the transmission from the floor to rear wings and hence the roof. Examination of the SEA models has shown that the dominant power flow into the windscreen when exciting the right floor panel is from the roof because the firewall is heavily damped. This would explain the poor agreement between the measured floor to windscreen ALD and the complex joint SEA model prediction. Simple joint model predictions give significantly inferior agreement to complex joint predictions for ALDs dominated by transmission across line panel boundaries.

6.6.3. Sound Pressure Levels - Engine Running

SPL in the saloon as a result of engine noise was measured for comparison with predicted results from the basic and the complex joint SEA models. Saloon SPLs were measured at three engine speeds (700, 3000 and 5700 rpm) with the car stationary and out of gear. Accurate prediction of SPLs using SEA requires equally accurate knowledge of the magnitude and location of the power inputs to structural and acoustic subsystems. Other measurements were taken to ascertain the various power inputs to the SEA models.

Structural Power Inputs

In order to estimate the structural power inputs the mechanical mobility measurements of the vehicle body were taken at the engine and exhaust mounting points using the methods described in Section 4.7. The engine/transmission and exhaust are connected through rubber isolators (Shown in Fig. 6.2) which were left in place during some of the mobility measurements. It was assumed that the impedance of the isolators was much less than that of the vehicle body and this was evident at least statically by the ease with which they could be deflected by hand. It was therefore assumed that measurements represented the mobility of the body only. At the left hand engine mount shown in Fig. 6.2 the mobility of the engine/transmission mounting point was measured in three perpendicular directions (x,y,z in Fig. 6.2). At the right hand engine mount mobility was only measured in the x and y direction due to lack of space. Only vertical (y) mobility measurements were carried out on the vehicle body at the rear engine centre member mounting point. This is roughly perpendicular to the body of the vehicle and represents the axis of highest mobility. Only vertical (y) mobility measurements were carried out at the exhaust mounts as rubber isolators allowed the exhaust pipe to move in the x-z plane with very little resistance by comparison to y direction. No attempt was made to measure the moment impedance of the structure at the mounting points.

Acceleration levels were measured at the engine and exhaust mounting points with the engine running but with the car stationery and out of gear. Structural power flow into the vehicle body at each of the engine and exhaust mounting points was calculated using equation (6.5).

$$P = \mathrm{Re}\left\{\frac{1}{Y}\right\}\frac{\langle a^2 \rangle}{\omega^2} \tag{6.5}$$

Only mobility measured along the vertical (y) axis and vertical acceleration levels were used to calculate the power inputs as these usually gave the largest power flow in equation (6.5). Power can flow from the rear engine mount into the engine centre member. This power may enter the vehicle body at the front or rear engine centre member mounting points (See Fig. 6.2). Power flowing into the vehicle body at the front engine centre mounting point was ignored as it must flow through a longer chain of subsystems than any of the other power inputs to reach the saloon.

Acoustic Power Inputs

Three acoustic power inputs were included in the SEA models. Some of the acoustic energy in the engine compartment flows into the firewall (104). The resulting power flow into the firewall was quantified by calculating the CLF between the air volume in the engine compartment and the firewall using Leppington *et al's*[33] radiation efficiency as described in Section 2.8.2 . Average SPL in the engine compartment was measured at the required engine speeds and used to calculate the acoustic energy of the air by using,

$$E = \frac{\langle p^2 \rangle}{\rho_0 c_0^2} V \tag{6.6}$$

Where V is the volume of the engine compartment and $\langle p^2 \rangle$ is mean squared pressure. Power flowing into the firewall is then given by $p_{1,2} = E\omega\eta_{1,2}$. Note that the volume V cancels in the power calculation. Figure 4.3 shows that the 95% confidence intervals for the SPL in the engine compartment is around $\pm$ 10dB between 100Hz and 5000Hz when the engine speed is 5700rpm. This means that predicted SPL or vibration levels resulting from this power input will have an equal or greater confidence interval. Figure 4.3 also shows that the 95% confidence intervals for engine compartment SPL with the engine running at 3000rpm is generally less than $\pm$ 6dB over the same frequency range. Direct non resonant power flow from the engine compartment to the saloon was calculated in a similar way. The CLF from the engine compartment to the saloon was calculated using,

$$\eta_{1,2} = \frac{c_0 S \langle \tau_{1,2} \rangle}{4\omega V_1} \tag{6.7}$$

where S is the area of the firewall and $\langle \tau_{1,2} \rangle$ is the average sound transmission coefficient calculated using the double panel model of the firewall and SBA described in Section 6.3. The Transmission Loss of the firewall/SBA is shown in Fig. 6.4. The remaining acoustic power input to the SEA models was direct transmission of sound through the floor of the vehicle into the saloon. This was included using the same method used for the firewall/SBA except that direct non resonant transmission through the floor panels was calculated using equation (2.90) for both floor panels (111 and 211). The six structural and three acoustic power inputs to the SEA models are tabulated in Table (6.8).

DESCRIPTION	SOURCE SUBSYSTEM	AXES MEASURED
Left Engine Mount	Front Left Wheel Arch (103)	x, y, z
Right Engine Mount	Front Right Wheel Arch (203)	x, y
Engine Centre Member Rear	Fire wall (104)	y
Front Left Exhaust Mount	Front Left Floor Panel (111)	y
Front Right Exhaust Mount	Front Right Floor Panel (211)	y
Rear Exhaust Mounts	Floor under Boot (209)	y
Acoustic from Engine Compartment	Fire wall (104)	
Direct Acoustic through Floor	Saloon (2)	
Direct Acoustic through Fire wall	Saloon (2)	

Table 6.8: Power inputs to SEA models for saloon SPL predictions with engine running.

The structural power inputs shown in Table (6.8) were fed directly into the panel subsystems in the vehicle. In a more elaborate model of the vehicle beam subsystems could have been included to represent the reinforced parts of the vehicle. The power would then be fed into these beams from where it could flow into the panels. The models described in this Chapter effectively assume that the energy flows directly from the reinforced parts into the body panels. Including beam structures and feeding the power into them could cause transmission of engine vibrations to be increased as the beams transport the power around the structure without travelling through the panels.

Measured SPLs in the saloon are show in Fig. 6.27 for each of the three (700, 3000 and 5700 rpm) engine speeds. These were measured as described in Chapter 4 and are averages from six positions in the saloon.

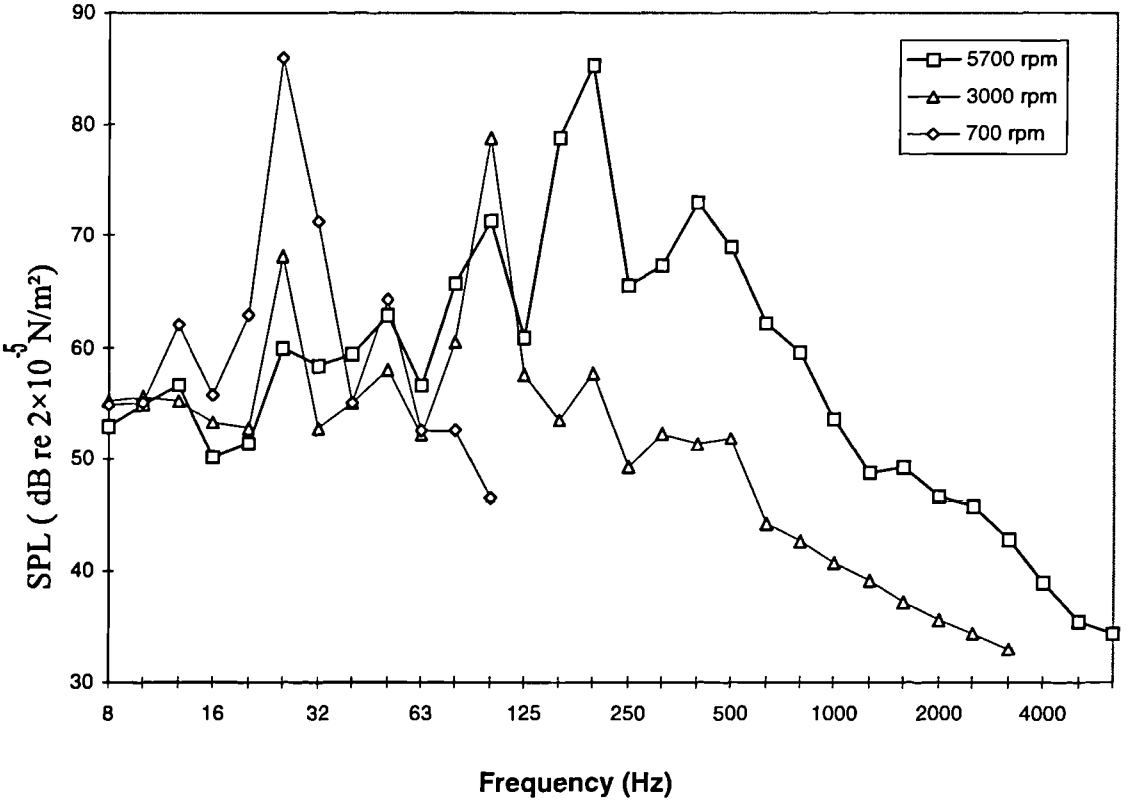

Figure 6.27: Measured Sound Pressure Levels in saloon at three engine speeds (700rpm, 3000rpm and 5700rpm) with front exhaust mounts connected.

The peak SPL at each engine speed occurred in the 1/3rd octave frequency band containing the second harmonic of engine speed. At 700 rpm this is the 25Hz band and the peak value is 86dB. The microphone used to measure saloon SPL had a flat response within ± 1dB between 50Hz and 10kHz so the levels below 50Hz are not as reliable. At 3000rpm the peak occurs in the 100Hz band and has a value of 79 dB. At 5700 rpm the peak occurs in the 200Hz band and also has a value of 79 dB. Saloon SPL was also measured at the three engine speeds with the front exhaust mounts disconnected in order to investigate a noise problem caused by exhaust misalignment. The misalignment was introduced deliberately in this case but it can occur when the exhaust system is replaced incorrectly after maintenance. Disconnecting the front exhaust mounts made little difference to the saloon SPL at running speeds of 700 and 3000rpm but at 5700 rpm the SPL reduced over part of the frequency range. The SPL measured at 5700 rpm with the mounts connected and disconnected are shown in Fig. 6.28 below.

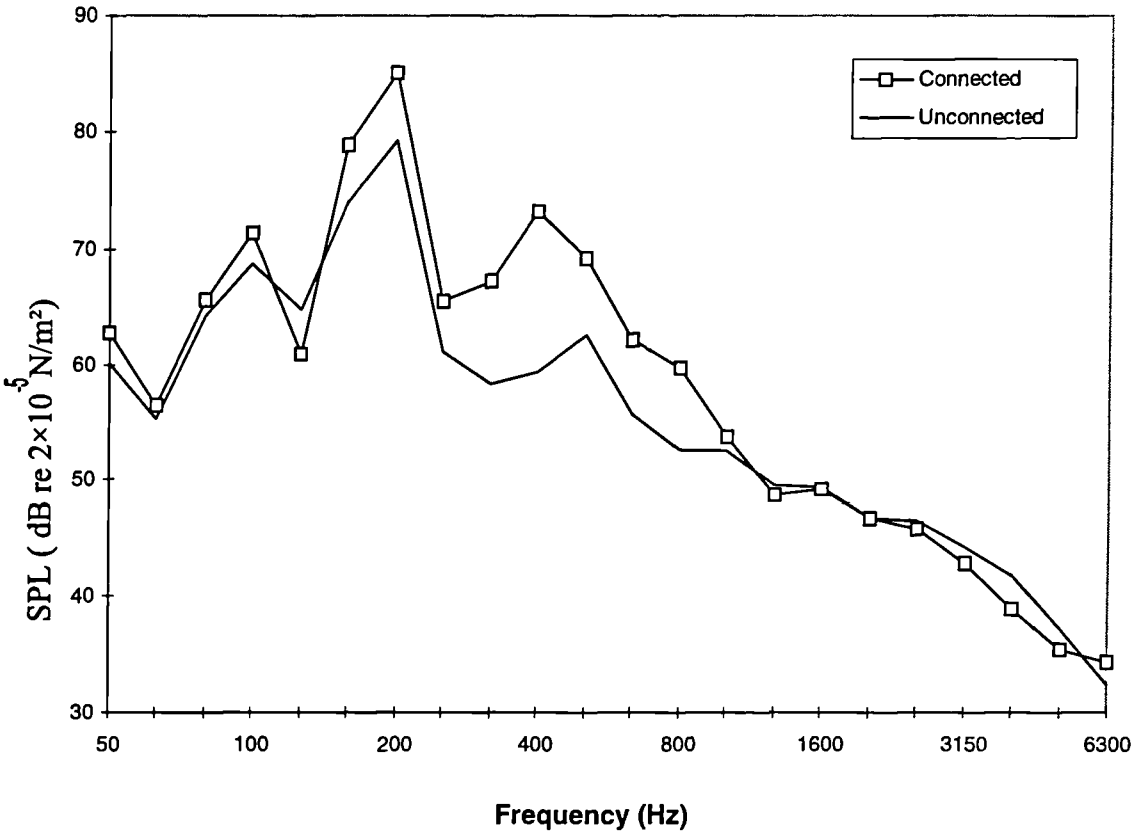

Figure 6.28: Measured Sound Pressure Levels in saloon at 5700rpm with front exhaust mounts connected and disconnected.

With the engine running at 5700rpm disconnecting the front exhaust mounts reduced the measured saloon SPL between 250Hz and 1000Hz, the difference (up to 13dB) was noticeable to the ear. This increase in SPL occurs only when the exhaust is attached with a slight misalignment. Predicted power inputs were used in the two SEA models of the vehicle to calculate the SPL in the saloon. Above 100Hz the predicted modal density of the saloon is sufficient for there to be more than one mode in each 1/3rd octave band on average. The predicted SPLs resulting from each power input considered separately are shown in Figs. 6.29 and 6.30 for an engine speed of 5700 rpm.

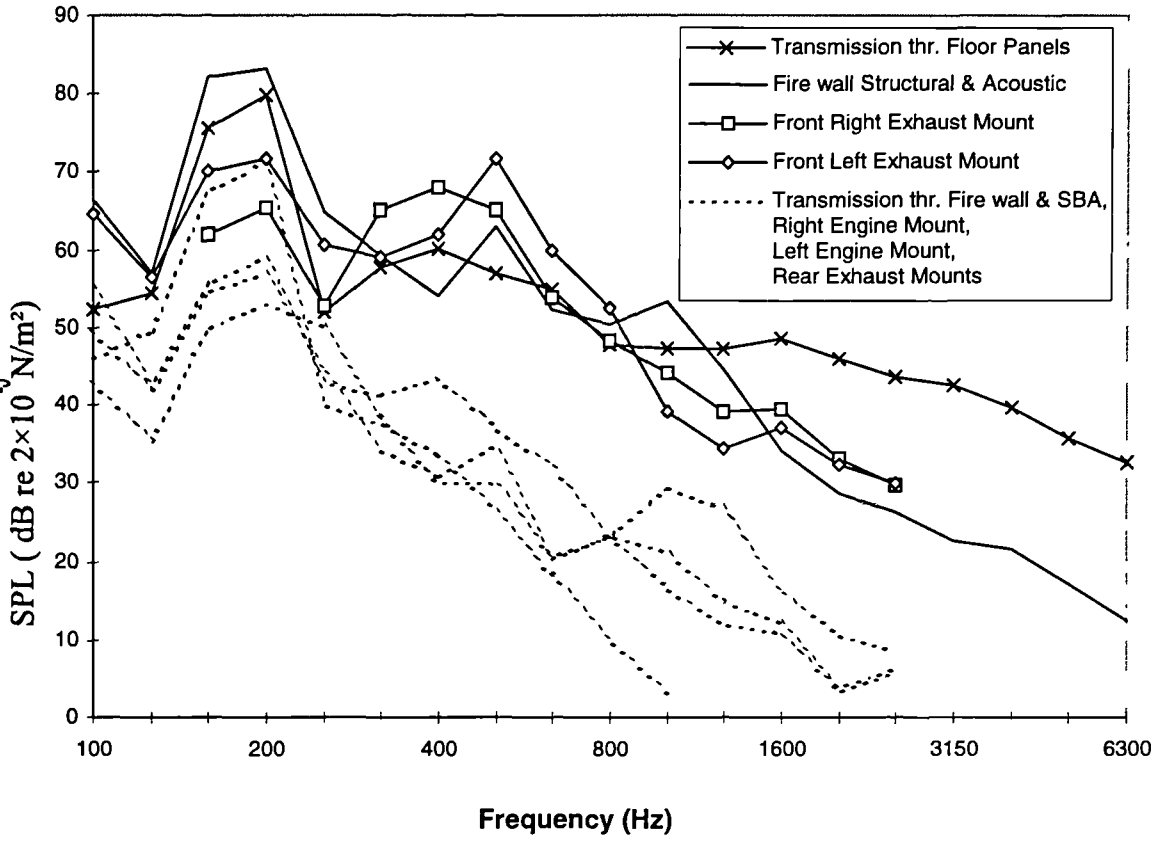

Figure 6.29: Predicted saloon SPL resulting from each power input using complex joint SEA model for an engine speed of 5700rpm.

Fig. 6.29 shows the saloon SPL resulting from each power input as predicted using the complex joint model. Fig 6.30 shows the same thing but predicted using the simple joint model. The lines in Figs. 6.29 and 6.30 are as follows. The solid line is the predicted saloon SPL resulting from the two power inputs into the firewall described in Table (6.8). The solid line with crosses is the predicted SPL resulting from direct transmission of sound through the floor panels (111,211) into the saloon. The solid line with square markers is the predicted SPL resulting from the power injected at the front right exhaust mount when the exhaust is attached. The solid line with diamond markers is the predicted SPL resulting from the power injected at the front left exhaust mount when the exhaust is attached. There are four dashed lines in Figs. 6.29 and 6.30 these represent the predicted saloon SPLs resulting from power inputs which have the least effect, they are as follows. Direct transmission through the firewall from the engine compartment to the saloon, power inputs at the right and left engine mounts and power injected at the rear exhaust mounts.

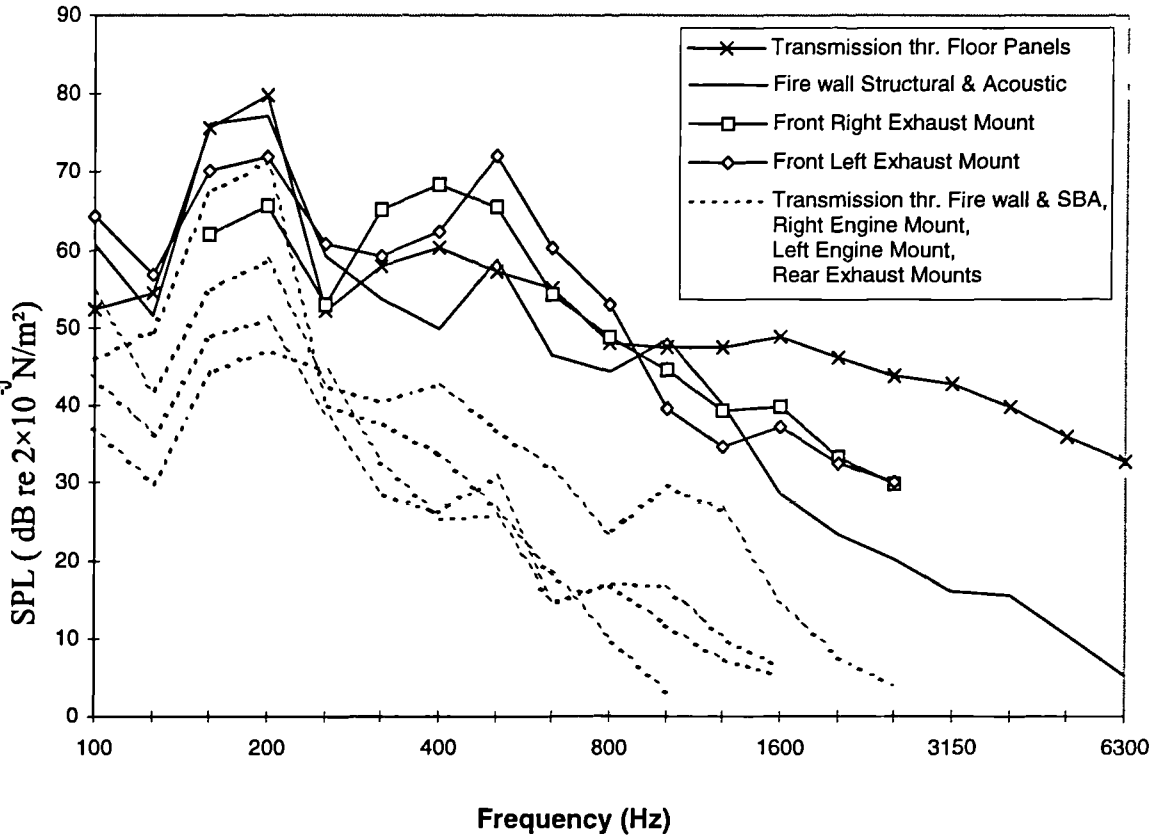

Figure 6.30: Predicted saloon SPL resulting from each power input using simple joint SEA model for an engine speed of 5700rpm.

Fig. 6.29 shows that according to the complex joint model the two power inputs flowing into the firewall (104) make the largest contribution to the SPL in the saloon below 250Hz. Between 250Hz and 800Hz the power flowing from the front exhaust mounts into the front floor panels (111,211) dominate the predicted SPL, this is consistent with the measurements for 5700rpm shown in Fig. 6.28. At frequencies above 1250Hz saloon SPL is dominated by the transmission of sound through the floor panels (211,111). Fig. 6.30 shows that the basic SEA model predicts a lower SPL as a result of the power inputs to the firewall than does the complex joint model. The dominant paths in both SEA models from structural vibration in the firewall to acoustic energy in the saloon were (firewall-windscreen-saloon) below 250Hz and (firewall-floor-saloon) above 250Hz. The complex joint model has higher transmission between the firewall and the floor than the simple joint model as demonstrated in Fig. 6.23. Transmission between the firewall and the windscreen is also stronger in the complex joint model than in the simple joint model. This is the reason why the complex model predicts higher saloon SPL as a result of the two power inputs to the firewall. It is clear from Figs. 6.29 and 6.30 that the power inputs to the left and right engine mounts (103,203), the rear exhaust mounts (209) and the

transmission of sound through the firewall have considerably less effect on saloon SPL than the other power inputs to the SEA models. Total predicted SPLs calculated using all the power inputs are plotted in Figs. 6.31 and 6.32 alongside measured values for 5700rpm.

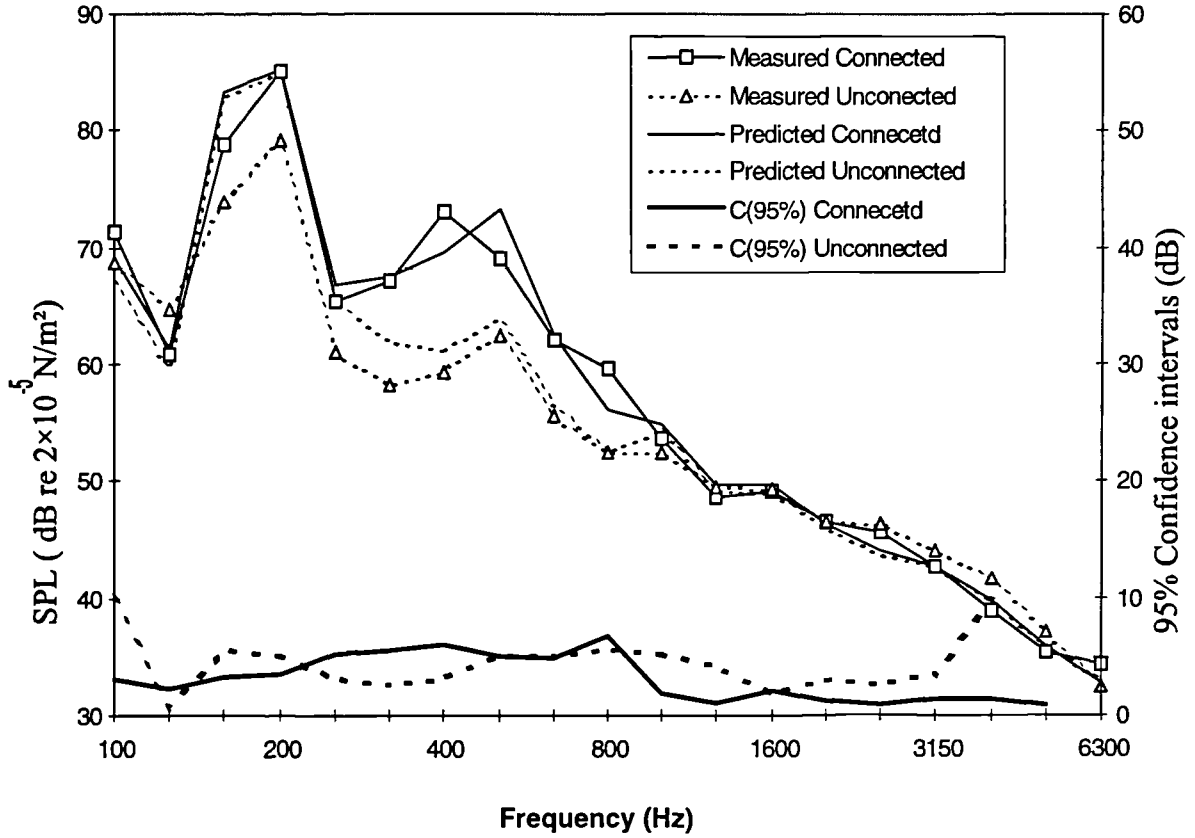

Figure 6.31: Measured and predicted (complex joint SEA model) saloon SPL at 5700 rpm with exhaust connected and unconnected, also showing the C(95%) confidence intervals in the measured SPLs.

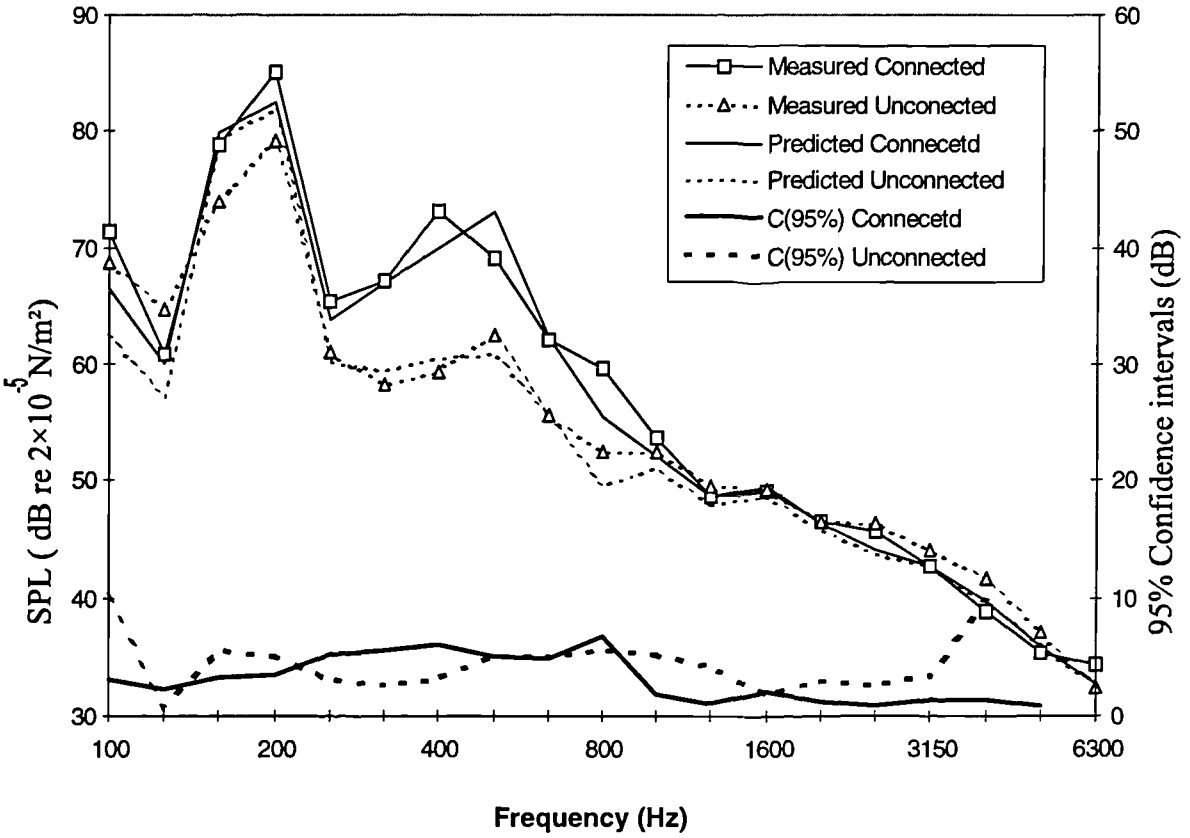

Figure 6.32: Measured and predicted (simple joint SEA model) saloon SPL at 5700 rpm with exhaust connected and unconnected, also showing the C(95%) confidence intervals in the measured SPLs..

Also shown on Figs. 6.31 and 6.32 are the measured saloon SPL 95% confidence intervals with the front exhaust mounts connected and disconnected. The unconnected confidence intervals are around ±4dB on average between 100Hz and 4000Hz. Between 250Hz and 800Hz the connected confidence intervals have an average value of ±5.6dB, at these frequencies both SEA models indicate that the saloon SPL in predominantly caused by power injected at the front exhaust mounts. The connected confidence intervals are larger than the unconnected ones between 250Hz and 800Hz despite the fact that more SPLs were measured in the saloon with the front exhaust mounts connected than unconnected. Possible reasons for the large variance in saloon SPL measured with the exhaust mounts connected are discussed in Section 4.4. Saloon SPL predictions in Figs. 6.31 and 6.32 with the front exhaust unconnected were produced by omitting the power inputs at those points. Both the complex joint (Fig. 6.31) and the simple joint (Fig. 6.32) SEA models clearly show the increase in SPL between 250Hz and 800Hz which is caused by the power injected at the front exhaust mounts. The large confidence intervals at these frequencies reduce the certainty in this conclusion because the difference in SPL could be

a random fluctuation. However the fact that the saloon SPL variance increases when the exhaust is connected is in its self an indication that the increase between 250Hz and 800Hz is a real phenomenon and not a random fluctuation.

According to both SEA models at 700 rpm the power inputs to the firewall dominate saloon SPL below around 250Hz and transmission of sound through the floor makes the largest contribution above 250Hz. A similar break down of the contributions to saloon SPL as shown in Figs. 6.29 and 6.30 suggests that at 3000rpm in both SEA models the two power inputs to the firewall dominate saloon SPL below 500Hz and transmission of sound through the floor dominates above 500Hz. Measured and predicted saloon SPL at 3000rpm are shown in Fig. 6.33 and Fig. 6.34.

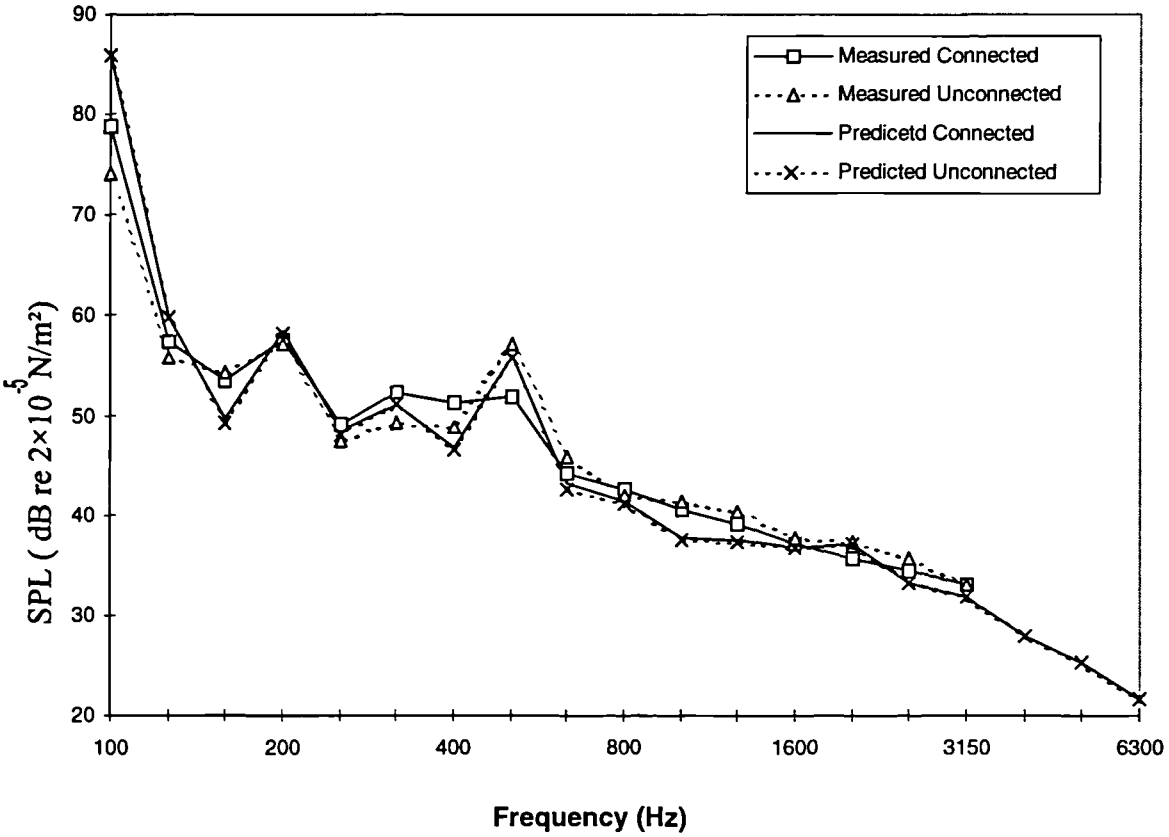

Figure 6.33: Measured and predicted (complex joint model) saloon SPL at 3000 rpm with front exhaust mounts connected and unconnected.

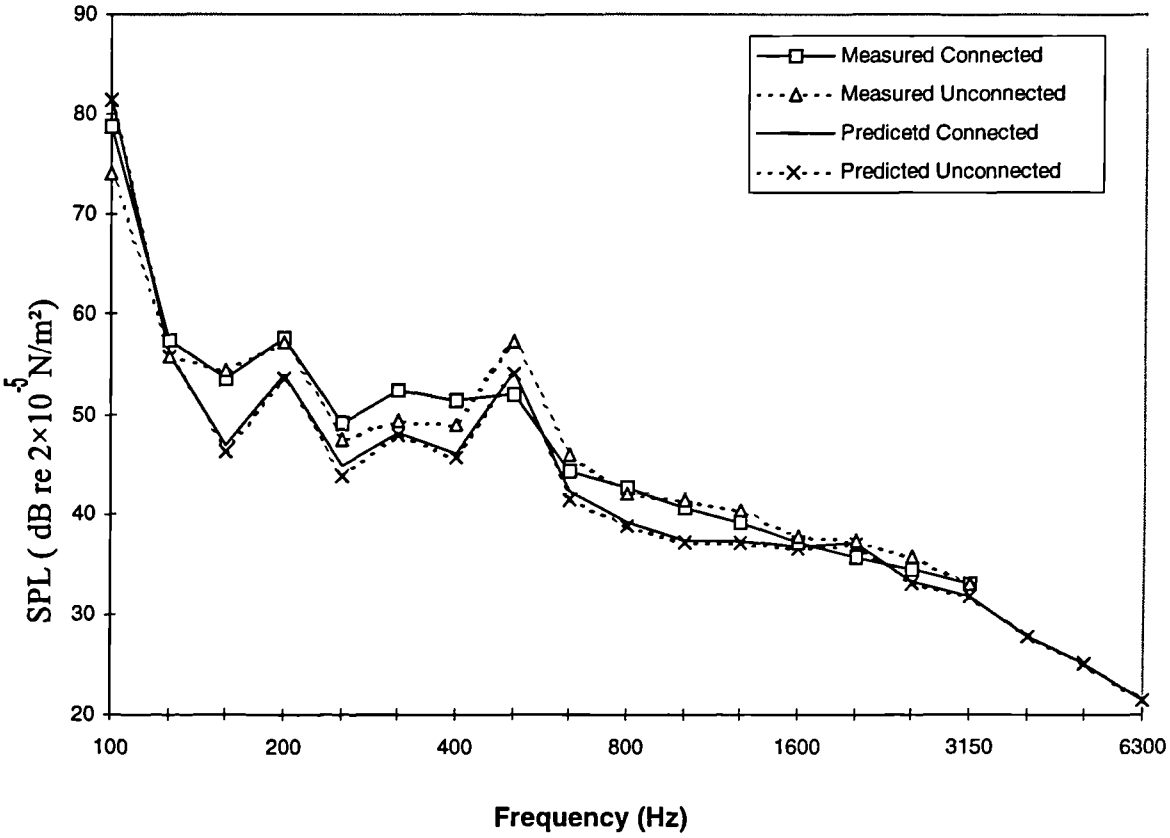

Figure 6.34: Measured and predicted (simple joint model) saloon SPL at 3000 rpm with front exhaust mounts connected and unconnected.

The complex joint SEA model shows good agreement over the frequency range at 3000rpm as shown in Fig. 6.33. The simple joint SEA model under predicts the saloon SPL by around 3 dB between 125Hz and 1600Hz. The basic model under predicts saloon SPL because of the weaker transmission between the firewall and floor and between the firewall and windscreen as discussed previously.

All the predicted saloon SPLs shown in Figs. 6.31-6.34 assumed a saloon reverberation time of 0.05s as shown in Fig. 6.6. If the measured TLF shown in Fig. 6.6 had been used in the SEA models then all the predicted SPLs would increase below 800Hz. The change in predicted SPL would increase as frequency reduced reaching a maximum value of approximately 7.5dB around 125Hz. The level of agreement between measured and predicted SPL at 5700rpm shown in Figs. 6.31 and 6.32 would be reduced particularly below 250Hz where the agreement was not so good anyhow. Saloon SPL at 3000rpm predicted using the complex joint model would not agree quite as well as shown in Fig. 6.33 at lower frequencies. The agreement between the simple joint SPL prediction at 3000rpm would be better than shown in Fig. 6.34.

The power inputs at the front exhaust mounts have no significant effect on any of the saloon SPL predictions when the engine is running at 3000rpm, this is apparent by the fact that the connected and unconnected predictions are almost identical. The measured SPL with the exhaust connected and unconnected fluctuate by up to 5dB in relation to one another over the frequency range 250Hz to 630Hz. The 95% confidence intervals for the saloon SPL measurements with the exhaust connected and unconnected are shown in Figs. 4.1 and 4.2. respectively. The 95% confidence intervals are around ±4dB (unconnected) and ±2dB(connected) between 250Hz and 630Hz which would suggest that the fluctuation between the connected and unconnected SPL could be random. Both SEA models suggest that the least significant power inputs at all three engine speeds are those into the left and right engine mounts on the front wheel arch panels (103,203). Power input at the rear exhaust mounts on panel 209 and transmission of sound through the firewall make only a minor contribution to saloon SPL at all three engine speeds according to both SEA models. Both models suggest that the two power inputs into the firewall (104) cause the greatest SPL in the saloon at lower frequencies. The acoustic and structural firewall power inputs are plotted in Figs. 6.35 and 6.36 in order to establish their relative importance. The structural power input is from the rear engine centre member mounting point and is shown using solid lines. The acoustic power is from the engine compartment and is shown using dashed lines.

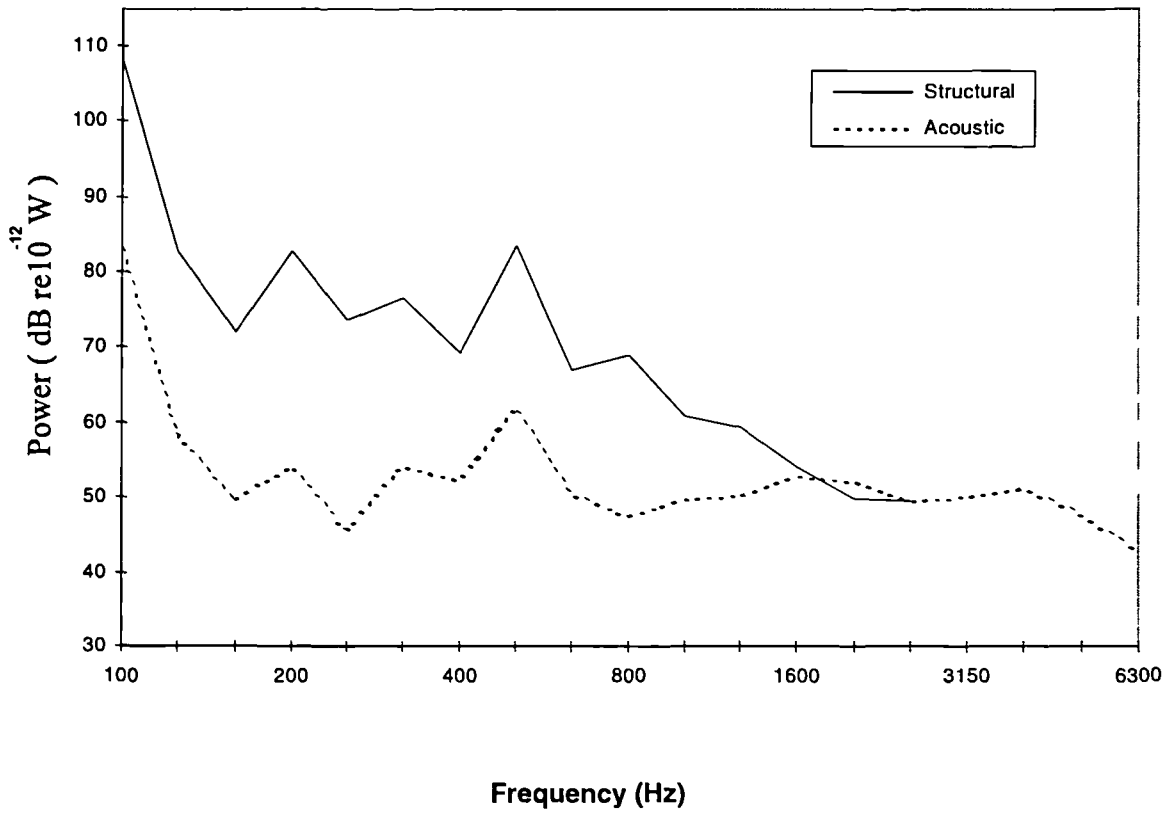

Figure 6.35: Structural and acoustic power inputs to the firewall (104) at 3000rpm.

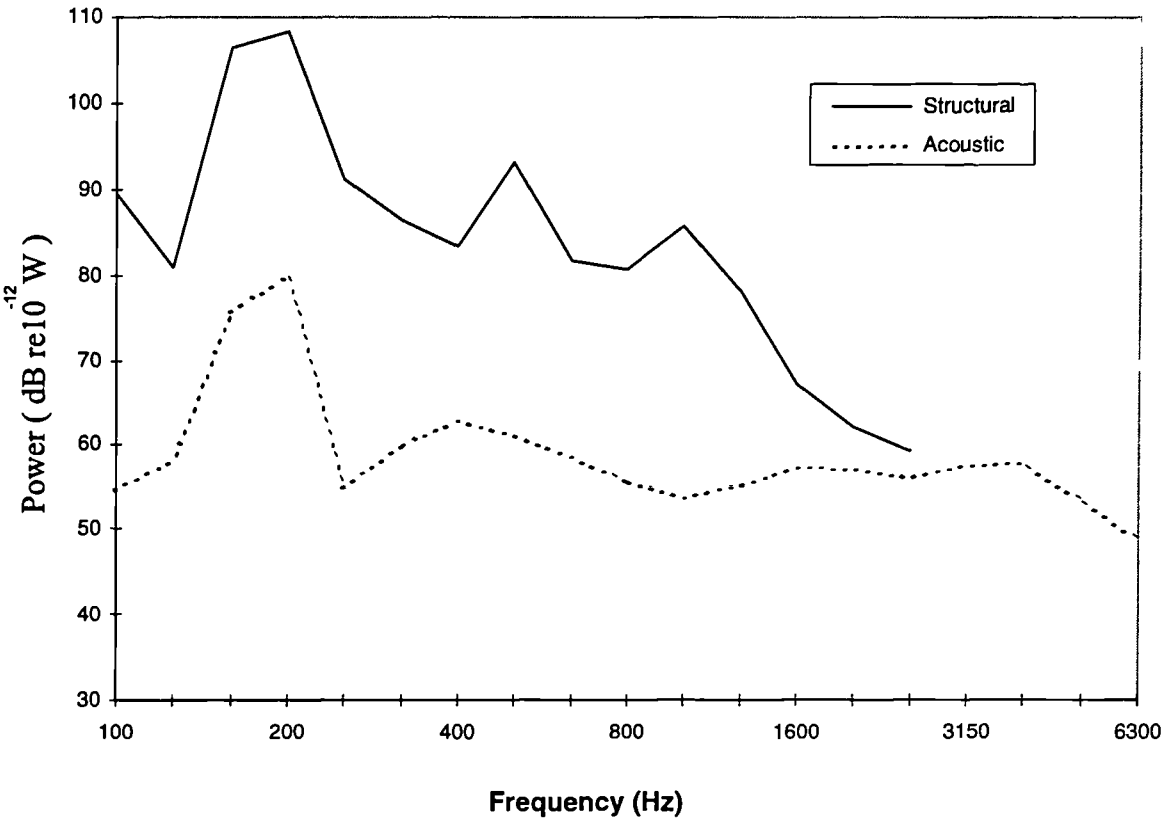

Figure 6.36: Structural and acoustic power inputs to the firewall (104) at 5700rpm.

Fig. 6.35 shows that at 3000rpm the acoustic power is most significant of the two above 1600 Hz with the structural input dominating below 1600Hz. Fig. 6.36 shows that at 5700rpm the dominant power is input to the firewall is structural below around 3000Hz and acoustic above this frequency. Structural power inputs are only given up to 2500Hz in Figs. 6.35 and 6.36 because the engine centre member rear mobility measurements were not available above this frequency.

6.7. In-Plane Wave Energy

The complex joint models include in-plane waves in the panels unlike the joints used in the basic SEA model. The SEA model which used the complex joint transmission coefficients considered only bending wave energy in the body panels. The transmission coefficients from bending to in-plane waves predicted by the complex joint models were omitted from the SEA model. This is equivalent to assuming that the in-plane energy generated in all the connected panels by an incident bending wave remains in the source panel as bending wave energy. It was assumed that the effect of this approximation would be minimal because bending to longitudinal and transverse wave transmission coefficients were usually at least 20dB less than bending to bending over the entire frequency range.

In order to test this assumption the basic joint SEA model was re run with bending longitudinal and transverse subsystems and CLFs. CLFs for the Bending Longitudinal and Transverse (BLT) model were calculated using the corner joint model described by Craven&Gibbs [6], the elastic joint was the simpler of the two joint models described by Mees&Vermeir [10]. The point and acoustic couplings in the BLT basic joint SEA model were identical to those of the bending only model. Within each panel the same ILFs (Table (6.3)) were used for bending and in-plane subsystems.

The bending TLFs and ALDs predicted using the BLT model differed from the bending only model by only a fraction of a dB over most of the frequency range shown in the results. Typically the bending TLFs and ALDs predicted using the BLT model were identical within one or two decimal places (in dB) to bending only model results across the frequency range.

Saloon SPLs resulting from all the engine noise power inputs discussed in Section 6.7.3 were calculated using the basic joint BLT model. SPLs resulting from the acoustic power inputs through the floor and firewall of the vehicle were unchanged. Saloon SPLs resulting from acoustic and structural power inputs to the firewall were at most 1dB higher at the upper end of the frequency range (6300Hz). This is because of flanking transmission(firewall to floor and firewall to windscreen) through the in-plane subsystems. Saloon SPL resulting from power injected at the front exhaust mounts was identical to within one decimal place (in dB). The total saloon SPL predicted using the BLT model resulting from all the engine noise power inputs differed by at most 0.6 dB from the bending only prediction between 100Hz and 6300Hz when the engine was running at 3000rpm. The BLT and bending only models were in better agreement than this for total saloon SPL using the 5700rpm power inputs.

As a further check the bending to bending CLFs from the BLT model were used in a bending only model and the results compared with those from the BLT model. The TLFs, ALDs and SPLs showed a similar level of agreement as the bending only model.

The bending to in-plane transmission coefficients predicted by the complex joint models were typically at least 20dB less than bending to bending over the entire frequency range. The bending to in-plane transmission coefficients predicted by the BLT models were less

than bending to bending but the difference was usually not as large as with the complex joint models. This would suggest that the complex joint SEA results will be less effected by the omission of in-plane subsystems than the basic joint results.

The omission of in-plane subsystems will also effect the predicted results when there are significant losses at the joint because the bending only model assumes that any bending wave energy incident upon the joint which is not transmitted is reflected or transmitted.

These tests show that the omission of in-plane wave energy from the SEA models presented in Sections 6.4 and 6.5 will not greatly effect the predicted results.

6.8. Losses in Joints

The elastic layers in the complex joint models were assumed to have a loss factor of 0.1 which is typical for rubber (See Cremer *et al* [1]). The elastic layers in the basic joint models were assumed to have no damping. The bending only model assumes that all the bending wave energy incident upon the joint that is not transmitted must be reflected as bending wave energy back into the source panel. This is not the case when some of the energy is lost in the joint. It was assumed that the energy lost to each panel in the joint would be small in relation to the panel damping losses. In any case the ILFs used in the models gave reasonable agreement between measured and predicted TLFs.

In order to ascertain the effect of joint damping the ILFs of the subsystems connected to elastic layers were increased to include the losses in the joints. One minus the sum of the transmission coefficients for an incident bending wave gives the joint losses in the form of a transmission coefficient. This may be used in equation (2.97) to calculate the additional ILF contribution from the joint for the source panel. Summing the additional damping for each elastic layer gives to total panel ILF adjustment.

With the joint damping included the predicted TLF of the roof panel increased by 0.8dB at 250Hz, this was the largest increase between 125Hz and 2500Hz. The firewall TLF increased by at most 0.3dB over the frequency range (125Hz - 2500Hz). The windscreen TLF increased by at most 1.5dB over the frequency range (125Hz - 2500Hz). The predicted ALD from the roof to windscreen using the adjusted ILFs is at most 1.5dB

lower than that shown in Fig. 6.22 and on average only 0.9 dB lower. The predicted ALD between the floor and the firewall is at most 0.9 dB lower than the complex joint prediction shown in Fig. 6.23. The predicted saloon SPL resulting from power injected into the floor is up to 0.03dB lower than predicted prior to the ILF adjustments. The predicted saloon SPL resulting from power injected into the firewall is 1.1dB lower than predicted prior to the ILF adjustments at 250Hz and around 0.5 dB lower on average between 100Hz and 6300Hz. The effects of increasing ILFs is to reduce transmission which is opposite to the effect observed by including in-plane waves within the model.

These results suggest that the effect of omitting the contribution to subsystem damping from the joint losses is minimal in the complex joint model, but this may not have been the case if the subsystem in question has a very low TLF.

6.9. Discussion

The ILFs of some materials used in the Micra may vary with frequency. To simplify the calculations the panel ILFs were assumed constant with frequency, this introduces an error as measured ILFs for isolated panels typically reduce by around 5 dB between 125 and 10kHz (see Fig 5.5). Some of the measured panel TLFs on the Micra dropped by up to 10dB between 125Hz and 10kHz whereas the predicted values only fell by about 5 dB. The difference is probably largely because the panel ILFs have been assumed constant. If the ILFs were assumed to reduce with frequency then the upward slope with frequency of the predicted ALD curves in Figs. 6.22 to 6.25 would be increased. Reverberation time measurements of coupled panels do not necessarily yield the TLF of the test panel as some of the energy flowing out of the test panel may flow back again and can result in non linear decay curves (See Lyon&DeJong[36]) however the error can be minimised by choosing the early part of the decay curve. Measured and predicted TLFs were usually within 5dB over the entire frequency range which suggests that the panel ILFs were realistic. Above 800 Hz Reverberation time tests on the saloon gave an almost constant value of 0.05s shown by the solid line in Fig. 6.6

The complex joint SEA model generally predicted the measured structural ALDs with reasonable accuracy, but only when the dominant transmission between the source and receiving panel was across line boundaries. Transmission up the rear side wing panels to

the roof was not accurately predicted by either SEA model. Transmission of vibration across door hinges was not accurately predicted by either model. The nature of the information required from an SEA model will determine which structural or acoustic couplings are the most important. For example, the transmission between the body panels at the rear of the vehicle were found to have a negligible effect on predicted saloon SPL resulting from engine noise. This means that the structural transmission at the rear of the vehicle and up the rear side wings need not be accurately known to calculate saloon engine noise. If one wished to predict the saloon SPL resulting from road noise then it may be important to accurately predict the structural transmission from the front and rear wheel arches into connected body panels. The accuracy of the predicted coupling between the wheel arches and the other panels was not tested experimentally. The rear wheel arch panels are more highly curved than most and this may have to be taken into account at lower frequencies when calculating transmission. If the objective were to predict saloon SPL resulting from aerodynamic noise then the transmission of sound through the roof(106)-cavity(5)-roof trim(305) could be an important path and SEA model may have to be refined in this area.

The complex joint SEA model predicted the saloon SPL accurately across the frequency range (200Hz - 6300Hz) with the engine running at 5700rpm and 3000rpm. When the engine was running at 700 rpm the measured saloon SPL was dominated by back ground noise at frequencies above 100Hz. The simple joint SEA model predicted the saloon SPL accurately across the frequency range (100Hz - 6300Hz) with the engine running at 5700rpm but under predicted the saloon SPL by around 3dB between 125Hz and 1600Hz when the engine was running at 3000rpm. The dominant path of power flow from the firewall to the saloon is via the windscreen below 250Hz and via the floor panels (111 and 211) above 250Hz. The complex joint model predicted stronger transmission between the firewall and the floor panels than the Basic model. This is why the saloon SPLs predicted using the complex joint model are higher than those of the basic model.

The dominant contributor to the SPL in the saloon at 5700 rpm with the front exhaust mounts disconnected is (according to the both SEA models) the structural power input into the firewall below around 300Hz and direct transmission of sound through the floor above around 1000Hz. When the front exhaust mounts are connected at 5700rpm they become the dominant cause of noise in the saloon between around 125Hz and 1kHz

according to both the complex and the basic SEA models. Both SEA models accurately predict the saloon SPL caused by the power injected at the exhaust mounts.

With the engine running at 3000rpm the power inputs to the firewall are the dominant causes of engine noise in the saloon below around 500 Hz according to both SEA models. There are two power inputs to the firewall in the SEA models. One is structural and represents the power flowing into the firewall from the engine centre member (shown in Fig. 6.2.) This power input was estimated as described in Section 6.5.3. There are a number of possible sources of error in this estimate. Only the vertical mobility and acceleration level of the attachment point was measured. Any additional power flowing into the body of the vehicle as a result of non vertical vibrations or twisting motions of the engine centre member will not be measured. This would lead to an under estimate of the power input rather than an overestimate. The mobility was measured with the engine centre member in place which will give a lower value than if it were disconnected. This increase in the real part of the impedance will lead to an over estimate of the power input given by equation (6.5). This effect was thought to be minimal however because the engine centre member is attached with bolts through rubber grommets which are likely to have a much higher mobility than the body of the vehicle. Another possible source of error in structural power flow calculations concerns the measured acceleration/velocity of the structure of the vehicle at the point of power injection. If the power source were disconnected completely from the vehicle, vibration would still occur at this point as a result of the other power inputs and one might erroneously calculate additional power flow. This error is most probably small however as the magnitude of vibration caused by a distant power source is likely to be small compared to that produced by one attached at the point of measurement, and if not it would suggest that the distant power input was much larger anyway.

The other power input to the firewall was due to acoustic excitation in the engine compartment. Estimates of this power flow were made as described in Section 6.5.3. These estimates were made on the assumption of a diffuse reverberant sound field in the engine compartment. This may not be particularly accurate because of the small size of the cavity between the engine and the firewall which is roughly 50-150mm wide. Fig. 4.3 shows the 95% confidence intervals for the measured SPL in the engine compartment. The 95% confidence intervals are around ± 10dB (between 125Hz and 6300Hz) when the

engine is running at 5700rpm and around ± 5dB at 3000rpm. These are large confidence intervals but cannot explain any low frequency discrepancies between measured and predicted saloon SPL as the acoustic power input to the firewall is only important above around 2500Hz as shown in Figs. 6.35 and 6.36.

Both the simple and the complex joint SEA models suggest that engine noise (at 3000rpm and 5700rpm) enters the saloon of the Nissan Micra mostly by radiation from or transmission through the floor panels above 250 Hz. Therefore a reduction in saloon engine noise above 250Hz might best be achieved by applying extra damping and or a Sound Barrier Assembly to the floor of the Vehicle.

Both SEA models had no acoustic coupling from the firewall into the saloon. Coupling was omitted because it was assumed that the Sound Barrier Assembly and the dash assembly reduced radiation into the saloon to a negligible level in relation to the other causes of saloon SPL. This assumption was not justified theoretically but there are two factors that suggest it is true. The large difference (Insertion Loss) evident between TL of the bare firewall and the firewall with SBA attached (Shown in Fig. 6.4) suggests a similarly large reduction in the radiation efficiency of the firewall is likely. The Transmission Losses shown in Fig. 6.4 are themselves conservative as they did not include the effect of the dash assembly or any of the other items attached to the firewall such as the fan/heater or the frame supporting the steering column. The other factor which would seem to justify omission of firewall radiation is the good level of agreement between the measured and predicted saloon SPLs when this coupling is omitted from the SEA models. More theoretical and experimental work is required to predict the radiation efficiency of body panels with Sound Barrier Assemblies and or dash boards attached.

The SEA models in this Chapter assume that the power injected at engine and exhaust mounts flow directly into the body panels. In a vehicle the power is injected into reinforced sections from which it flows into the body panels. It is possible that a significant proportion of power could flow through the reinforced sections in the form of bending torsional and longitudinal waves thereby increasing the transmission of energy through the car. This behaviour could possibly be modelled by including beam subsystems into the model. The omission of beam subsystems is unlikely to effect the

predicted ALDs as the power is input directly into the body panels during these tests and the complex joint model can calculate the transmission across the beams.

The omission of beam structures, radiation from the firewall and cross mobility terms from the power injection measurements reduce the certainty in the SPL predictions. It has not been proved in this work that these can be omitted in general from an SEA model of a car.

Given the simplistic nature of some of the approximations discussed in this Chapter the accuracy of the predicted ALDs and SPLs using the SEA models were reasonable. Ranking the sources and paths of noise in order of importance as demonstrated in Section 6.5.3. would allow a manufacturer to target their noise countermeasures effectively. This would be considerably more efficient and less time consuming than trial and error alone.

6.10. Conclusions

Complex joint modelling techniques described in Chapter 3 are reasonably effective in predicting transmission between the body panels of a modern motor vehicle, where the boundary length is greater than one wave length and the joint is reasonably uniform along its length. Results showed best agreement when panels were only slightly curved. It is possible to calculate transmission between cylindrical panels but the panels in the SEA models of this Chapter were flat.

Simple right angled joints between panels with no beam at the joint do not in general accurately predict transmission between the body panels of a modern motor vehicle.

Some of the panel joints in the Micra are too short to be treated as infinite in length at lower frequencies and should probably be treated as point contacts.

Transmission across door hinges can not be accurately treated as simple point contacts between flat panels. Some form of modelling which takes into account the complex shapes of the sheet metal pressings from which doors and hatches are made must be developed.

The SPL in the saloon as a result of engine noise was measured in 1/3rd octave bands at three engine speeds (700rpm, 3000rpm, 5700rpm). The peak value at each engine speed occurred in the band containing the second harmonic of engine speed. Saloon SPL was predicted accuracy by the complex joint SEA model and the simple SEA model at 5700rpm. The complex joint model accurately predicted saloon SPL at 3000rpm and the basic joint model under predicted saloon SPL over most of the frequency range by around 3dB.

Plotting the predicted SPLs resulting from the various acoustic and structural power inputs separately allowed them to be ranked in order of their contribution to saloon SPL.

At 5700 rpm with the exhaust system connected the SPL in the saloon is dominated by three noise sources. Below around 300Hz the power flowing into the firewall through the rear engine mount makes the largest contribution to saloon SPL. Between around 300Hz and 1000Hz the SPL is dominated by power injected at the front exhaust mounts. This was caused by exhaust misalignment which was introduced to investigate the problem. Above 1000Hz the saloon SPL is caused largely by the transmission of sound through the floor of the vehicle. At 5700 rpm with the exhaust system disconnected the SPL in the saloon is dominated by power flowing into the firewall and the sound transmitted through the floor.

At 3000rpm SPL in the saloon is dominated by two sources. Below around 500Hz the dominant cause of saloon noise is the structural and acoustic power injected into the firewall. Above around 500Hz transmission of sound through the floor of the vehicle is the dominant cause of noise in the saloon.

Both the SEA models suggest that the most important paths of power flow from the firewall into the saloon are via the windscreen below 250Hz and via the floor panels above 250Hz.

Chapter 7

Conclusions

7.1 Introduction

This research was undertaken to investigate the application of SEA to the prediction of noise in a motor vehicle. The emphasis is primarily on structural transmission and improving the accuracy of structural CLFs by including more joint details into calculations of wave transmission. Results and conclusions from each chapter are summarised here followed by a discussion of future research.

7.2 Summary of Results and Conclusions

Chapter 2 describes some of the theory concerning the transmission of vibrations in structures. It was concluded that bending wave energy is probably the most important form of structural vibration energy in motor vehicle body panels. This is because their low mechanical impedance tends to bring about high energy levels and their transverse motion can cause high levels of acoustic radiation. It was further concluded in Chapter 2 that thin plate bending theory is adequate for the treatment of bending waves in typical motor vehicle body panels within the audible frequency range. The radiation and transmission of sound by body panels and windows was also discussed in Chapter 2.

Chapter 3 describes complex joint modelling techniques which allow the calculation of wave transmission coefficients between flat and or curved panels joined at line boundaries. Junctions of arbitrary complexity can be built up in the model from simple elements which will account for the effect of resonances within the joint itself. The joints between the body panels of a modern motor-vehicle are typically reinforced with steel pressings spot welded into place. This construction method produces complex joint structures which may be studied using the techniques in Chapter 3.

A curved corner joint between identical semi-infinite flat panels was investigated by assembling a rounded section of panel and two semi-infinite flat panels in the model. Bending waves are almost completely transmitted below a limiting angle of incidence, above this angle the bending waves are almost completely reflected. As the frequency

rises this angle increases asymptotically toward 90°. Dispersion curves for the rounded panel section were examined to provided an explanation for the abrupt change in transmission with the angle of incidence. Complete transmission occurs when the curved panel bending wave exists on the curved section with the required trace wave number along the boundary, this is a bending wave similar to that found on flat plates. When this wave is not present with the required trace wave number the incoming wave is largely reflected.

Chapter 5 presents an experimental investigation of curved corner joint transmission. These experiments were designed to test the accuracy of curved panel joint transmission coefficients predicted using the model discussed in Chapter 3. Steel panels were rolled over a short section near the middle to form two flat panels joined by a rounded section. One of the panels was coated with damping treatment. ELDs were measured when the undamped panel was tapped randomly with a hammer. Transmission coefficients for the joints were predicted as in Chapter 3 and were used in SEA and WIA models of the panels to predict the ELD.

Two Curved corner joint experimental apparatus were constructed with different joint radii. The measured ELD for the two different joint curvatures were nearly identical over the frequency range (125Hz-3150Hz). Between 3150Hz and 10kHz the ELD for the panels connected by the larger radius joint was slightly larger (stronger transmission) than for those connected by the smaller radius joint. Predicted ELD using WIA for the larger radius joint was lower (lower transmission) at low frequencies and higher at high frequencies than for the smaller radius joint. The same was true of the ELDs predicted using SEA but the difference between small and large radii results were less.

At low frequencies (below 300Hz) the SEA predictions were in reasonable agreement with the measured ELDs. As the frequency increased the ELDs predicted using SEA became higher (stronger transmission) than the measured ELDs by around 5-10dB.

At 125Hz the ELDs predicted using WIA were around 10-15dB below the measured values. The WIA predicted ELDs approached the measured values at higher frequencies and were in good agreement in the 8kHz and 10kHz $1/3^{rd}$ octave bands for both joint radii.

The ELDs for the two different joint radii predicted using SEA were generally within 2dB over most of the frequency range. The ELDs predicted using WIA were more sensitive to the radius of the joint at low frequencies and differed by up to approximately 7dB. The measured ELDs for the two joint radii differ by a maximum of around 3dB at high frequencies. therefore it would appear that the SEA model shows a more realistic sensitivity to the joint radius at low frequencies than the WIA model.

ELD predictions were also made using transmission coefficients for a sharp corner panel joint using both SEA and WIA models. Using these transmission coefficients SEA over predicted transmission across the rounded joints by around 5dB over most of the frequency range. WIA was in fairly good agreement over the entire frequency range using the sharp corner transmission coefficients.

None of the predictions matched the shape of the measured ELD curves particularly well and a number of possible explanations were offered. The work in Chapter 5 neither validated nor invalidated the curved joint transmission coefficients, more research is required in this area.

For comparison with rounded results a panel was folded to form two joined by a sharp corner joint. These panels were irregular in shape. SEA and WIA were again used to predict the ELD. Predicted ELD using SEA and WIA were similar and gave good agreement with the measured results. This is probably because the irregular shape of the panels encourage more diffuse wave fields.

The body panels of motor vehicles are typically irregular in shape. Irregularity in curvature will make SEA modelling less straight forward but irregularity in the shape and number of panel boundaries are likely to improve the accuracy with which SEA can predict structural transmission.

The WIA field symmetry assumption which states that the wave intensity in a panel must have axes of symmetry parallel to all completely reflective boundaries was investigated. In the two panel systems tested it made less than 2dB difference to the predicted ELDs.

Chapter 6 describes two SEA models of a Nissan Micra motor vehicle. The models consist of flat plates and acoustic volumes. Only bending wave energy was considered on the panels. One of the models (complex joint model) used CLFs across line boundaries

calculated with the complex joint modelling techniques of Chapter 3, the other (simple joint model) used only simple right angled panel joints with elastic layers around windows. Coupling across door and other hinges was modelled as simple point contacts between panels in both models. Structure borne sound transmission was measured in the form of ALDs between the panels of the vehicle when tapping the source with a hammer.

The SEA model using the complex joint CLFs showed noticeably improved agreement with measured ALD results for panels in situations where the ALDs were sensitive to the influence of line coupling.

The SPL in the saloon due to engine noise was measured as was the acceleration level of engine and exhaust mounts. Mechanical mobility at engine and exhaust mounts were measured and these used along with the acceleration levels to estimate the structural power inputs. Acoustic power inputs were predicted using measured SPL in the engine compartment and underneath the vehicle with calculated values for the radiation efficiency and transmission loss of the firewall and vehicle floor. Saloon SPL was measured with and without the front exhaust mounts connected in order to investigate a noise problem caused by exhaust misalignment. The misalignment was introduced deliberately but can occur during maintenance if the exhaust system is incorrectly fitted. Saloon SPL was predicted accurately by the complex joint SEA model and the simple joint SEA model at 5700rpm. The complex joint model accurately predicted saloon SPL at 3000rpm and the basic joint model under predicted saloon SPL over most of the frequency range by around 3dB.

Plotting the predicted SPLs resulting from the various acoustic and structural power inputs separately allowed them to be ranked in order of their contribution to saloon SPL.

At 5700 rpm with the exhaust system connected the SPL in the saloon is dominated by three sources. Below around 300Hz the power flowing into the firewall makes the largest contribution to saloon SPL. Between around 300Hz and 1000Hz the SPL is dominated by power injected at the front exhaust mounts. This was caused by exhaust misalignment which was deliberately introduced to investigate the problem. Above 1000Hz the saloon SPL is caused largely by the transmission of sound through the floor of the vehicle. At

5700 rpm with the exhaust system disconnected the SPL in the saloon is dominated by power flowing into the firewall and the sound transmitted through the floor.

At 3000rpm SPL in the saloon is dominated by two sources. Below around 500Hz the dominant cause of saloon noise is the structural and acoustic power injected into the firewall. Above around 500Hz transmission of sound through the floor of the vehicle is the dominant cause of noise in the saloon.

The most important paths of power flow from the firewall into the saloon are via the windscreen below 250Hz and via the floor panels above 250Hz.

Both the SEA models suggested that most of the engine noise in the saloon is generated by radiation from or transmission through the floor panels. The floor panels are therefore probably the best areas to apply noise countermeasures such as extra damping or Sound Barrier Assemblies.

At 5700 rpm both SEA models correctly predicted the saloon SPL at around 400 Hz which was dominated by the power injected at the front exhaust mounts. This was caused by exhaust misalignment which was deliberately introduced to investigate the problem.

The noise problem at 5700rpm resulting from exhaust misalignment was investigated. At around 400Hz the measured SPL with the exhaust connected was 10dB higher than when not connected. SEA predictions also clearly showed the effect with the exhaust mount becoming the dominant power input around 400Hz.

The omission of beam structures, radiation from the firewall and cross mobility terms from the power injection measurements reduce the certainty in the SPL predictions. It has not been proved in this work that these can be omitted in general from an SEA model of a car.

The ability of SEA to predict which power inputs and paths are the most important would allow a car manufacturer to focus their noise countermeasures more quickly and effectively than by trial and error alone. In addition SEA models can be built before the vehicle exists physically which could give the manufacturer a head start in bringing the noise in a new production model down to acceptable levels prior to releasing it for sale.

This could reduce the time from conception of a vehicle to its release which is an objective that car manufacturers devote a large amount of time and resources to achieving.

7.3 Future Research

The complex joint modeller is very useful as it stands but a number of additional elements would be helpful in calculating CLFs for motor-vehicle structures. Orthotropic plate elements would allow some measure of the effect of corrugations frequently used to stiffen panels in cars. Three or four node solid elements could be introduced to allow very detailed modelling of the precise cross section for example, a rubber joints around the windows. At present the modeller can calculate transmission from, and too, curved panels joined along a straight line parallel to the axis of curvature. It would be useful to calculate transmission across arbitrary lines of intersection between panels curved in more than one axis this is considerably more complicated however.

Further research is required into rounded corner joints as the inability of complex joint model to predict the transmission was not fully explained. It would be interesting to compare the measured and predicted results with analytical results from a Finite Element model. More experimental work would also be use full to see if a change in transmission with joint curvature can be observed.

The SEA models in the Micra study contained only flat panels in bending, the next logical step is to use complex joint models in an SEA model where the subsystems include curved body panels and cylinders for the sills and door pillars. A future study could also investigate the effects of in-plane wave subsystems and in-plane power inputs at engine and exhaust mounts.

The increase in Transmission Loss through the firewall as a result of the Sound Barrier Assembly was calculated. The reduction in radiation efficiency caused by the Sound Barrier Assembly was not calculated. Experimental and theoretical investigation of the reduction in the radiation efficiency caused by the Sound Barrier Assembly is needed. The effect of the dash assembly attached to the firewall on the Transmission Loss and radiation efficiency of the firewall was not investigated in this study. A study of these effects would also be very helpful in building motor vehicle SEA models in future.

A method of predicting transmission into doors and other parts of the vehicle connected at "point" or short line contacts is required which includes the effect of joint structure details.

References

[1] L. Cremer, M. Heckl, and E. E. Ungar (1988) " Structure-Borne Sound", 2nd Edition, Springer Verlag

[2] E. Eichler (1964) "Plate-Edge Admittance", Journal of the Acoustical Society of America 36, 2, 344-348

[3]G. L. Lamb Jr (1961) "Input Impedance of a Beam Coupled to a Plate", Journal of the Acoustical Society of America 33, 5, 628-633

[4] H. G. D. Goyder and R. G. White (1980), "Vibration Power Flow From Machines into Built-Up Structures, Part II: Wave Propagation and Power Flow in Beam-Stiffened Plates", Journal of Sound and Vibration **68, 1,** 77-96

[5] B. M. Gibbs and C. L. S. Gilford (1976), "The use of Power Flow Methods for Assessment of Sound Transmission in Building Structures", Journal of Sound and Vibration **49,** 267-286

[6] P. G. Craven and B. M. Gibbs (1981), "Sound Transmission and Mode Coupling at Junctions of Thin Plates, Part I: Representation of the Problem", Journal of Sound and Vibration **77, 3** 417-427

[7] B. M. Gibbs and P. G. Craven (1981), "Sound Transmission and Mode Coupling at Junctions of Thin Plates, Part II: Parametric Survey", Journal of Sound and Vibration **77, 3,** 429-435

[8] R. S. Langley, and K. H. Heron (1990), "Elastic Wave Transmission Through Plate/Beam Junctions.", Journal of Sound and Vibration **143** 241-253

[9] R. S. Langley (1994), "Elastic Wave Transmission Coefficients and Coupling Loss Factors For Structural Junctions Between Curved Panels. ", Journal of Sound and

Vibration **169** 297-317

[10] P. Mees, and G. Vermeir (1993), "Structure-Borne Sound Transmission at Elastically Connected plates", Journal of Sound and Vibration **166**

[11] I. Bosmans, P. Mees, and G. Vermeir (1996), "Structure-Borne Sound Transmission Between Thin Orthotropic Plates: Analytical Solutions", Journal of Sound and Vibration **191,** 1, 75-90

[12] G. Fraser and J. A. Steel (1996), " Structural Coupling at Joints in Motorvehicles" Proceedings of *internoise96* , 1411-1414

[13] K. De Langhe, I. Moens P. Sas and D. Vandepitte (1996), "The Application of Finite Elements Models to Study the Energy Flow Properties of Structural Junctions", Proceedings of *internoise96* , 2891-2894

[14] K. De Langhe, P. Sas and D. Vandepitte (1996), "The Use of Wave-Absorbing Elements for the Evaluation of Transmission Characteristics of Beam Junctions", Transactions ASME Journal of Vibration and Acoustics

[15] K. De Langhe, I. Moens P. Sas and D. Vandepitte (1994), "Numerical Simulation of Waves in Beams by Using the Finite Element Method", Proceedings ISMA 19, 1, 471-480, Leuven, Belgium

[16] C. Simmons (1991), "Structure-Borne Sound Transmission Through Plate Junctions and Estimates of SEA Coupling Loss Factors using the Finite Element Method", Journal of Sound and Vibration **144,** 2, 215-227

[17] J. A. Steel and R. J. M. Craik (1994), "Statistical Energy Analysis of Structure-Borne Sound Transmission by Finite Element Methods", Journal of Sound and Vibration **178,** 4, 553-561

[18] J. W. S. Rayleigh (1877), " Theory of Sound", Dover Publications

[19] L. Cremer, (1942), "Theorie der Schalldammung dunner Wande bei Schragen einfall" Akust. Ztg. 7, 81

[20] F. Fahy, (1985), "Sound and Structural Vibration Radiation, Transmission and Response", Academic Press Inc. London

[21] E. C. Sewell, (1970), " Transmission of Reverberant Sound Through a Single Leaf Partition Surrounded by an Infinitely Ridged Baffle", Journal of Sound and Vibration **12,** 21-32

[22] F. G. Leppington, K. H. Heron and E. G. Broadbent (1987) and S. M. Mead " Resonant and Non Resonant acoustic properties of elastic panels. II. The Transmission Problem", Proceedings of the Royal Society of London, A412, 309-337

[23] L. L. Beranek, and G. A. Work (1949), "Sound Transmission Through Multiple Structures Containing Flexible Blankets", Jounrnal of the Acoustical Society of America, 21, 419-428

[24] L. L. Beranek, (1947), "Aacoustic Properties of Homogeneous, Isotropic Rigid Tiles and Flexible Blankets", Jounrnal of the Acoustical Society of America, 19, 4, 556-568

[25] M. J. Crocker and A. J. Price (1969), " Sound Transmission Using Statistical Energy Analysis", Journal of Sound and Vibration **9,** 469-486

[26] R. J. M. Craik and R. Wilson (1995), " Sound Transmission Through Masonry Cavity Walls", Journal of Sound and Vibration **179, 1,** 79-96

[27] J. S. Bolton, N. M. Shiau, and Y. J. Kang (1996), " Sound Transmission Through Multi-Panel Structures Lined With Elastic Porous Materials", Journal of Sound and Vibration 191, 3, 317-345

[28] J. S. Bolton and E. R. Green (1993), " Normal Incidence Sound Transmission Through Double-Panel Systems Lined with Relatively Stiff, Partially Reticulated Polyurethane Foam", Applied Acoustics 39, 23-51

[29] R. E. Wentzel and P. Saha (1995), "Empiricaly Predicting the Sound Transmission Loss of Double-Wall Sound Barrier Assemblies", SAE paper 951268

[30] C. E. Wallace (1972), " Radiation Resistance of a Rectangular Plate", Journal of the Acoustical Society of America, 51, 946-952

[31] G. Maidanik (1962), " Response of Ribbed Panels to Reverberant Acoustic Fields", Journal of the Acoustical Society of America, 34, 6, 809-826

[32] R. H. Lyon, and G. Maidanik (1962), "Power Flow Between Linearly Coupled Oscillators.", Journal of Acoustical Society of America **34** 623-639

[33] F. G. Leppington, E. G. Broadbent, F. R. S. and K. H. Heron (1982), " The Acoustic Radiation Efficiency of Rectangular Panels", Proc. R. Soc. Lond. A382, 245-271

[34] F. G. Leppington, E. G. Broadbent, F. R. S. and K. H. Heron (1984), "Acoustic Radiation from Rectangular Panels with Constrained Edges", Proc. R. Soc. Lond. A393, 67-84

[35] F. G. Leppington (1996), " Acoustic Radiation from Plates into a Wedge-Shaped Fluid Region: Application to the Free Plate Problem", Proc. R. Soc. Lond. A452, 1745-1764

[36] R. H. Lyon and R.G. Dejong (1995), "Theory and Application of Statistical Energy Analysis 2nd ed.", Butterworth-Heinemann, ISBN 0-7506-9111-5

[37] H. G. Davies (1971), "Exact Solutions for Response of Some Coupled Multimodal Systems", Journal of Acoustical Society of America **51, 1,** p387-401

[38] F. J. Fahy and A. D. Mohammed (1992), " A Study of Uncertainty in Applications of SEA to Coupled Beam and Plate Systems Part I: Computational Experiments", Journal of Sound and Vibration 158, p45-67

[39] R. J. M. Craik, J. A. Steel and D. I. Evans (1991), "Statistical Energy Analysis of Structure Borne Sound at Low Frequencies", Journal of Sound and Vibration 144, p95-107

[40] R. H. Lyon (1969), "Statistical Analysis of Power Injection and Response in Structures and Rooms", Journal of Acoustical Society of America 51, p393

[41] A. J. Kean and W. G. Price (1987), "Statistical Energy Analysis of Strongly Coupled Systems", Journal of Sound and Vibration 117, p363-386

[42] B. R. Mace (1992) "Power Flow Between Two Continuos One -Dimensional Subsystems : a Wave Solution", Journal of Sound and Vibration 154, p289-319

[43] P. W. Smith, Jr. (1962), " Response and Radiation of Structural Modes Excited by Sound", Journal of Acoustical Society of America **34,** p827

[44] E. Eichler (1965), "Thermal Circuit Approach to Vibrations in Coupled Systems and Noise Reduction of a Rectangular Box", Journal of Acoustical Society of America **37** , p995-1007

[45] R. H. Lyon (1963), " Noise Reduction in Rectangular Enclosures with One Flexible Wall", Journal of Acoustical Society of America **35,** p1791

[46] M. C. Bhattacharya, R. W. Guy and M. J. Croker (1971),"Coincidence Effect with Sound Waves in Finite Plates", Journal of Sound and Vibration 18, p157

[47] F. J. Fahy and R. B. S. Wee (1968), "Some Experiments with Stiffened Plates under Acoustic Excitation", Journal of Sound and Vibration 7, p431-436

[48] D. C. Green (1961), "Vibration and Sound Radiation of Damped and Undamped Flat Plates", Journal of Acoustical Society of America **33,** p1315

[49] R. V. Waterhouse (1968), "Statistical Properties of Reverberant Sound Fields", Journal of Acoustical Society of America **43,** p1436-1444

[50] S. H. Crandall, "Structural Response Patterns Due to Wide-Band Random Excitation", p366-389 of B. L. Clarkson *et al* (1977), "Stochastic Problems in Dynamics" Pitman, London

[51] P. J. Remington and J. E. Manning (1975), "Comparison of Statistical Energy Analysis Power Flow Predictions with 'exact' Calculation", Journal of Acoustical Society of America **57, 2,** p347-379

[52] E. K. Dimitriadis and A. D. Pierce(1988), "Analytical Solution for the Power Exchange Between Strongly Coupled Plates Under Random Excitation: A Test of Statistical Energy Analysis Concepts", Journal of Sound and Vibration 123, p397-412

[53] A. J. Kean and W. G. Price (1991), "A Note on the Power Flowing Between Two Conservatively Coupled Multi-Modal Subsystems", Journal of Sound and Vibration, 144, p185-196

[54] P. W. Smith (1979), "Statistical models of Coupled Dynamical Systems and the Transition from Weak to Strong Coupling", Journal of Acoustical Society of America **65,** p695-698

[55] T. D. Sharton and R. H. Lyon (1968), "Power Flow and Energy Sharing in Random Vibration", Journal of Acoustical Society of America 43, p1332-1343

[56] R. S. Langley (1989), "A General Derivation of the Statistical Energy Analysis Equations for Coupled Dynamic Systems.", Journal of Sound and Vibration **135** 499-508

[57] K. H. Heron (1990), " The Development of a Wave Approach to Statistical Energy Analysis", Proceedings of *internoise90*, Gothenburg, Sweden

[58] B. M. Gibbs (1974), "The Direct and Indirect Transmission of Vibrational Energy in Buildings", PhD Thesis, Aston University

[59] R. J. M. Craik (1980), "A Study of Sound Transmission Through Building Structures

Using Statistical Energy Analysis", PhD Thesis, Heriot Watt University

[60] J. A. Steel (1990), "Structural Vibration Transmission in Framed Buildings Using Statistical Energy Analysis", PhD Thesis, Heriot Watt University

[61] R. J. M. Craik (1996), " Sound Transmission Through Buildings: Using Statistical Energy Analysis", Gower Publishing Ltd.

[62] J. Trach, Jr (1985), "Vibration Transmission Through Machinery Foundations and Ship Bottom Structures", MSc Thesis, MIT

[63] R. G. Dejong (1985), "A Study of Vehicle Interior Noise Using Statistical Energy Analysis", SEA paper no. 850960, Surface Vehicle Noise and Vibration Conference Traverse City, p1-7

[64] B. Cimerman, P. Bremner, Y. Qian, J. A. Van Buskirk (1995), " Incorperating Layered Acoustic Trim Materials in Body Structural-Acoustic Models", SAE paper no. 951307

[65] L. L. Beranek and I. L. Ver (1992), "Noise and Vibration Control Engineering: Principles and Applications", John Wiley & Sons Inc.

[66] J. A. Steel (1996), " The Prediction of Structural Vibration Transmission Through a Motor Vehicle Using Statistical Energy Analysis", Journal of Sound and Vibration **193, 3,** p 691-703

[67] J. A. Steel (1994), " Sound Transmission Between Plates in Framed Structures", Journal of Sound and Vibration **178, 3,** p 379-394

[68] B. Dong, M. Green, M. Voutyras, P. Bremner, and P. Kasper (1995), "Road Noise Modelling Using Statistical Energy Analysis", SEA paper no. 951327, p761-765

[69] X. Huang, M. J. Moeller, J. J. Lee and R. Powell (1997), "Application of Statistical Energy Analysis (SEA) to the Development of a Light Truck Sound Package", SAE paper

[70] R. E. Powell, J. Zhu and J. E. Manning (1997), " SEA Modeling and Testing for Air borne Transmission Through Vehicle Sound Packages", SAE paper no. 971973

[71] D A. Bies , and S. Hamid (1980), "In Situe Determination of Loss Factors by Power Injection Method.", Journal of Sound and Vibration **70** 187-204

[72] J. Woodhouse (1981), "An Approach to the Theoretical Background of Statistical Energy Analysis Applied to Structural Vibration.", Journal of Acoustical Society of America **69**

[73] C. H. Hodges, P. Nash and J. Wood House (1987), "Measurement of Coupling Loss Factors by Matrix Fitting: An Investigation of Numerical Proceedures", Applied Acoustics, 22, p47-69

[74] B. L. Clarkson, and M. F. Ranky (1983), "On the Measurement of the Coupling Loss Factor of Structural Connections", Journal of Sound and Vibration, **94,** p249-261

[75] N. Lalor (1987), "The Maesurement of SEA Loss Factors on a Fully Assembled Structure.", ISVR technical Report no. 150

[76] N. Lalor (1990), "Practical considerations for the Measurement of Internal and Coupling Loss Factors on Complex Structures.", ISVR technical Report no. 182

[77] I. Carr and N. Lalor (1989), "The Prediction and Reduction of Noise from Engine Covers Using Statistical Energy Analysis", ISVR Contract Report no. 89/13, University of Southhampton

[78] L. Wu, A. Agren and U. Sundback (1991), " An Evaluation of System Modeling for Statistical Energy Analysis on a Fully Assembled Diesel Engine", Lulea University, Sweden, Research Report, Tulea 1991:30

[79] L. Wu, A. Agren and U. Sundback (1994), "Determination of Loss Factors for Statistical Energy Analysis of a Diesel Engine with Geometric Averaging Approach ", Acta Acustica, 2, p127-142

[80] J. Plunt, C. Fredo, and M. Sanderson (1993), "On the Use and Misuse of Statistical Energy Analysis for Vehicle Noise Control.", SAE Paper number 931301, p319-328

[81] H. Chen, M. O'Keefe, and P. Bremner (1995), "A Comparison of Test-Based and Analytic SEA Models for Vibro-acoustics of a Light truck.", SEA Paper no. 951329, p777-783

[82] J. L. Guyader, C. Boisson, C. Lesueur and P. Millot (1986), " Sound Transmission By Coupled Structures: Application to Flanking Transmission in Buildings", Journal of Sound and Vibration, **106,** p289-310

[83] K. H. Heron (1994), "Advanced Statistical Energy analysis.", Philosophical Transactions of the Royal Society of London SERIES A, **346,** p501-511

[84] R. S. Langley (1992), "A Wave Intensity Technique for the Analysis of High Frequency Vibrations", Journal of Sound and Vibration, **159,** p503-525

[85] R. S. Langley (1992), "A Dynamic Stiffness Technique for the Vibration Analysys of Stiffened Shell Structures", Journal of Sound and Vibration, **138,** p521-540

[86] C. Boisson, J. L. Guyader, P. Millot and C. Lesueur (1982), "Energy Transmission in Finite Coupled Plates, Part II: Application to an L Shaped Structure", Journal of Sound and Vibration, **81,** p93-105

[87] J. E. Manning (1994), " Formulation of SEA Parameters Using Mobility Functions.", Philosophical Transactions of the Royal Society of London SERIES A **346** 477-489

[88] W. T. Thomson (1988), "Theory of Vibration with Applications", 3rd Ed. Unwin Hyman Ltd.

[89] H. Kuttruff (1979), " Room Acoustics", 2nd Ed. Applied Science Publishers Ltd. London.

[90] F. G. Leppington, K. H. Heron and E. G. Broadbent and S. M. Mead (1986), " Resonant and Non Resonant acoustic properties of elastic panels. I. The Radiation Problem", Proceedings of the Royal Society of London, A406, 139-171

[91] Private communication of Expression for Free-Free Panel Radiation Efficiency by K. H. Heron to R. J. M.Craik of Heriot Watt University Dept. of Building Engineering and Surveying who passed the information to the author.

[92] A. J. Price, M. J. Crocker (1970), " Sound Transmission through Double Panels Using Statistical Energy Analysis", Journal of the Acoustical Society of America, **47**, p683-693

[93] K. H. Heron (1997), " Predictive SEA Using Line Wave Impedance's", IUTAM symposium on SEA, Southampton.

[94] R. S. Langley (1994), "Wave Motion and Energy Flow in Cylindrical Shells", Journal of Sound and Vibration, **169**, p29-42

[95] S. Timoshenko and S. Woinowsky-Kreiger (1959) "Theory of Plates and Shells", New York: McGraw-Hill

[96] D. J. Mead and N. S. Bardell (1986) "Free Vibration of a Thin Cylindrical Shell With Discrete Axial Stiffeners", Journal of Sound and Vibration **111**(2), p229-250

[97] S. Smith (1997), "Sound Transmission Through Light Weight Parallel Plates", PhD Thesis, Heriot Watt University

[98] T. Conely (1996), "Sound Transmission Through Ship Structures Using Statistical Energy Analysis", Proceedings of *internoise96*, p 2939-2942

[99] W. H. Press, B. P. Flannery, S. A. Teukolsky and W. T. Vetterling, "Numerical

Recipes in C , The Art of Scientific Computing", Cambridge University Press, 1988.

[100] B&K2032 Narrow Band dual Channel Analyser Instruction Manual.

[101] B&K2131 1/3rd octave Band Analyser Instruction Manual.

[102]. B&K2148 Portable Analyser Instruction Manual.

[103] E. Kreyszig (1993) "Advanced Engineering Mathematics" 7th Ed

[104] R. S. Langley (1994), "The Modal Density and Mode Count of Thin Cylinders and Curved Panels.", Journal of Sound and Vibration **169,** p43-53